

POWDER PROCESSING AND MECHANICAL PROPERTIES OF  $\text{Ag}_{0.86}\text{Pb}_{19}\text{SbTe}_{20}$  (LAST)  
AND  $\text{Pb}_{0.95}\text{Sn}_{0.05}\text{Te} - \text{PbS}$  8% (PbTe-PbS) THERMOELECTRIC MATERIALS

By

Jennifer Elisabeth Ni

A DISSERTATION

Submitted to  
Michigan State University  
in partial fulfillment of the requirements  
for the degree of

DOCTORATE OF PHILOSOPHY

Materials Science Engineering

2012

## ABSTRACT

### POWDER PROCESSING AND MECHANICAL PROPERTIES OF $\text{Ag}_{0.86}\text{Pb}_{19}\text{SbTe}_{20}$ (LAST) AND $\text{Pb}_{0.95}\text{Sn}_{0.05}\text{Te} - \text{PbS}$ 8% (PbTe-PbS) THERMOELECTRIC MATERIALS

By

Jennifer Elisabeth Ni

Thermoelectric (TE) materials convert between thermal and electrical energy and when used with existing processes will increase the efficiency via waste heat recovery.

$\text{Ag}_{0.86}\text{Pb}_{19}\text{SbTe}_{20}$  (LAST) and  $\text{Pb}_{0.95}\text{Sn}_{0.05}\text{Te} - \text{PbS}$  8% (PbTe-PbS) materials exhibit good thermoelectric (TE) properties and have potential applications as thermoelectric generators in waste heat recovery. However, to fully characterize the thermo-mechanical behavior of LAST and PbTe-PbS materials under in-service conditions, knowledge is needed of the mechanical and thermal properties at room and high temperature.

As fracture strength is inversely proportional to the square root of grain size, cast ingots were powder processed to reduce powder particle size. Three different powder processing methods were used (1) dry milling only, (2) wet milling only, or (3) dry milling and wet milling. The specimens were fabricated using hot pressing or pulsed electric current sintering (PECS) from planetary ball milled powders.

In this study, elastic moduli, including Young's modulus, shear modulus, and Poisson's ratio, were measured dynamically using resonant ultrasound spectroscopy (RUS) at room temperature and as a function of temperature up to 663 K. The room temperature porosity dependence for Young's modulus followed the empirical exponential relationships common for brittle materials, with a material dependent constant  $b_{PE}$  of 3.5 and 1.3 for LAST and PbTe-PbS,

respectively. The room temperature Young's modulus for a theoretically dense specimen was  $58.4 \pm 0.6$  GPa and  $56.2 \pm 0.4$  GPa for for LAST and PbTe-PbS, respectively. For hot pressed PbTe-PbS specimens, the Vickers indentations mean hardness and fracture toughness was  $1.18 \pm 0.09$  GPa and  $0.35 \pm 0.04$  MPa·m<sup>1/2</sup>.

The coefficient of thermal expansion is important for understanding the mechanical response of a material to a thermal gradient or a thermal transient. For PbTe-PbS the coefficient of thermal expansion measured using dilatometry and high temperature x-ray diffraction was  $21.5 \times 10^{-6}$  K<sup>-1</sup>.

Bloating during post-densification annealing was measured indirectly using resonant ultrasound spectroscopy and dilatometry and directly using scanning electron microscopy. Dry milled only PECS-processed PbTe-PbS specimens did not bloat during post-densification anneals up to 936 K. Hot pressed and PECS-processed specimens processed from wet milled and dry and wet milled powder bloated during densification anneals at temperatures over 603 K.

## DEDICATION

For my brother,  
David Randolph Ni

## ACKNOWLEDGMENTS

It is a pleasure to thank the many people who made this thesis possible.

It is difficult to overstate my gratitude to my Ph.D. supervisor, Professor Eldon Case. With his enthusiasm, his inspiration, and his great efforts to explain things clearly and simply, he helped to make Materials Science fun for me. Throughout my thesis-writing period, he provided encouragement, sound advice, good teaching, and extensive editing. I would have been lost without him.

I would like to acknowledge the help of my lab colleagues, Dr. Fei Ren, for his guidance in learning the equipment in lab, especially teaching me the RUS analysis, Robert Schmidt, Ryan Stewart, and Daniel Kleinow for powder processing, Kristen Khabir for help with laser particle size analysis, Edward Timm for hot pressing and Karl Dresch for PECS-processing.

Thank you to the Center for Advanced Microscopy at Michigan State University. They carefully maintained each of the scanning electron microscopes that were used in this dissertation, as well as provided advice and encouragement.

Thank you to the High Temperature Materials Laboratory at Oak Ridge National Laboratory. The temperature dependent elastic moduli and thermal expansion measurements were performed using the equipment at the High Temperature Materials Laboratory. I would like to offer thanks to both Edgar Lara-Curzio and Rosa Trejo for their advice, training and guidance during my visits to Oak Ridge National Laboratory.



2.8.1 Mounting in epoxy.....	40
2.8.2 Mounting on an aluminum stub.....	41
2.8.3 Polishing specimens.....	42
2.8.4 Washing the polishing wheel by hand.....	42
2.8.5 Washing the polishing wheel using an ultrasonic cleaner .....	44
2.9.0 Index of refraction and extinction coefficient measured via ellipsometry.....	45
2.10.0 X-ray diffraction .....	45
2.11.0 Hardness measured via Vickers indentations.....	46
2.11.1 Calibration of indenters at each load.....	46
2.11.2 Vickers Hardness.....	46
2.13.0 Fracturing specimens .....	47
2.14.0 Thermal annealing to determine grain size and generate bloating .....	47
2.15.0 Grain size measured by linear intercept method.....	48
2.16.0 Room temperature elastic moduli measured via Resonant Ultrasound Spectroscopy (RUS).....	51
2.17.0 High temperature elastic moduli measured via RUS .....	53
2.18 Calculating the acoustic Debye temperature.....	55
2.19 Thermal Expansion Measurements.....	56
2.19.1 Maximum temperature of the thermal cycle during thermal expansion measurements was 603 K in each experiment .....	56
2.19.2 Thermal expansion measured using two different maximum Temperatures.....	56
2.20.0 References.....	57
3.0 Porosity dependence of elastic moduli in LAST Lead-antimony-silver-tellurium) thermoelectric materials.....	59
3.1. Introduction.....	60
3.2. Background.....	61
3.2.1 Effect of porosity on physical properties .....	61
3.2.2 Effect of porosity on thermoelectric properties .....	62
3.3. Experimental procedure .....	66
3.3.1 Specimen preparation.....	66
3.3.2 Specimen Preparation and Microstructural Examination .....	69
3.3.3 Resonant Ultrasound Spectroscopy (RUS) measurements .....	69
3.4. Results and Discussion .....	69
3.4.1 Microstructural analysis .....	69
3.4.2. Room temperature elastic moduli as a function of porosity .....	70
3.4.2.1. Young's modulus and shear modulus as a function of porosity.....	72
3.4.2.2. Simulation of errors in modulus-porosity parameters as a function of the uncertainty in mass density measurement.....	81
3.4.2.3. Poisson's ratio as a function of porosity .....	83
3.5. Summary and Conclusions .....	87

3.6 References.....	90
4.0 Room temperature Young’s modulus, shear modulus, Poisson’s ratio and hardness of PbTe-PbS thermoelectric materials.....	94
4.1 Introduction .....	95
4.2 Experimental Procedure .....	96
4.3 Results and Discussion .....	101
4.4. Summary and Conclusions .....	120
4.5 References.....	122
5.0 Bloating in $(\text{Pb}_{0.95}\text{Sn}_{0.05}\text{Te})_{0.92}(\text{PbS})_{0.08}$ -0.055% $\text{PbI}_2$ thermoelectric specimens as a result of processing conditions .....	128
5.1 Introduction .....	129
5.2 Experimental Procedure .....	131
5.3 Results and Discussion .....	133
5.4 Summary and Conclusions .....	139
5.5 References.....	142
6.0 Fracture mode, microstructure, and temperature-dependent elastic moduli for thermoelectric composites of PbTe-PbS with SiC nanoparticle additions .....	144
6.1.0 Introduction.....	145
6.2.0 Background: Nanostructures in thermoelectric materials.....	147
6.3.0 Experimental Procedure.....	148
6.4.0 Results and Discussion .....	154
6.4.1 Measurements on as-densified specimen.....	154
6.4.1.1 Room temperature elasticity measurements of as-densified specimens.....	158
6.4.1.2 Microstructure of as-densified fracture surfaces.....	158
6.4.1.3 Mechanical property implications of $\text{SiC}_{\text{np}}$ additions .....	162
6.4.2 Room temperature microstructure and elastic moduli analysis following post-densification annealing .....	163
6.4.2.1 Volume change after post-densification annealing .....	163
6.4.2.2 Bloating-induced porosity generated by post-densification annealing .....	166
6.4.2.3 Effect of $\text{SiC}_{\text{np}}$ additions on bloating and grain growth .....	166
6.4.2.4 Cleaning of powder surfaces by PECS .....	170
6.4.3 High Temperature elasticity measurements .....	171
6.4.3.1 Temperature behavior of Poisson’s ratio as a function of $\text{SiC}_{\text{np}}$ addition.....	180
6.4.3.2 Hysteresis in elastic moduli measurements for hot pressed specimens.....	181
6.4.3.3 Observations in the literature of elasticity changes due to bloating during post-densification annealing of other	



Appendices.....	238
Appendix A: Room temperature elastic moduli and Vickers hardness of hot pressed LLZO cubic garnet.....	240
A.1.0 Introduction .....	241
A.2.0 Experimental Procedure .....	241
A.2.1 Specimen Preparation .....	241
A.2.2 X-ray diffraction and scanning electron microscopy .....	241
A.2.3 Vickers indentation measurements.....	244
A.2.4 Resonant ultrasound spectroscopy (RUS) measurements .....	244
A.3.0 Results and Discussion.....	245
A.3.1 Microstructure and lattice parameter of LLZO specimens .....	245
A.3.2 Elastic moduli measured via RUS .....	248
A.3.3 Hardness measured via Vickers indentation testing.....	248
A.3.4 Comparison of LLZO elastic moduli and hardness with literature data for other garnets .....	250
A.4.0 Summary and Conclusions.....	254
A.5.0 References.....	256
Appendix B: Milling parameters and processing conditions for PbTe-PbS PECS specimens ..	261

## LIST OF TABLES

Table 2.1 .....	37
The maximum temperatures, pressures and times used for sintering via pulsed electric current sintering (PECS) PbTe-PbS specimens in this study.	
Table 2.2 .....	43
Diamond Polish Table. Each diamond grit was used in succession to polish a specimen until reaching the desired polished surface on the specimen. The last polish used was either the 1 $\mu\text{m}$ or 0.5 $\mu\text{m}$ polishing grit compound.	
Table 3.1 .....	67
Processing method, chemical composition, dimensions, and mass for the specimens included in this study. All specimens were rectangular parallelepipeds.	
Table 3.2 .....	68
Processing conditions, including maximum temperature, maximum pressure and total time at maximum temperature for the hot pressed specimens used in this study.	
Table 3.3 .....	80
Parameters $b_{PE}$ , $E_D$ , $b_{PG}$ , and $G_D$ obtained from the least-squares fit to the linear (Eqs. 3.4 and 3.5) and exponential (Eqs. 3.1 and 3.2) empirical relationships for the Young's and shear moduli. N is the number of specimens included in each analysis and $r^2$ is the coefficient of determination	
Table 3.4 .....	83
Using perturbed density data (Section 3.4.2.2), a least-squares analysis was used to simulate the effect of the uncertainty in density measurement. This table lists maximum, minimum and standard deviations (std) of parameters $b_{PE}$ , $E_D$ , $b_{PG}$ , and $G_D$ and $r^2$ (coefficient of determination) obtained from the least-squares fit to the linear (Eqs. 3.4 and 3.5) and exponential (Eqs. 3.1 and 3.2) empirical relationships for the Young's and shear moduli using the perturbed density data.	
Table 4.1 .....	104
Comparison of Vickers indentation hardness for the polycrystalline (PC) specimens included in this study (Pb <sub>0.95</sub> Sn <sub>0.05</sub> Te–8% PbS) with hardness data from the literature for PbTe-PbS, PbTe and PbS polycrystalline (PC) and single-crystal (SC) specimens for N indentations per specimen.	
Table 4.2a .....	112
Fracture toughness, $K_{IC}$ , determined using Vickers indentation for the hot pressed polycrystalline (PC) Pb <sub>0.95</sub> Sn <sub>0.05</sub> Te–8% PbS specimens included in this study.	

Table 4.2b.....	113
<p>The fracture toughness (<math>K_C</math>) for polycrystalline (PC) or glasses (G) from literature for various thermoelectrics, semiconductors, and chalcogenides using Vickers indentation (VI), single edged notched beam (SENB), or double-torsion and double-cantilever-beam (DTDCB) methods.</p>	
Table 4.3 .....	117
<p>Room temperature Young's modulus, E, shear modulus, G, and Poisson's ratio, <math>\nu</math>, measured by Resonant Ultrasound Spectroscopy (RUS) for the <math>\text{PbTe-PbS}</math> (<math>\text{Pb}_{0.95}\text{Sn}_{0.05}\text{Te-8\% PbS}</math>) polycrystalline (PC) specimens included in this study compared to doped and un-doped polycrystalline (PC) and single-crystal (SC) room-temperature modulus data from the literature.</p>	
Table 5.1 .....	132
<p>The powder processing conditions and sintering parameters for the hot pressed (HP) and pulsed electric current sintering (PECS) densified specimens processed using powders that were crushed, ground, sieved, and re-ground (CGSR) powder was either (1) set aside for densification, (2) dry milled (DM), (3) dry milled and then wet milled (D/WM), or (4) wet milled (WM). For the post-densification anneals, the heating and cooling rates were 5 K/min and 2 K/min for specimens prepared for SEM observation and RUS elasticity measurements, respectively.</p>	
Table 6.1 .....	149
<p>The processing conditions for twenty-six (<math>(\text{Pb}_{0.95}\text{Sn}_{0.05}\text{Te})_{0.92}(\text{PbS})_{0.08-0.055\% \text{ PbI}_2}</math>) specimen included in this study. Using resonant ultrasound spectroscopy, the temperature-dependent elastic moduli (<math>E(T)</math>) were measured for twelve specimens and the room-temperature elastic moduli as a function of porosity (<math>E(P)</math>) were measured for four specimens. The microstructure (M) was examined using scanning electron microscopy for 15 specimens.</p>	
Table 6.2a .....	152
<p>A comparison of the as-densified specimens mean grain sizes, <math>GS_{DNS}</math>, for different powder processing (dry milling (DM), wet milling (WM), and dry and wet milling (D/WM)) and sintering techniques (hot pressed (HP) and PECS-processed). The difference in powder processing is the likely cause of the factor of two difference between the four wet milled hot pressed and PECS processed specimens and six dry milled PECS-processed specimens. The PECS specimens were sintered at the stated temperature for 20 minutes. For the as-densified dry milled PECS-processed specimens, the mode-mixity was calculated as the areal fraction of the transgranular grains appearing on a specimen's fracture surface. In general, as the mode mixity increased to 1.0, transgranular fracture dominates and the fracture toughness increases.</p>	

Table 6.2b .....	153
<p>Mean grain sizes of the as-densified and the annealed specimens are designated by <math>GS_{DNS}</math> and <math>GS_{ANN}</math>, respectively. For dry milled PECS-processed specimens with 0.0 vol% <math>SiC_{np}</math>, the <math>GS_{ANN}</math> increased in three specimens after post-densification anneals up to 936 K. However, the inclusion of <math>SiC_{np}</math> limited grain growth in three specimens during post-densification anneals up to 873 K.</p>	
Table 6.3 .....	155
<p>The least-squares fitting parameters <math>E_{P=0}</math> and <math>b_{PE}</math> (Eq. (6.4a)) and <math>G_{P=0}</math> and <math>b_{PG}</math> (Eq. (6.4b)) to the Young's modulus and shear modulus to the four as-densified and four post-densified specimens in Figure 6.1.</p>	
Table 6.4 .....	165
<p>The relative volume change twelve specimens for each HT-RUS heating/cooling cycle.</p>	
Table 6.5 .....	168
<p>In this study, the inclusion of <math>SiC_{np}</math> inhibited porosity (bloating) for PECS-processed PbTe-PbS specimens. After a post-densification anneal at 693 K for two hours, for the PbTe-PbS specimen without <math>SiC_{np}</math>, PECS-01, the volume fraction porosity, <math>P</math>, however, for two specimens with <math>SiC_{np}</math>, <math>P</math> increased only by 20%. <math>E</math> is the Young's modulus measured at room temperature using resonant ultrasound spectroscopy.</p>	
Table 6.6 .....	174
<p>The least-squares fitting parameters, <math>E_{RT}</math> and <math>b_{TE}</math>, equation (6.6a) for the seven hot pressed and five PECS-processed PbTe-PbS thermoelectrics included in this study. <math>P</math> is the volume fraction porosity before thermal cycling, <math>N</math> is the number of <math>E</math> versus temperature data points in the least-squares fit and <math>r^2</math> is the coefficient of determination for the least-squares fit to equation (6.6a). For specimens where there was no observable hysteresis, a single entry is given. Specimens HP-53 #A, HP -53 #C-TC2, HP -54 #2, and HP -55 #1 have an observable hysteresis in <math>E</math> versus <math>T</math>, thus there are two entries, one for heating and one for cooling.</p>	
Table 6.7 .....	175
<p>In the open literature for doped PbTe-based thermoelectrics, <math>E_{RT}</math> and <math>b_{TE}</math>, the least-squares fitting parameters from equation (6.6a), are similar to the least-squares fitting parameters in this study (Table 6.2). <math>P</math> is volume fraction porosity, <math>N</math> is the number of data points in the least-squares fit and <math>r^2</math> is the coefficient of determination.</p>	

Table 7.1a .....	199
<p>The processing conditions for specimens included in this study that were measured using dilatometry (TMA), high-temperature x-ray diffraction (HT-XRD) and scanning electron microscopy (SEM) All PbTe-PbS powder and bulk specimens have the same composition, <math>(\text{Pb}_{0.95}\text{Sn}_{0.05}\text{Te})_{0.92}(\text{PbS})_{0.08}</math>-0.055% <math>\text{PbI}_2</math></p>	
Table 7.1b .....	200
<p>The powder processing, measurement technique, ramp rate and temperature ranges for the CTE measurements included in this study. For each dilatometer test, the atmosphere was flowing 96 % Ar-4% <math>\text{H}_2</math>, whereas for the HT-XRD measurements the atmosphere was 96 % <math>\text{N}_2</math>-4% <math>\text{H}_2</math>.</p>	
Table 7.2.....	205
<p>The mean CTE, calculated from the TMA thermal expansion data for 4 hot pressed (HP-specimens), 1 PECS pressed (PECS- specimens) and two cast ingot (CIW) processed <math>(\text{Pb}_{0.95}\text{Sn}_{0.05}\text{Te})_{0.92}(\text{PbS})_{0.08}</math>-0.055% <math>\text{PbI}_2</math> specimens. For each specimen, the thermal expansion measurements were performed on six to twelve half thermal cycles, where a heating and a cooling half cycle comprises a full thermal cycle. The full temperature range over which the measurements were performed are indicated. The temperature range over which the data was analyzed was 325 K – 595 K. Note that the average CTE values are very similar for both the hot pressed and PECS specimens and CTE values are relatively constant for each half cycle during the TMA measurement process on a given specimen.</p>	
Table 7.3.....	209
<p>The average CTE for the powder and bulk specimens measured using HT-XRD. The coefficient of determination, <math>r^2</math>, is for the slope upon cooling for the temperature dependent lattice parameter.</p>	
Table 7.4 .....	215
<p>The average CTE for thermoelectrics in the literature. The fabrication technique, density, temperature range, and measurement method for each composition.</p>	
Table A.1 .....	235
<p>The specimen geometry, dimensions, density, volume fraction porosity, P and measurement techniques for the LLZO rectangular parallelepiped, RP, and crescent-shaped, CR, specimens included in this study. The specimens were powder processed from ingot and densified by hot pressing. The elastic moduli were measured using resonant ultrasound spectroscopy (RUS) and the hardness was measured via Vickers indentations.</p>	

Table A.2 .....	249
<p>The density, volume fraction porosity, P, Young's modulus, E, bulk modulus, B, shear modulus, G, and Poisson's ratio, <math>\nu</math>, for the hot pressed rectangular parallelepiped specimens included in this study as well as for polycrystalline garnet specimens from the literature.</p>	
Table A.3 .....	251
<p>The exponents <math>m_B</math>, <math>m_G</math>, and <math>m_H</math> obtained by a least-squares fit to equation (2) for bulk modulus, B, shear modulus, G, and hardness, H data, respectively from the literature for various cubic crystalline structures. The coefficient of determination, <math>r^2</math>, along with the number of particular compositions of a given crystal structure included in the least-squares fit, N, are listed within the parentheses given below each of the numerical values of the fitted exponents.</p>	
Table B.1 .....	263
<p>The powder processing for each PECS-processed specimen. All milling was performed using a planetary mill in an argon-atmosphere glove box. The specimens were fabricated using powders that were (1) dry milled, (2) wet milled, or (3) dry and wet milled. The media referenced in this table were alumina spheres. The mix mill refers to the planetary milling of PbTe-PbS powders with SiC nanoparticles (SiC).</p>	

## LIST OF FIGURES

Figure 1.1 .....	3
Diagram of a thermoelectric module. The application of a temperature differential causes an electric current to run through the specimen. After from Riffat <i>et al</i> , Thermoelectrics: a review or present and potential applications, Applied thermal engineering 23 (2003).	
Figure 1.2 .....	8
Schematic of elastic moduli change with temperature. The elastic moduli decrease with temperature in each regions. Region I is from 0 K to approximately $0.3\theta_D$ and $0.5\theta_D$ . Region II is a linear region. Region III is the viscoelastic or anelastic region, beginning at the onset temperature of grain boundary sliding, $T_{ONSET}$ .	
Figure 2.1 .....	24
Schematic of powder processing procedure for PbTe-chalcogenides in this study. Both the powder particles and the bulk specimens were characterized using scanning electron microscopy.	
Figure 2.2 .....	38
Temperature-Pressure versus time for pressing specimens C-PTS-P-09. The maximum temperature and pressure was 823 K and 60 MPa, respectively. The heating rate was 50 K/minute and the cooling rate was 5 K/minute. The pressure reached a maximum of 60 MPa 60 seconds after the temperature reached a maximum of 823 K.	
Figure 2.3 .....	39
Temperature-Pressure versus time for pressing specimens C-PTS-P-11 and C-PTS-P-12. The maximum temperature and pressure was 823 K and 60 MPa, respectively. The heating rate was 50 K/minute and the cooling rate was 5 K/minute. During cooling, the specimen was thermally annealed at 573 K for 200 minutes to reduce residual stresses.	
Figure 2.4 .....	52
Schematic of the Resonant Ultrasound Spectroscopy (RUS) apparatus used for Young's modulus measurements. The specimen was balanced on the three transducers.	
Figure 2.5 .....	52
An example of an acoustic vibrational spectrum induced in a mechanically driven specimen. The resonant peak positions were functions of the elastic moduli, geometry, dimensions and mass density of the specimen This spectrum is from C-PTS-P-07 at 363 K.	
Figure 3.1 .....	68
Time-temperature profile for the fabrication of the five ingots specimens included in this study. N138 ( $Ag_{0.43}Pb_{18}Sb_{1.2}Te_{20}$ ), N155, and N160-4,-5 and -9 ( $Ag_{0.86}Pb_{19}Sb_{1.0}Te_{20}$ ) (Table 3.2a). Specimens N160-4, -5 and -9 were cut from a single ingot.	

Figure 3.2 .....	71
SEM micrographs of the as polished surfaces of specimens (a) HP3 ( $P = 0.01$ ) (b) HP30 ( $P = 0.01$ ) (c) HP7 ( $P = 0.10$ ), as well as the thermally etched surfaces (d) HP3 ( $P = 0.01$ , thermally etched at 598 K for 2 hrs) (e) HP30 ( $P = 0.01$ , thermally etched at 673 K for 2 hrs) (f) HP7 ( $P = 0.10$ , thermally etched at 698 K for 2 hrs)	
Figure 3.3a .....	73
For the hot pressed specimens only (compositions $\text{Ag}_{0.43}\text{Pb}_{18}\text{Sb}_{1.2}\text{Te}_{20}$ and $\text{Ag}_{0.86}\text{Pb}_{19}\text{Sb}_{1.0}\text{Te}_{20}$ ), the solid line indicates the least-squares fit to linear relationship (Eq. 3.4) for Young's modulus (determined by room temperature RUS) as a function of porosity.	
Figure 3.3b .....	74
For the combined data set (12 hot pressed specimens and 5 cast specimens), the solid line indicates the least-squares fit to linear relationship (Eq. 3.4) for Young's modulus (determined by room temperature RUS) as a function of porosity.	
Figure 3.3c .....	75
For the hot pressed specimens only, the solid line indicates the least-squares fit to linear relationship (Eq. 3.5) for shear modulus (determined by room temperature RUS) as a function of porosity.	
Figure 3.3d .....	76
For the combined data set (12 hot pressed specimens and 5 cast specimens), the solid line indicates the least-squares fit to linear relationship (Eq. 3.5) for shear modulus (determined by room temperature RUS) as a function of porosity.	
Figure 3.3e .....	77
For the combined data set (12 hot pressed specimens and 5 cast specimens), the solid line indicates the least-squares fit to the exponential relationship (Eq. 3.2) for shear modulus (determined by room temperature RUS) as a function of porosity.	
Figure 3.3f .....	78
For the hot pressed specimens only, the Poisson's ratio determined by room temperature RUS measurements versus volume fraction porosity.	
Figure 3.3g .....	79
For the combined data set (12 hot pressed specimens and 5 cast specimens), Poisson's ratio determined by room temperature RUS measurements versus volume fraction porosity of the combined data (hot pressed and cast ingot specimens).	

Figure 4.1 .....	98
Particle size distribution obtained from laser light scattering apparatus.	
Figure 4.2 .....	.103
SEM micrographs of the as-polished surfaces of $\text{Pb}_{0.95}\text{Sn}_{0.05}\text{Te} - \text{PbS}$ 8% specimens fabricated by (a) casting from the melt and (b and c) hot pressing.	
Figure 4.3 .....	.105
SEM micrographs of annealed fractured surfaces of hot pressed $\text{Pb}_{0.95}\text{Sn}_{0.05}\text{Te}-8\%$ PbS specimens cut from hot pressed billets (a) MSUHP-53 and (b) MSUHP-54. MSUHP-53 was annealed for 5 hours at 573 K and MSUHP-54 was annealed for 5 hours at 693 K, both in a 96% Ar + 4% $\text{H}_2$ atmosphere.	
Figure 4.4 .....	.106
SEM micrograph of wet milled powders used to fabricate billet MSUHP-54. Note that a significant factor of the powders particles have a diameter less than about 100 nm, which is below the effective measurement threshold of the laser scattering apparatus. A fracture surface of a specimen hot pressed from this powder is shown in Figure 4.3b.	
Figure 4.5 .....	.110
The mean hardness as a function of the applied Vickers indentation load for hot pressed (open symbols) and cast (filled symbols) specimens in the PbTe-PbS system. The mean hardness values, averaged over all loads for the $\text{Pb}_{0.95}\text{Sn}_{0.05}\text{Te}-8\%$ PbS hot pressed MSUHP-53 and MSUHP-54 specimens are shown by the dotted and dashed lines, respectively. The mean hardness values averaged over all loads for the $\text{Pb}_{0.95}\text{Sn}_{0.05}\text{Te}-8\%$ PbS cast NW-Ingot G and MSU-Ingot 7A specimens are indicated by the dot-dashed and dot-dot-dashed lines, respectively. The hardness data from Darrow <i>et al.</i> [36] for cast PbTe-PbS 5% and PbTe-PbS 10% specimens is shown for comparison (half-filled symbols).	
Figure 4.6 .....	114
SEM micrographs of Vickers indentations at a) 0.25 N, b) 2.0 N, and c) 4.9 N for MSU-In #7A, and d) 0.25 N for MSUHP-54 #C, e) 2 N for MSUHP-53 #3, and f) 4.9 N for MSUHP-54 #C.	
Figure 5.1 .....	134
The as-densified fracture surfaces of (a) HP-DM-01 and (c) HP-CGSR-01 do not show bloating. Annealing (b) HP-DM-01 at 723 K for 4 hours and (d) HP-CGSR-01 at 973 K for 6 hours resulted in bloating as evidenced by the increased porosity of the internal fracture surfaces. All annealing was performed in flowing Ar.	

- Figure 5.2 ..... 135  
 The as-densified fracture surfaces of (a) HP-D/WM-01 and (c) PECS-WM-01 do not show bloating. Annealing (b) HP-D/WM-01 at 693 K for 2 hours and (d) PECS-WM-01 at 823 K for 2 hours resulted in bloating as evidenced by the increased porosity of the internal fracture surfaces. All annealing was performed in flowing Ar or Ar (96%)-H<sub>2</sub> (4%).
- Figure 5.3 ..... 136  
 In contrast to the annealing behavior depicted in Figures 5.1 and 5.2, the (a) as-densified PECS-DM-02 did not bloat after annealing at (b) 663 K for 2 hours, (c) 823 K for 2 hours, and (d) 936 K for 2 hours. All annealing was performed in flowing Ar (96%)-H<sub>2</sub> (4%).
- Figure 5.4 ..... 138  
 The bloating (Figures 5.1 and 5.2) or lack of bloating (Figure 5.3) observed in the SEM study is also evident in the RUS measurements of Young's modulus, E, versus volume fraction porosity, P. For the nine as-densified HP and PECS specimens along with the 32 annealing measurements on the same nine specimens (Table 1), as P increased, E decreased. The filled symbols and open symbols represent the E values for the as-densified and annealed specimens, respectively. Equation (5.1), widely used to describe the E versus P behavior for brittle materials [10, 11], also fits the E versus P behavior well ( $r^2 = 0.990$ ) for the 41 RUS measurements included in this study. The dashed line represents the least-squares fit to equation (5.1).
- Figure 6.1 ..... 156  
 The porosity dependence of the (a) Young's modulus, E, shear modulus, G, and (b) Poisson's ratio for four as-densified PECS-processed specimens (filled symbols) and four thermally annealed hot pressed and PECS-processed specimens with 0.0 vol% SiC<sub>np</sub>. Each individual specimen is represented by the same symbol in figure (a) and (b). The least-squares fit to Eq. (6.4a) to these 8 specimens is represented by the dashed line. The solid line and dotted lines represent the average and standard deviation in Poisson's ratio, respectively.
- Figure 6.2 ..... 159  
 The as-densified and post-densification fracture surfaces of (a, b) D/WM PECS-10, (c, d) DM PECS-20 and (e, f) DM PECS -18 (with 2.0 vol% SiC<sub>np</sub>). Few pores are evident in the SEM micrographs of the as-densified fracture surfaces. Annealing at 936 K for 2 hours resulted in bloating for (b) D/WM PECS-10 and (f) DM PECS -18 (with 2.0 vol% SiC<sub>np</sub>) specimens as evidenced by the increased porosity of the internal fracture surface while, in contrast, the (d) DM PECS-20 specimen did not bloat after annealing under identical conditions.

Figure 6.3 .....	160
The (a) as-densified and (b) post-densification fracture surfaces of PECS-10. After post-densification annealing to 936 K for 2 hours, long lenticular pores were observable on the fresh fracture surface of D/WM PECS-10.	
Figure 6.4 .....	161
The (a) fracture surfaces of the specimen without added SiC <sub>np</sub> , PECS-15, exhibits a much higher fraction of intergranular fracture than (b) the specimen with 2.5 vol% SiC <sub>np</sub> , PECS-16 (Table 6.2a). Both specimens were PECS-processed at 673 K for 20 minutes using a pressure of 60 MPa.	
Figure 6.5 .....	172
Schematics of hysteresis between heating and cooling in Young's modulus due to (a – c) microcracking and (d) due to bloating. In this study, the specimen HP-54#2 bloated when thermally cycled to 663 K (d). The dashed and dashed-dot lines represent the least-squares fit to Eq. (6.6a) to heating and cooling, respectively.	
Figure 6.6 .....	176
Temperature dependence of the (a - d) Young's modulus, E, (d) shear modulus, G, and (e- f) Poisson's ratio, $\nu$ , for hot pressed (HP) and PECS-processed PbTe-PbS specimens upon heating (filled symbols) and cooling (open symbols). For E and G, the symbol size is greater than the error bars. In parentheses, next to the specimen label, is the maximum temperature for each thermal cycle. The least-squares fit to Eq. (6.6a) to the Young's modulus during heating, cooling, and heating/cooling is represented by the dashed, dotted, and solid lines, respectively. A least-squares fit to Eq. (6.7) to the temperature-dependent Poisson's ratio is represented by the dashed-dot line. The hysteresis in E versus T for specimens HP-53 #A, HP-53 #C-TC2, HP -54 #2, and HP -55 #1 is not apparent in the figures because of the number of temperature-dependent Young's moduli data points.	
Figure 6.7 .....	183
The Young's modulus as a function of volume fraction porosity, P, for Ti-6Al-4V specimens after post-densification anneals up to 1303 K [Oppenheimer 2010]. This behavior is consistent with the empirical exponential decrease common to brittle materials (Eq. (6.4a)). The solid line represents a least-squares fit to Eq. (6.4a) of the Oppenheimer <i>et al.</i> Young's modulus versus P data [Oppenheimer 2010].	
Figure 7.1 .....	203
The dimension change as a function of temperature for (a) a cast ingot (CIW040S), (b) a PECS-processed specimen (PECS-15) and (c) a hot pressed specimen (HP-55). There were a total of 6 or 8 half cycles, where HT1, 2, 3, and 4, are the first, second, third and fourth heating cycles, and CL1, 2, 3, and 4 are the first, second, third and fourth cooling cycles. For the hot pressed specimen (c), half cycles 1 to 6 are from 297 K to 603 K and the half cycles 7 – 12 are from 297 K to 663 K. The heating/cooling rates were 2.0 K/min for all runs. Notice that for MSUHP-55 #1 the hysteresis between heating and cooling increased when the maximum temperature increased	

Figure 7.2 .....	207
<p>The lattice parameter as a function of temperature for powder that was powder that was dry milled only (a) CIW064S and wet and dry milled (b) CIW041S, (c) PbTe-PbS 9, (d) CIW036S, (e) CIW040S and (f) CIW063S. The dash-dotted line is an extrapolation of the least-squares fit to the lattice parameters between 303 K and 483 K using equation (7.3b) The dotted line is a least-squares fit to the cooling data.</p>	
Figure 7.3 .....	211
<p>The micrographs for the as-pressed fractured surfaces for (a) HP-53, (c) PECS-02, and (e) PECS-10S. The fractured pieces were annealed at 773 K, for MSUHP-53, and 823 K, for PECS-02, and PECS-10S, for 2 hours in flowing 96% Ar + 4% H<sub>2</sub> gas and then re-fractured upon cooling. The new fractured surfaces for (b) HP-53, (d) PECS-02, and (f) PECS-10S were examined for bloating. The annealed fractured surfaces for HP-53 and PECS-02 surfaces showed evidence of bloating, where as PECS-10S did not show evidence of bloating.</p>	
Figure A.1 .....	246
<p>The fracture surfaces for the hot pressed specimens (a) LLZO-01 and (c – d) LLZO-02. The fracture surface of LLZO-02 was examined at (e) five different sites along the diametral fracture. Each site was roughly 3 mm apart and sites 1 and 5 were approximately 0.5 mm from the specimen edge. For each micrograph the grain size was measured using the linear intercept method and a stereographic projection factor of 1.5 [15].</p>	
Figure A.2 .....	252
<p>The (a) Young's modulus, (b) shear modulus, and (c) hardness as a function of lattice parameter for the aggregate average values for single crystal garnet data in the literature (open symbols) and the LLZO garnet specimens in this study (filled symbol). In (a), (b), and (c) the dashed line represents the least-squares fit of equation (A.2) to the data in this study and single crystal garnet in the literature [27, 33 - 38]. The scatter in hardness, H, is likely due to the different mechanisms that can affect H (Section A.3.3).</p>	
Figure B.1 .....	268
<p>The temperature-pressure-time profile for PECS-processed specimens, C-PTS-P-01, C-PTS-P-02, C-PTS-P-03, and C-PTS-P-04. The heating rate and cooling rate was 50 K/minute and 5 K/minute, respectively. The ramp rate for pressure during heating was 5 MPa/min and 0.5 MPa/min during cooling. The specimens were sintered at the maximum temperature and pressure for 20 minutes</p>	

Figure B.2 .....	268
The temperature-pressure-time profile for PECS-processed specimens, C-PTS-P-05, C-PTS-P-06, and C-PTS-P-07. The heating rate and cooling rate was 50 K/minute and 5 K/minute, respectively. The maximum temperature was held for 20 minutes. The pressure was held at 20 MPa during heating until the specimen reached the maximum temperature. Once the specimen reached 823 K, the pressure was increased to 60 MPa.	
Figure B.3 .....	269
The temperature-pressure-time profile for PECS-processed specimen, C-PTS-P-08. The heating rate and cooling rate was 50 K/minute and 5 K/minute, respectively. The maximum temperature was held for 20 minutes. The pressure was held at 20 MPa during heating until the specimen reached the maximum temperature, 873 K. Once the specimen reached 873 K, the pressure was increased to 60 MPa.	
Figure B.4 .....	269
The temperature-pressure-time profile for PECS-processed specimen, C-PTS-P-09. The heating rate and cooling rate was 50 K/minute and 5 K/minute, respectively. The maximum temperature was held for 30 minutes. The pressure was held at 20 MPa during heating until the specimen reached the maximum temperature, 873 K. Once the specimen reached 823 K, the pressure was increased to 60 MPa. The longer sintering time was due to a miscommunication with Karl Dresch.	
Figure B.5 .....	270
The temperature-pressure-time profile for PECS-processed specimens, C-PTS-P-10, C-PTS-P-11, and C-PTS-P-12. The heating rate and cooling rate was 50 K/minute and 5 K/minute, respectively. The maximum temperature was held for 20 minutes. The pressure was held at 20 MPa during heating until the specimen reached the maximum temperature. Once the specimen reached 823 K, the pressure was increased to 60 MPa. To reduce possible residual stresses, the specimen was cooled to 573 K and thermally annealed for 120 minutes. The pressure was slowly reduced in steps during cooling.	
Figure B.6 .....	271
The temperature-pressure-time profile for PECS-processed specimens, C-PTS-P-13, C-PTS-P-14, C-PTS-P-15, C-PTS-P-16, C-PTS-P-17, C-PTS-P-18, and C-PTS-P-19. The heating rate and cooling rate was 50 K/minute and 5 K/minute, respectively. The maximum temperature was held for 20 minutes. The pressure was held at 20 MPa during heating until the specimen reached the maximum temperature. Once the specimen reached 673 K, the pressure was increased to 60 MPa. To reduce possible residual stresses, the specimen was cooled to 573 K and thermally annealed for 120 minutes. The pressure was slowly reduced in steps during cooling.	

Figure B.7 .....	272
The temperature-pressure-time profile for PECS-processed specimens, C-PTS-P-20, C-PTS-P-21, C-PTS-P-22, C-PTS-P-23, and C-PTS-P-24. The heating rate and cooling rate was 50 K/minute and 5 K/minute, respectively. The maximum temperature was held for 20 minutes. The pressure was held at 20 MPa during heating until the specimen reached the maximum temperature. Once the specimen reached 723 K, the pressure was increased to 60 MPa. The pressure decreased during cooling at a ramp rate of 0.64 MPa/minute.	
Figure B.8 .....	273
The temperature-pressure-time profile for PECS-processed specimens C-PTS-P-25 and C-PTS-P-29. The maximum temperature of 723 K was held for 16 minutes. The heating rate and cooling rate was 100 K/minute and 10 K/minute, respectively. The pressure was held at 60 MPa until the specimen reached room temperature.	
Figure B.9 .....	273
The temperature-pressure-time profile for PECS-processed specimens C-PTS-P-26 and C-PTS-P-30. The maximum temperature of 723 K was held for 16 minutes. The heating rate and cooling rate was 100 K/minute and 5 K/minute, respectively. The pressure was held at 60 MPa until the specimen reached room temperature.	
Figure B.10 .....	274
The temperature-pressure-time profile for PECS-processed specimens C-PTS-P-27 and C-PTS-P-31. The heating rate and cooling rate was 50 K/minute and 5 K/minute, respectively. The ramp rate for pressure during heating was 5 MPa/min and 0.5 MPa/min during cooling. The specimens were sintered at the maximum temperature and pressure for 20 minutes.	
Figure B.11 .....	274
The temperature-pressure-time profile for PECS-processed specimen C-PTS-P-28. The heating rate and cooling rate was 50 K/minute and 5 K/minute, respectively. The ramp rate for pressure during heating was 5 MPa/min and 0.5 MPa/min during cooling. The specimen was sintered at the maximum temperature and pressure for 5 minutes.	
Figure B.12 .....	275
The temperature-pressure-time profile for PECS-processed specimens, C-PTS-P-32, C-PTS-P-36, and C-PTS-P-37. The heating rate and cooling rate was 50 K/minute and 5 K/minute, respectively. The ramp rate for pressure during heating was 5 MPa/min and 0.5 MPa/min during cooling. The specimens were sintered at the maximum temperature and pressure for 5 minutes.	
Figure B.13 .....	275
The temperature-pressure-time profile for PECS-processed specimen C-PTS-P-33. The heating rate and cooling rate was 50 K/minute and 5 K/minute, respectively. The ramp rate for pressure during heating was 5 MPa/min and 0.5 MPa/min during cooling. The specimen was sintered at the maximum temperature and pressure for 5 minutes.	

Figure B.14 ..... 276  
The temperature-pressure-time profile for PECS-processed specimen C-PTS-P-34. The heating rate and cooling rate was 50 K/minute and 5 K/minute, respectively. The ramp rate for pressure during heating was 5 MPa/min and 0.5 MPa/min during cooling. The specimen was sintered at the maximum temperature and pressure for 5 minutes.

Figure B.15 ..... 276  
The temperature-pressure-time profile for PECS-processed specimen C-PTS-P-35. The heating rate and cooling rate was 50 K/minute and 5 K/minute, respectively. The ramp rate for pressure during heating was 5 MPa/min and 0.5 MPa/min during cooling. The specimen was sintered at the maximum temperature and pressure for 5 minutes.

## 1.0 Introduction

PbTe-based chalcogenide thermoelectrics have potential in waste-heat recovery applications due to a relatively high figure of merit of roughly 1.5 at 650 K. During waste-recovery, the thermoelectric, TE, materials will undergo both thermal and mechanical stresses. Therefore, mechanical properties, such as the Young's modulus, shear modulus, Poisson's ratio, and coefficient of thermal expansion will be needed for stress-strain analysis (Section 1.3). The PbTe-chalcogenide work has focused on: (i) hot pressing (HP) and pulsed electric current sintering (PECS) of dry and wet milled LAST or PbTe-PbS powders (ii) measurements of the temperature-dependent elastic moduli and thermal expansion, (iii) measurements of the of the room temperature elastic moduli and hardness and (iv) comparison of the bloating behavior of hot pressed and PECS-processed specimens.

### 1.1.0 Thermoelectrics for use in waste heat recovery

Thermoelectric (TE) materials have a variety of potential uses as generators that convert waste heat into electricity. For low power supply uses, TE modules power a wristwatch [Snyder 2008, Riffat 2003] or remote sensing wireless systems [Riffat 2003]. For high power generation, for the past 30 years TE modules have provided long-term power for deep space probes [Rowe 2006, Snyder 2008, Riffat 2003]. However, there is a terrestrial interest in thermoelectrics for use in automotive waste-heat recovery. Automotive engine automobiles use roughly 25% of fuel energy for accessory power and propulsion [Yang 2006]. The remaining fuel energy is lost as coolant and waste heat, as well as parasitic losses due to friction [Yang 2006]. Thermoelectric modules, through waste heat recovery, could provide electric power to accessories which would aid in fuel economy.

In a thermoelectric module electrical power is produced from the heat flow across temperature differential (Figure 1.1) [Riffat 2003, Snyder 2008]. An applied temperature difference causes charged carriers in the material to diffuse from the hot side to the cold side. The heat source drives electrons in the n-type element toward the cooler region, creating a current through the circuit. Holes in the p-type element then flow in the direction of the current. Therefore, thermal energy is converted into electrical energy. The introduction of a current causes an inverse of this process, with the result of cooling instead of power generation and is known as the Peltier effect [Nolas 2001, Riffat 2003, Fushillo 1960, Tritt 1999].

### 1.2.0 Figure of merit as a measure of efficiency for thermoelectrics

The dimensionless figure of merit, ZT,

$$ZT = \frac{S^2 \sigma T}{k} \quad (1.1)$$

is a function of the Seebeck coefficient, S, electrical conductivity,  $\sigma$ , the total thermal conductivity, k, and temperature, T. The Seebeck's coefficient, S, is the ratio of the voltage change, dV, to the temperature difference, dT

$$S = \frac{dV}{dT}. \quad (1.2)$$

For TE materials, it has been empirically understood that if the conductors obey Ohm's law, the thermoelectric voltage is therefore dependent on the temperature difference ( $\Delta T$ ) and the actual properties of the conductors [Fushillo 1960]. Therefore, a TE material must be engineered with a high Seebeck coefficient, a high electrical conductivity, and a low thermal conductivity in order to have a high ZT value and therefore a high efficiency.

A thermoelectric thermocouple (Figure 1.1) usually consists of one semiconductor (n-

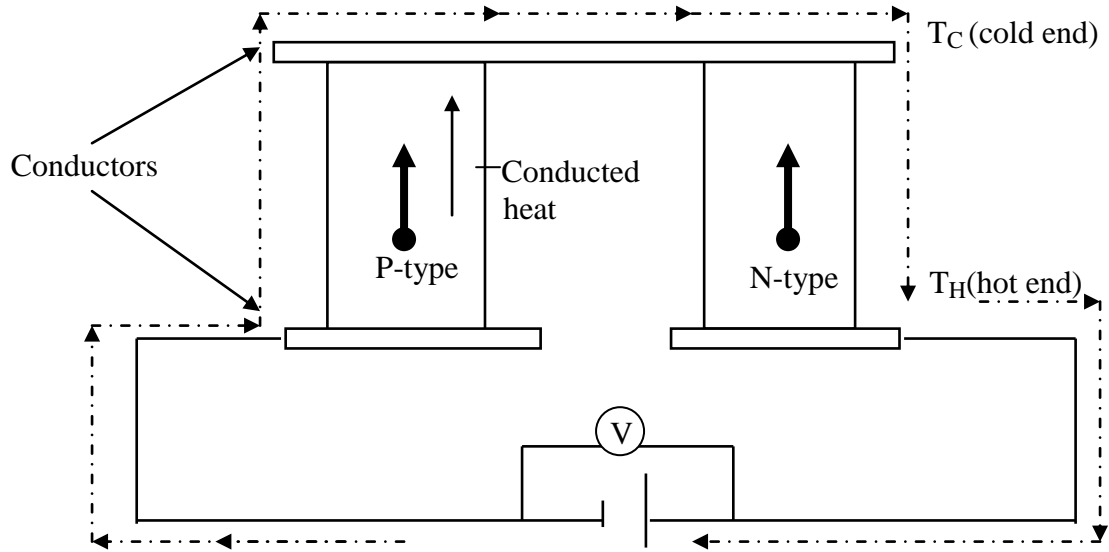


Figure 1.1 Diagram of a thermoelectric module. The application of a temperature differential causes an electric current to run through the specimen. After from Riffat *et al*, Thermoelectrics: a review of present and potential applications, Applied thermal engineering 23 (2003).

type) paired with another semiconductor (p-type) to form a thermoelectric device or module [Riffat 2003]. These thermocouples are electrically connected in series and thermally in parallel when used in modules [Riffat 2003]. Ignoring contributions such as contact resistance and radiation effects, the figure of merit is then

$$ZT = \frac{S^2 \sigma T}{k} \quad (1.3)$$

where  $\sigma$  is the electrical conductivity and  $k$  is the total thermal conductivity (from the lattice and electronic contributions) where the subscript “n” and “p” denotes the contribution from the n- and p-type TE leg, respectively [Tritt, 2006].

The efficiency,  $\eta$ , of a TE generator depends on the temperature differential between the hot,  $T_H$ , and cold,  $T_C$ , sides of the thermoelectric module (Figure 1.1) and the figure of merit [Cadoff 1960, Yang 2006]

$$S = \frac{dV}{dT} \quad (1.4)$$

The transport properties of the n- and p-type legs (Figure 1.1) vary as a function of temperature, so therefore  $ZT$  varies with temperature [Riffat 2003]. Equation (1.4) demonstrates that a high efficiency needs both a high  $ZT$  and a large temperature differential across the thermoelectric. However, there is no known thermoelectric material with a high average  $ZT$  over a large temperature range. Most TE materials have a high average  $ZT$  over a limited temperature range, such as  $\text{Bi}_2\text{Te}_3$ , which has a  $ZT$  of around 0.8 between 250 K and 450 K [Yang 2006]. A thermoelectric with a figure of merit of around 3 has the potential of approaching 50% of the Carnot efficiency [Nolas 2001, Yang 2006].

### 1.3.0 Importance of mechanical properties for thermoelectric materials

As the  $ZT$  is a measure of the efficiency of a TE (Eq. (1.4)) and is a function of the Seebeck coefficient and the thermal and electrical conductivity (Eq. (1.1)), most literature focuses on these three properties. However, mechanical properties, such as hardness, fracture strength, elastic moduli, and fracture toughness are important in understanding the response of the TE material to in-service conditions. Hardness,  $H$ , is associated with the machinability of a material as well as its resistance to wear [Ren 2006]. Fracture toughness is a measure of the resistance to crack propagation in a given material [Lawn 1993, Rogl 2011]. The elastic moduli are needed for numerical or analytical stress-strain calculations due to thermal fatigue, and can also be used to monitor the accumulation of microcrack damage [Case 2002, Ren 2009].

### 1.3.1 Thermal shock/thermal fatigue resistance

Thermal shock/thermal fatigue resistance is especially important for applications for TE that involves the recovery of waste heat from engines. When electrical energy is harvested from automobile exhaust, the TE elements are subjected to both temperature gradients and thermal transients. The TE waste heat recovery systems must be able to withstand hundreds or thousands thermal fatigue cycles. The thermal stress induced by thermal cycling is a function of the dimensionless parameter, Biot modulus ( $Bi$ )

$$Bi = \frac{a(T)h(T)}{k(T)} \quad (1.5)$$

where  $h(T)$  (surface heat transfer coefficient,  $W/m^2 K$ ) measures the heat energy per unit time transferred across the specimen/quench medium interface per unit area per Kelvin,  $k(T)$  (thermal conductivity,  $W/mK$ ) measures the rate that heat energy in the specimen can be transferred to the

interface, and  $a(T)$  (characteristic specimen dimension, m) is the distance from the centerline of the specimen to the interface [Case 2002]. Thus  $Bi$  characterizes the flow of thermal energy during quenching [Case 2002].

The maximum thermal stress,  $\sigma_{\max}$ , due to thermal cycling at the surface of a plate can be estimated as

$$\sigma_{\text{TH max}} = \frac{E\alpha_{\text{TH}}\Delta T}{1-\nu} \left[ \frac{1}{1.5 + 3.25/Bi} \right] \text{ for } 0 < Bi < 5 \quad (1.6)$$

$$\sigma_{\text{TH max}} = \frac{E\alpha_{\text{TH}}\Delta T}{1-\nu} \left[ \frac{1}{1.5 + 3.25/Bi - 0.5 \exp(-16/Bi)} \right] \text{ for } 0 < Bi < 20 \quad (1.7)$$

where  $\sigma_{\text{TH}}$  is thermal stress,  $\nu$  is the Poisson's ratio,  $E$  is the Young's modulus,  $\alpha_{\text{TH}}$  is the coefficient of linear thermal expansion, and  $\Delta T$  is the quench temperature difference [Case 2002, Ren 2008]. As  $E$ ,  $\alpha_{\text{TH}}$ ,  $\nu$ ,  $Bi$  are all functions of temperature, knowing how these mechanical properties change with temperature is key to understanding how the materials withstands the thermal transients [Case 2002, Ren 2008].

### 1.3.2 Elastic moduli

Elastic moduli are sensitive to defects such as microcracks and pores, thus elasticity measurements also provide a diagnostic tool that can be used to determine the onset and the magnitude of damage, such as microcracking due to thermal shock and thermal fatigue, leg and module fabrication, mechanical vibration and impact [Case 2002]. A variety of thermo-mechanical stresses are generated during the application of thermoelectric electric (TE)

materials.

For waste heat recovery applications, stresses arise from the thermal gradients across the TE element, thermal transients superimposed on the gradients, mechanical vibration, and thermal expansion mismatch stresses among the TE module components (legs, electrical interconnects, mounting plates, etc.). These stresses can induce macrocracks, microcracks, and failure of the TE materials. The response of the material to the applied stress is a function of the microstructure (grain size, porosity, inclusions), and elastic moduli, including Young's modulus (E) and Poisson's ratio ( $\nu$ ). Therefore, the elastic moduli are required for stress analyses, including a finite element analysis (FEA) of stress and strain in components.

Since the elastic moduli are needed for stress-strain calculations (Eqs. (1.6) and (1.7)), it is important to understand how the elastic moduli decrease with increasing temperature. The elastic moduli can be considered in terms of three temperature regimes (Figure 1.2). The low temperature regime (Region I) corresponds to temperatures  $T > 0.3$  to  $0.5$  of the Debye temperature,  $\theta_D$ , where slope  $dE/dT$  or  $dG/dT$  decreases as the temperature approaches 0 K (Figure 1.2). The Debye temperature is the highest temperature for the normal mode of vibration for a given material. In the literature,  $\theta_D$  for LAST was approximately 175 K [Ren 2009] and for skutterudites  $Ce_{0.9}Fe_{3.5}Co_{0.5}Sb_{12}$  and n-type  $Co_{0.95}Pd_{0.05}Te_{0.05}Sb_3$  was roughly 300 K [Schmidt 2012].

In Region II, the elastic moduli decrease linearly with increasing temperature. For elastic polycrystalline solids, the temperature-dependent elastic moduli in Region I and II are described well by Wachtman [Wachtman 1961, Schmidt 2012]

$$E(T) = E_0 - bT \exp(-T_0/T) \quad (1.8)$$

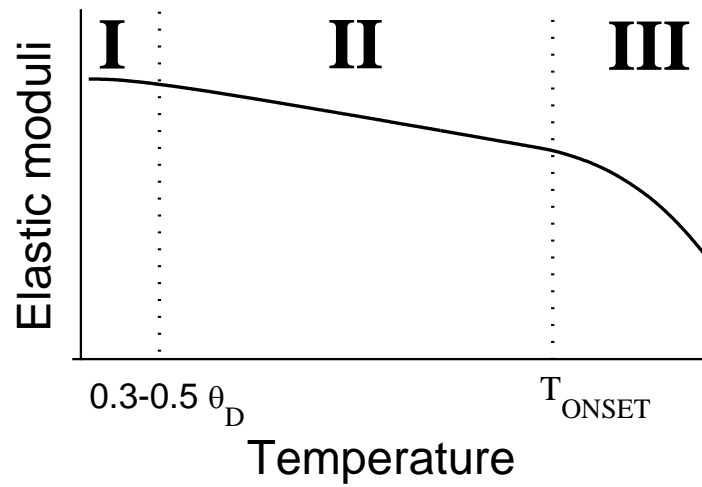


Figure 1.2 Schematic of elastic moduli change with temperature. The elastic moduli decrease with temperature in each regions. Region I is from 0 K to approximately  $0.3\theta_D$  and  $0.5\theta_D$ . Region II is a linear region. Region III is the viscoelastic or anelastic region, beginning at the onset temperature of grain boundary sliding,  $T_{ONSET}$ .

and Varshni [Varshni 1970] relationships

$$E(T) = E_0 - cT^2 / (T + d) . \quad (1.9)$$

For both the Wachtman [Wachtman 1961] and the Varshni [Varshni 1970] relationships,  $E_0$  is the Young's moduli at 0 K, and  $b$ ,  $c$ , and  $d$  are constants [Wachtman 1961, Varshni 1970]. Anderson [Anderson 1966] approximates  $T_0$  in the Wachtman equation as  $0.3\theta_D$  to  $0.5\theta_D$  [Anderson 1966, Schreiber 1973]. In Region III, begins at a temperature  $T_{ONSET}$  (Figure 1.2) where grain boundary sliding, twins and microcracks cause  $dE/dT$  to increase. The increase in  $dE/dT$  is known as “anelastic” or “viscoelastic” behavior [Schmidt 2011 in press].

In the literature, there is limited data for the room temperature or temperature dependent PbTe-based chalcogenides. For LAST thermoelectric materials (lead-antimony-silver-tellurium) with compositions  $Ag_{0.86}Pb_{19}Sb_{1.0}Te_{20}$  and  $Ag_{0.43}Pb_{18}Sb_{1.2}Te_{20}$ , Ren et al. measured the temperature dependent elastic moduli from 300 K to 773 K. The cast and hot pressed LAST specimens were described well by the Wachtman relationship. The room temperature Young's modulus for LAST and pure PbTe for a theoretically dense specimen was roughly 60 GPa. As the Young's modulus is a function of defects such as microcracks or pores, monitoring the Young's modulus yields valuable information regarding microstructural variations between specimens (such as pores) or damage during in use conditions (microcracking) [Ren 20909]

### 1.3.3 Coefficient of thermal expansion

In the literature, the average CTE values measured by dilatometry and high temperature x-ray diffraction ranged between  $20$  and  $24 \times 10^{-6} K^{-1}$  for cast and hot pressed LAST

thermoelectric materials (compositions  $\text{Ag}_{0.86}\text{Pb}_{19}\text{Sb}_{1.0}\text{Te}_{20}$  and  $\text{Ag}_{0.43}\text{Pb}_{18}\text{Sb}_{1.2}\text{Te}_{20}$  [Ren 2009]). For undoped PbTe single crystals grown by the Czochralski technique, Houston et al. [Houston 1968] used capacitive cell measurements to measure an average room temperature CTE value of about  $20.4 \times 10^{-6} \text{ K}^{-1}$ . In comparison, the CTE for  $\text{Ba}_8\text{Ga}_{16}\text{Ge}_{30}$  and  $\text{Sr}_8\text{Ga}_{16}\text{Ge}_{30}$ , other candidate TE materials for waste heat recovery, are roughly  $14.2 \times 10^{-6} \text{ K}^{-1}$  over the temperature range of 300 to 973 K [Okamoto 2008].

#### 1.3.4 Bloating at elevated temperatures

During in-use conditions at elevated temperatures, TE materials can bloat. Bloating is an increase in porosity that appears during annealing of densified specimens in the absence of a confining pressure. Bloating can occur to specimens densified using elevated temperature and pressure (hot pressing and PECS processes used in this study) when a densified specimen is thermally annealed without the confining pressure of the hot press or PECS. Bloating can result from a decomposition reaction in which a gaseous species evolves internally during thermal annealing in the absence of an external confining pressure. Decomposition reactions that cause bloating were observed in a wide range of material systems such as carbonates and sulfates [Kingery 1976].

In this study, bloating refers to an increase in porosity generated by post-densification annealing in the absence of a confining pressure. Bloating of as-densified specimens is known to be a problem for hot pressed  $\text{Ce}_{0.9}\text{Fe}_{3.5}\text{Co}_{0.5}\text{Sb}_{12}$  [Schmidt 2011 submitted],  $\text{Co}_{0.95}\text{Pd}_{0.05}\text{Te}_{0.05}\text{Sb}_3$  [Schmidt 2011 submitted], and LAST-T [Ren unpublished data]. Eliminating bloating improves specimen performance by providing microstructural thermal

stability for the as-sintered specimens.

Since porosity affects a broad spectrum of physical properties, pores generated by bloating have the potential to significantly affect the performance and mechanical integrity of thermoelectrics.

### 1.3.5 Effect of porosity in brittle materials

Porosity can affect electrical and thermal transport properties as well as elastic moduli and strength. Porosity affects many physical properties including mechanical properties such as hardness [Hoepfner 2003], elastic moduli [Rice 2000], and fracture strength [Rice 2000]. For TE materials, porosity affects both the mechanical integrity of thermoelectrics for in-service environments and electrical and thermal transport properties [He 2008, Yang 2004, Yang 2011, Zhang 2010].

It is empirically believed that the mechanical and thermal transport properties,  $A$ , depend on the volume fraction porosity,  $P$ , such that

$$A(P) = A_d \exp(-b_{PA}P) \quad (1.10a)$$

where  $A_d$  is the property of a dense material, and  $b_{PA}$  is a material-dependent constant [Rice 2000]. For sufficiently small values of  $b_{PA}P$  [Rice 2000] the above relationship can be approximated using a Taylor series with the linear form

$$A(P) = A_d(1 - b_{PA}P). \quad (1.10b)$$

For polycrystalline ceramic materials

$$\nu = \frac{E}{2G} - 1 \quad (1.11)$$

where  $\nu$  is the Poisson's ratio,  $E$  is the Young's modulus and  $G$  is the shear modulus [Rice 2000]. As the Poisson's ratio is a function of both  $E$  and  $G$ , in literature the  $\nu$  has been observed to increase, decrease or remain constant as a function of porosity.

Phani shows for polycrystalline  $\text{Al}_2\text{O}_3$ ,  $\text{ZnO}$  and  $\text{MgO}$ , [Phani 2008 JACS] the Poisson's ratio,  $\nu$ , can increase, decrease or remain the constant as a function of temperature. The  $\nu$  of  $\text{Al}_2\text{O}_3$  is relatively insensitive to volume fraction porosity,  $P$ , for  $0 \leq P \leq 0.30$   $\nu$  for  $\text{ZnO}$  decreases for  $0 \leq P \leq 0.30$ .  $\nu$  for  $\text{MgO}$ , measured by different researchers show opposite trends where in one case,  $\nu$  increases with increasing  $P$  and in the other case  $\nu$  decreases with increasing  $P$  [Phani 2008 JACS].

### 1.3.6 Effect of porosity in thermoelectrics

In the literature, there is work to reduce the thermal conductivity by phonon scattering using nanostructures or porosity to increase the  $ZT$  [Yang 2011, Zhang 2010]. Nanostructures are formed by either (1) during densification through precipitation or spinodal decomposition [Johnsen 2011, Kanatzidis 2010] or (2) by adding powder nanoparticles during fabrication [Li 2006, Liu 2011, Li 2011, Xiong 2009]. Porosity occurs naturally due to incomplete densification [Pedersen 2010, Kingery 1976], but can also be introduced using foaming agents [Pedersen 2010] or fillers that burn out during densification [Kingery 1976, Pedersen 2010]. Both the electrical conductivity and thermal conductivity will decrease with increasing porosity (Eq. (1.10a)), which implies that the  $ZT$  (Eq. (1.1)) can also change with porosity, depending on how much the properties change relative to each other.

For BiTe-thermoelectrics, volume fraction porosities of 0.0181, 0.0332 and 0.0446 were

intentionally introduced using ferrocene [Zhang 2010] which sublimed during PECS-processing. The authors did not indicate the volume fraction porosity of the PECS-processed specimen fabricated without ferrocene or how the density was measured [Zhang 2010]. The porosity was quasi-spherical, 100-500 nm in diameter and inhomogenously distributed throughout the matrix. Both the thermal and electrical conductivity decreased with increasing porosity (Eq. (1.10a)) over the temperature range investigated, 293 K to 473 K [Zhang 2010]. However, the Seebeck coefficient for the specimens with  $P = 0.0181$  and  $0.0332$  was 10% higher than the specimen with  $P = 0.0446$  and the specimen fabricated without ferrocene over the entire temperature range [Zhang 2010]. Due to efficient phonon scattering of the “nanopores” to reduce thermal conductivity, a maximum ZT of 1.38 at 473 K for the specimen with  $P = 0.0332$  was roughly 50% higher than the ZT for the specimens with  $P = 0.0181$  and  $0.0446$  [Zhang 2010].

Pedersen et al. PECS-processed  $Zn_4Sb_3$  thermoelectric specimens with  $P$  ranging from roughly 0.0 to 0.15 by varying the sintering pressure, temperature and sintering time [Pedersen 2006]. The density of each specimen was measured using the Archimedes method [Pedersen 2006]. For the  $Zn_4Sb_3$  specimens with  $P > 0.03$ , the Seebeck coefficient was roughly double at 400 K than the specimens with  $P < 0.09$  [Pedersen 2006]. Consistent with equation (1.10a and 10b), the electrical and thermal conductivity also decreased with increasing porosity over the entire temperature range, 0 K to 400 K [Pedersen 2006]. Similar to the BiTe-thermoelectrics [Zhang 2010], a maximum ZT of 0.5 at 320 K was obtained for the specimen with  $P = 0.03$  [Pedersen 2006]. Furthermore, the higher porosity specimens,  $P = 0.09$  and  $0.15$ , had ZT values less than 50% of the theoretically dense specimen [Pedersen 2006], indicating that there was a saturation of beneficial effects of the pores.

In the literature, there is little work for the mechanical properties as a function of

porosity for thermoelectrics. Rogl et al. compiled a discussion of hardness, Young's modulus and shear modulus as a function of composition, porosity, and temperature for unfilled and filled skutterudites [Rogl 2011]. For five different compositions of skutterudites [Rogl 2011], the hardness decreased with increasing porosity monotonically (Eq. (1.10)) over a narrow porosity range,  $0.005 \geq P \geq 0.03$ . For a skutterudite with composition  $DD_{0.65}Fe_3CoSb_{12}$  [Rogl 2011], where DD was didymium, the Young's modulus decreased with increasing porosity consistent with the empirical exponential (Eq (1.9)) relationship over  $0.02 > P > 0.09$ . A material dependent constant  $b_{PE}$  was 3.5 and the Young's modulus of the theoretically dense material,  $E_D$ , was 138.8 GPa (Eq. (10a)).

#### 1.4.0 Fabrication and mechanical testing of thermoelectric materials

Thermoelectrics fabricated using a casting method typically have grain sizes on the order of several hundreds of microns [Ren 2006, Pilchak 2007]. The fracture strength,  $\sigma_f$ , of brittle materials is function of the inverse square root of grain size [Barsoum 2003]. Therefore, TE legs fabricated using casting can have a low fracture strength, and therefore poor mechanical integrity. Thermoelectric materials, including LAST, a lead telluride doped with silver and antimony, have low mechanical strength. Ren *et al.* reported a biaxial fracture strength of  $\sim 15$  MPa for a cast Ag-Sb-Sn-doped PbTe with a mean grain size of  $706 \mu\text{m}$  [Ren 2006]. The use of planetary milling reduces the particle size cast ingots and therefore produces grain sizes that range from the submicron to ten's of microns when densified via hot pressing [Ren 2009, Horio 2004, Ueno 2005, Caillat 1997] or pulse electric current sintering [Jiang 2005, Kishimoto 2002].

The elastic modulus can be measured using static or dynamic methods. Current static

methods used are nanoindentation and Knoop indentation. Dynamic methods include sonic resonance, pulse echo, and resonance ultrasonic spectroscopy. For nanoindentation, the elastic recovery is measured during unloading at relative low loads [Oliver 1992], and for Knoop indentation the elastic recovery of the in-plane indentation is measured [Marshall 1982, Rogerio de Oliveira Hein 2010]. The dynamic methods, though not destructive, need a precise geometry in order to accurately calculate the elastic moduli. For some materials, the fabrication and machinability of parallelepipeds and cylinders is difficult and therefore the static methods are needed.

There has been interest in adding nanoparticle additions, such as SiC or ZnO, to thermoelectric materials to increase phonon scattering [Zhao 2008, Li 2006]. In addition to possibly enhancing the thermal transport properties, nanoparticles can improve the mechanical properties by inhibiting grain growth. When the grain size is greater than or equal to the critical flaw, hardness, fracture toughness and fracture strength are all proportional to the inverse square root of grain size [Barsoum 2003]. Therefore, if the grain growth is inhibited, the hardness, fracture toughness and fracture strength will remain constant during thermal cycling. The nanoparticles selected are insoluble in the thermoelectric matrix at the processing and use temperatures, have a higher fracture toughness than the matrix, to allow for crack deflection, and inhibit grain growth induced during long periods at high temperatures. If the fracture toughness increases the fracture strength increases for the composite thermoelectric.

In this study, the LAST and PbTe-PbS thermoelectric specimens were fabricated using hot pressing or pulse electric current sintering (PECS) with powders that were planetary ball milled from ingots. Room temperature hardness and fracture toughness were measured using Vickers indentation. The room temperature and high temperature elastic moduli were measured using

resonant ultrasound spectroscopy. Both dilatometry and high temperature x-ray diffraction were used to determine the coefficient of thermal expansion for bulk and powder specimens, respectively.

## REFERENCES

### 1.5.0 References

- [Anderson 1966] O.L. Anderson, Derivation of Wachtman's equation for temperature dependences of elastic moduli of oxide compounds, *Phys. Rev.* 144 (1966) 553-557.
- [Androulakis 2007] J. Androulakis, C-H Lin, H-J Kong, C. Uher, C-I Wu, T. Hogan, B.A. Cook, T. Caillat, K.M. Paraskevopoulos, M. G. Kanatzidis, Spinodal Decomposition and Nucleation and Growth as a Means to Bulk Nanostructured Thermoelectrics: Enhanced Performance in  $Pb_{1-x}Sn_xTe$ -PbS, *J. Am. Chem. Soc.* 129 (2007) 9780-9788.
- [Barsoum 2003] M.W. Barsoum, *Fundamentals of Ceramics*, Institute of Physics Publishing Ltd, Philadelphia, Pennsylvania, 2003.
- [Cadoff 1960] I. Cadoff, E Miller, *Thermoelectric materials and devices*, Reinhold Publishing Corporation, New York, 1960, p. 18-29.
- [Caillat 1997] T. Caillat, J-P Fleurial, A. Borshchevsky, Preparation and thermoelectric properties of semiconducting  $Zn_4Sb_3$ , *J. Phys. Chem Solids* 58 (1997)1119-1125.
- [Case 2002] E. D. Case, *The Saturation of Thermomechanical Fatigue in Brittle Materials, Thermo-Mechanical Fatigue and Fracture*, WIT Press, Southampton, UK, editor M. H. Alibadi, 2002, pp. 137 – 208.
- [Fushillo 1960] N. Fuschillo, edited by I. Cadoff, E Miller, *Thermoelectric materials and devices*, Reinhold Publishing Corporation, New York, 1960, p. 1-17.
- [Hoepfner 2003] T. P. Hoepfner and E. D. Case, The influence of the microstructure on the hardness of sintered hydroxyapatite, *Ceram. Int.* 29 (2003) 699-706.
- [Horio 2004] Y. Horio, H. Yamashita, T. Hayashi, Microstructure and thermoelectric properties of hot-pressed p-type  $Bi_{0.5}Sb_{1.5}Te_3$  alloys prepared by rapid solidification technique, *Mat. Trans.* 45 (2004) 3309-3313.
- [Houston 1968] B. Houston, R. E. Strakna, H. S. Belson, Elastic Constants, Thermal Expansion, and Debye temperature of Lead Telluride, *J Appl Phys* 39 (1968) 3913-3917.
- [Hsu 2004] K. F. Hsu, S. Loo, F. Guo, W. Chen, J. S. Dyck, C. Uher, T. Hogan, E. K. Polychroniadis, M. G. Kanatzidis, Cubic  $AgPb_mSbTe_{2+m}$ : Bulk thermoelectric materials with high figure of merit, *Science*, 303 (2004) 818-821.
- [Jiang 2005] J. Jiang, L. Chen, S. Bai, Q. Yao, Q. Wang, Fabrication and thermoelectric performance of textured n-type  $Bi-2(Te,Se)(3)$  by spark plasma sintering, *Mater. Sci. Eng. B* 117 (2005) 334-338.
- [Johnsen 2011] Johnsen S, He JQ, Androulakis J, Dravid VP, Todorov I, Chung DY, Kanatzidis

- MG. High Performance Thermoelectrics from Earth-Abundant Materials: Enhanced Figure of Merit in PbS by Second Phase Nanostructures, *J Am Chem Soc* 2011; 133: 3460-3470.
- [Joshi 2008] G. Joshi, H. Lee, Y. Lan, X. Wang, G. D. Wang, R.W. Gould, D.C. Cuff, M.Y. Tang, M.S. Dresselhaus, G. Chen, and Z. Ren, Enhanced Thermoelectric Figure-of-Merit in Nanostructured p-type Silicon Germanium Bulk Alloys, *Nano Lett.*, 8 (2008) 4670-4674.
- [Kingery 1976] W.D. Kingery, H.K. Bowen, D.R. Uhlmann, *Introduction to Ceramics*, John Wiley and Sons, New York, 1976, 505.
- [Kishimoto 2002] K. Kishimoto, T. Koyanagi, Preparation of sintered degenerate n-type PbTe with a small grain size and its thermoelectric properties, *J. Appl. Phys.* 92 (2002) 2544-2549.
- [Lawn 1993] B Lawn, *Fracture of brittle solids*, 2nd Edition, Cambridge University Press, New York, 1993.
- [Li 2006] J-F Li, J Liu, Effect of nano-SiC dispersion on thermoelectric properties of Bi<sub>2</sub>Te<sub>3</sub> polycrystals, *Phys. Stat. Sol. (a)* 203 (2006) 3768 – 3773
- [Li 2006] Li J-F, Liu J. Effect of nano-SiC dispersion on thermoelectric properties of Bi<sub>2</sub>Te<sub>3</sub> polycrystals, *Phys Stat Sol* 2006; 203: 3768–3773.
- [Li 2011] Li F, Huang X, Sun Z, Ding J, Jiang J, Jiang W, Chen L. Enhanced thermoelectric properties of n-type Bi(2)Te(3)-based nanocomposite fabricated by spark plasma sintering, *J Alloy Compd* 2011;509: 4769–4773.
- [Liu 2011] Liu D-W, Li J-F, Chen C, Zhang B-P. Effects of SiC Nanodispersion on the Thermoelectric Properties of p-Type and n-Type Bi(2)Te(3)-Based Alloys, *J Electron Mater* 2011; 40: 992-998.
- [Marshall 1982] D. B. Marshall, T. Noma, and A. G. Evans, A Simple Method for Determining Elastic-Modulus-to-Hardness Ratios using Knoop Indentation Measurements, *Communications of the American Ceramic Society* 65 (1982) C175-C176.
- [Nolas 2001] G. S. Nolas, J. Sharp, H. J. Goldsmid, *Thermoelectrics: Basic Principles and New Material Developments* (Springer series in material science, v 45), Springer, Germany, 2001.
- [Nolas 2006] George S. Nolas, Joe Poon, Mercuri Kanatzids, Recent Developments in bulk thermoelectric properties, *MRS Bulletin*, 31, March 2006, pp. 199-205.
- [Okamoto 2008] NL Okamoto, T Nakano, K Tanaka, H Inui, Mechanical and thermal properties of single crystals of the type-I clathrate compounds Ba<sub>8</sub>Ga<sub>16</sub>Ge<sub>30</sub> and Sr<sub>8</sub>Ga<sub>16</sub>Ge<sub>30</sub>, *J. Appl. Phys.* 104 (2008) 013529.

- [Oliver 1992] W.C. Oliver, G.M. Pharr, An improved technique for determining hardness and elastic modulus using load and displacement sensing indentation experiments, *J. Mater. Res.* 7 (1992) 1564-1583.
- [Pedersen 2006] B. L. Pedersen, H. Birkedal, B. B. Iversen, M. Nygren, and P. T. Frederiksen, Appl Influence of sample compaction on the thermoelectric performance of Zn<sub>4</sub>Sb<sub>3</sub>, *Appl. Phys. Lett.* 89 (2006) 242108
- [Phani 2008 JACS] K. K. Phani, A novel method of predicting ultrasonic and elastic properties of isotropic ceramic materials after sintering from the properties of partially sintered or green compacts, *J. Amer. Ceram. Soc.* 91 (2008) 215 – 222.
- [Pilchak 2007] A. L. Pilchak, F. Ren, E. D. Case, E.J. Timm, H.J. Schock, C-I Wu, T.P. Hogan, Characterization of dry milled powders of LAST (lead-antimony-silver-tellurium) thermoelectric material, *Phil. Mag.* 87 (2007) 4567-4591.
- [Pudel 2008] B. Poudel, Q. Hao, Y. Ma, Y. Lan, A. Minnich, B. Yu, X. Yan, Dezhi Wang, A. Muto, D. Vashaee, X. Chen, J. Liu, M.S. Dresselhaus, G. Chen, Z. Ren, High-Thermoelectric Performance of Nanostructured Bismuth Antimony Telluride Bulk Alloys, *Science* 320 (2008) 634-638.
- [Ren 2006] F. Ren, E. D. Case, E. J. Timm, M. D. Jacobs, H. J. Schock, Weibull analysis of the biaxial fracture strength of a case p-type LAST-T thermoelectric material, *Philosophical Magazine Letters*, 86 (2006) 673 – 682.
- [Ren 2008] F. Ren, E. D. Case, J.R. Sootsman, M.G. Kanatzidis, H. Kong, C. Uher, E. Lara-Curzio, R.M. Trejo, The high-temperature elastic moduli of polycrystalline PbTe measured by resonant ultrasound spectroscopy, *Acta Materiala*, 56 (2008) 5954-5963.
- [Ren 2009] Ren, F. , Hall, B. D. , Case, E. D. , Timm, E. J., Trejo, R. M. , Meisner, R. A. and Lara-Curzio, E. Temperature-dependent thermal expansion of cast and hot-pressed LAST (Pb-Sb-Ag-Te) thermoelectric materials', *Philosophical Magazine*, 89 (2009) 1439 — 1455.
- [Ren unpublished data]
- [Rice 2000] R. W. Rice, *Mechanical Properties of Ceramics and Composites*, Marcel Dekker Inc., New York, 2000.
- [Riffat 2003] S.B. Riffat, X. Ma, Thermoelectrics: a review of present and potential applications, *Applied thermal engineering* 23 (2003) 913-935.
- [Rogerio de Oliveira Hein 2010] L. Rogerio de Oliveira Hein, K. Amato de Campos, P. Carelli Reis de Oliveira Caltabiano, A. Lúcia Horovistiz, 3-D reconstruction by extended depth-of-field in failure analysis – Case study I: Qualitative fractographic investigation of fractured bolts in a partial valve, *Engineering Failure Analysis* 17 (2010) 515–520.

- [Rogl 2011] Gerda Rogl and Peter Rogl, Mechanical Properties of Skutterudites, *Science of Advanced Materials* 3 (2011) 517–538.
- [Rowe 2006] D.M. Rowe, Thermoelectric waste heat recovers as a renewable energy source, *International Journal of Innovations in Energy Systems and Power*, 1 (2006) 13-23.
- [Schmidt 2011 submitted] R.D. Schmidt, E. D. Case, J.E. Ni, J.S. Sakamoto, R.M. Trejo, E. Lara-Curzio, E.A. Payzant, M.J. Kirkham, R.A. Peascoe-Meisner, The temperature dependence of thermal expansion for p-type  $\text{Ce}_{0.9}\text{Fe}_{3.5}\text{Co}_{0.5}\text{Sb}_{12}$  and n-type  $\text{Co}_{0.95}\text{Pd}_{0.05}\text{Te}_{0.05}\text{Sb}_3$  skutterudite thermoelectric materials, *Philosophical Magazine*, accepted.
- [Schreiber 1973] E. Schreiber, O.L. Anderson, N. Soga, Elastic constants and their measurement, McGraw-Hill, New York, 1973.
- [Snyder 2008] G. Jeffrey Snyder, Small Thermoelectric Generators, *The Electrochemical Society Interface* (2008) 54-56
- [Tritt 1999] T. Tritt, Holey and unholey semiconductors, *Science* 283 (1999) 804-805.
- [Ueno 2005] K. Ueno, A Yamamoto, T. Inoue, S. Sodeoka, and H. Obara, Optimization of hot-press conditions of  $\text{Zn}_4\text{Sb}_3$  for high thermoelectric performance III. Effect of starting particle size on thermoelectric and mechanical properties, *J. Alloys Compds.* 392 (2005) 295-299.
- [Varshni 1970] Y. P. Varshni, Temperature dependence of the elastic constants, *Phys. Rev. B*, 2 (1970) 3952-3958.
- [Wachtman 1961] J.B. Wachtman, Jr., W.E. Tefft, D.G. Lam, Jr., C.S. Apstein, Exponential temperature dependence of Young's modulus for several oxides, *Phys. Rev.* 122 (1961) 1754-1758.
- [Wei 2007] W. Wei, J. Li, H. Zhang, X. Cao, C. Tian, J. Zhang, Macrostructural influence on the thermoelectric properties of SiC ceramics, *Scripta Mater.* 57 (2007) 1081 – 1084.
- [Xiong 2009] Xiong Z, Chen X, Zhao X, Bai S, Huang X, Chen L. Effects of nano-TiO(2) dispersion on the thermoelectric properties of filled-skutterudite  $\text{Ba}_{0.22}\text{Co}_{0.4}\text{Sb}_{1.2}$ , *Solid State Sci* 2009;11: 1612-1616
- [Yang 2004] L. Yang, J.S. Wu, L.T. Zhang, Synthesis of filled skutterudite compound  $\text{La}_{0.75}\text{Fe}_3\text{CoSb}_{12}$  by spark plasma sintering and effect of porosity on thermoelectric properties *J. Alloy. Compd.* 364 (2004) 83-88.
- [Yang 2006] J. Yang, T. Caillat, Thermoelectric materials for space and automotive power generation, *MRS Bulletin*, 31 (2006) 224-229.

[Zhang 2010] Y.H. Zhang, G.Y. Xu, F. Han, Z. Wang, and C.C. Ge, Preparation and Thermoelectric Properties of Nanoporous Bi<sub>2</sub>Te<sub>3</sub>-Based Alloys, *Journal of electronic materials*, 39 (2010) 1741-1745.

[Zhao 2008] L. D. Zhao., B. Zhang, J. Li, M. Zhou. W. Liu, and J. Liu, Thermoelectric and mechanical properties of nano-SiC-dispersed Bi<sub>2</sub>Te<sub>3</sub> fabricated by mechanical alloying and spark plasma sintering, *J. Alloys Comps.* 455 (2008) 259-264.

## 2.0 Experimental Procedure

### 2.1.0 Ingot Fabrication

Ingots were fabricated at both Michigan State University and Northwestern University. High purity elemental and compound powders of the correct concentration for LAST, LAST-T, and PbTe-PbS were placed in a sealed silica ampoule and cast using a rocking furnace. The constituent elements were heated at a maximum temperature of 1350 K for 10 hours and then cooled over 24 hours.

### 2.2.0 Powder processing

All powder processing was undertaken in an argon atmosphere glove box (Omni-Lab double glove box with oxygen sensor and moisture sensor, Vacuum Atmospheres Company, Hawthorne, CA) (Figure 2.1). After powder processing, the powders were stored in the glove box under argon atmosphere until sintering or characterization.

#### 2.2.1 CGSR (Crushed, Ground, Sieved, Reground)

After ingot fabrication, ingots were either cut into specimens or used for powder processing. The ingot was crushed into centimeter sized pieces using a mortar and pestle or the broad side of a wrench. For both the LAST and PbTe-PbS specimens, the larger centimeter sized pieces were ground and re-ground using a tungsten carbide mortar and pestle (Retsch RM200, Retsch GmbH, Haan, Germany) until they all passed through a 53 micron sieve (8" diameter x 2" height ASTM E 11 sieve, Retsch GmbH, Haan, Germany). A sieve with a larger grid (250 microns, 8" diameter x 2" height ASTM E 11, model 60.150.000, Retsch GmbH, Haan, Germany) was placed

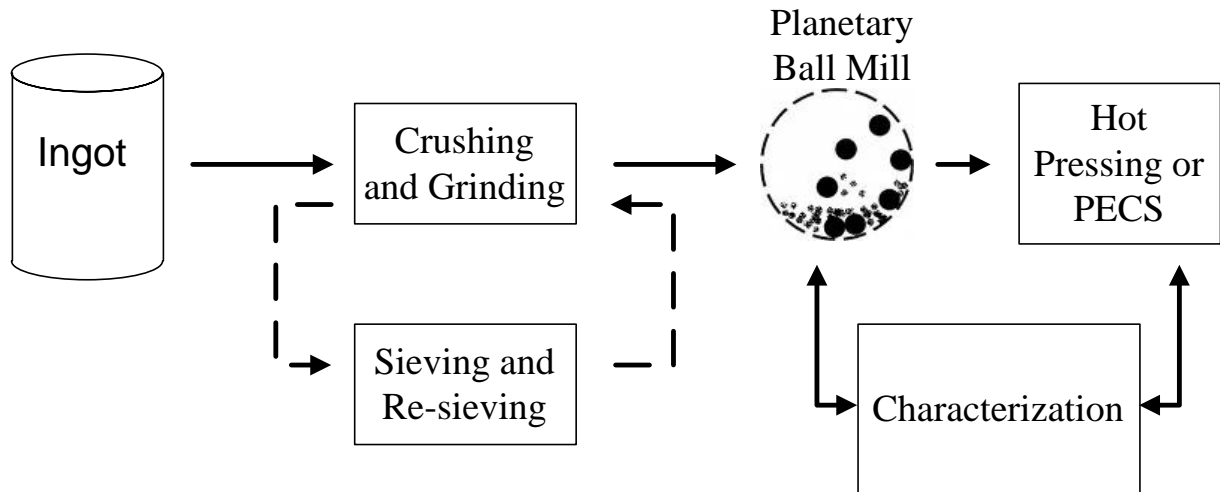


Figure 2.1: Schematic of powder processing procedure for PbTe-chalcogenides in this study. Both the powder particles and the bulk specimens were characterized using scanning electron microscopy.

on top of the 53 micron sieve to limit the larger pieces from damaging the sieve. A vibrating stage (Retsch AS 200) was used for five minutes to vibrate and aid sieving. After five minutes, the powder that passed through the 53 micron sieve was put aside, the powders that did not pass through were re-ground using the mortar and pestle until all the powder passed through the sieve. All powders that passed through the sieve were referred as CGSR (Crushed, Ground, Sieved, Reground).

After each powder processing step, approximately three grams of powder was set aside for characterization (via scanning electron microscopy, SEM, Section 2.4, or laser particle analysis, Section 2.5). After all powders passed through the sieve the powders were stored in 25 ml glass vials with plastic stoppers (RPI 121000, Research Products International Corp., Mt. Prospect, IL) with the ingot name, date of collection, milling time, speed, and any wet milling liquid used on the outside of the vial and on the lid with a permanent marker.

### 2.2.2 Milling jar and Media for milling

Alumina spherical media, with diameters of 3 mm (Retsch 05.368.0019), 10 mm (99.5% alumina, 10mm diameter grinding ball , 0076-05, Union Process, Akron Ohio) and 20 mm (Retsch 05.368.0054), was used in a 250 ml alumina lined jar (Retsch 01.462.0219) . Before the media was first used and after each cleaning with aqua regia (Section 2.3.0), the media was cleaned using 200 proof ethyl alcohol for five minutes in the ultrasonic cleaner to remove any surface contaminants. The ethanol was drained and the media was rinsed with RO water for five minutes. The media was then allowed to dry in air in a 250 mL Pyrex beaker

### 2.2.3 Milling

Each composition of LAST and PbTe-PbS had a unique alumina-lined milling jar and spherical alumina media to limit cross-contamination between compositions. Powder processing for the LAST and the PbTe-PbS compositions used the same dry milling procedure (Section 2.3.1). All powder processing was performed in an argon atmosphere glove box

#### 2.2.3.1 Dry milling

To further reduce the particle size after CGSR the powders were dry milled with a planetary mill (PM200, Retsch). For dry milling, approximately 25 grams of CGSR (Crushed, Ground, Sieved, Reground) powders were poured into the 250 ml alumina milling jar with 50 (116 g) 10 mm diameter alumina spherical media. The alumina lined lid was clamped onto the jar, securing it in place. The milling jar was placed in the planetary mill and secured using a clamp. The milling jar was loaded into the planetary mill, and milled for three hours at 150 rpm [Hall 2008].

After dry milling, approximately 3 grams was taken out and stored in a glass vial until removed for characterization (SEM, laser particle analysis). Powder that was caked on the alumina media was removed using a vibrating stage (Retsch AS 200) for five minutes. During vibrations, the alumina media was placed in a 750 micron sieve (Retsch 05.368.0054). The powder that was caked along the sides was scraped off using a metal spatula (VWR 57952-253, VWR LabShop, Batavia, IL). A 2-3 gram sample was again removed for characterization and stored in a glass vial.

The 10 mm diameter alumina spherical media was removed and placed in a labeled plastic bag and the remaining powder was placed in a labeled glass vial and stored in the glove

box. The labeled bag for the media was to ensure that there was no cross contamination from other materials that were also powdered processed in the same glove box.

#### 2.2.3.2 LAST milling – Wet milling with 10 mm diameter media and hexane

To further reduce powder particle size after dry milling, ~25 g of powder was planetary milled with 25 ml of hexane and alumina spherical media. The alumina media was a combination of 10 mm diameter spherical media and 3 mm diameter media, 140 g and 60 g respectively [Hall 2008]. Once the powder, media and milling liquid was in the milling jar the lid was clamped on and the jar was placed in the planetary mill. The planetary mill ran for 6 hours at a rate of ~110 rpm.

After milling was completed, the mill jar was removed from the planetary mill and the clamp and lid were removed. The contents of the jar, the media, powder and hexane was placed on top of the 53 micron sieve and placed in the antechamber of the double glove box. Once the pressurized antechamber reached ~0.2 MPa (30 psi), the evacuation valve was closed and argon was slowly introduced to the chamber, over 30 minutes. The vibratory stage was turned on and the powder passed through the 53 micron sieve. The milled powder was placed in a glass vial and stored in the glove box.

#### 2.2.3.3 LAST and PbTe-PbS wet milling with 20 mm and 3 mm diameter alumina media with hexane

After dry milling, additional milling can further reduce particle size. Wet milling involved adding a liquid to use as a wetting agent to limit caking and further reduce particle size. For wet milling, a milling liquid were added; in this case 25 mL hexane (the amount was

independent of the powder charge). The milling media consisted of 7 20 mm diameter alumina media and approximately 60g of 3 mm diameter alumina media. The mill jar was again returned to the planetary mill for additional milling for 6 hours at rpms that ranged from 100-120.

The slight difference in rpm's from batch to batch (100 rpm – 125 rpm) was due to the accuracy of the planetary mill. At 100 rpm the mill would sometime become unbalanced and stop running every 10 – 15 minutes. By slightly increasing the rpm, the mill would not unbalance and finish the milling cycle. This procedure was based on what was developed by Bradley Hall [Hall 2008]. After milling was completed, the powder was removed using the procedure described in Section 2.2.4.

#### 2.2.3.4 PbTe-PbS Wet milling 20 mm and 3 mm diameter with ethanol – No Dry milling

Wet milling with hexane resulted in significant caking along the sides of the jar for the skutterudite powders [Schmidt Master's Thesis]. Therefore, skutterudite powders were wet milled with ethanol, which reduced caking of the skutterudite powders along the sides of the jar [Schmidt Master's Thesis].

For the PbTe-PbS powders milled with ethanol, there was not a previous dry milling step. The powders were taken after being crushed, ground and reground until all passed through a 53 micron sieve (CGSR powders). Approximately 20 - 30 grams of CGSR powders were poured in the 250 ml alumina milling jar along with 25 - 42 mL of hexane and approximately 135 g of 20 mm diameter spherical alumina media and 60 g of 3 mm diameter spherical alumina media. The lid was clamped on and the mill jar was placed in the planetary mill. The mill was run for nine hours at 150 rpm. After the milling was completed the media and powder was removed. Removing media and powder from milling jar after wet milling.

#### 2.2.3.5 Mixing nanoparticle additions with PbTe-PbS powders

For nanoparticle composites, the nanoparticles were mixed with the matrix powders using the planetary mill to ensure a homogenous distribution. The nanosized powder amount was based on the desired volumetric total and added to the milling jar. The milling media, 115 g of 10 mm diameter alumina spheres, was added to the powders and the lid was then clamped on. There was no milling liquid added.

The milling jar was then placed in the planetary mill and milled for 3 hours at 110 rpm. After milling, the clamp and lid was removed. Powder that has clumped to the sides was moved using a metal spatula. The powder and media was poured onto a 75 micron sieve. The sieve was clamped into the sieve shakers on top of the collecting pan. The sieve shaker was run for 5 minutes. At this point all the powder was poured from the collecting pan into a labeled glass vial and the media was removed from the sieve. The labeled glass vial was stored in an argon atmosphere glove box.

#### 2.2.4 Removing media and powder from milling jar after wet milling.

After wet milling, in the argon atmosphere glove box, the clamp was removed from the jar and the lid was removed. The milling jar, with both the powder and alumina media, were placed in the smaller evacuation chamber to evaporate the milling liquid. The 710 micron sieve was placed on top of the milling jar to limit the powder and media from moving around the chamber. The evacuation chamber door was then sealed and the chamber was slowly evacuated (the knob was turned to halfway between evacuation and off). It was key to do this step slowly, as the chamber is evacuated quickly (opening the evacuation valve completely) the milling liquid

will boil rapidly and cause the powders to fly around the chamber.

Once the pressure reached approximately 0.21 MPa (30 psi), the evacuation valve can be opened all the way. The chamber was then kept at the evacuation valve opened all the way for 30 minutes. After 30 minutes has passed, the evacuation valve was turned off and the inlet valve was opened partway to slowly replenish the chamber with argon.

Once atmospheric pressure was reached, the chamber was then opened again to the glove box and the jar was removed. The jar was then scrapped along the sides to remove any powder clumps and media and powder were overturned into the large 710 micron sieve. The 710 micron sieve was placed over the sieve tray and secured into the vibrator. After vibrating for 6 minutes the media was contained in the 710 micron sieve and then powder has passed through the sieve into the bottom tray. Media and powder were now separated and ready for weighing.

### 2.3.0 Cleaning the media, jar, and sieves

#### 2.3.1 Cleaning the alumina milling media

After approximately 10 milling runs, the media was cleaned using an aqua regia mixture. The aqua regia was mixed using 1 part nitric acid ( $\text{HNO}_3$ ) to three parts hydrochloric acid ( $\text{HCl}$ ). All mixing of aqua regia and cleaning of media was performed under a fume hood. The media was placed in a 500 ml Pyrex beaker and enough aqua regia was made to submerge the media (usually 400 mL of aqua regia, 300 mL of  $\text{HCl}$  and 100 mL of  $\text{HNO}_3$ ). Once submerged, the media and aqua regia combination was left under the hood until all the aqua regia had evaporated, approximately 72 hours. The spherical alumina media was then rinsed using an ultrasonic bath of RO water for five minutes and then ethyl alcohol for five minutes, then another

5 minutes using RO water.

### 2.3.2 Cleaning the alumina lined milling jar

The alumina lined part of the jar was cleaned using aqua regia before being re-used for a different composition. Using aqua regia needs to be approached with caution. Aqua regia reacted with the outer stainless steel case of the milling jar causing discoloration and eventually pitting. All cleaning of the milling jar with aqua regia was performed under a hood using proper safety gear: a splash shield, safety glasses, lab coat, acid apron, and safety gloves.

To clean the 250 mL alumina-lined milling jars, 100 mL of aqua regia was made in a 250 mL Pyrex beaker, 25 mL nitric acid to 75 mL hydrochloric acid. The aqua regia was carefully poured into the milling jar to limit excess splashing or dripping. The milling jar was then slightly tipped in a circular fashion so the aqua regia would coat the entire inside, for approximately five minutes. The top of the jar and lid was cleaned by applying a little aqua regia to a paper towel and gently and carefully applying the aqua regia to the alumina rim along the top of the milling jar and the alumina plate on the lid. Care was taken not to touch the stainless steel.

After the aqua regia was evaporated over the course of 48 hours, the milling jar was rinsed twice with RO water to remove any residual aqua regia in the jar. The milling jar was air dried upside down on paper towels.

### 2.3.3 Cleaning the sieves

Before the sieves were either (1) used with a new powder composition or (2) began to clog with residual powder, the sieves were cleaned in soapy water. The sieves were placed in an

ultrasonic cleaner (VWR, 98000-336) with DI water and anti-bacterial soap for 5 minutes. After 5 minutes, the sieve was rinsed using RO water and placed in a 340 K furnace for 30 minutes to remove any residual moisture from the surface of the grid.

#### 2.4.0 Powder particle size determination using SEM

After each step in the powder processing procedure, (1) CGSR, (2) dry milling, and (3) wet milling, approximately 3 grams of powder samples were set aside for powder particle size and morphology characterization. To qualitatively assess the powder particle size, the powders were observed using scanning electron microscopy, SEM. The one side of a SEM stub (12 mm x 10 mm, 1503L-MB, SPI) was covered using adhesive carbon tabs (05077-BA, SPI) or carbon tape (05072-AB, SPI). Approximately 0.1 grams of powders were removed from the vial using a metal spatula and gently placed on the adhesive tape. Loose powder was removed by several short bursts of canned air.

The powders were observed in the SEM (JEOL, 6400) at an accelerating voltage of 15 kV and a working distance of 15 mm. Images were taken at several magnifications, ranging from 100x-10,000x. A qualitative range of the particle sizes can be determined using the SEM micrographs.

#### 2.5.0 Powder particle size determination using laser particle analysis

A qualitative measurement of the powder size distribution was performed by a laser particle analysis apparatus (Saturn DigiSizer 5200 Particle Size Analyzer, Micromeritics). To ensure that the results from the particle size analyzer were consistent, proper care and maintenance was

performed regularly. The three rinses are necessary to ensure accurate results by clearing out the sample line and limit collection of particles on the sample cell. At the beginning of a series of powder particle size distribution measurements (approximately every 24 hours or when a fresh batch of sucrose solution was used), (1) three rinse cycles with the analysis solution and (2) a background analysis was performed. The background analysis of the analysis solution shows the intensity versus angle when no sample was present in the system to scatter light (Figure 2.2).

Approximately every several months or when the Saturn DigiSizer 5200 Particle Size Analyzer sample cell was cleaned, the laser particle analysis apparatus was calibrated with a garnet reference powder (004-16811-00, Micromeritics). If the powder size distribution of the garnet reference powder did not agree with vendor specified powder particle size distribution, then the system was cleaned by rinsing out the analysis liquid, cleaning the sample cell, and cleaning the optics.

### 2.5.1 Analysis liquid for laser particle analysis

A 50% sucrose solution was used to ensure that the powders remain suspended in the liquid solution during analysis particle size distribution analysis. The sucrose solution was made with degassed RO (reverse osmosis) and sucrose crystals (4005-06, J.T. Baker). The RO water was degassed (AquaPrep II, 056-00000-00, Micromeritics) for two hours to remove dissolved air in the water. Dissolved air generates tiny bubbles which distorts the precision of the laser particle analysis. The 50 wt% sucrose solution was made by mixing equal parts by weight of lab quality sucrose crystals and degassed RO water.

### 2.5.2 Batch runs for laser particle analysis

Before a powder batch was analyzed in the laser particle size unit, approximately 0.3 grams of powder was dispersed ultrasonically (Ultramet III, Buehler, Evanston, IL) in 35 mL of surfactant solution contained in a 50 mL Pyrex beaker for approximately 5 minutes. A surfactant was added to the dispersion solution to aid in de-agglomeration of the powders during the laser particle analysis. Either a 0.1 wt% sodium pyrophosphate (3850-1, J.T. Baker, Austin, TX) or a 0.1 wt% sodium lignosulfonate (Daxad 23, Micromeritics, Norcross, GA) solution was used as a surfactant.

The laser particle analysis unit was rinsed three times with the sucrose solution, or until  $<0.1\%$  obscuration was obtained. (The obscuration was the percentage of light diffracted by the solution. An obscuration of  $<0.1\%$  indicates that the system was free of powder residue and thus a new particle size distribution measurement can be initiated). The reservoir of the laser particle analysis unit was cleaned with foam swabs (89022-988, VWR) and Tech Spec lens cleaner to remove residual powders from previous test batches.

Once an  $<0.1\%$  obscuration was obtained and the powders were dispersed in either the sucrose solution or a surfactant solution (to limit agglomeration), the dispersed powder solution was slowly added to the reservoir in the laser particle analysis unit until a obscuration of 15% was obtained.

At least 2 separate particle size distribution runs were done for each powder batch to (1) ensure that sampling error of the particles did not occur and (2) to obtain some consistency between runs. Before each subsequent run in the laser particle analysis unit, the powder solution was then re-dispersed in the ultrasonic bath before adding to the liquid reservoir.

## 2.6.0 Densification via Hot pressing (HP)

The hot pressed specimens induced in this study were densified using an inductively heated hot press (Hot Press Model HP200, Thermal Technology LLC, Santa Rosa, CA) at Michigan State University. This hot press (HP) simultaneously supplies heat and pressure on the green powder compact to aid in sintering and densification. The powder was stored in the argon atmosphere double glove box before loading in a 22 mm diameter graphite die. The powder was loaded into the die while the powder and die were both in the glove box.

The die was lined with Grafoil (GrafTec, Parma, Ohio) which is used to aid in removing the pressed billet from the die. The powder was cold pressed in the die before removing from the glove box to ensure that the plungers did not displace when removed from the glove box and transferred to the hot press. The maximum pressure was 60 MPa and the maximum temperatures ranged from 623 K to 723 K.

The hot pressing cycle began with heating the die from room temperature to 523 K at 0 MPa pressure over 20 minutes, then to 623 K to 723 K and 74.4 MPa of pressure over 20 minutes. While maintaining pressure, the temperature was raised to the maximum temperature over 10 minutes and then held for 90 minutes. After holding at the maximum temperature, the temperature was lowered to 100 K less than sintering temperature and pressure reduced to 0 MPa over 20 minutes. Finally the temperature was reduced to a set temperature of 323 K over 120 minutes before allowing cooling to room temperature, but, in practice, cooling occurred at a slower rate due to the natural slow cooling rate of the furnace. A typical cycle takes about 1 day to complete due to the speed of cooling to room temperature.

### 2.7.0 Densification via Pulsed Electric Current Sintering (PECS)

The Pulsed Electric Current Sintering (PECS) system (SPS 10-4, Thermal Technology LLC, Santa Rosa, CA) was investigated as an alternative to hot pressing due to the shorter fabrication times (in comparison to inductive heating hot pressing). The PECS system can rapidly heat a specimen by sending a pulsed electric current through both the die and green compact while simultaneously also applying pressure. This therefore localizes the heating and results in the specimen reaching temperature at a faster rate. The faster heating results in shorter overall pressing times.

As with hot pressing, the powders were stored in an argon atmosphere glove box before being pressed using the PECS system. The 22 mm graphite die was lined with Grafoil to aid with specimen removal after pressing (this was done outside the glove box). The powders were added to the die (with a disc of Grafoil along the top and bottom of the powder along the punches) and were cold pressed using a table top Arbor press to secure the powder and punches in the glove box. The die was then placed in a one quart resealable plastic bag (00140 737840, Gold Seal) before it was removed from the glove box to limit oxygen from interacting with the powders. The punches and die were inserted into the PECS chamber and set up according to manufactures directions. An initial pressure of 5 MPa was placed on the specimen during loading. The chamber was then pumped down for five minutes and then backfilled with 99.999% pure argon. During the pressing run, there was flowing argon. The controller was programed with the rates and times for pressure and temperature during ramp up and down of the pressure and temperature. The temperature-time-pressure profiles varied between specimens to determine the optimal profile (Table 2.1, Figures 2.2-2.3, Appendix B) . The sintering time ranged between five to 30 minutes and the maximum temperature ranged between 273 K and

Table 2.1 The maximum temperatures, pressures and times used for sintering via pulsed electric current sintering (PECS) PbTe-PbS specimens in this study.

<b>Specimen Label</b>	<b>SiC<sub>np</sub> volume percent</b>	<b>Temperature (K)</b>	<b>Pressure (MPa)</b>	<b>Time (minutes)</b>
C-PTS-P-01	0.0	823	60	20
C-PTS-P-02	0.0	823	60	20
C-PTS-P-03	2.5	823	60	20
C-PTS-P-04	2.5	823	60	20
C-PTS-P-05	0.0	823	60	21
C-PTS-P-06	1.0	823	60	21
C-PTS-P-07	3.5	823	60	21
C-PTS-P-08	0.0	873	60	21
C-PTS-P-09	0.0	823	60	30
C-PTS-P-10	0.0	823	60	20
C-PTS-P-11	0.0	823	60	20
C-PTS-P-12	2.5	823	60	20
C-PTS-P-13	0.0	673	60	20
C-PTS-P-14	3.0	673	60	20
C-PTS-P-15	0.0	673	60	20
C-PTS-P-16	2.5	673	60	20
C-PTS-P-17	3.0	673	60	20
C-PTS-P-18	2.0	673	60	20
C-PTS-P-19	0.0	673	60	20
C-PTS-P-20	0.0	723	60	20
C-PTS-P-21	0.0	723	60	20
C-PTS-P-22	0.0	723	60	20
C-PTS-P-23	0.0	723	60	20
C-PTS-P-24	0.0	723	60	20
C-PTS-P-25	0.0	823	60	16
C-PTS-P-26	0.0	823	60	16
C-PTS-P-27	0.0	823	60	20
C-PTS-P-28	0.0	673	60	5
C-PTS-P-29	0.0	823	60	16
C-PTS-P-30	0.0	823	60	16
C-PTS-P-31	0.0	823	60	20
C-PTS-P-32	0.0	623	60	5
C-PTS-P-33	0.0	573	60	5
C-PTS-P-34	0.0	533	60	5
C-PTS-P-35	0.0	493	60	5

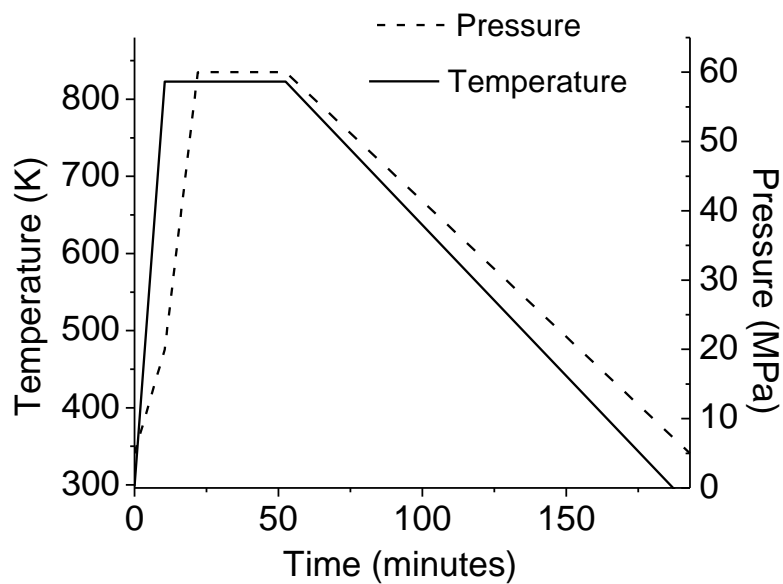


Figure 2.2 Temperature-Pressure versus time for pressing specimens C-PTS-P-09. The maximum temperature and pressure was 823 K and 60 MPa, respectively. The heating rate was 50 K/minute and the cooling rate was 5 K/minute. The pressure reached a maximum of 60 MPa 60 seconds after the temperature reached a maximum of 823 K.

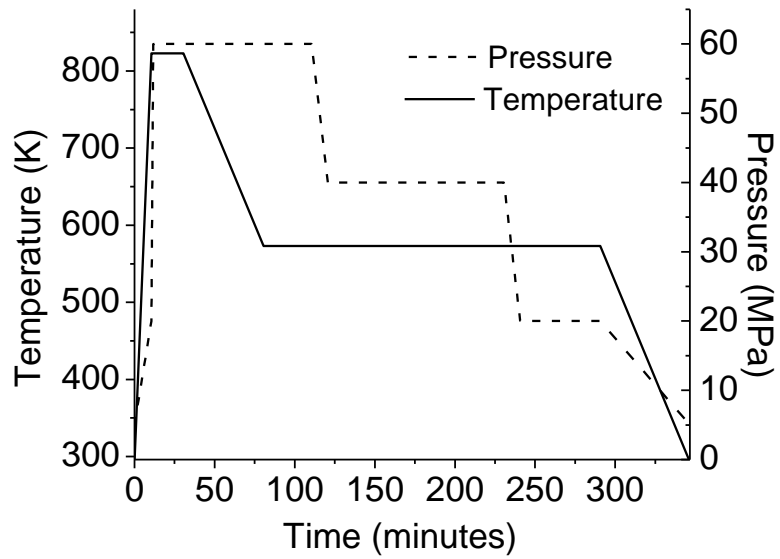


Figure 2.3 Temperature-Pressure versus time for pressing specimens C-PTS-P-11 and C-PTS-P-12. The maximum temperature and pressure was 823 K and 60 MPa, respectively. The heating rate was 50 K/minute and the cooling rate was 5 K/minute. During cooling, the specimen was thermally annealed at 573 K for 200 minutes to reduce residual stresses.

873 K (Appendix B). The maximum pressure remained constant at 60 MPa for all the specimens (Table 2.1).

### 2.8.0 Specimen Cutting and polishing

For ingot specimens, the cast ingot cylinder was cut into discs that were approximately 5 mm thick. For both pressed (hot pressed and PECS) discs and ingot discs, specimens were diced using a slow speed saw. The dimensions of the specimens varied from 7 mm x 5 mm x 4 mm to 10 mm x 7 mm x 5 mm

For ellipsometry measurements (Chapter 2, Section 10.0), grain size analysis, indentation tests, and fracture tests, a polished mirror surface was needed. Depending on the type of test, the specimens were mounted on aluminum stubs or in epoxy.

### 2.8.1 Mounting in epoxy

For a specimen mounted in epoxy, a specimen with at least one flat edge was needed. The mass and dimensions were measured to determine density (when possible). If the specimen is irregularly shaped, the mass was measured.

The epoxy (Epoxicure Resin, Buehler, Evanston, IL) and hardener (Epoxicure Hardener, Buehler, Evanston, IL) were mixed using a five to one weight ratio, respectively, per the vendor's instructions. The epoxy was measured into a 1 oz polypropylene cup (4304002301, Medical Action) using an electronic balance (Adventurer AR2140, Ohaus Corp, Pine Brook, NJ). The hardener was added using a syringe to the epoxy to match the five to one ratio of epoxy to hardener.

The epoxy and hardener were mixed using a wooden rod (740745, Royal Paper), using

small circular motions to limit air bubbles in the epoxy mixture. The specimens were placed flat side down on an 8 in x 8 in aluminum plate (McMaster-Carr, 89155K32) and 1" outer diameter Bakelite rings (811-221, LECO, St. Joseph, MI) were placed around the specimens. The mixed epoxy and hardener was poured over the specimens, filling the Bakelite rings and covering the specimens. The specimens were left to cure for a minimum of one day, and then engraved with the specimen label using a rotary tool on both the side of the Bakelite ring and top of the epoxy. Any epoxy that leaked under the phenolic ring was cut off with a steel razor.

### 2.8.2 Mounting on an aluminum stub.

An alternate way to prepare specimens for polishing were to mount them using thermoplastic on an aluminum stub. The aluminum stubs were made by cutting a 6061 aluminum rod (McMasterCarr, 8974K133) into 2.5 cm diameter stubs. Before setting in thermoplastic, the mass of the each specimen was measured using an electronic balance (Adventurer AR2140, Ohaus Corp, Pine Brook, NJ). The specimen dimensions were measured using micrometers (Mitutoyo CD-6"CSX, Kanagawa, Japan). The thermoplastic (Lakeside 70, Buehler, Evanston, IL) was placed on the aluminum stub along with the specimens during heating on the hot plate (Stirrer/Hot Plate Model 4658, Cole-Palmer, Chicago, IL). To reduce thermal transients in the specimen and the potential for thermal shock, specimens were heated slowly on the hot plate, over approximately 30 minutes. The thermoplastic was arranged around the specimen when it became malleable (at approximately 350 K). The specimen edges were oriented as nearly parallel to the aluminum stub as possible. The hot plate was then slowly cooled to room temperature.

### 2.8.3 Polishing specimens

Specimens in epoxy or thermoplastic were polished with a Leco automated polishing wheel (Leco Vari/Pol VP-50, Leco Corporation, St. Joseph, MI). Three to six specimens were mounted in a 12-specimen polishing wheel. The specimens were affixed to the polishing wheel by tightening screws into the sides of the aluminum or Bakelite ring. Care was taken to ensure the specimens were as level as possible. Affixed to each of the polishing laps was an adhesive polishing pad. For grits between 6 microns to 90 microns a White Tec pad was used (White Tec #812-454, Leco, St. Joseph, MI), for grits less than 6 microns an adhesive red felt polishing pad (Red Tec #812-445, Leco, St. Joseph, MI) was used. When the polishing pads became contaminated the pads were removed and the polishing laps were cleaned.

The diamond compound grit was placed on the polishing pads in a spiral pattern of dots approximately 10 cm apart. Diamond compound extender (Microid Diamond Compound Extender #811-004, Leco, St. Joseph, MI) was added by squeeze bottle to wet the surface of the polishing pad. Polishing extender was applied during the polishing process approximately every 15 minutes to lubricate the polishing pads. The specimens were polished using a series of pastes with the following diamond sizes: 90 micron, 67 micron, 35 micron, 25 micron, and 10 micron, 6 micron, and 1 until a mirror finish was achieved on the specimen surface (Table 2.2). Before each subsequent step the specimen holder was washed thoroughly to remove the previous diamond grit to reduce contamination.

### 2.8.4 Washing the polishing wheel by hand

Between each diamond compound grit, the specimens and polishing holder was washed

Table 2.2: Diamond Polish Table. Each diamond grit was used in succession to polish a specimen until reaching the desired polished surface on the specimen. The last polish used was either the 1  $\mu\text{m}$  or 0.5  $\mu\text{m}$  polishing grit compound.

<b>Nominal Diamond Grit Size</b>	<b>Diamond Grit Size Range</b>	<b>Manufacturer</b>	<b>Part Number</b>
90 $\mu\text{m}$	80-100 $\mu\text{m}$	Warren Superabrasives, Anaheim, CA	80-100MB MUS 20gm
67 $\mu\text{m}$	54-80 $\mu\text{m}$	Warren Superabrasives, Anaheim, CA	54-80MB MUS 20gm
35 $\mu\text{m}$	Not listed	Warren Diamond Powder Company, Olyphant, PA	#35 MUS MB 20G
15 $\mu\text{m}$	Not listed	Warren Diamond Powder Company, Olyphant, PA	#15 MUS MB 20G
9 $\mu\text{m}$	Not listed	Leco Corporation, St. Joseph, MI	810-913
6 $\mu\text{m}$	Not listed	Warren Diamond Powder Company, Olyphant, PA	#6 MUS MB 20G
1 $\mu\text{m}$	Not listed	Leco Corporation, St. Joseph, MI	810-870
0.5 $\mu\text{m}$	Not listed	Leco Corporation, St. Joseph, MI	810-868

with soap and water to limit cross contamination. A dime-sized drop of soap was placed on each specimen and rinsed under a running faucet (with a steady flow) for five minutes. The thermoplastic and epoxy was also visually examined to determine if there were macropores in the epoxy that were sequestering diamond compound. The tip of a push pin was used to remove any polishing compound that remained. The cleaning between diamond compound steps was important to limit contamination.

#### 2.8.5 Washing the polishing wheel using an ultrasonic cleaner

To clean the polishing holder an ultrasonic cleaner (VWR, 98000-336) that was large enough to immerse the polishing holder was used (with interior dimensions 30 cm x 15 cm x 15 cm). The ultrasonic cleaner was filled with RO water and Aquinox liquid soap. The amount of liquid soap added was per the soap manufacturer's directions (14.5 milliliters per 4 liters of water). Before immersion in the ultrasonic cleaner the specimen holder was rinsed with soap and water in the sink to remove residual polishing compound. The specimen holder was immersed in the ultrasonic cleaner for 5 minutes to thoroughly clean the specimens.

#### 2.9.0 Index of refraction and extinction coefficient measured via ellipsometry

Optical ellipsometry [Blanchard 2010] determined the real and imaginary parts of the optical index of refraction for the n-type skutterudite, n-type LAST, and PbTe-PbS specimen using facilities. The indices of refraction were used for to determine the particle size distribution with the laser particle analysis unit.

The thermoelectric specimens for which index of refraction measurement were

performed included: n-type skutterudite ( $\text{Ce}_{0.1}\text{Co}_{0.95}\text{Pd}_{0.05}\text{Te}_{0.05}\text{Sb}_3$ ), PbTe-PbS, and LAST specimens which were parallelepipeds, with dimensions between 10 mm x 10 mm x 6.7 mm to 10 mm x 7 mm x 5 mm. The 10 mm x 10 mm and 10 mm x 7 mm surfaces were polished to a mirror-like finish using a series of diamond paste with grit size ranging from 67 microns to 1 micron (Section 2.8).

The ellipsometer (EC110, J. A. Woollam Co.) and corresponding software (WVASE32 v3.154, J. A. Woollam Co.) were calibrated using a  $\text{SiO}_2$  wafer standard provided by the manufacturer (J. A. Woollam Co.). The optical scans were performed over the range of 4138 Å to 7463 Å, with measurements taken approximately every 75 Å. Each of the ellipsometer scans were taken at a different location on the 10 mm X 10 specimen surface. (The specimen was translated on the instrument stage using metal tweezers). For the Skutterudite, LAST, and PbTe-PbS specimens, 25 total ellipsometer scans were performed.

#### 2.10.0 X-ray diffraction

Approximately 3 grams of dry milled powders (Section 2.2.3.1) was set aside for x-ray diffraction. In this study, the high temperature x-ray diffraction was performed at Oak Ridge National Laboratory (ORNL) [Payzant 2010]. The XRD stage (Anton Paar XRK900) at ORNL was 14 mm in diameter and 0.5 mm in depth. For the high temperature XRD testing, approximately 0.63 g of powder PbTe-PbS was used. The XRD at ORNL was a Panalytical X'Pert Rom MPD (instrument type: PW3040-PRO). A mixture of 96% $\text{N}_2$ -4% $\text{H}_2$  gas flowed in the reaction chamber during the entire heating and cooling cycle. The temperature range was 30°C to 420°C using 30°C intervals. The diffraction scan was from  $2\theta = 15^\circ$  to  $2\theta = 140^\circ$  with a

step size of  $0.02^\circ$ . After the run, the lattice parameter was determined using reitveld analysis using commercial software (X'Pert HighScore Plus , PANalytical, v2.2.4) .

## 2.11.0 Hardness measured via Vickers indentations

### 2.11.1 Calibration of indenters at each load

Prior to the hardness testing, the Vickers indenters (Buehler Semimacro Indenter and Shimadzu HMV-2000) were calibrated using a standard calibration block with hardness of 7.75 GPa (761-048, Yamamoto Scientific Tools Lab, Co LTD, Japan). The calibration factor was determined by doing 10 indents at each testing load for both the Buehler, at loads of 2.94 N and 4.9 N, and Shimadzu, at loads of 0.98 N, 1.9 N, 2.94 N and 4.9 N, indenter. The measured hardness was then compared to the expected hardness to determine the calibration factor.

### 2.11.2 Vickers Hardness

The specimen's hardness,  $H$ , was determined using the Buehler Semimacro Indenter and Shimadzu HMV-2000 indenters with 10 to 20 Vickers indentations on the polished specimen surfaces using a 2.94 N load and a loading time of 5 seconds. The indentation centers were placed at least 500 microns apart, and at least 1000 microns from the specimen edge. After each indentation, the indentation width,  $2c$ , was measured using the indenter's microscope.

In addition to the indentation testing at a fixed (2.94 N) load, a possible load dependence of hardness was explored using the Shimadzu HMV-2000 with Vickers indentations made as a function of load, with 10 indentations per load, (0.25 N, 0.49 N, 0.98 N, 1.96 N, 2.94 N, 4.90 N, and 9.81 N).

For all of the Vickers indentation data, the hardness,  $H$ , was calculated from equation

[Wachtman 2009]

$$H = \frac{1.854 P}{a^2} \quad (2.1)$$

where  $2a$  is the diagonal length of the indentation impression and  $P$  is the indentation load.

When a developed radial cracks system was present, the fracture toughness,  $K_{IC}$ , was estimated using equation (2.2), which in the literature was the most frequently used form of the relationship for the indentation fracture toughness of brittle materials via Vickers indentations [Barsoum 2003].

$$K_{IC} = \alpha \left( \frac{E}{H} \right)^{1/2} \frac{P}{c^{3/2}} \quad (2.2)$$

where  $E$  is the Young's modulus,  $P$  is the indentation load,  $c$  the radial crack length for Vickers indentation and  $\alpha$  is 0.016.

### 2.13.0 Fracturing specimens

Specimens, both LAST and PbTe-PbS were fractured in order to examine the microstructure, such as grain size and porosity. The specimens were fractured by wrapping them loosely in a Kimwipe. The sharp edge of a razor blade was placed against the specimen and then the razor blade was tapped sharply with a hammer to fracture the specimen.

### 2.14.0 Thermal annealing to determine grain size and generate bloating

Specimens with both fractured surfaces and polished surfaces were thermally annealed for grain size analysis. For all specimens, the mass was measured using an electronic balance before annealing to aid in documenting volatilization during the annealing process and to aid in

identifying specimens after anneal if they were jostled during set-up.

A mullite tube, an alumina D-tube, alumina boat, and furnace seal was dedicated to each chemical composition in order to limit contamination. The selected mullite tube, D-tube, alumina boat and specimen were placed in a resistance-heated furnace (Carbolite, Watertown, Wisconsin). The specimens were placed on the alumina D-tube and the alumina boat was set over the specimens to avoid mullite dust from the muffle tube from settling on the specimen during annealing. The mullite tube was evacuated using a mechanical pump for 5 minutes and then backfilled with Argon (before July 2009) or 96% Ar + 4% H<sub>2</sub> gas (post August 2009). Then the mullite tube was refilled with the gas until there was positive pressure in the mullite tube. At this point the furnace seal was checked to be air tight using a soap-water solution. The mullite tube was evacuated and backfilled three more times, for a total of 4 times.

After the final backfill of Ar or 96% Ar + 4% H<sub>2</sub> or Ar gas, the outlet was connected to a bubbler valve. The gas flow was maintained where there was approximately 1 bubble per every 10 seconds. The furnace controller was set to the maximum temperature and time. The cooling and heating rates ranged between 2 K/min to 5K/min. The specimens were annealed from 1 hour to 4 hours at temperatures that ranged from 543 K to 936 K.

#### 2.15.0 Grain size measured by linear intercept method

For grain size analysis, both as-fractured and polished surfaces were imaged using a SEM at magnifications ranging from 300x to 10,000x. The grain size was measured using the linear intercept method on (1) thermally etched polished surfaces and (2) freshly fractured surfaces of as-densified and annealed specimens. For the linear intercept method, a set of approximately

20 to 30 straight lines were randomly drawn over a micrograph. The total length of each line was measured and scaled using the imprinted scale bar. For each line, the number of grain boundary a line crossed was counted. At least 200 grain boundary intercepts per micrograph were evaluated. The sum of the scaled line length was divided by the sum of grain boundary intercepts to calculate an average intercept length. The average intercept length was multiplied by a stereographic projection factor, 1.5 [Fullman 1953].

To compare grain sizes among specimens and to determine grain growth due to post-densification annealing, a statistically sufficient number of micrographs per specimen,  $N$ , was calculated to reduce the uncertainty in grain size measurements. Assuming a lognormal distribution for the grain size,  $GS$ , for the PbTe-chalcogenide matrix, we determined  $N$  using a lognormal 95% confidence interval such that

$$\left( \frac{\overline{GS}^*}{\bar{s}^{*2}}, \overline{GS}^* \left( \frac{\bar{s}^{*2}}{\bar{s}^{*2}} \right) \right) = (LL, UL) \quad (2.3)$$

where  $\overline{GS}^*$  was the log transformed grain size and  $\bar{s}^*$  is the empirical standard deviation [Limpert 2001]. A conservative estimate of the  $GS$  range of the PbTe-PbS matrix was assumed to be 1 micron to 15 microns, the lower limit,  $LL$ , and upper limit,  $UL$ , respectively. Using the conservative estimate of the  $UL$  and  $LL$ , we solved for  $\bar{s}^*$

$$\frac{\overline{GS}^* \left( \frac{\bar{s}^{*2}}{\bar{s}^{*2}} \right)}{\overline{GS}^* / \bar{s}^{*2}} = \frac{UL}{LL} \rightarrow \frac{\left( \frac{\bar{s}^{*2}}{\bar{s}^{*2}} \right)}{1/\bar{s}^{*2}} = \bar{s}^{*4} \rightarrow \frac{UL}{LL} = \frac{15}{1} = 15.$$

$$\bar{s}^{*4} = \frac{UL}{LL} = \frac{15}{1} = 15$$

$$\bar{s}^{*4} = \left[ \exp \left( \left[ \frac{1}{N-1} \sum_{i=1}^N \log \left( \frac{GS_i}{\overline{GS}^*} \right) \right]^2 \frac{1}{2} \right) \right]^4 = 15$$

Using Limpert et al. [Limpert 2001] definition of  $\overline{GS}^*$  and  $\bar{s}^*$

$$\overline{GS}^* = \exp \left( \frac{1}{N} \sum_{i=1}^N \log(GS_i) \right) = \left( \prod_{i=1}^N GS_i \right)^{\frac{1}{N}} \quad (2.4)$$

and

$$\bar{s}^* = \exp \left( \left[ \frac{1}{N-1} \sum_{i=1}^N \log \left( \frac{GS_i}{\overline{GS}^*} \right) \right]^2 \frac{1}{2} \right) \quad (2.5)$$

we solved for N as follows,

$$\begin{aligned} \bar{s}^{*4} = 15 &\rightarrow \bar{s}^* = 15^{1/4} \rightarrow \bar{s}^* = \left[ \exp \left( \left[ \frac{1}{N-1} \sum_{i=1}^N \log \left( \frac{GS_i}{\overline{GS}^*} \right) \right]^2 \frac{1}{2} \right) \right] = 15^{1/4} \\ \rightarrow \ln(15^{1/4}) &= \left[ \frac{1}{N-1} \sum_{i=1}^N \log \left( \frac{GS_i}{\overline{GS}^*} \right) \right]^2 \frac{1}{2} \rightarrow \left( \ln(15^{1/4}) \right)^2 = \frac{1}{N-1} \sum_{i=1}^N \left[ \log \left( \frac{GS_i}{\overline{GS}^*} \right) \right]^2 \\ \rightarrow N-1 &= \frac{1}{\left( \ln(15^{1/4}) \right)^2} \sum_{i=1}^N \left[ \log \left( \frac{GS_i}{\overline{GS}^*} \right) \right]^2 \rightarrow N = \frac{1}{\left( \ln(15^{1/4}) \right)^2} \sum_{i=1}^N \left[ \log \left( \frac{GS_i}{\overline{GS}^*} \right) \right]^2 + 1 \end{aligned} \quad (2.6)$$

Ten ‘pilot studies’ were used to determine N, the sample size. Each ‘pilot study’ consisted of ten randomly generated grain sizes [Matlab] that were between the lower limit of 1 micron and an upper limit of 15 microns. Using Eq. (2.4) and the ten randomly generated grain sizes, GS,  $\overline{GS}^*$  was calculated for each pilot study. For the ten ‘pilot studies’, N ranged between 1.9 to 4.7, indicating a statistically sufficient number of micrographs per specimen, N, was five.

#### 2.16.0 Room temperature elastic moduli measured via Resonant Ultrasound Spectroscopy (RUS)

The elastic moduli measurements at ORNL and at MSU were performed using Resonant Ultrasound Spectroscopy (RUS) (Figure 2.4) to evaluate the elastic moduli, Young’s modulus, shear modulus and Poisson’s ratio. All specimens in this study were either parallelepipeds or cylindrical discs. The parallelepipeds ranged in size from 2 mm x 1.5 mm x 5 mm to 10 mm x 12 mm x 7 mm. The cylindrical discs were 20 mm in diameter and ranged in height from 2 mm to 5 mm.

The specimens were placed on a tripod arrangement of RUS transducers, with one driver transducer and two pickup transducers (Figure 2.4). The mechanical resonance frequencies of each specimen were determined from a driving frequency range of 20 kHz to 700 kHz. For a difference in driving frequencies  $\Delta f$ , were  $\Delta f = \max f - \min f$ , during the “sweep” of the frequencies by the hardware, each frequency increment (step)  $\Delta f/29,999$ . The frequency range was chosen to encompass at least the 75 lowest resonance frequencies for a given specimen. At each frequency step the sinusoidal frequency was applied by the driving transducer. A resonance frequency response was detected as a spike in the amplitude from either of the two pickup transducers (Figure 2.5).

At least three RUS resonant spectra were taken for each specimen. For each RUS

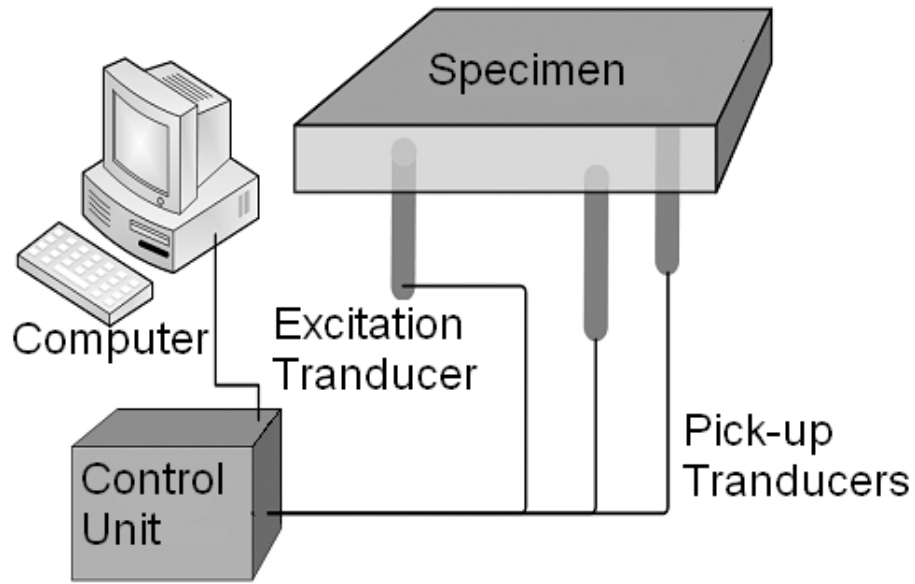


Figure 2.4: Schematic of the Resonant Ultrasound Spectroscopy (RUS) apparatus used for Young's modulus measurements. The specimen was balanced on the three transducers.

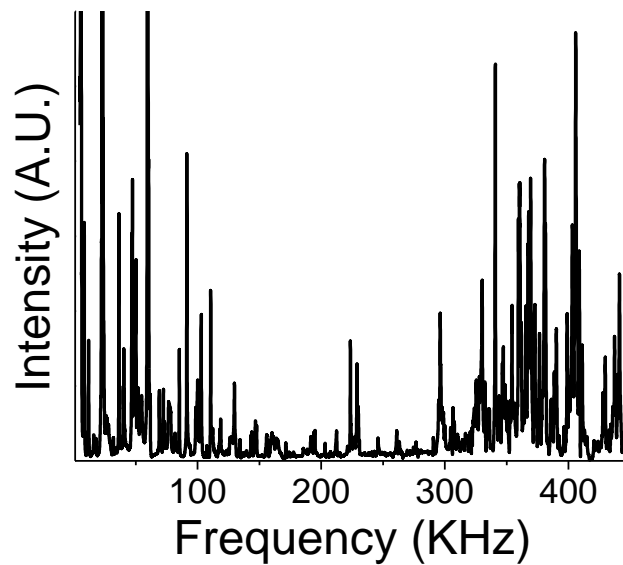


Figure 2.5: An example of an acoustic vibrational spectrum induced in a mechanically driven specimen. The resonant peak positions were functions of the elastic moduli, geometry, dimensions and mass density of the specimen. This spectrum is from C-PTS-P-07 at 363 K.

measurement the specimen was rotated or repositioned to limit the loss of peaks due to the specimen being positioned on an anti-node of the standing wave [Ren 2009]. The resonance frequency spectra that was that chosen for analysis displayed the resonant frequencies that were sharp and distinct.

Based on the specimen dimensions, mass, and resonant frequency spectrum, the Young's modulus, shear modulus and Poisson's ratio were calculated using the software available on the RUS apparatus (Quasar Galaxy RI2000 with RPMModel and CylModel software, Quasar International). The software was chosen depending on the geometry of the specimen, parallelepiped (RPMModel) or cylindrical disc (CylModel). Between approximately 12 and 40 resonance frequencies from the RUS spectra were used to calculate the elastic moduli for each specimen. Initial estimates for Young's modulus and Poisson's ratio, were required to iterate the resonance expected frequencies. Initial guesses of Young's modulus and Poisson's ratio were first taken from published values for similar PbTe-chalcogenides [Ren 2009, Simmons 1971]. The commercial software was iterated with the measured frequencies from the RUS spectra until the RMS error of the fitted model was less than 0.20% or 0.40% , for the parallelepiped and cylindrical discs, respectively.

#### 2.17.0 High temperature elastic moduli measured via RUS

All temperature-dependent modulus measurements were performed using the apparatus at Oak Ridge National Laboratories, which was similar to that used at Michigan State University for room temperature RUS measurement (Section 2.16), with the addition of a custom-built high temperature chamber for the specimen.

The high temperature transducers (Quasar International, Albuquerque, NM) were

commercially fabricated with a high temperature silicon nitride probe extending from the transducer approximately 15 cm, ending in a spherically rounded tip. The ends of each of the three probes extended through a bottom refractory plate. The ends of the three transducers were aligned in the middle of the chamber, positioned to support a specimen in a tripod arrangement. Once the specimen was in the desired location on the transducers, the thermocouple was placed approximately 1 cm from the specimen. An additional thermocouple, located at the bottom of the high temperature chamber, was used to measure the temperature of the thermal chamber. A ceramic refractory plate was placed on top of the high-temperature heating chamber and then the metallic lid of the chamber was tightened in place.

The furnace chamber was pumped down using a mechanical pump for approximately 10 minutes until the pressure gauge read -600 Torr. The chamber was then backfilled with argon or argon 96% + hydrogen 4% mixture until there was positive pressure in the chamber. The chamber was again pumped down and refilled with gas three more times. During this gas purging process, RUS scans were taken to ensure that the specimen had not fallen off the transducers during either pump-down or backfilling. After the chamber was refilled the last time the gas output was connected to a bubbler. The gas line was connected to a rotameter (FL1442-S, Omega Engineering, Inc., Stamford, CT) that controlled the flow to 100 mm.

Concurrently with the set-up of the heating chamber, the furnace controller was programmed with the desired temperature-time profile. Three different temperature time profiles were used for the LAST and PbTe-PbS system. For each of the three temperature profiles, between succeeding RUS measurements, the temperature increased at a rate of 5 K per minute. The LAST specimens had a RUS spectra taken every 50 degrees from room temperature to 873 K, both during heating and cooling. In contrast, the hot pressed and PECS-processed LAST

PbTe-PbS specimens had a RUS spectra taken every 30 degrees during heating and cooling cycles where the maximum temperatures ranged from 543 K to 663 K. At each temperature interval there was a 10 minute hold . At approximately 8 minutes into the dwell time, the RUS spectra were taken.

## 2.18 Calculating the acoustic Debye temperature

In addition to measuring the elastic moduli, the RUS spectra is also a function of the shear and longitudinal velocities,  $v_s$  and  $v_l$ . The acoustic Debye temperature,  $\theta_D$ , for the specimens in this study were calculated from the longitudinal acoustic velocity,  $v_l$ , and shear acoustic velocity,  $v_s$ , using [Anderson 1966].

$$\theta_D = \frac{h}{k} \left[ \frac{3q N \rho}{4\pi M} \right]^{1/3} v_m \quad (2.7)$$

where  $h$  is Plank's constant,  $k$  is Boltzmann's constant,  $N$  is Avogadro's number,  $\rho$  is the mass density,  $M$  is the molecular weight, and  $v_m$  is the averaged sound velocity. The polycrystalline hot pressed and PECS processed specimens in this study are assumed to be isotropic, therefore the average sound velocity,  $v_m$ , was determined using [Anderson 1966].

$$v_m = \left( \frac{1}{3} \left[ \frac{2}{v_s^3} + \frac{1}{v_l^3} \right] \right)^{-1/3} \quad (2.8)$$

where  $v_l$  and  $v_s$  were measured using RUS at 293 K.

## 2.19 Thermal Expansion Measurements

Thermal expansion was measured on bulk specimens using a Thermomechanical Analyzer (TMA) (Q400, TA Instruments, New Castle, DE) in the High Temperature Materials Laboratory at Oak Ridge National Laboratories. The TMA was calibrated using standard weights following the software instructions and recalibrated after any change in the machine components. A constant 0.1 N force was applied and maintained throughout testing with the glass expansion probe. The chamber was flushed with 50 mL/min of 96% Argon 4% Hydrogen gas for an hour before testing. The chamber is not sealed, so to limit the amount of oxygen during testing, 1 hour isothermal hold was conducted before thermal cycling.

2.19.1 Maximum temperature of the thermal cycle during thermal expansion measurements was 603 K in each experiment

The temperature dependent thermal expansion was measured for LAST and PbTe-PbS specimens from room temperature to 603 K back to room temperature. This thermal cycle was repeated two to four times, with heating and cooling rates of 1.5 K/minute.

2.19.2 Thermal expansion measured using two different maximum temperatures

To monitor bloating of PbTe-PbS specimens, the thermal expansion was measured using two different maximum temperatures, 603 K and 663 K. The first temperature profile was a cycle from room temperature to 603 K and back, for 3 heating and cooling cycles, for a total of 6 half cycles. Immediately following the first temperature profile, the specimens were cycled from room temperature to 663 K for an additional 3 heating and cooling cycles (6 half cycles). The heating and cooling rate was 2 K/minute for both temperature profiles.

## REFERENCES

## 2.20.0 References

- [Anderson 1966] O.L. Anderson, Derivation of Wachtman's equation for temperature dependences of elastic moduli of oxide compounds, *Phys. Rev.* 144 (1966) 553-557.
- [Blanchard 2010] Gary J. Blanchard, Department of Chemistry, Michigan State University, East Lansing, MI.
- [Fullman 1953] R. L. Fullman, Measurement of particles in opaque bodies *Trans AIME* 197 (1953) 447 – 452.
- [Hall 2008] Bradley D. Hall, Masters of Science Thesis, “Powder processing, powder characterization, and mechanical properties of LAST (Lead-Antimony-Silver-Tellurium) and LAST-T (Lead-Antimony-Silver-Tellurium-Tin) thermoelectric materials”, Materials Science, College of Engineering, Michigan State University, 2008.
- [Limpert 2001] Limpert E, Stahel WA, Abbt M. Log-normal distributions across the sciences, *BioScience* 51; 2001: 341-352.
- [Payzant 2010] Dr. E. Andrew Payzant, High temperature Materials Laboratory, Oak Ridge National Laboratory, Oak Ridge, TN.
- [Ren 2009] Ren, F., Case, E. D., Ni, J. E., Timm, E. J., Lara-Curzio, E., Trejo, R. M., Lin, C. -H. and Kanatzidis, M. G. Temperature-dependent elastic moduli of lead telluride-based thermoelectric materials, *Philosophical Magazine*, 89 (2009) 143 — 167
- [Schmidt 2010] Robert Schmidt, Masters of Science Thesis, “Mechanical properties of thermoelectric skutterudite materials”, Materials Science, College of Engineering, Michigan State University, 2010.
- [Simmons 1971] G. Simmons and H. Wang, *Single Crystal Elastic Constants and Calculated Aggregate Properties. A Handbook*, 2nd edition, The MIT Press, 1971.
- [Wachtman 2009] J.B. Wachtman, *Mechanical Properties of Ceramics*, Wiley and Sons, New York, 2009.

The full citation for this chapter is: Jennifer E. Ni, Fei Ren, Eldon D. Case, Edward J. Timm, Porosity dependence of elastic moduli in LAST (Lead–antimony–silver–tellurium) thermoelectric materials, *Materials Chemistry and Physics* 118 (2009) 459–466

### 3.0 Porosity dependence of elastic moduli in LAST (Lead-antimony-silver-tellurium) thermoelectric materials

Jennifer E. Ni<sup>1,\*</sup>, Fei Ren<sup>1</sup>, Eldon D. Case<sup>1</sup>, Edward J. Timm<sup>2</sup>

<sup>1</sup> Chemical Engineering and Materials Science Department, Michigan State University, East Lansing, MI 48824 USA

<sup>2</sup> Mechanical Engineering Department, Michigan State University, East Lansing, MI 48824 USA

#### Abstract

Porosity in thermoelectric materials affects the thermal, electrical and mechanical properties of the materials. In this study, the Resonant Ultrasound Spectroscopy technique was used to determine the Young's modulus,  $E$ , shear modulus,  $G$ , and Poisson's ratio,  $\nu$ , of 12 hot pressed and five cast polycrystalline specimens of the thermoelectric material LAST (lead-antimony-silver-tellurium) as a function of volume fraction porosity,  $P$ , for  $P$  ranging from 0.01 to 0.14. A least-squares fit of the Young's and shear moduli data to the relationships  $E = E_D (1 - b_{PE} P)$  and  $G = G_D (1 - b_{PG} P)$ , respectively yielded  $E_D = 58.4 \pm 0.6$  GPa and  $G_D = 23.0 \pm 0.2$  GPa, where  $E_D$  and  $G_D$  are the estimated Young's modulus and shear modulus at room temperature for theoretically dense specimens, respectively. The unitless, material-dependent constants  $b_{PE}$  and  $b_{PG}$  were  $b_{PE} = 3.5 \pm 0.2$  and  $b_{PG} = 3.5 \pm 0.2$ .

Keywords: semiconductors, elastic properties, ultrasonic measurements, microstructure

Please direct correspondence to: Jennifer E Ni, Chemical Engineering and Materials Science Department, Room 2527 Engineering Building, Michigan State University, East Lansing, Michigan, 48824-1226, USA, e-mail [nijennif@egr.msu.edu](mailto:nijennif@egr.msu.edu), FAX (517)-432-1105.

### 3.1. Introduction

Thermoelectric materials in use today are predominantly heavily doped semiconductors [1] although a number of ceramic oxide materials have been investigated as thermoelectrics [2 - 4]. Although the thermal and electric properties of thermoelectric materials have been studied extensively, there is limited mechanical property information available for many thermoelectric materials. Furthermore, there is currently no study in the literature that includes a systematic characterization of the elasticity-porosity relationship for any thermoelectric material.

This study of the porosity dependence of elastic moduli in LAST was motivated in part by the lack of elasticity-porosity data in the literature, which is significant when one considers recent observations of the enhancement of thermoelectric properties with increasing porosity for volume porosity ranges similar [5, 6] to the 0.01 to 0.14 range of the LAST specimens included in the present study. Thus, given the interest in the effects of porosity on thermoelectric properties, it is important to also consider the effects of similar porosity levels on the mechanical properties of thermoelectric materials.

In this study, the Young's modulus, shear modulus and Poisson's ratio of five cast and 12 hot pressed LAST (lead-antimony-silver-tellurium) specimens were measured by Resonant Ultrasound Spectroscopy (RUS). The observed decrease in the Young's and shear moduli with increasing porosity can be described relatively well by either an empirical exponential or linear function of porosity. For the range of volume fraction porosity (0.01 to 0.14) included in this study, this result is consistent with the trends found in the literature for other brittle materials [7, 8]. The behavior of Poisson's ratio as a function of porosity is more complex than that observed for the Young's and shear moduli, with the literature showing that the Poisson's ratio may increase, decrease, or remain approximately constant as a function of porosity. In this study, the

Poisson's ratio decreased slowly with increasing porosity. In addition, selected specimens were examined by SEM for microstructural study.

### 3.2. Background

In general, porosity can occur during specimen fabrication via either casting or sintering. In this study, polycrystalline LAST specimens are produced by (i) casting and by (ii) hot pressing powders obtained by milling the cast ingots [9]. Since the strength of brittle materials tends to increase with the reciprocal square root of the grain size [10, 11], hot pressing has the advantage of producing stronger materials with smaller grain size than cast materials [12 – 14]. In addition to strength considerations, the elastic moduli are required for either numerical or analytical stress-strain calculations for both the cast and hot pressed materials.

#### 3.2.1 Effect of porosity on physical properties

This section is a brief overview of the role of porosity in the physical properties of materials (including mechanical properties) while the following two sections address the effect of porosity effects on the thermal and electric properties of thermoelectric materials.

While this study focuses on the porosity-induced changes in the elastic moduli of LAST, it is important to note that in addition to the elastic moduli, porosity in brittle materials affects a wide range of electrical, thermal and mechanical properties, such as electrical conductivity [5,15], dielectric constant [16], thermal conductivity/diffusivity [5, 6, 15, 17, 18], hardness [19], and the fracture strength [7]. For example, exponential decreases in hardness [19], dielectric constant [16], fracture strength [7, 20], Young's modulus and shear moduli [7] have been observed for a variety of materials as porosity increases. In particular, the dependence of Young's modulus,  $E$ ,

on the volume fraction porosity,  $P$ , can be written as [7]

$$E(P) = E_D \exp(-b_{PE}P) \quad (3.1)$$

where  $E$  is a function of the volume fraction porosity,  $P$ ,  $E_D$  is the Young's modulus of dense material, and  $b_{PE}$  is a material-dependent constant. Similarly, the porosity dependence of the shear modulus,  $G$ , can be written as [7]

$$G(P) = G_D \exp(-b_{PG}P) \quad (3.2)$$

where  $G$  is a function of the volume fraction porosity,  $P$ ,  $G_D$  is the shear modulus of dense material, and  $b_{PG}$  is a material-dependent constant.

For small  $P$ , expanding  $\exp(-b_{PE}P)$  in Taylor series gives

$$E(P) = E_D \left( 1 - b_{PE}P + \frac{b_{PE}^2 P^2}{2} - + \dots \right) \quad (3.3)$$

For sufficiently small values of  $b_{PE}P$  the above relationship can be approximated with the linear form

$$E(P) = E_D (1 - b_{PE}P) \quad (3.4)$$

Similarly, as with the exponential form, the linear form for the porosity dependence of the shear modulus,  $G$ , can be written as

$$G(P) = G_D (1 - b_{PG}P) \quad (3.5)$$

### 3.2.2 Effect of porosity on thermoelectric properties

The dimensionless figure of merit,  $ZT$ , for a thermoelectric material can be written as

$$ZT = \frac{S^2 \sigma T}{k} \quad (3.6)$$

where  $S$  = the Seebeck coefficient,  $\sigma$  = the electrical conductivity,  $S^2 \sigma$  = the power factor,  $k$  = the thermal conductivity, and  $T$  = the temperature in Kelvin. Most thermoelectric materials (including LAST) that are promising for applications such as converting waste heat into electricity have a peak  $ZT > 1$ .

As discussed in the previous section, the electrical conductivity and thermal conductivity are functions of porosity. In addition, the Seebeck coefficient,  $S$ , has recently been observed to increase as a function of increasing porosity [5, 6]. Thus,  $ZT$  can either increase or remain relatively constant as a function of porosity due mainly to the porosity dependence of the electrical conductivity and the thermal conductivity.  $ZT$  is crucial in technical applications since the energy conversion efficiency,  $\eta$ , for a thermoelectric device with a heat source temperature  $T_H$  and a heat sink temperature  $T_C$  is in turn related to  $ZT$  of the thermoelectric material such that [21]

$$\eta = \left( \frac{T_H - T_C}{T_H} \right) \left( \frac{\sqrt{1 + ZT} - 1}{\sqrt{1 + ZT} + \left( \frac{T_C}{T_H} \right)} \right) \quad (3.7)$$

Thus, if  $ZT$  increases by changing the porosity, then the energy conversion efficiency of the thermoelectric material also increases.

Three recent studies report the effect of porosity on the transport properties of thermoelectric materials [5, 6, 15]. For two specimens of filled skutterudite  $\text{La}_{0.75}\text{Fe}_3\text{CoSb}_{12}$ , Yang and coworkers studied the effect of volume fraction porosity,  $P$  ( $P = 0.003$  and  $0.148$ ), on the dimensionless figure of merit,  $ZT$ , over the temperature range 300 K to 475 K [5]. The filled

skutterudite specimen with  $P = 0.003$  has a thermal conductivity approximately two times higher than the skutterudite specimen with  $P = 0.148$  over the entire temperature range [5].

Conversely, the electrical resistivity for the specimen with  $P = 0.148$  is approximately two times higher than the low porosity specimen ( $P = 0.003$ ) over the entire temperature range [5]. Thus, the effects of porosity leave the electrical conductivity/thermal conductivity ratio essentially unchanged. Yang et al. [5] also found the Seebeck coefficient to be a weak function of porosity that generally increases with increasing porosity, which implies that  $ZT$  is also a weak function of porosity as well (Eq. 3.6). Thus despite the difference in the porosity levels ( $P = 0.003$  and  $0.148$ ), over the temperature range from 300 K to 475 K, the  $ZT$  values of the filled skutterudite  $\text{La}_{0.75}\text{Fe}_3\text{CoSb}_{12}$  specimens are essentially the same, with a  $ZT$  of approximately 0.3 at 475 K [5].

Wei et al. compared the thermal conductivities, electrical resistivity, and  $ZT$  between SiC foam ceramic and bulk ceramic for temperatures between 300 K and 873 K [15]. At 873 K, the estimated  $ZT$  values are  $1.338 \times 10^{-4}$  for SiC foam and  $0.365 \times 10^{-4}$  for bulk SiC [15]. Thus, at 873 K the  $ZT$  of the highly porous SiC foam was about 3.6 times higher than that of the dense SiC bulk specimen at the same temperature.

For two different skutterudite compositions,  $\text{Co}_{0.9}\text{Ni}_{0.1}\text{Sb}_3$  and  $\text{Co}_{0.8}\text{Ni}_{0.2}\text{Sb}_3$ , He et al. studied the electrical conductivity, thermal conductivity, Seebeck coefficient, and  $ZT$  of porous ( $P = 0.08$ ) and fully dense specimens over the temperature range of 300 K to 773 K [6]. For both skutterudite compositions ( $\text{Co}_{0.9}\text{Ni}_{0.1}\text{Sb}_3$  and  $\text{Co}_{0.8}\text{Ni}_{0.2}\text{Sb}_3$ ), the introduction of porosity did not alter the electrical conductivity [6]. However, the porosity reduced the thermal conductivity by approximately 75% for both compositions [6]. In addition the porosity increased

the Seebeck coefficients by at least  $\sim 50 \mu\text{V/K}$  (approximately 25%) and  $\sim 100 \mu\text{V/K}$  (approximately 75%) for  $\text{Co}_{0.9}\text{Ni}_{0.1}\text{Sb}_3$  and  $\text{Co}_{0.8}\text{Ni}_{0.2}\text{Sb}_3$ , respectively over the temperature range [6]. At 773 K the ZT of the porous skutterudite specimens were approximately 0.55 (for composition  $\text{Co}_{0.9}\text{Ni}_{0.1}\text{Sb}_3$ ) and 0.65 (for composition  $\text{Co}_{0.8}\text{Ni}_{0.2}\text{Sb}_3$ ). In contrast, the ZT values of the dense specimens were approximately 0.3 ( $\text{Co}_{0.9}\text{Ni}_{0.1}\text{Sb}_3$ ) and 0.15 ( $\text{Co}_{0.8}\text{Ni}_{0.2}\text{Sb}_3$ ) [6]. Thus, for the porous specimens of  $\text{Co}_{0.9}\text{Ni}_{0.1}\text{Sb}_3$  and  $\text{Co}_{0.8}\text{Ni}_{0.2}\text{Sb}_3$  at 773 K, ZT was approximately two to four times higher, respectively, than the dense specimens [6].

Therefore, in addition to affecting the mechanical properties of materials (as will be discussed in the following sections) porosity can affect the transport properties of thermoelectric materials. In terms of ZT, the filled skutterudite  $\text{La}_{0.75}\text{Fe}_3\text{CoSb}_{12}$  is not sensitive to porosities between about 0.003 and 0.15 [5] while highly porous SiC foams yield ZT values of up to 3.6 times higher than the bulk, dense SiC [15]. Also, compared to dense specimens, a modest porosity of  $P = 0.08$  resulted in up to a four-fold increase in the ZT of cobalt-nickel-antimonide skutterudites [6].

Porosity in thermoelectric materials can occur as an unintended consequence of the fabrication process. For example, hot pressing may result in a residual porosity of several percent or more, depending on the hot pressing conditions. However, as reviewed in this section, recently some researchers have intentionally processed thermoelectric materials to include porosity in an attempt to tailor the ZT value [5, 6, 15,].

Thus, porosity in thermoelectric materials is of great interest both in terms of their thermoelectric and mechanical performance. In this paper we focus on the effects of porosity on Young's modulus, shear modulus and Poisson's ratio of two compositions in the LAST family of

thermoelectric materials.

### 3.3. Experimental procedure

#### 3.3.1 Specimen preparation

A total of 17 specimens were investigated in the current work including five cast and 12 hot pressed specimens. High purity elemental powders for ingot specimens N138, N155, N160-4, N160-5, and N160-9 (Table 3.1) were sealed in fused silica ampoules and placed in a three-zone split tube rocking furnace. Ingot N138 has composition  $\text{Ag}_{0.43}\text{Pb}_{18}\text{Sb}_{1.2}\text{Te}_{20}$ , where as ingots N155 and N160 have composition  $\text{Ag}_{0.86}\text{Pb}_{19}\text{Sb}_{1.0}\text{Te}_{20}$ . Figure 3.1 shows the time-temperature profiles for the cast ingots.

The hot pressed specimens HP5, HP6, and HP7 have the same composition as N138 ( $\text{Ag}_{0.43}\text{Pb}_{18}\text{Sb}_{1.2}\text{Te}_{20}$ ) (Table 3.1); while specimens HP10M, HP10N, HP12, HP11, HP20, HP30, HP38, HP40, and HP41 have the same composition as ingots N155 and N160 ( $\text{Ag}_{0.86}\text{Pb}_{19}\text{Sb}_{1.0}\text{Te}_{20}$ ) (Table 3.1). All hot pressed specimens were processed using powder that was milled from the cast ingots [9]. Table 3.2 summarizes the hot pressing conditions for the hot pressed specimens used in this study. Using a low speed diamond saw, the cast ingots and hot pressed billets were cut into rectangular parallelepipeds. Table 3.1 summarizes the dimensions, mass, composition, and processing method of each specimen included in this study.

The mass density was calculated from the mass and dimensions of each of the cast and hot pressed specimens. The length, height and width of each specimen were measured five times using an electronic caliper (Mitutoyo, 500-196-20, Aurora, IL) with has a vendor specified uncertainty of  $\pm 0.0025$  cm. The volume was computed using the mean of the measured

Table 3.1. Processing method, chemical composition, dimensions, and mass for the specimens included in this study. All specimens were rectangular parallelepipeds.

Specimen	Processing Technique	Composition	Dimensions (mm)	Mass (g)	Density (g/cm <sup>3</sup> )	Volume Fraction Porosity
N138	Cast	Ag <sub>0.43</sub> Pb <sub>18</sub> Sb <sub>1.2</sub> Te <sub>20</sub>	6.32 x 4.81 x 3.83	0.921	7.91	0.02
HP6	HPed	Ag <sub>0.43</sub> Pb <sub>18</sub> Sb <sub>1.2</sub> Te <sub>20</sub>	10.54 x 7.58 x 2.26	1.360	7.54	0.06
HP7	HPed	Ag <sub>0.43</sub> Pb <sub>18</sub> Sb <sub>1.2</sub> Te <sub>20</sub>	13.98 x 9.57 x 3.29	3.239	7.23	0.10
HP3	HPed	Ag <sub>0.43</sub> Pb <sub>18</sub> Sb <sub>1.2</sub> Te <sub>20</sub>	7.12 x 4.92 x 4.92	1.378	8.00	0.01
HP10M	HPed	Ag <sub>0.86</sub> Pb <sub>19</sub> Sb <sub>1.0</sub> Te <sub>20</sub>	6.96 x 4.65 x 4.54	1.180	8.05	0.03
HP10N	HPed	Ag <sub>0.86</sub> Pb <sub>19</sub> Sb <sub>1.0</sub> Te <sub>20</sub>	6.99 x 4.59 x 4.54	1.176	8.08	0.03
HP12	HPed	Ag <sub>0.86</sub> Pb <sub>19</sub> Sb <sub>1.0</sub> Te <sub>20</sub>	7.15 x 5.10 x 5.10	1.324	7.13	0.14
HP20	HPed	Ag <sub>0.86</sub> Pb <sub>19</sub> Sb <sub>1.0</sub> Te <sub>20</sub>	7.07 x 4.89 x 4.88	1.378	8.15	0.02
HP30	HPed	Ag <sub>0.86</sub> Pb <sub>19</sub> Sb <sub>1.0</sub> Te <sub>20</sub>	6.88 x 4.90 x 4.94	1.345	8.08	0.03
HP38	HPed	Ag <sub>0.86</sub> Pb <sub>19</sub> Sb <sub>1.0</sub> Te <sub>20</sub>	6.61 x 4.92 x 4.91	1.291	8.09	0.03
HP40	HPed	Ag <sub>0.86</sub> Pb <sub>19</sub> Sb <sub>1.0</sub> Te <sub>20</sub>	6.94 x 5.05 x 4.92	1.515	8.07	0.03
HP41	HPed	Ag <sub>0.86</sub> Pb <sub>19</sub> Sb <sub>1.0</sub> Te <sub>20</sub>	7.07 x 4.91 x 4.93	1.377	8.05	0.03
HP 11	HPed	Ag <sub>0.86</sub> Pb <sub>19</sub> Sb <sub>1.0</sub> Te <sub>20</sub>	7.18 x 4.59 x 4.54	1.155	7.71	0.07
N155	Cast	Ag <sub>0.86</sub> Pb <sub>19</sub> Sb <sub>1.0</sub> Te <sub>20</sub>	12.6 x 9.00 x 2.50	2.363	8.14	0.02
N160-4	Cast	Ag <sub>0.86</sub> Pb <sub>19</sub> Sb <sub>1.0</sub> Te <sub>20</sub>	6.72 x 4.93 x 4.93	1.327	8.15	0.02
N160-5	Cast	Ag <sub>0.86</sub> Pb <sub>19</sub> Sb <sub>1.0</sub> Te <sub>20</sub>	6.85 x 4.92 x 5.00	1.354	8.04	0.03
N160-9	Cast	Ag <sub>0.86</sub> Pb <sub>19</sub> Sb <sub>1.0</sub> Te <sub>20</sub>	7.00 x 4.95 x 4.95	1.383	8.07	0.03

Table 3.2 Processing conditions, including maximum temperature, maximum pressure and total time at maximum temperature for the hot pressed specimens used in this study.

Specimen	Maximum Temperature (K)	Maximum Pressure (MPa)	Time (Minutes)
HP3	673	75	235
HP6	623	60	235
HP7	573	60	235
HP10M	673	75	235
HP10N	673	75	235
HP11	623	60	365
HP12	673	75	365
HP20	673	75	365
HP30	673	75	235
HP38	673	75	235
HP40	673	75	235
HP41	673	75	235

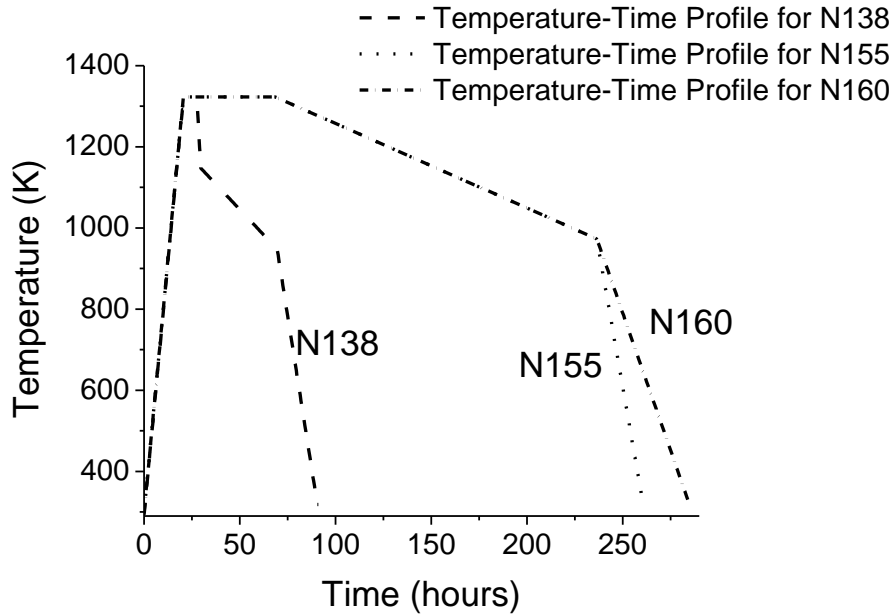


Figure 3.1 Time-temperature profile for the fabrication of the five ingots specimens included in this study. N138 ( $\text{Ag}_{0.43}\text{Pb}_{18}\text{Sb}_{1.2}\text{Te}_{20}$ ), N155, and N160-4, -5 and -9 ( $\text{Ag}_{0.86}\text{Pb}_{19}\text{Sb}_{1.0}\text{Te}_{20}$ ) (Table 3.2a). Specimens N160-4, -5 and -9 were cut from a single ingot.

dimensions for the length, height and width. The mass was determined using an electronic balance (Ohaus Adventurer, AR2140, Pinebrook, NJ) with a vendor-specified precision of  $\pm 1.0 \times 10^{-4}$  g.

### 3.3.2 Specimen Preparation and Microstructural Examination

Specimens were polished using a series of diamond pastes with grit sizes down to 0.5 micron. After ultrasonically cleaning the specimen surfaces, the as-polished surfaces of each specimen were examined with a scanning electron microscope (JEOL 6400, JEOL Ltd., Japan) using a working distance of 15 mm and an accelerating voltage of 15 kV. The as-polished specimen surfaces allowed the surface pores to be viewed. Also, the as-polished surfaces of each specimen were carefully examined to determine whether or not cracks were present. Thermal etching on selected specimens was performed in a sealed mullite tube in flowing argon gas at temperatures of 598 K to 698 K for times between 1 hour and 4 hours.

### 3.3.3 Resonant Ultrasound Spectroscopy (RUS) measurements

Room temperature resonant ultrasound spectroscopy (RUS) [22] was performed in air using a commercial RUS system (RUSpec, Quasar International Inc., Albuquerque, NM, USA) with a tripod transducer configuration. Details of the RUS experimental procedure and calculations are given elsewhere [23].

## 3.4. Results and Discussion

### 3.4.1 Microstructural analysis

The as-polished surfaces of the specimens were examined via SEM. No cracks were

visible in the as-polished surfaces of the hot pressed and cast specimens, although the specimens did show varying amounts of porosity. The presence of pores and the absence of detectable surface cracks in the as-polished specimens are significant. While increasing porosity decreases the elastic moduli of materials [7, 8] cracks also act to decrease the elastic moduli [24]. Also, in additional work by the present authors, the Young's and shear modulus versus temperature data of specimens N138 and HP6 did not show hysteresis between the heating and cooling curves [25]. The absence of a modulus-temperature hysteresis indicates there was no significant microcracking in those specimens [24]. In addition, no hysteresis has been observed for modulus-temperature measurements performed by the authors on LAST specimens not included in this study. The SEM observations included in this study and our previous study on the modulus-temperature of LAST materials [25] indicate that pores rather than cracks or microcracks are likely responsible for the decrease in elastic moduli observed in this study. Also, as will be discussed in Section 3.4.2.2, the modulus decrease is a relatively smooth function of porosity which suggests that additional modulus decrement mechanisms (such as cracks) are either absent or at a constant level in each specimen.

SEM images of thermally etched surfaces (Figs. 3.2d - 3.2e) show that the grain size distribution is bimodal for hot pressed specimens. The larger grain sizes varied from about 20 (Figs. 3.2e and 3.2f) to 50 microns (Fig. 3.2d). The smaller grained matrix included grains from roughly 1 to 10 microns in diameter (Figs. 3.2d – 3.2f). Similarly prepared cast LAST specimens have grain sizes in the range of 500 – 700 microns [25].

### 3.4.2. Room temperature elastic moduli as a function of porosity

Room temperature RUS measurements were performed on a total of 17 specimens (Table 3.1) to determine the behavior of the elastic moduli as a function of porosity (Fig. 3.3). In the

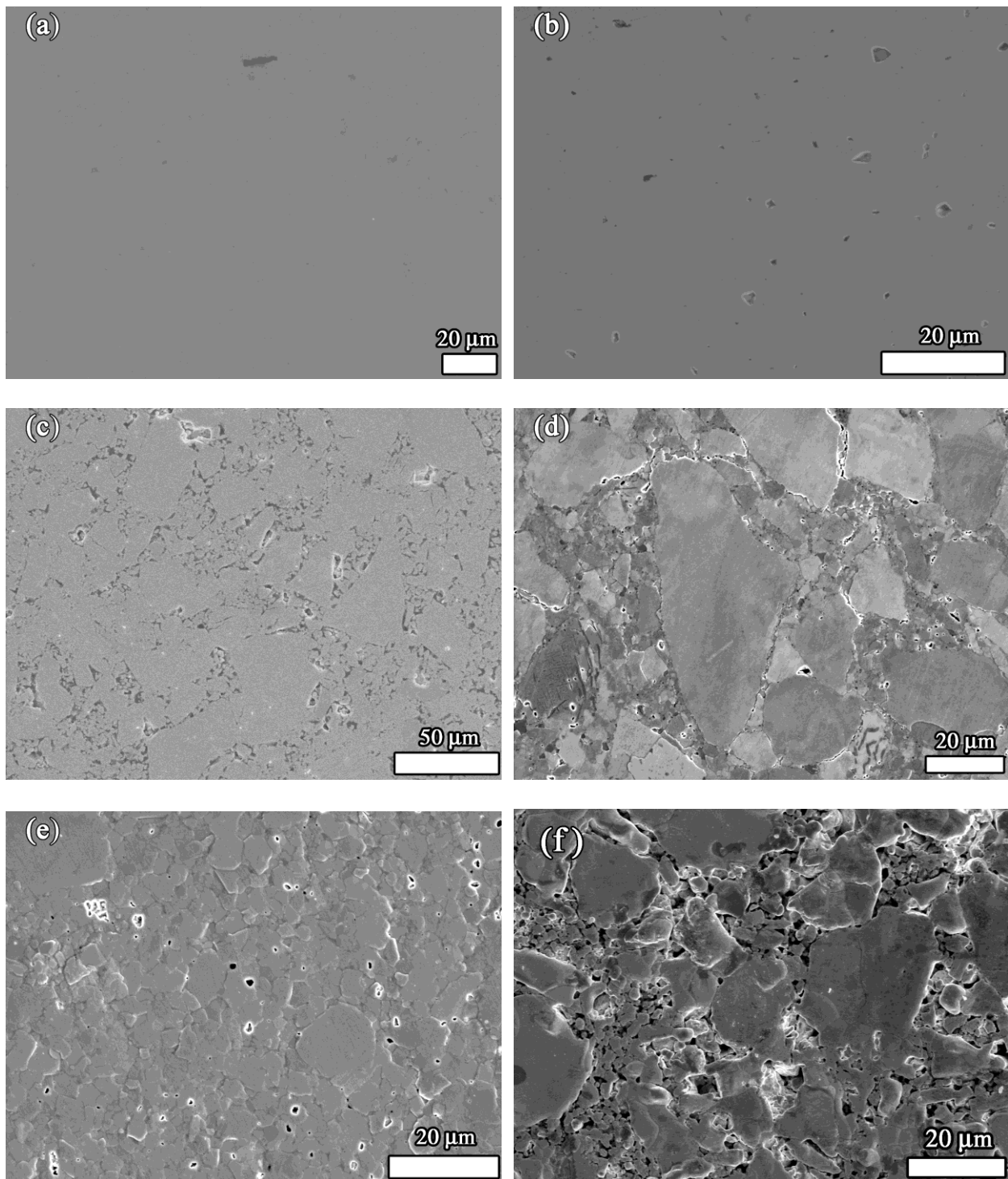


Figure 3.2 SEM micrographs of the as polished surfaces of specimens (a) HP3 ( $P = 0.01$ ) (b) HP30 ( $P = 0.01$ ) (c) HP7 ( $P = 0.10$ ), as well as the thermally etched surfaces (d) HP3 ( $P = 0.01$ , thermally etched at 598 K for 2 hrs) (e) HP30 ( $P = 0.01$ , thermally etched at 673 K for 2 hrs) (f) HP7 ( $P = 0.10$ , thermally etched at 698 K for 2 hrs)

following section, we discuss the observed porosity-induced-changes in both Young's modulus and shear modulus, which can be described in terms of an exponential or a linear function of the volume fraction porosity, P (Section 3.2.1, Eqs. 3.1, 3.2, 3.4, and 3.5). Changes in Poisson's ratio as a function of porosity will be discussed in Section 3.4.2.3.

### 3.4.2.1. Young's modulus and shear modulus as a function of porosity

The decreasing Young's modulus with increasing porosity data was fit to both the exponential and linear functions given by Eqs. (3.1) and (3.4). For both the hot pressed and the combined hot pressed-cast data sets, the linear relationship was a slightly better fit to the data (Table 3.3).

For the 12 hot pressed specimens, the linear fit of the room temperature Young's modulus data to Eq. (3.4) was excellent,  $E_D = 58.3 \pm 0.3$  GPa,  $b_{PE} = 3.6 \pm 0.1$  and an coefficient of determination,  $r^2 = 0.994$  (Fig.3a, Table 3.3). When the five cast ingot specimens were included in the combined data set with the hot pressed specimens (a total of 17 specimens),  $E_D = 58.4 \pm 0.6$  GPa,  $b_{PE} = 3.5 \pm 0.2$  with an  $r^2$  of 0.962 (Fig. 3.3b, Table 3.3). The  $r^2$  values obtained by fitting to the linear and exponential relationships (Eqs. 3.1 and 3.4) were essentially the same for the Young's modulus data for the hot pressed specimens, that is,  $r^2$  for the fit to the exponential equation (Eq. 3.1) was 0.988 and  $r^2$  for the fit to the linear relationship (Eq. 3.4) was 0.994 (Table 3.3). However, for the combined data set (the 5 cast and 12 hot pressed specimens), the fit of the Young's modulus-porosity data to the linear equation (Eq. 3.1) gave a  $r^2$  value of 0.962, while  $r^2$  was somewhat lower (0.949) for the fit to the exponential equation

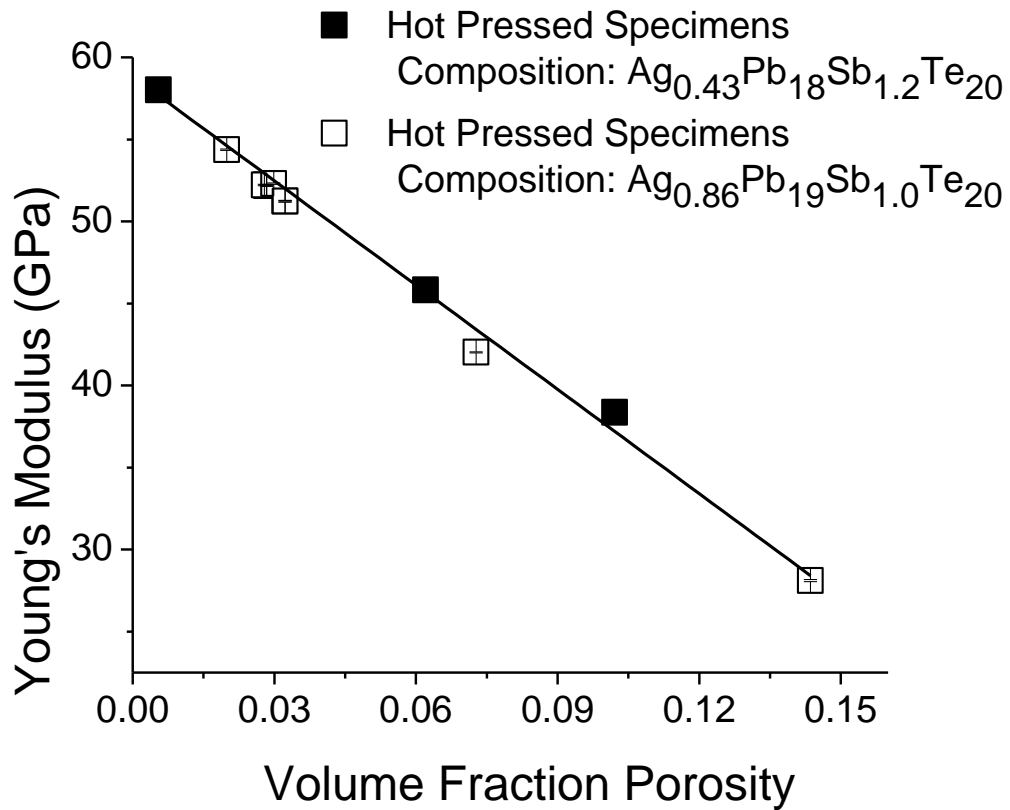


Figure 3.3a For the hot pressed specimens only (compositions  $\text{Ag}_{0.43}\text{Pb}_{18}\text{Sb}_{1.2}\text{Te}_{20}$  and  $\text{Ag}_{0.86}\text{Pb}_{19}\text{Sb}_{1.0}\text{Te}_{20}$ ), the solid line indicates the least-squares fit to linear relationship (Eq. 3.4) for Young's modulus (determined by room temperature RUS) as a function of porosity.

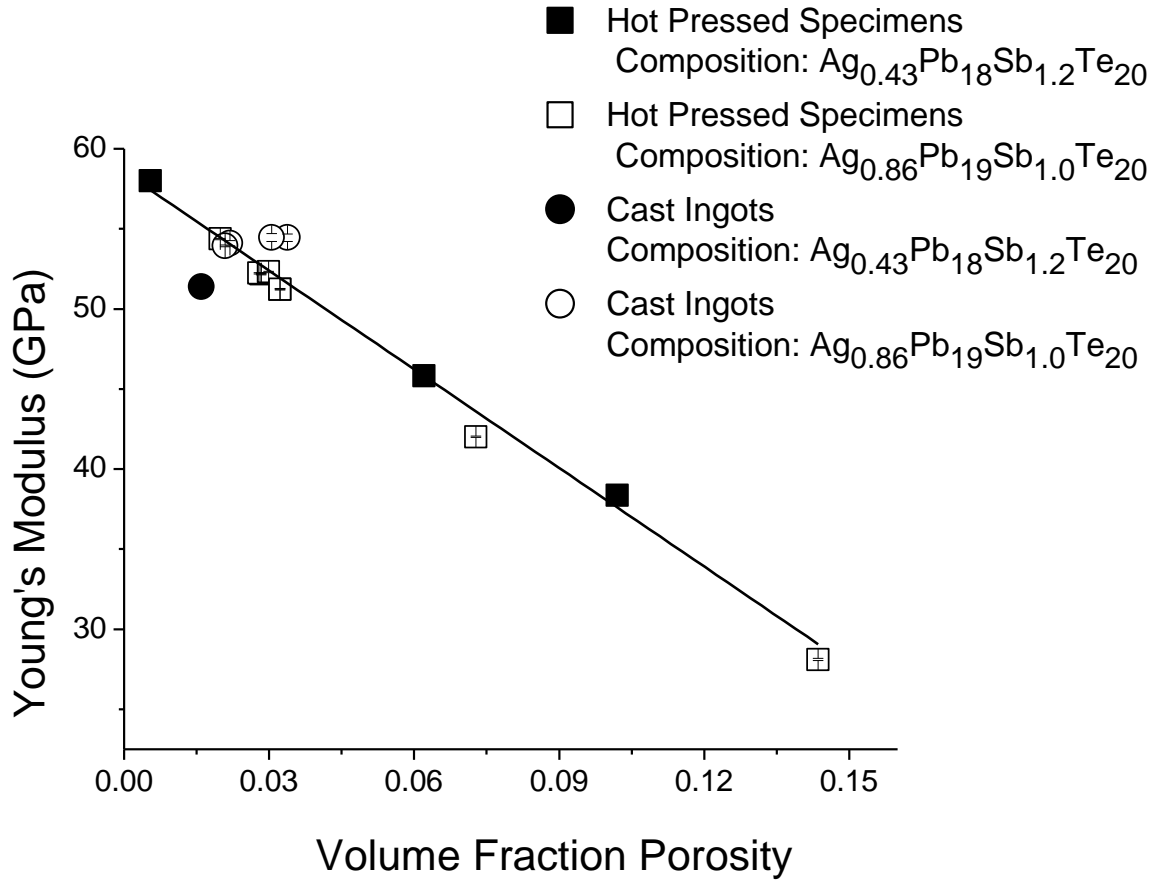


Figure 3.3b For the combined data set (12 hot pressed specimens and 5 cast specimens), the solid line indicates the least-squares fit to linear relationship (Eq. 3.4) for Young's modulus (determined by room temperature RUS) as a function of porosity.

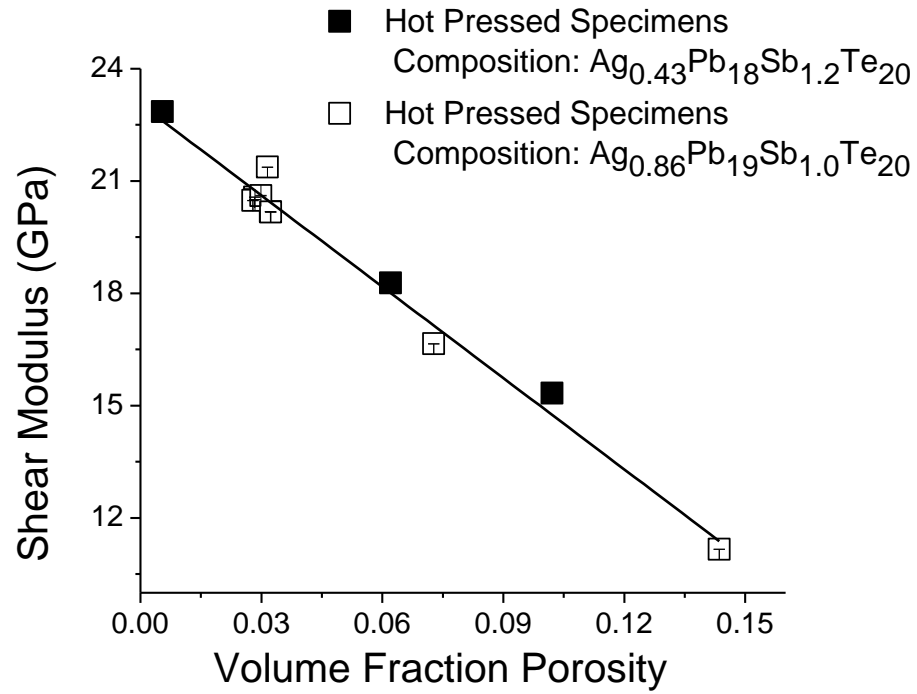


Figure 3.3c For the hot pressed specimens only, the solid line indicates the least-squares fit to linear relationship (Eq. 3.5) for shear modulus (determined by room temperature RUS) as a function of porosity.

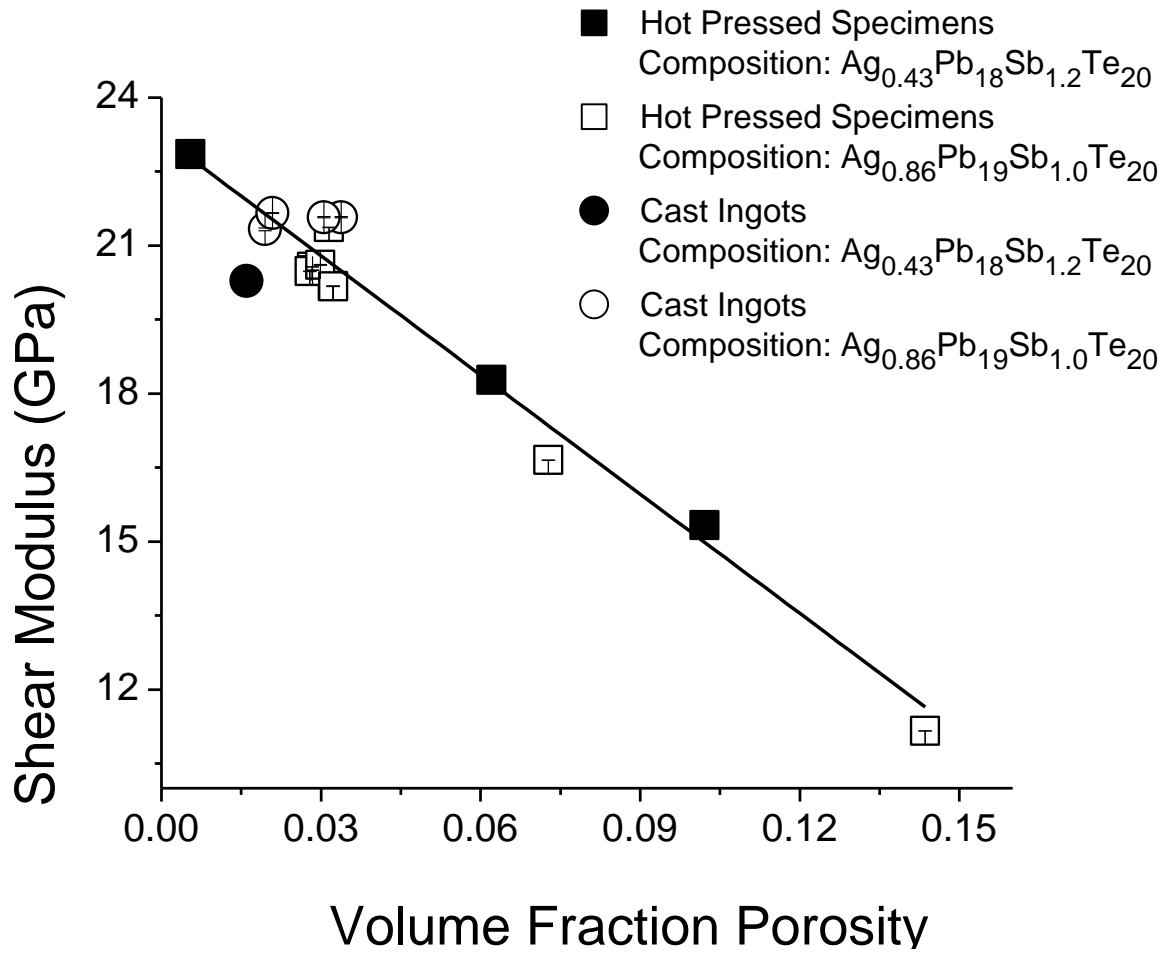


Figure 3.3d For the combined data set (12 hot pressed specimens and 5 cast specimens), the solid line indicates the least-squares fit to linear relationship (Eq. 3.5) for shear modulus (determined by room temperature RUS) as a function of porosity.

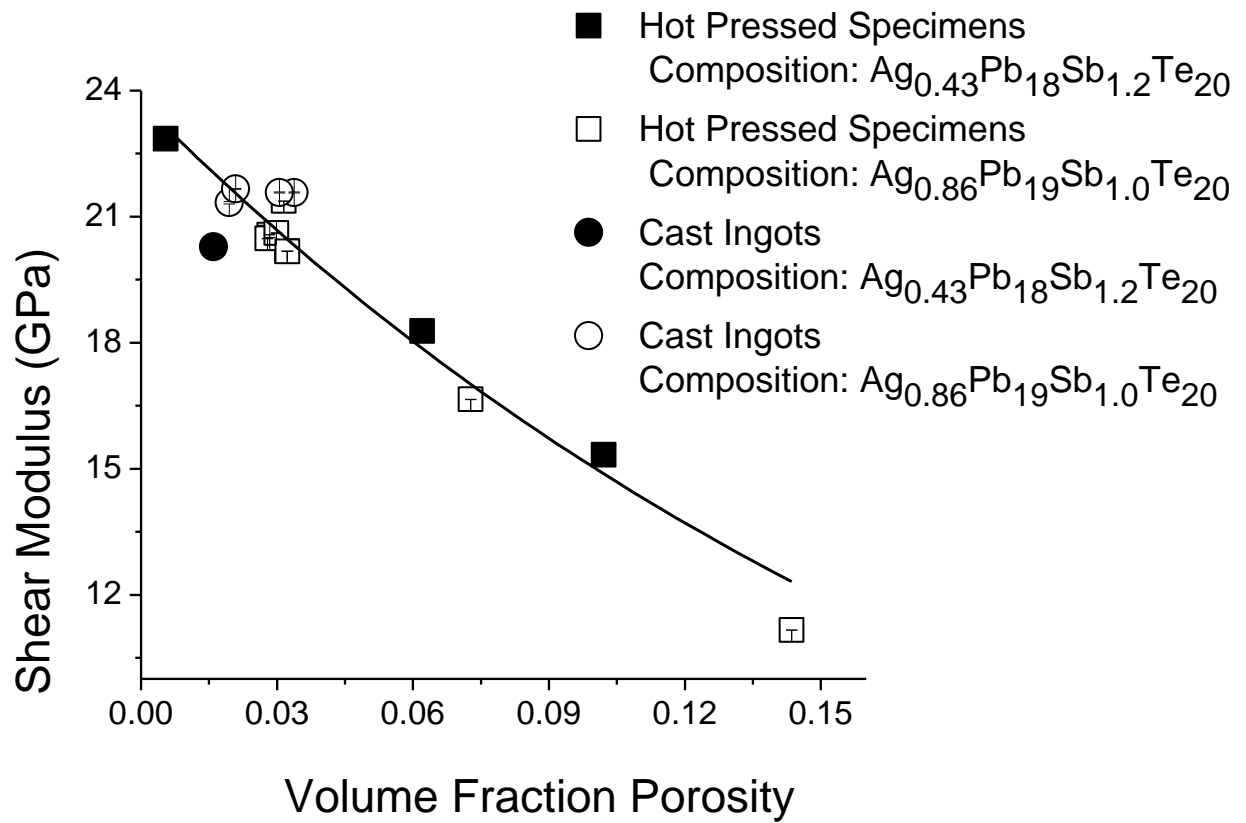


Figure 3.3e For the combined data set (12 hot pressed specimens and 5 cast specimens), the solid line indicates the least-squares fit to the exponential relationship (Eq. 3.2) for shear modulus (determined by room temperature RUS) as a function of porosity.

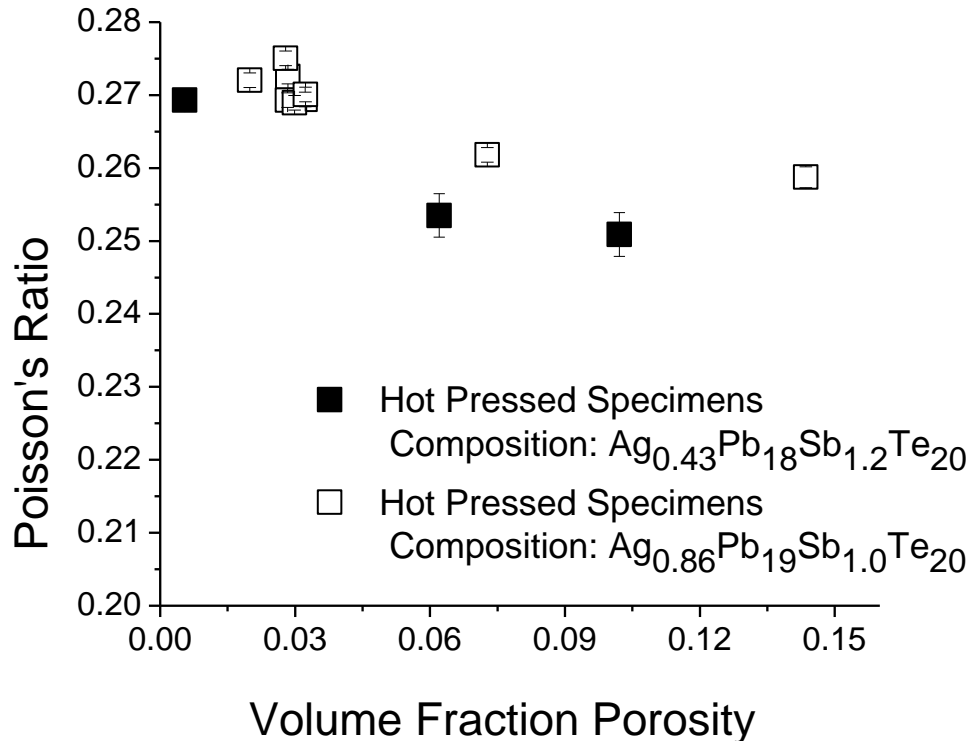


Figure 3.3f For the hot pressed specimens only, the Poisson's ratio determined by room temperature RUS measurements versus volume fraction porosity.

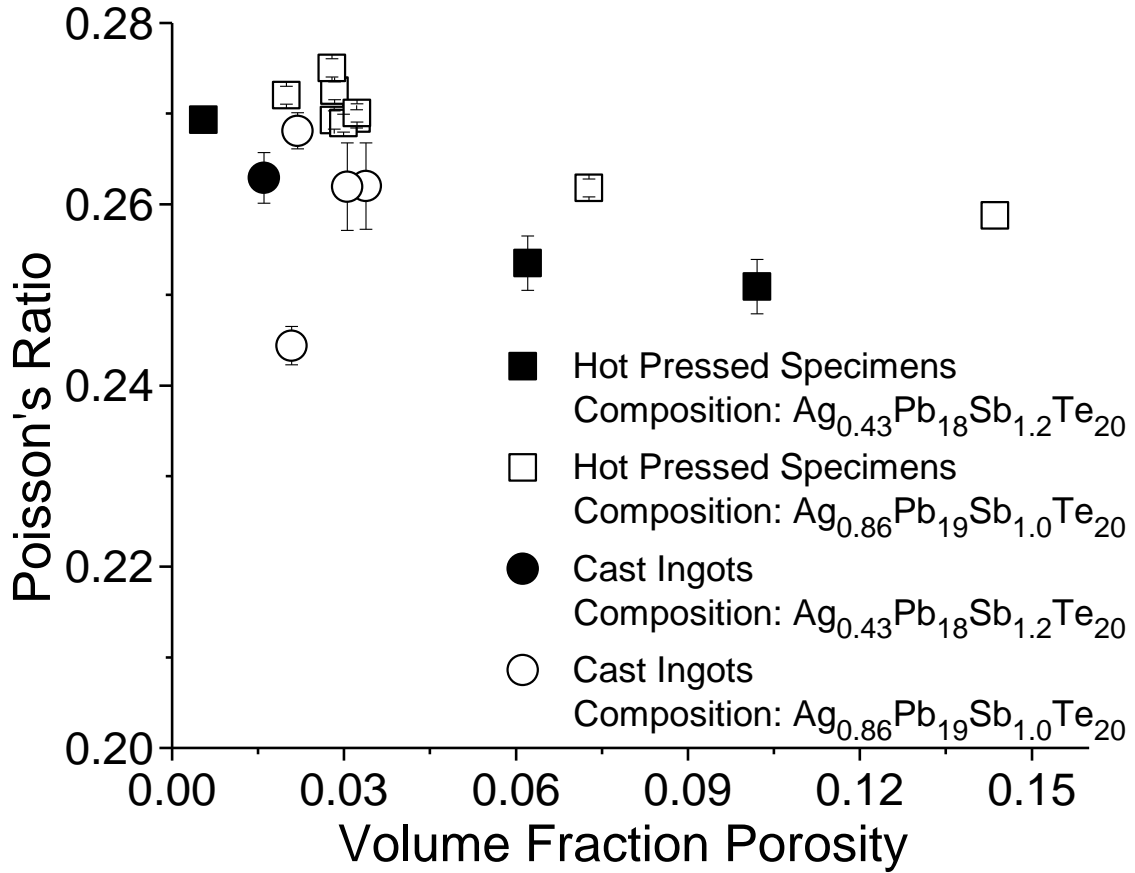


Figure 3.3g For the combined data set (12 hot pressed specimens and 5 cast specimens), Poisson's ratio determined by room temperature RUS measurements versus volume fraction porosity of the combined data (hot pressed and cast ingot specimens).

Table 3.3. Parameters  $b_{PE}$ ,  $E_D$ ,  $b_{PG}$ , and  $G_D$  obtained from the least-squares fit to the linear (Eqs. 3.4 and 3.5) and exponential (Eqs. 3.1 and 3.2) empirical relationships for the Young's and shear moduli. N is the number of specimens included in each analysis and  $r^2$  is the coefficient of determination

<b>Young's Modulus</b>					
<b>Empirical relationship</b>	<b>Specimens</b>	<b>N</b>	<b><math>r^2</math></b>	<b><math>b_{PE}</math></b>	<b><math>E_D</math> (GPa)</b>
Exponential	Hot Pressed	12	0.988	$4.8 \pm 0.2$	$60.0 \pm 0.5$
Linear	Hot Pressed	12	0.994	$3.6 \pm 0.1$	$58.3 \pm 0.3$
Exponential	Cast and Hot Pressed	17	0.949	$4.7 \pm 0.3$	$59.8 \pm 0.8$
Linear	Cast and Hot Pressed	17	0.962	$3.5 \pm 0.2$	$58.4 \pm 0.6$

<b>Shear Modulus</b>					
<b>Empirical relationship</b>	<b>Specimens</b>	<b>N</b>	<b><math>r^2</math></b>	<b><math>b_{PG}</math></b>	<b><math>G_D</math> (GPa)</b>
Exponential	Hot Pressed	12	0.984	$4.7 \pm 0.2$	$23.5 \pm 0.2$
Linear	Hot Pressed	12	0.991	$3.5 \pm 0.1$	$22.9 \pm 0.1$
Exponential	Cast and Hot Pressed	17	0.942	$4.6 \pm 0.3$	$23.6 \pm 0.3$
Linear	Cast and Hot Pressed	17	0.956	$3.5 \pm 0.2$	$23.0 \pm 0.2$

(Table 3.3).

As was the case for the Young's modulus, the decrease in shear modulus with increasing porosity was fit to both the linear and exponential forms (Eqs. 3.2 and 3.5). The fit to the linear relationship (Eq. 3.5) for the hot pressed data gave  $G_D = 22.9 \pm 0.1$  GPa,  $b_{PG} = 3.5 \pm 0.1$  with  $r^2 = 0.991$  (Fig. 3.3c). For the shear modulus, a fit to the linear relationship (Eq. 3.5) for the 17 specimen combined data set gave  $G_D = 23.0 \pm 0.2$  GPa,  $b_{PG} = 3.5 \pm 0.2$  with  $r^2 = 0.956$  (Fig. 3.3d, Table 3.3). The  $r^2$  values for the fit to the exponential and linear equations for the combined data set were 0.942 and 0.956, respectively. To illustrate the apparently improved fit of the linear equation (Eq. 3.5) compared to the exponential equation (Eq. 3.2), we include plots of shear modulus versus porosity for the combined data sets for both the linear (Fig. 3.3d) and exponential fit (Fig. 3.3e).

Thus, for the range of  $P$  included in this study ( $0.01 \leq P \leq 0.14$ ), the Young's and shear modulus behavior as a function of porosity described relatively well by either the linear relationships (Eqs. 3.4 and 3.5) or the exponential relationships (Eqs. 3.1 and 3.2), with the linear relationships having a somewhat better fit in some cases (Table 3.3, Figs. 3.3b - 3.3e).

3.4.2.2. Simulation of errors in modulus-porosity parameters as a function of the uncertainty in mass density measurement.

Since there are uncertainties in the measurements of the dimensions and mass of the specimens (Section 3.3), there is a subsequent uncertainty in the mass density (and hence also in the volume fraction porosity,  $P$ ) of the specimens. In order to estimate the effect of the uncertainty in mass density measurements on the least-squares determination of the parameters

$E_D$  and  $b_{PE}$  (Eqs. 3.1 and 3.4) as well as  $G_D$  and  $b_{PG}$  (Eqs. 3.2 and 3.5), a numerical study was performed.

The uncertainty,  $\Delta\rho$  in the determination of mass density,  $\rho$ , calculations was obtained from the following equation

$$\Delta\rho = \sqrt{\left(\frac{\partial\rho}{\partial m}\right)^2 (\Delta m)^2 + \left(\frac{\partial\rho}{\partial l}\right)^2 (\Delta l)^2 + \left(\frac{\partial\rho}{\partial h}\right)^2 (\Delta h)^2 + \left(\frac{\partial\rho}{\partial w}\right)^2 (\Delta w)^2} \quad (3.8)$$

where  $l$  = average specimen length,  $w$  = average specimen width,  $h$  = average specimen height,  $m$  = specimen mass, and  $\rho$  = specimen mass density. The uncertainty in mass measurement,  $\Delta m$ , was assigned the value of  $1.0 \times 10^{-4}$  g, which is the vendor specified precision of the Ohaus Adventurer electronic balance used in this study. The uncertainties assigned to each of the dimensional measurements ( $\Delta l$ ,  $\Delta h$  and  $\Delta w$ ) was 0.0025 cm, which the vendor specified precision of the electronic caliper (Mitutoyo, 500-196-20, Aurora, IL) used in this study. The calculated uncertainty in  $\rho$ ,  $\Delta\rho$ , was  $0.07 \text{ g/cm}^3$ .

A series of modulus-porosity data sets were generated (Table 3.4) in which the measured mass density,  $\rho$ , for each specimen was perturbed by adding a quantity  $\delta\rho$  to the measured mass density for each of the 17 specimens in the entire (cast plus hot pressed, Table 3. 1) modulus-porosity data set. The calculated  $\delta\rho$  values were distributed randomly and uniformly over the interval from  $\Delta\rho$  to  $-\Delta\rho$  (where  $\Delta\rho = 0.07 \text{ g/cm}^3$ ) using a commercial uniform random number generator (Matlab v7.20.232). After adding the uniformly distributed uncertainties  $\delta\rho$  to the mass density values, a least-squares fit of the “perturbed” Young’s

Table 3.4. Using perturbed density data (Section 3.4.2.2), a least-squares analysis was used to simulate the effect of the uncertainty in density measurement. This table lists maximum, minimum and standard deviations (std) of parameters  $b_{PE}$ ,  $E_D$ ,  $b_{PG}$ , and  $G_D$  and  $r^2$  (coefficient of determination) obtained from the least-squares fit to the linear (Eqs. 3.4 and 3.5) and exponential (Eqs. 3.1 and 3.2) empirical relationships for the Young's and shear moduli using the perturbed density data.

<b>Young's Modulus</b>				
<b>Specimens</b>	<b>Empirical relationship</b>	<b><math>r^2</math> range (std)</b>	<b><math>b_{PE}</math> range (std)</b>	<b><math>E_D</math> (GPa) range (std)</b>
Hot Pressed Data (12 specimens)	Exponential	0.951 - 0.986 (0.010)	4.5-5.0 (0.2)	58.9 – 60.5 (0.4)
	Linear	0.971 - 0.988 (0.006)	3.4 - 3.7 (0.1)	57.5 - 58.4 (0.2)
Hot Pressed and Cast Data (17 specimens)	Exponential	0.890 - 0.949 (0.017)	4.1 - 4.8 (0.2)	58.6 - 60.3 (0.5)
	Linear	0.921 - 0.967 (0.014)	3.2 - 3.7 (0.1)	57.7 - 58.9 (0.4)
<b>Shear Modulus</b>				
<b>Specimens</b>	<b>Empirical relationship</b>	<b><math>r^2</math> range (std)</b>	<b><math>b_{PG}</math> range (std)</b>	<b><math>G_D</math> (GPa) range (std)</b>
Hot Pressed Data (12 specimens)	Exponential	0.950 - 0.980 (0.009)	4.5 - 4.8 (0.1)	23.3 - 23.8 (0.2)
	Linear	0.961 - 0.987 (0.007)	3.4 - 3.6 (0.1)	22.8 - 23.1 (0.1)
Hot Pressed and Cast Data (17 specimens)	Exponential	0.881 - 0.941 (0.020)	4.0 - 4.7 (0.2)	23.1 - 23.7 (0.2)
	Linear	0.913 - 0.964 (0.016)	3.2 - 3.6 (0.1)	22.7 - 23.2 (0.2)

modulus versus porosity (Eqs. 3.1 and 3.4) and shear modulus (Eqs. 3.2 and 3.5) versus porosity data was performed to determine the shift in the fitting coefficients that resulted from the perturbation in the mass density values. The minimum, maximum, and standard deviation were calculated for the Young's modulus and shear modulus, for both the 17 specimens (hot pressed and cast) and the 12 specimens (hot pressed) (Table 3.4).

For the full data set, including the 5 cast specimens and 12 hot pressed specimens, the ranges of the parameters obtained from the least-squares fit on the perturbed data is significantly wider than that for the 12 specimen (hot pressed specimens only) data set (Table 3.4). The five cast specimens lie in a limited porosity range  $0.02 \leq P \leq 0.03$ , which could explain the wider ranges of parameters obtained from the least-squares fit. The uncertainty range,  $\Delta\rho$ , is fixed, and therefore, the calculated  $\delta\rho$  (generated by a uniform random generator) added to the mass density are more significant when applied to the lower porosity range.

The computer simulations (Table 3.4) indicate that due to the uncertainty in mass density measurement, the  $r^2$  values for the experimental data (Table 3.3) are likely too similar to allow a definitive choice of which empirical form (linear or exponential) best fits the modulus-porosity data. Regardless of the details of the least squares calculations, the plots of Young's modulus versus porosity (Figs. 3.3a and 3.3b) and shear modulus versus porosity (Figs. 3.3c – 3.3e) demonstrate that in this study the modulus-porosity relationships are generally quite linear

#### 3.4.2.3. Poisson's ratio as a function of porosity

In this study and in the literature, the Young's modulus and shear modulus of solid materials decrease monotonically with increasing volume fraction porosity  $P$  [7]. However, for the Poisson's ratio,  $\nu$ , the situation is much more complicated. The Poisson's ratio has been

observed to increase, decrease or remain constant as a function of porosity. For example, in a review of the literature data for polycrystalline  $\text{Al}_2\text{O}_3$ ,  $\text{ZnO}$  and  $\text{MgO}$ , Phani [26] shows that  $\nu$  of  $\text{Al}_2\text{O}_3$  is relatively insensitive to porosity,  $P$ , for  $0 \leq P \leq 0.30$ , while in contrast  $\nu$  for  $\text{ZnO}$  decreases for approximately the same interval of  $P$ . Even for a single material (polycrystalline  $\text{MgO}$ ),  $\nu$  measured by different researchers show opposite trends where in one case  $\nu$  increases with increasing  $P$  and the other case,  $\nu$  decreases with increasing  $P$  [26]. In another review of the literature, Boccaccini presented  $\nu$  versus  $P$  data on 16 oxides as well as graphite and  $\text{AlN}$  [27]. Although there was considerable scatter in the data for the 18 materials, Boccaccini classified the data in terms of  $\nu_0$  (the Poisson's ratio of the fully dense material). Boccaccini found that for materials with  $\nu_0 > 0.25$ ,  $\nu$  tends to decrease with increasing  $P$  and for  $\nu_0 < 0.25$  Poisson's ratio tends to increase with increasing  $P$  [27]. In addition to polycrystalline materials, Poisson's ratio of glassy materials is also a function of  $P$ . For example,  $\nu$  values of porous  $\text{Pd}_{42.5}\text{Cu}_{30}\text{Ni}_{7.5}\text{P}_{20}$  glassy alloys decreased monotonically from approximately 0.40 for dense specimens to about 0.31 for a  $P = 0.60$  [28].

In addition to the experimental observations, several researchers have proposed models of  $\nu$  versus  $P$  behavior. A number of the theories that treat the porosity dependence of Poisson's ratio [26, 29 - 31] are based on the Mori-Tanaka effective field model (MTM) [32], which describes the elastic properties of two phase composite materials in terms of an effective or mean strain field. In the MTM, the composite is modeled as an elastically isotropic solid with a matrix phase with spheroidal inclusions distributed randomly and homogeneously throughout the bulk of the solid [32]. Work by Tandon and Wang [29], Zhao et al. [30] as well as Dunn and

Ledbetter [31] extend the MTM to include non-spherical inclusions (the pore phase). Based on their model, Dunn and Ledbetter note that “Unlike the other elastic constants which monotonically decrease with pore concentration, Poisson's ratio may increase, decrease, or remain unchanged as a function of pore concentration, depending on the pore shape and Poisson's ratio of the bulk solid” [31]. Thus, in addition to emphasizing pore shape (pore aspect ratio) Dunn and Ledbetter’s theoretical work supports Boccaccini’s observation that the  $\nu$  versus  $P$  behavior is a function of  $\nu_0$ .

However, there are a number of difficulties in applying the theories such those by Dunn and Ledbetter [31], Tandon [29] and Zhao [30]. If one sinters a powder compact, the pores morphology evolves continuously during the densification process [33, 34], so the pore aspect ratio differs for differing values of  $P$ . For example, based on theoretical work by Zhao [30], Martin et al. predict that during densification, the pore aspect ratio first increases, then goes through a maximum and then decreases for sintered ZnO, Fe and MgO [34]. Thus applying these theories to materials undergoing densification means that both the pore aspect ratio and the total volume porosity  $P$  varies simultaneously. In addition, direct experimental measurement of the pore size and aspect ratio is extremely difficult [35]. Also, adding to difficulties with both experiment and theory, rather than having a single pore size or a pore aspect ratio, experimentally a given specimen has a distribution of pore sizes and aspect ratios and the nature of these distributions may depend on the details of the powder processing technique for sintered material. Thus, while the literature shows that  $\nu$  may increase, decrease or remain constant with increasing  $P$ , there are difficulties in applying the available theories to a given data set. Furthermore, the theories of Dunn and Ledbetter [31], Tandon [29] and Zhao [30] all assume an isotropic, homogeneous spatial distribution of pores, but depending on the details of processing it

may be expected that in some cases specimens may exhibit inhomogeneous pore distributions.

In this study, the Poisson's ratio was 0.27 for the most dense specimen ( $P = 0.01$ ). With increasing volume fraction porosity, Poisson's ratio tended to decrease slowly with increasing volume fraction porosity (Figs. 3.3f and 3.3g), which was in agreement with the literature review of Poisson's ratio-porosity data by Boccaccini [27]. Comparing the data for the hot pressed specimens only (Fig. 3.3f) with the data for the combined data set (Fig. 3.3g), the scatter in the Poisson's ratio values for the volume fraction porosity range  $0.02 \leq P \leq 0.03$  is accentuated by the scatter in Poisson's ratio data for the cast specimens, where  $P$  for each of the five cast specimens lies in the porosity range  $0.02 \leq P \leq 0.03$ .

### 3.5. Summary and Conclusions

For the 17 LAST specimens (12 hot pressed and five ingot specimens) included in this study the Young's modulus, shear modulus and Poisson's ratio were determined using resonant ultrasound spectroscopy as a function of the volume fraction porosity,  $P$ , for  $0.01 \leq P \leq 0.14$ . For the 12 hot pressed specimens, the least-squares fit of the  $E$  versus  $P$  data  $E = E_D (1 - b_{PE}P)$  (Eq. 3.4), yielded  $E_D = 58.3 \pm 0.3$  GPa and  $b_{PE} = 3.6 \pm 0.1$  with a coefficient of determination,  $r^2 = 0.994$  (Fig. 3a, Table 3.3). If the five ingot specimens (which have a more limited porosity range) are included in the analysis along with the 12 hot pressed specimens,  $r^2$  decreases to 0.962 with no significant changes in the  $E_D$  and  $b_{PE}$  values (Table 3.3). For the shear modulus,  $G$ , versus  $P$  behavior was similar to that observed for  $E$  versus  $P$  with a linear decrease in  $G$  with increasing  $P$  (Eq. 3.5). For the 12 hot pressed specimens, the linear fit yielded  $G_D = 22.9 \pm 0.1$  GPa,  $b_{PG} = 3.5 \pm 0.1$  with  $r^2 = 0.991$  (Fig. 3.3c, Table 3.3). When the five ingot specimens (17

specimens total) are included in the analysis,  $r^2 = 0.956$  (Fig. 3d, Table 3.3). As was the case for the Young's modulus combined data set, there are no significant changes (Table 3.3) in the  $G_D$  and  $b_{PG}$  values compared to the fit obtained from the hot pressed specimens only. The fit to the linear relationships (Eqs. 3.4 and 3.5) was in each case either slightly better than the exponential relationships (Eqs. 3.1 and 3.2) (Table 3.3). The Poisson's ratio tended to decrease slowly with increasing volume fraction porosity.

In Section 4.2.2, we considered the effect of the uncertainty in mass density calculation on the least-squares fit of the modulus-porosity relationships (Eqs. 3.1, 3.2, 3.4, and 3.5). When computer-generated perturbations in density  $\delta\rho$  (uniformly distributed between  $\Delta\rho$  and  $-\Delta\rho$ , Eq. 3.8), were added to the measured specimen densities, a subsequent least-squares analysis of the perturbed data (Table 3.4) shows that for the data included in this study it is difficult to definitively determine whether the linear or exponential empirical equations best fit the experimental data (Table 3.3). This is consistent with the numerical values of volume fraction porosity,  $P$ , and the coefficients  $b_{PE}$  and  $b_{PG}$  being such that the exponential function is well approximated by a linear function (Eq. 3.3), as shown graphically in Figures 3.3a - 3.3e.

Knowledge of the porosity dependence of the elastic moduli is critical to numerical or analytical stress-strain calculations for both the cast and hot pressed materials (where the Young's modulus is needed). For the specimens included in this study, no microcracking was observed, however when microcracking is present, understanding the decrement in moduli due to porosity can help us separate the effects of microcracking and porosity for a given porous, microcracked specimen.

Furthermore, in the literature, researchers have recently intentionally included porosity in

thermoelectric materials in an effort to enhance the  $ZT$  values and hence the energy efficiency of the thermoelectric. This interest in intentionally fabricating porous thermoelectrics also gives impetus to the study of the elasticity of porous thermoelectric materials such as LAST.

#### Acknowledgements

The authors acknowledge the financial assistance of the U. S. Department of Energy Grant DE-FC26-04NT42281 and Office of Naval Research MURI Grant number N000140310789. The authors also acknowledge the Defense University Research Instrumentation Program (DURIP) Grant No. N00014-09-1-0785, Office of Naval Research, which provided funding for the purchase of the Resonant Ultrasound Spectroscopy apparatus utilized in this research.

## REFERENCES

### 3.6 References

- [1] T. P. Hogan, A. Downey, J. Short, J. D'Angelo, C.-I Wu, E. Quarez, J. Androulakis, P.F.P. Poudeu, J.R. Sootsman, D.Y. Chung, M.G. Kanatzidis, S. D. Mahanti, E.J. Timm, H. Schock, F. Ren, J. Johnson, E.D. Case, Nanostructured thermoelectric materials and high-efficiency power-generation modules, *J. Elect. Mater.* 36 (2007) 704.
- [2] S. Urata, R. Funahashi, T. Mihara, A. Kosuga, S. Sodeoka, T. Tanaka, Power generation of a p-type  $\text{Ca}_3\text{Co}_4\text{O}_9$ /n-type  $\text{CaMnO}_3$  module, *Int. J. Appl. Ceram. Technol.* 4 (2007) 535.
- [3] R. Funahashi, S. Urata, Fabrication and application of an oxide thermoelectric system, *Int. J. Appl. Ceram. Technol.* 4 (2007) 297.
- [4] D. Flahaut, T. Mihara, R. Funahashi, N. Nabeshima, K. Lee, H. Ohta, K. Koumoto, Thermoelectrical properties of A-site substituted  $\text{Ca}_{1-x}\text{Re}_x\text{MnO}_3$  system, *J. Appl. Phys.* 100 (2006) 084911.
- [5] L. Yang, J.S. Wu, L.T. Zhang, Synthesis of filled skutterudite compound  $\text{La}_{0.75}\text{Fe}_3\text{CoSb}_{12}$  by spark plasma sintering and effect of porosity on thermoelectric properties, *J. Alloy. Compd.* 364 (2004) 83.
- [6] Q. He, S. Hu, X. Tang, Y. Lan, J. Yang, X. Wang, Z. Ren, Q. Hao, G. Chen, The great improvement effect of pores on ZT in  $\text{Co}_{1-x}\text{Ni}_x\text{Sb}_3$  system *Appl. Phys. Lett.* 93 (2006) 042108.
- [7] R. W. Rice, *Porosity of Ceramics*, Marcel Dekker, Inc., New York, 1998, pp. 100-131.
- [8] E. A. Dean, J. A. Lopez, Empirical dependence of elastic moduli on porosity for ceramic materials, *J. Am. Ceram. Soc.* 66 (1983) 366.
- [9] A. L. Pilchak, F. Ren, E. D. Case, E.J. Timm, H.J. Schock, C.-I Wu, T. P. Hogan, *Phil. Mag.* 87 (2007) 4567.
- [10] M. W. Barsoum, *Fundamentals of Ceramics* McGraw Hill, New York, 1997, pp. 377 – 378.
- [11] R. W. Rice, *Mechanical Properties of Ceramics and Composites: Grain and Particle Effects*, Marcel Dekker, Inc., New York, 2000, p. 9.
- [12] F. Ren, B. D. Hall, J. E. Ni, E. D. Case, J. Sootsman, M. G. Kanatzidis, E. Lara-Curzio, R. M. Trejo, E. J. Timm, in: T.P. Hogan(Ed.), J. Yang(Ed.), R. Funahashi(Ed.), T. Tritt(Ed.), *Thermoelectric Power Generation*, Mater. Res. Soc. Symp. Proc. Vol. 1044, Warrendale, PA, 2008, p. 121-126.
- [13] S. S. Kim, S. Yamamoto, T. Aizawa, Thermoelectric properties of anisotropy-controlled p-type Bi-Te-Sb system via bulk mechanical alloying and shear extrusion, *J. Alloys and*

Compd. 375 (2004) 107.

- [14] K. Ueno, A. Yamamoto, T. Noguchi, T. Inoue, S. Sodeoka H. Obara, Optimization of hot-press conditions of  $Zn_4Sb_3$  for high thermoelectric performance. II. Mechanical properties, *J. Alloy. Compd.* 388 (2005) 118.
- [15] W. Wei, J. Li, H. Zhang, X. Cao, C. Tian, J. Zhang, Macrostructural influence on the thermoelectric properties of SiC ceramics, *Scripta Mater.* 57 (2007) 1081.
- [16] T. P. Hoepfner, E. D. Case, The porosity dependence of the dielectric constant for sintered hydroxyapatite, *J. Biomed. Mater. Res.* 60 (2002) 643.
- [17] R. Barea, M. A. Osendi, J. M. F. Ferreira, P. Miranzo, Thermal conductivity of highly porous mullite material, *Acta Mat.* 53 (2005) 3313.
- [18] B. Nait-Ali, K. Haberko, H. Vesteghem, J. Absi, D.S. Smith, Thermal conductivity of highly porous zirconia, *J. Eur. Ceram. Soc.* 26 (2006) 3567.
- [19] T. P. Hoepfner, E. D. Case, The influence of the microstructure on the hardness of sintered hydroxyapatite, *Ceram. Int.* 29 (2003) 699.
- [20] SY Shan, JF Yang, JQ Gao, WH Zhang, ZH Jin, R Janssen, T. Ohji, Porous silicon nitride ceramics prepared by reduction-nitridation of silica, *J. Am. Ceram. Soc.* 88 (2005) 2594.
- [21] T. M. Tritt, M. A. Subramanian, Thermoelectric materials, phenomena, and applications: A bird's eye view, *MRS Bulletin* 31, 2006, pp 188-194.
- [22] A. Migliori, J. L. Sarrao, *Resonant Ultrasound Spectroscopy: Applications to Physics, Materials Measurements, and Nondestructive Evaluation*, Academic Press, New York, 1997, p. 28.
- [23] F. Ren, E. D. Case, J. R. Sootsman and M. G. Kanatzidis, H. Kong, C. Uher E. Lara-Curzio and R. M. Trejo, C. Uher, The high-temperature elastic moduli of polycrystalline PbTe measured by resonant ultrasound spectroscopy, *Acta Mat.* 56 (2008) 5954.
- [24] E. D. Case, in: M. H. Alibadi (Ed.), *Thermo-Mechanical Fatigue and Fracture*, WIT Press, UK, 2002, pp. 137 – 208.
- [25] F. Ren, E.D. Case, J. E. Ni, E.J. Timm, E. Lara-Curzio, R.M. Trejo, C.-H. Lin, M.G. Kanatzidis, Temperature-dependent elastic moduli of lead telluride-based thermoelectric materials, *Phil. Mag.* 89 (2009) 143.
- [26] K. K. Phani, A novel method of predicting ultrasonic and elastic properties of isotropic ceramic materials after sintering from the properties of partially sintered or green compacts, *J. Amer. Ceram. Soc.* 91 (2008) 215.

- [27] A. R. Boccaccini, Effective elastic moduli of porous ceramic materials, *J. Amer. Ceram. Soc.* 77 (1994) 2779.
- [28] M. Fukuhara, T. Wada, A. Inoue, Ultrasonic characteristics of porous Pd<sub>42.5</sub>Cu<sub>30</sub>Ni<sub>7.5</sub>P<sub>20</sub> glassy alloys, *J. Appl. Phys.* 102 (2007) 083502.
- [29] G. P. Tandon, G. J. Weng, Average stress in the matrix and effective moduli of randomly oriented composites, *Comp. Sci. Tech.* 27 (1986) 111.
- [30] Y. H. Zhao, G. P. Tandon, G. J. Wang, Elastic moduli for a class of porous materials, *Acta Mech.* 76 (1989) 105.
- [31] M. L. Dunn, H. Ledbetter, Poissons ratio of porous and microcracked solids-theory and application to oxide semiconductors, *J. Mater. Res.* 10 (1995) 2715.
- [32] T. Mori, K. Tanaka, Average stress in matrix and average elastic energy of materials with misfitting inclusions, *Acta Met.*, 21 (1973) 571.
- [33] J. B. Wachtman, *Mechanical Properties of Ceramics*, Wiley Interscience, New York, 1996, pp. 33-35, 412.
- [34] L. P. Martin, D. Dadon, M. Rosen, Evaluation of ultrasonically determined elasticity-porosity relations in zinc oxide, *J. Amer. Ceram. Soc.* 79 (1996) 1281.
- [35] J. Kovacic, Correlation between elastic modulus, shear modulus, Poisson's ratio and porosity in porous materials, *Advanced Engineering Materials* 10 (2008) 250.

The full citation for this chapter is: Jennifer E. Ni, Eldon D. Case, Kristen N. Khabir, Ryan C. Stewart, Chun-I Wu, Timothy P. Hogan, Edward J. Timm, Steven N. Girard, Mercouri G. Kanatzidis, Room temperature Young's modulus, shear modulus, Poisson's ratio and hardness of PbTe-PbS thermoelectric materials, *Mat. Sci. Eng. B*, 170, 58–66 (2010)

#### 4.0 Room temperature Young's modulus, shear modulus, Poisson's ratio and hardness of PbTe-PbS thermoelectric materials

Jennifer E. Ni<sup>1</sup>, Eldon D. Case<sup>1\*</sup>, Kristen N. Khabir<sup>1</sup>, Ryan C. Stewart<sup>1</sup>, Chun-I Wu<sup>2</sup>, Timothy P. Hogan<sup>2</sup>, Edward J. Timm<sup>3</sup>, Steven N. Girard<sup>4</sup>, Mercouri G. Kanatzidis<sup>4</sup>

<sup>1</sup> Chemical Engineering and Materials Science Department, Michigan State University, East Lansing, MI 48824 USA,

<sup>2</sup> Electrical and Computer Engineering Department, Michigan State University, East Lansing, MI 48824 USA

<sup>3</sup> Mechanical Engineering Department, Michigan State University, East Lansing, MI 48824 USA

<sup>4</sup> Department of Chemistry, Northwestern University, Evanston, IL, USA

#### Abstract

Two-phase PbTe-PbS materials, in which PbS is a nanostructured phase, are promising thermoelectric materials for the direct conversion of heat energy into electricity. In this study, a Vickers indentation mean hardness of  $1.18 \pm 0.09$  GPa was measured for hot pressed specimens Pb<sub>0.95</sub>Sn<sub>0.05</sub>Te – PbS 8% while the mean hardness of cast specimens was  $0.68 \pm 0.07$  GPa. The mean fracture toughness of the not pressed specimens was estimated as  $0.35 \pm 0.04$  MPa·m<sup>1/2</sup> via Vickers indentation. Resonant Ultrasound Spectroscopy (RUS) measurements on hot pressed specimens gave mean values of Young's modulus, shear modulus and Poisson's ratio of 53.1 GPa, 21.4 GPa and 0.245, respectively while for the cast specimens the Young's and shear moduli were about 10 percent lower than for the hot pressed, with a mean value of Poisson's ratio of 0.245. The differences between the hardness and elastic moduli values for the cast and hot pressed specimens are discussed.

Keywords: thermoelectric; lead telluride; powder processing; elasticity; hardness

#### 4.1.0 Introduction

PbTe-PbS is an emerging thermoelectric material that has potential for waste-heat recovery applications. For the PbTe-PbS system [1] and other thermoelectric materials such as LAST (Lead-Antimony-Silver-Tellurium) [2, 3] and LASTT (Lead-Antimony-Silver-Tellurium-Tin) [3, 4], phonon scattering from nanometer scale heterogeneities reduces the lattice thermal conductivity and hence enhances  $ZT$ , the non-dimensional figure of merit for thermoelectric materials [5]. For the PbTe-PbS system in particular, both PbTe-rich and PbS-rich nanoregions have been observed [1].

The characterization of hardness and elastic moduli is important in order to better understand the thermoelectric material's response to thermal and mechanical stresses generated by in-service conditions. For example, hardness is associated with a material's machinability as well as its resistance to wear [6]. The elastic moduli are required for stress-strain calculations [7 - 9] and, in addition, the elastic moduli can be used to monitor the level of microcrack damage that may accumulate during processing, fabrication or use of thermoelectric materials [10 - 12].

The mechanical property data in the open literature is very limited for most thermoelectric materials, although recently the authors and co-workers have studied the mechanical properties of PbTe-based thermoelectric materials, including PbTe, LAST, and LASTT [6, 13 - 18]. These studies include the fracture strength and Weibull modulus of LASTT [13], the fracture strength of LAST [19], the Young's modulus as a function of composition for LAST [14], the high temperature elastic moduli of polycrystalline PbTe [15], LAST [16, 17] and LASTT [19], the porosity dependence of the elastic moduli of LAST [18], and the composition dependence of the hardness of LAST [6].

However, for the PbTe-PbS material system, no data on the elastic moduli exists in the

literature. Hardness data for the PbTe-PbS 5% and PbTe-PbS 10% is present in the literature, but no hardness data is available for the particular thermoelectric composition  $\text{Pb}_{0.95}\text{Sn}_{0.05}\text{Te} - \text{PbS}$  8%. In this study, we used resonant ultrasound spectroscopy (RUS) to determine the Young's modulus, shear modulus, and Poisson's ratio of cast and hot pressed  $\text{Pb}_{0.95}\text{Sn}_{0.05}\text{Te} - \text{PbS}$  8% specimens. The hardness of the cast and hot pressed specimens were measured by Vickers indentation. In addition, the fracture toughness of the hot pressed specimens was estimated from Vickers indentation. Both cast and hot pressed specimens were included since for the PbTe-PbS materials included in this study, the initial step of specimen fabrication casting, but the specimens are then powder processed and hot pressed in order to reduce the mean grain size and thereby enhance the mechanical integrity of the specimens.

#### 4.2.0 Experimental Procedure

The  $\text{Pb}_{0.95}\text{Sn}_{0.05}\text{Te} - \text{PbS}$  8% ingots included in this study were fabricated either at Michigan State University (MSU) or at Northwestern University (NW) using the same procedures. The raw materials for all ingots (used either for mechanical properties or for powder processing) consisted of Pb, Te, SnTe, and PbS powders of at least 99.99% purity. The constituent powders were loaded into a 22 mm diameter fused silica ampoule, sealed under a pressure of  $\sim 10^{-4}$  Torr and then heated to 1323 K for 12 hours in a rocking furnace. The sealed ampoule was held at the melting temperature for 6 hours with 2 hours of rocking. The specimen was then cooled with an isothermal hold at 773 K for at least 10 hours. The ingots were then cooled from 773 K to room temperature during a 5 hour period.

All powder processing steps for the  $\text{Pb}_{0.95}\text{Sn}_{0.05}\text{Te} - \text{PbS}$  8% ingots were performed in an

argon atmosphere inside a double glove box (Omni-Lab, Vacuum Atmospheres Company, CA). The as-cast ingots were powder crushed and ground using a mechanical mortar and pestle (Retsch RM200, Retsch GmbH, Germany). The powders were sieved and re-ground until all powder passed through a 53 micron sieve. The powders were then loaded into a planetary ball mill (Glenn Mills, Retsch, PM100, NJ), also located within the argon atmosphere of the double glove box. The powders were then dry milled for 3 hours at 150 rpm using a 250 ml alumina mill jar with approximately 113 g of 10 mm diameter spherical alumina milling media.

Following the dry milling, the powders were then wet milled for 6 hours at 150 rpm using 25 cc of hexane with 200 g of alumina media (140 g of 20 mm diameter spheres and 60 g of 3 mm diameter spheres). Dry milling, followed by wet milling was employed in this study since while dry milling decreases the particle size more quickly than wet milling, wet milling can give a smaller final particle size and less tendency for powder agglomeration during milling [20 - 22].

The particle size distributions of the dry/wet milled PbTe-PbS powders were analyzed using a laser light scattering apparatus (Micromeritics Saturn DigiSizer 5200 Low Volume Liquid Sample Handling Unit) with a 50 wt% sucrose solution as the analysis liquid. (The sucrose adjusts the settling rate of the powders in the liquid so that powders remain suspended during the analysis). Each measurement of particle size distribution consisted of eight consecutive trials where the particle size distribution was calculated from the mean of the eight trials (Figure 4.1). Prior to adding the powders to the sucrose solution, they were dispersed ultrasonically in RO water with a 0.1 wt% sodium lignosulfonate dispersant added to reduce powder agglomeration during the particle size analysis.

The PbTe-PbS powders were hot pressed using a maximum pressure of ~75 MPa, a maximum temperature of 723 K, and the total time was 5 hours to press a 32 mm diameter billet.

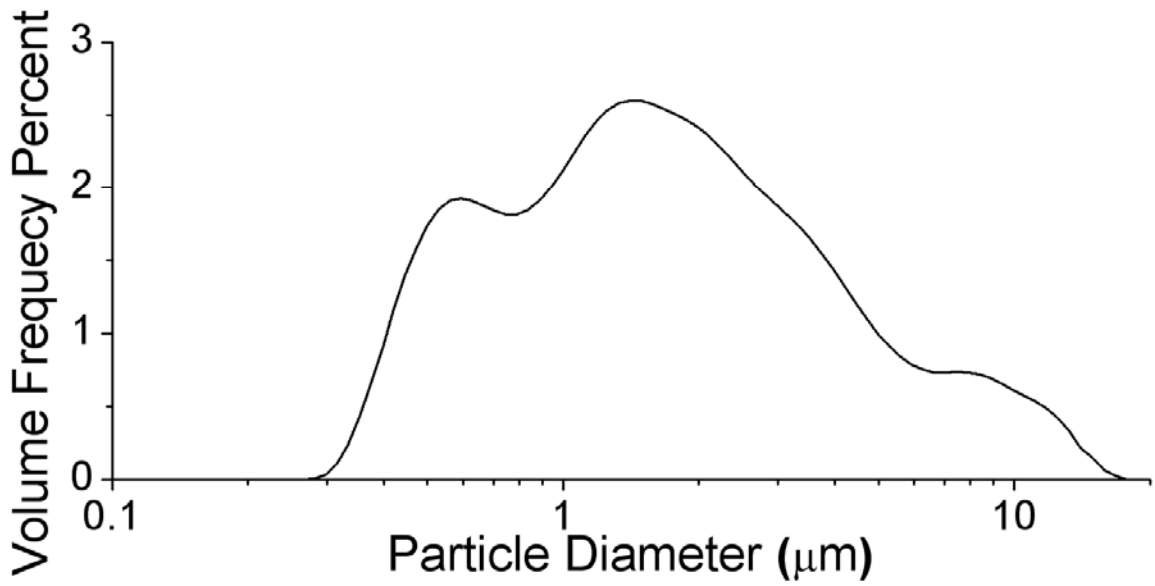
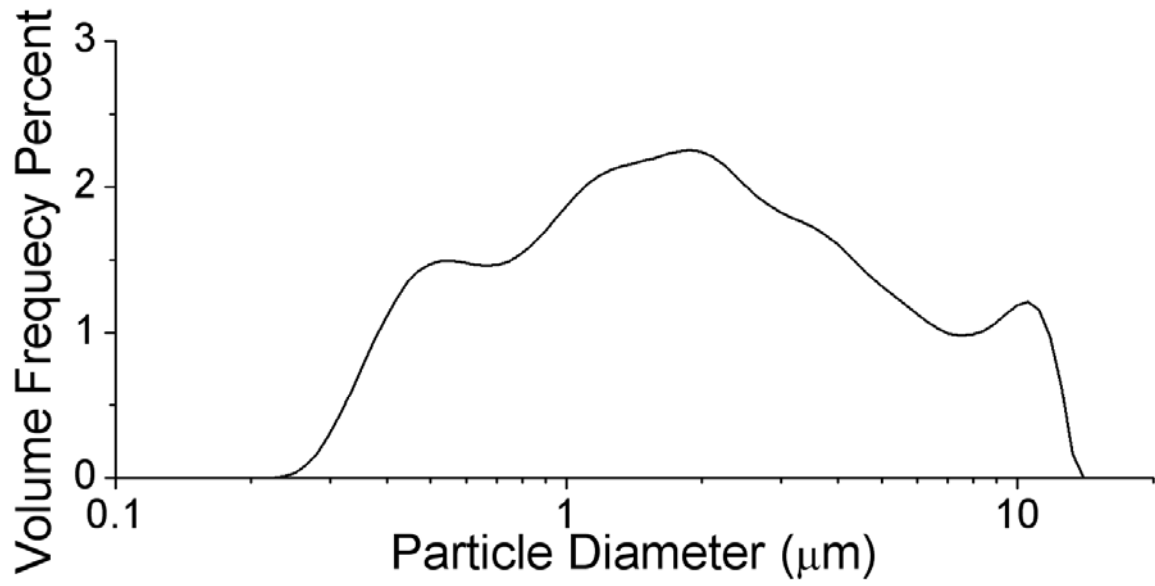


Figure 4.1. Particle size distribution obtained from laser light scattering apparatus.

F

The hot pressed billets were cut into parallelepiped specimens using a low speed diamond saw. The mass density of the rectangular parallelepiped specimens was calculated from the average dimensions measured by electronic calipers (Mitutoyo, 500-196-20, Aurora, IL, with a vendor-specified uncertainty of  $\pm 0.0025$  cm) and the specimen mass determined by an electronic balance (Ohaus Adventurer, AR2140, Pinebrook, NJ, with a vendor-specified precision of  $\pm 1.0 \times 10^{-4}$  g).

Prior to microstructural analysis or Vickers indentation, the specimens were polished using successively smaller diamond grit from 90 microns to 1 micron. Both the as-polished and fractured specimen surfaces were examined using a scanning electron microscope (JEOL 6400, JEOL Ltd., Japan) using a working distance of 15 mm and an accelerating voltage of 15 kV. The as-polished specimen surfaces were cleaned ultrasonically and then examined to determine the size and shape of the surface pores and to determine whether or not surface-breaking cracks were present.

The fractured hot pressed specimens MSUHP-53 and MSUHP-54 were annealed at 573 K for 5 hours and 693 K for 2 hours, respectively, to determine grain size. Both specimens were annealed in a mullite muffle tube with flowing 96% Ar + 4% H<sub>2</sub> gas in a resistance-heated furnace (Carbolite, Watertown, Wisconsin). A thermal etch on a fracture surfaces was used rather than a chemical etch, since chemical etching of PbTe-based materials is problematic. For example, in a biaxial fracture strength study of a cast p-type LASTT (lead-antimony-silver-tellurium-tin) thermoelectric material (Ag<sub>0.9</sub>Pb<sub>9</sub>Sn<sub>9</sub>Sb<sub>0.6</sub>Te<sub>20</sub>), Ren et al. [13] used a solution of 1.0M KOH + 0.7M K<sub>3</sub>(Fe(CN))<sub>6</sub> in deionized water at room temperature as a wet chemical etchant [23] to reveal grain boundaries in the LASTT specimens. Although Robozarov et al. [23]

developed their etchant solution for use on lead chalcogenide compounds, it was still very difficult to obtain a suitable etch on the cast LASTT materials in the biaxial strength study [13] and essentially impossible to obtain an adequate chemical etch on specimens of hot pressed LASTT and both cast and hot pressed LAST. Thus, in subsequent mechanical property studies of PbTe-based compounds by the authors, microstructural analyses have been performed on fracture sections or on thermally etched surfaces [6, 14, 16, 18].

Prior to the hardness testing, the Vickers indenters (Buehler Semimacro Indenter and Shimadzu HMV-2000) were calibrated using a standard calibration block (761-048, Yamamoto Scientific Tools Lab, Co LTD, Japan). Following the calibration, the specimen's hardness,  $H$ , was determined using the Buehler indenter with at least 20 Vickers indentations on the PbTe-PbS specimen surfaces using a 2.94 N load and a loading time of 5 seconds. In addition to the indentation testing at a fixed (2.94 N) load, a possible load dependence of hardness was explored using the Shimadzu HMV-2000 with Vickers indentations made as a function of load, with 10 indentations per load. For all of the Vickers indentation data, the hardness,  $H$ , was calculated from equation (4.1).

$$H = \frac{1.854 P}{a^2} \quad (4.1)$$

where  $2a$  = the diagonal length of the indentation impression and  $P$  = the indentation load.

Also, using the Vickers indentations, the fracture toughness,  $K_C$ , was estimated using equation (4.2), which in the literature is the most frequently used form of the relationship for the indentation fracture toughness of brittle materials via Vickers, Berkovich or cube corner indentation [24, 25].

$$K_C = \alpha \left( \frac{E}{H} \right)^{1/2} \frac{P}{c^{3/2}} \quad (4.2)$$

where E = the Young's modulus, H = the hardness, P = the indentation load, c = the radial crack length for Vickers indentation, in this case. While  $\alpha$  is a function of the indenter angle [25], for Vickers indentation, the constant  $\alpha = 0.016 \pm 0.004$  [26].

The room temperature elastic moduli (Young's modulus, E, shear modulus, G, and Poisson's ratio,  $\nu$ ) were measured using a commercial resonant ultrasound spectroscopy (RUS) apparatus (RUSpec, Quasar International Inc., Albuquerque, NM, USA). The spectrum of acoustic resonances was analyzed using commercial software supplied by the RUS vendor [27]. Details of the RUS measurement technique are given elsewhere [15, 16]

#### 4.3.0 Results and Discussion

As measured by the laser scattering apparatus, the powder particle size for both hot pressed MSUHP-53 and MSUHP-54 ranged in size from ~200 nm to ~15 microns (Figures 4.1 a and b). The mean and median powder particle sizes were 2.4 microns and 1.5 microns, respectively for MSUHP-53, while the mean and median powder particle sizes were 2.1 microns and 1.4 microns, respectively for MSUHP-54. Per the operator's manual provided by the vendor [28], the laser light scattering apparatus has a measurement range of 100 nanometers to 750 microns equivalent particle diameter [28]. For equivalent particle diameters between 100 nanometers and one micron, the laser light scattering apparatus has accuracy of  $\pm 10\%$ , and for those particles with equivalent diameters between one and 750 microns, the accuracy is  $\pm 3\%$  [28]. Thus, the particle size determination is less accurate for the submicron particle sizes than for particles one micron and larger in diameter and furthermore, particles smaller than the lower threshold of

instrumental resolution (about 100 nm) will not be represented in the mean particle size determination.

The mass density of the cast  $\text{Pb}_{0.95}\text{Sn}_{0.05}\text{Te} - \text{PbS}$  8% specimens included in this study ranged from about  $7.85 \text{ g/cm}^3$  to  $8.08 \text{ g/cm}^3$  while the mass densities of the hot pressed specimens were  $7.71 \text{ g/cm}^3$  and  $7.91 \text{ g/cm}^3$ , respectively (Table 4.1). For the cast specimens the microstructural analysis of the as-polished specimens showed the majority of pores were isolated and quasi-spherical from roughly one to five microns in diameter with a few oblong pores having a major axis length up to  $\sim 20$  microns (Figure 4.2a). For the hot pressed specimens (Figures 4.2b and 4.2c), most pores were quasi-spherical with diameters less than about one micron (Figures 4.2b and 4.2c), although occasionally pores as large as five microns across were observed (Figure 4.2c). No surface cracks were observed in the hot pressed specimens (Figures 4.2b and 4.2c) although a few large cracks were observed in the surfaces of the cast specimens prepared for microstructural study (Figure 4.2a).

For the as-cast specimens, grains about 1 mm across and larger were observable by the unaided eye. For each of the two hot pressed billets (MSUHP-53 and MSUHP-54), the average grain size was determined using the linear intercept method [29] on two SEM micrographs for each billet with at least 270 intercepts per micrograph. A stereographic projection factor of 1.5 [29] was used to convert the mean intercept length to a grain size for a planar surface, with an additional correction factor of 1.10 applied to account for the fracture surfaces [30]. The calculated mean grain sizes for hot pressed specimens MSUHP-53 and MSUHP-54 were 1.4 microns and 1.2 microns, respectively (Figures 4.3a and b). Thus, the mean grain sizes for the hot-pressed specimens correspond relatively well with the median powder particle sizes (1.5

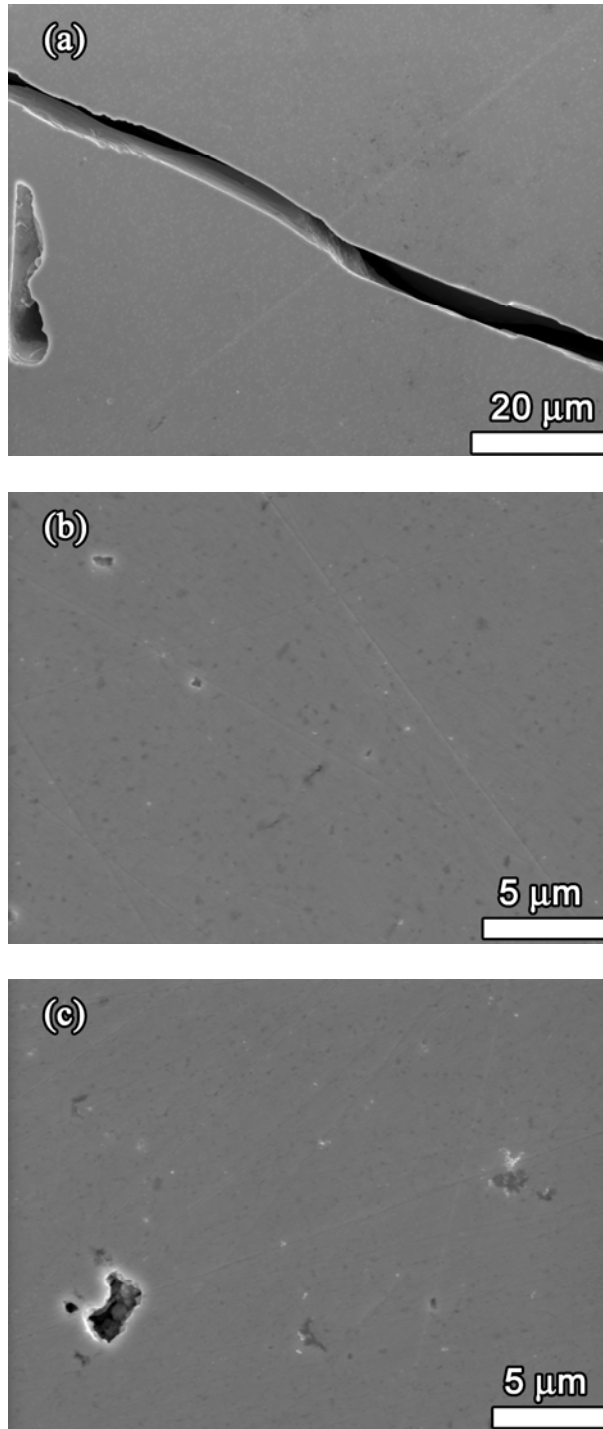


Figure 4.2. SEM micrographs of the as-polished surfaces of  $\text{Pb}_{0.95}\text{Sn}_{0.05}\text{Te} - \text{PbS}$  8% specimens fabricated by (a) casting from the melt and (b and c) hot pressing.

Table 4.1. Comparison of Vickers indentation hardness, H, for the polycrystalline (PC) specimens included in this study ( $\text{Pb}_{0.95}\text{Sn}_{0.05}\text{Te}-8\% \text{PbS}$ ) with hardness data from the literature for PbTe-PbS, PbTe and PbS polycrystalline (PC) and single-crystal (SC) specimens for N indentations per specimen.

Specimen Label	Fabrication Technique	Crystallinity	Avg. Density ( $\text{g/cm}^3$ )	Avg. Porosity	Indentation Load (N)	N	H (GPa)	Reference
NW-In #F	Cast	PC	8.05	0.02	2.9	20	$0.63 \pm 0.02$	This study
NW-In #G	Cast	PC	8.05	0.02	2.9	20	$0.64 \pm 0.05$	This study
MSU-In #7A	Cast	PC	7.85	0.04	2.9	20	$0.75 \pm 0.06$	This study
MSU-In #7B	Cast	PC	7.85	0.04	2.9	20	$0.70 \pm 0.06$	This study
MSUHP-53 #2	HP <sup>a</sup>	PC	7.71	0.06	2.9	20	$1.10 \pm 0.07$	This study
MSUHP-53 #3	HP <sup>a</sup>	PC	7.71	0.06	2.9	20	$1.15 \pm 0.07$	This study
MSUHP-53 #4	HP <sup>a</sup>	PC	7.71	0.06	2.9	20	$1.10 \pm 0.08$	This study
MSUHP-54 #A	HP <sup>a</sup>	PC	7.91	0.03	2.9	20	$1.28 \pm 0.05$	This study
MSUHP-54 # B	HP <sup>a</sup>	PC	7.91	0.03	2.9	20	$1.23 \pm 0.06$	This study
MSUHP-54 #C	HP <sup>a</sup>	PC	7.91	0.03	2.9	20	$1.21 \pm 0.07$	This study
PbTe-PbS 5%	Cast	PC	NS <sup>b</sup>	NS <sup>b</sup>	0.15	10	$0.72^d$	[36]
PbTe-PbS 10%	Cast	PC	NS <sup>b</sup>	NS <sup>b</sup>	0.15	10	$0.81^d$	[36]
Un-doped PbTe	Cast	PC	NS <sup>b</sup>	NS <sup>b</sup>	0.39	10	$0.37^d$	[36]
Un-doped PbTe	NS	SC	NS <sup>b</sup>	SC <sup>c</sup>	0.49	10	$0.29^d$	[37]
Un-doped PbS	Cast	PC	NS <sup>b</sup>	NS <sup>b</sup>	0.39	10	$0.73^d$	[36]
Un-doped PbS	NS	SC	NS <sup>b</sup>	SC <sup>c</sup>	0.49	10	$0.59^d$	[37]

<sup>a</sup> Hot pressed

<sup>b</sup> Not stated.

<sup>c</sup> Single crystal specimen, presumably near theoretical density

<sup>d</sup> The standard deviation in the H data was not given by the authors.

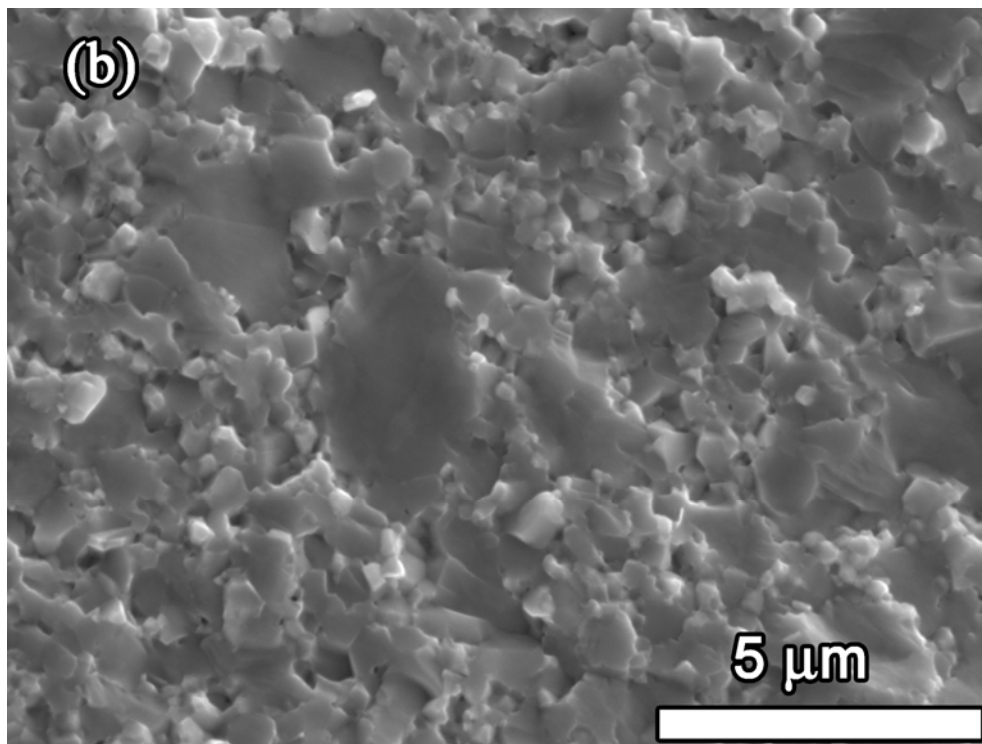
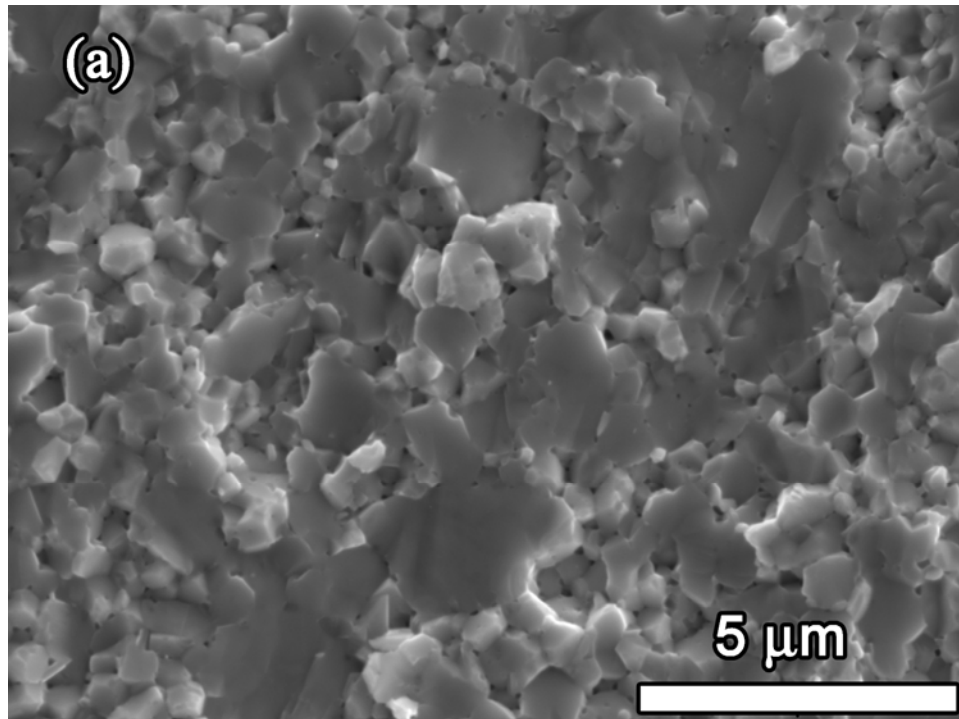


Figure 4.3. SEM micrographs of annealed fractured surfaces of hot pressed  $\text{Pb}_{0.95}\text{Sn}_{0.05}\text{Te} - \text{PbS}$  8% specimens cut from hot pressed billets (a) MSUHP-53 and (b) MSUHP-54. MSUHP-53 was annealed for 5 hours at 573 K and MSUHP-54 was annealed for 5 hours at 693 K, both in a 96% Ar + 4%  $\text{H}_2$  atmosphere.

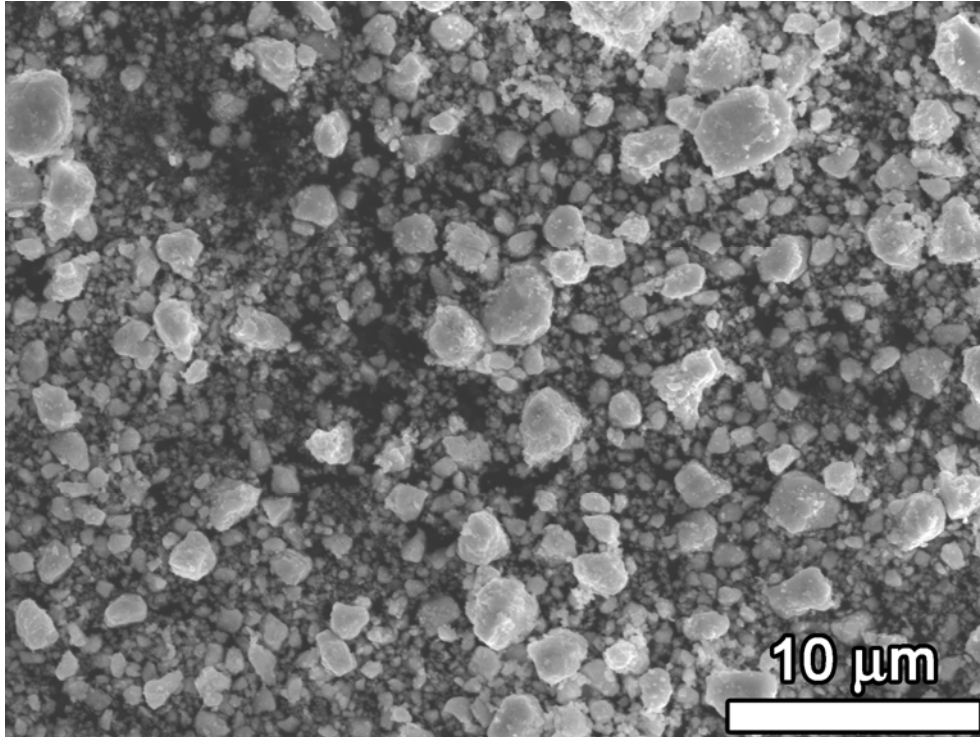


Figure 4.4. SEM micrograph of wet milled powders used to fabricate billet MSUHP-54. Note that a significant factor of the powders particles have a diameter less than about 100 nm, which is below the effective measurement threshold of the laser scattering apparatus. A fracture surface of a specimen hot pressed from this powder is shown in Figure 4.3b.

microns and 1.4 microns, respectively for MSUHP-53 and MSUHP-54) measured by the laser scattering apparatus. SEM micrographs of the processed powders used to hot press the specimens show a significant fraction of powder particles with sizes in the submicron range, including powder particles with diameters on the order of 100 nm and smaller (Figure 4.4).

The Vickers indentation hardness and the elastic moduli (Young's modulus,  $E$ , shear modulus,  $G$ , and Poisson's ratio,  $\nu$ ) were measured for both (i) cast ingots and (ii) powder processed and hot pressed specimens (Tables 4.1 and 4.3). For the PbTe-PbS specimens, Vickers indentation at a 2.94 N load gave a mean hardness of  $0.68 \pm 0.07$  GPa for cast specimens and  $1.18 \pm 0.09$  GPa for hot pressed specimens (Table 4.1). The differences in hardness for the hot pressed and cast specimens are consistent with the general trend that hardness increases as the grain size decreases [31], where the mean grain size of the hot pressed specimens was approximately one micron while the grain size of the as-cast specimens was at least several hundred microns.

From the literature, for both metals [32] and ceramics [33, 34] with grain sizes in the micron range, the observed hardness-grain size relationships often described by the Hall-Petch relationship, namely

$$H = H_0 + kd^{-0.5} \quad (4.3)$$

where  $H_0$  = the hardness of a single crystal,  $k$  = the material-dependent Hall-Petch constant and  $d$  = the grain diameter [33, 34]. Thus, the "normal" Hall-Petch relationship for hardness describes the increase in  $H$  with decreasing grain size. However, for nanocrystalline materials with grains in the size range less than about 50 to 100 nm, the hardness can either decrease or remain relatively constant with decreasing grain size [32, 33, 35]. In this study, the mean grain sizes are in the micron range, so one would expect the  $H$  versus grain size behavior to be described by

equation (4.3). This is consistent with the observation that the hardness of the hot pressed specimens is higher than the hardness of the cast specimens.

In comparison, for polycrystalline specimens indented at 0.15 N load, Darrow et al. [36] obtained H values of 0.72 GPa and 0.81 GPa for PbTe-PbS 5% and PbTe-PbS 10%, respectively (Table 4.1), which lie between the H values obtained in this study for the cast and hot pressed  $\text{Pb}_{0.95}\text{Sn}_{0.05}\text{Te} - \text{PbS}$  8% specimens. Although Darrow et al. [36] do not specify the grain size for their PbTe-PbS 5% and PbTe-PbS 10% specimens, they do state that their specimens were cast from a melt, which implies a large (typically several hundred microns or larger) grain size. Thus the hardness data obtained for the PbTe-PbS specimens included in this study is consistent with H data for similar (but not identical) compositions found in the literature [36].

No hardness data other than that given by Darrow et al. [36] currently exists in the literature for PbTe-PbS materials, however hardness data is available for undoped PbTe and PbS in the both the polycrystalline (cast) [36] and the single crystal [37] forms (Table 4.1). The cast polycrystalline [36] and single crystal [37] undoped PbTe and PbS specimens have lower H values than those measured for the PbTe-PbS system by Darrow et al. [36] and in this study (Table 4.1), but as expected from equation (4.3), the single crystal H values for the single crystal specimens of PbTe and PbS were lower than the polycrystalline (cast) specimens of the corresponding compositions (Table 4.1).

As a further comparison of the results of this study to the H values measured for PbTe-based materials, the range of H measured for the cast PbTe-PbS specimens included in this study (0.63 to 0.75 GPa) is roughly comparable to the range of H values measured for 14 different chemical compositions of cast LAST ( $\text{Ag}_a\text{Pb}_b\text{Sb}_c\text{Te}_d$ ) [6]. As is the case for the PbTe-PbS data reported in Table 4.1 for this study, Vickers indentation at a 2.94 N load was used to determine the cast

LAST ( $\text{Ag}_a\text{Pb}_b\text{Sb}_c\text{Te}_d$ ) hardness, which ranged from  $H = 0.53$  GPa for  $a = 0.006$ ,  $b = 0.480$ ,  $c = 0.011$  and  $d = 0.503$  to  $H = 0.92$  GPa for  $a = 0.030$ ,  $b = 0.422$ ,  $c = 0.042$  and  $d = 0.506$  [6].

In addition to grain size effects, for indentation hardness measurements one must also consider the possibility of indentation size (indentation load dependent) effects. For a number of metals and brittle materials, the measured hardness can have been observed to increase as the load decreases, which is typically called the Indentation Size Effect or ISE [38 - 40]. More recently, a Reverse Indentation Size Effect (RISE) also has been identified where the measured hardness decreases as the load decreases [41, 42]. The Vickers indentation hardness data from Darrow [36] on the cast PbTe-PbS 5% and PbTe-PbS 10% specimens was collected using a lower Vickers indentation load (0.15 N) than the 2.94 N load for this study's  $\text{Pb}_{0.95}\text{Sn}_{0.05}\text{Te} - \text{PbS}$  8% data given in Table 4.1. Thus the lower H values for the Darrow cast specimens than for the hot pressed specimens included in this study could be due to either to a reverse indentation size effect, a grain size effect, or a combination of the two effects. In order to distinguish among these possibilities, a series of 10 indentations per load were performed at each of seven loads (0.25 N, 0.49 N, 0.98 N, 1.96 N, 2.94 N, 4.90 N, and 9.81 N) for specimens from hot pressed billets MSUHP-53 and MSUHP-54 (Figure 4.5). The H values for the hot pressed specimens were relatively independent of load, where for the total of 70 indentations per billet, the mean and standard deviation of H was  $1.14 \pm 0.04$  GPa and  $1.04 \pm 0.08$  GPa respectively for MSUHP-53 and MSUHP-54 (Figure 4.5).

For the two cast  $\text{Pb}_{0.95}\text{Sn}_{0.05}\text{Te} - \text{PbS}$  8% specimens, 10 indentations per load were performed at six loads from 0.25 N and 4.90 N (Figure 4.5). The cast specimens showed extensive chipping and multiple cracking near the Vickers indentation impressions for an

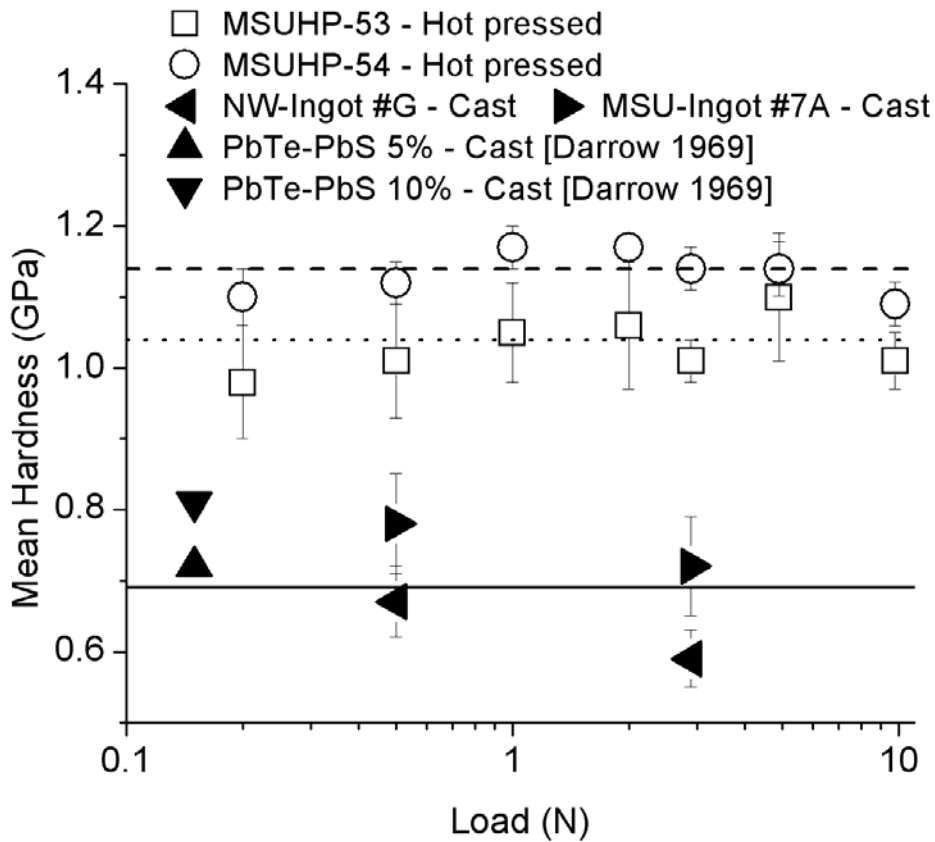


Figure 4.5. The mean hardness as a function of the applied Vickers indentation load for hot pressed (open symbols) and cast (filled symbols) specimens in the PbTe-PbS system. The mean hardness values, averaged over all loads for the  $\text{Pb}_{0.95}\text{Sn}_{0.05}\text{Te} - \text{PbS}$  8% hot pressed MSUHP-53 and MSUHP-54 specimens are shown by the dotted and dashed lines, respectively. The mean hardness values averaged over all loads for the  $\text{Pb}_{0.95}\text{Sn}_{0.05}\text{Te} - \text{PbS}$  8% cast NW-Ingots G and MSU-Ingots 7A specimens are indicated by the dot-dashed and dot-dot-dashed lines, respectively. The hardness data from Darrow et al. [36] for cast PbTe-PbS 5% and PbTe-PbS 10% specimens is shown for comparison (half-filled symbols).

indentation load of 9.81 N, so no data is given here for cast specimens indented 9.81 N (Figure 4.5). (Chipping and multiple cracking is often observed for large-grained and single crystal specimens indented at high loads). Averaging the H values obtained from both cast specimens for the entire load range gives a mean and standard deviation of  $0.77 \pm 0.07$  GPa and  $0.64 \pm 0.06$  GPa for the cast  $\text{Pb}_{0.95}\text{Sn}_{0.05}\text{Te} - \text{PbS}$  8% MSU-Ingots 7a and NW-Ingots G, respectively. These values are comparable to H values of 0.72 GPa and 0.82 GPa reported by Darrow et al. [36] for cast specimens of PbTe-PbS 5% and PbTe-PbS 10%, respectively (Figure 4.5).

From Figure 4.5, no ISE or RISE are apparent for the cast and hot pressed  $\text{Pb}_{0.95}\text{Sn}_{0.05}\text{Te} - \text{PbS}$  8% specimens included in this study, meaning that the hardness is essentially independent of load over the a relatively broad load range (0.25 N to 9.81 N for the hot pressed specimens and 0.25 to 4.90 N for the cast specimens). In addition, the H values for Darrow's cast PbTe-PbS 5% and PbTe-PbS 10% specimens [36] are comparable to the H measured for the cast  $\text{Pb}_{0.95}\text{Sn}_{0.05}\text{Te} - \text{PbS}$  8% specimens included in this study (Figure 4.5). However, the H values of the hot pressed and cast  $\text{Pb}_{0.95}\text{Sn}_{0.05}\text{Te} - \text{PbS}$  8% are significantly different. In the absence of an indentation size effect, the difference between the H values for the hot pressed and cast materials is most likely attributable to a grain size effect (equation (4.3)).

The average fracture toughness of the PbTe-PbS 8% specimens was approximately  $0.35 \pm 0.04 \text{ MPa}\cdot\text{m}^{1/2}$  (Table 4.2a). SEM micrographs of the indentations showed that no radial cracks occurred for the ingot specimens while usable radial crack systems occurred only the 1.96 N, 2.94 N and 4.90 N loads (Figure 4.6). For the hot pressed specimens, the 0.25 N and 0.49 N indentations did not produce radial cracks, while the 0.98 N indentations produced an incomplete set of radial cracks. For the 1.96 N, 2.94 N and 4.90 N loads, Vickers indentation produced a

Table 4.2a Fracture toughness,  $K_{Ic}$ , determined using Vickers indentation for the hot pressed polycrystalline (PC)  $Pb_{0.95}Sn_{0.05}Te-8\%$  PbS specimens included in this study.

<b>Specimen Label</b>	<b>Load (N)</b>	<b><math>K_{Ic}</math> (MPa·m<sup>1/2</sup>)</b>	<b>Coefficient of Variation</b>	<b>Number of indentations with complete radial crack systems</b>	<b>Total Number of indentations attempted</b>
MSUHP-53 #2	4.90	0.35 ± 0.03	0.08	9	20
MSUHP-53 #3	2.94	0.35 ± 0.04	0.10	19	20
MSUHP-53 #3	1.96	0.36 ± 0.01	0.03	6	10
MSUHP-53 #3	4.90	0.37 ± 0.03	0.08	14	20
MSUHP-53 #4	2.94	0.34 ± 0.04	0.11	20	20
MSUHP-54 #A	2.94	0.31 ± 0.01	0.04	20	20
MSUHP-54 #B	2.94	0.32 ± 0.02	0.05	19	20
MSUHP-54 #C	2.94	0.34 ± 0.03	0.08	20	20
MSUHP-54 #C	4.90	0.44 ± 0.04	0.08	8	10

Table 4.2b. The fracture toughness ( $K_c$ ) for polycrystalline (PC) or glasses (G) from literature for various thermoelectrics, semiconductors, and chalcogenides using Vickers indentation (VI), single edged notched beam (SENB), or double-torsion and double-cantilever-beam (DTDCB) methods.

Composition	Crystallinity	Measurement method	$K_c$ MPa·m <sup>1/2</sup>	Reference
$\epsilon$ -Zn <sub>4</sub> Sb <sub>3</sub>	PC	SENB	0.6 – 1.0	[48]
Bi <sub>2</sub> Te <sub>3</sub> + x vol% SiC <sub>np</sub> nanoparticles (x = 0, 0.1, 0.5, 1.0)	PC	VI	1.12 – 1.35	[49]
Binary Ge–Se & Ternary Ge–Sb–Se	G	VI	0.2 - 0.8	[50]
62.5(GeS <sub>2</sub> )– 12.5(Sb <sub>2</sub> S <sub>3</sub> )–25(CsCl) (mol%)	G	VI	0.12 – 0.2	[51]
Ge <sub>x</sub> Se <sub>100-x</sub> (x = 0, 5, 10, 15, 20)	G	VI	0.09 – 0.59	[52]
ZnSe	PC	DTDCB	0.9	[53]
ZnS	PC	VI	1.0	[47]

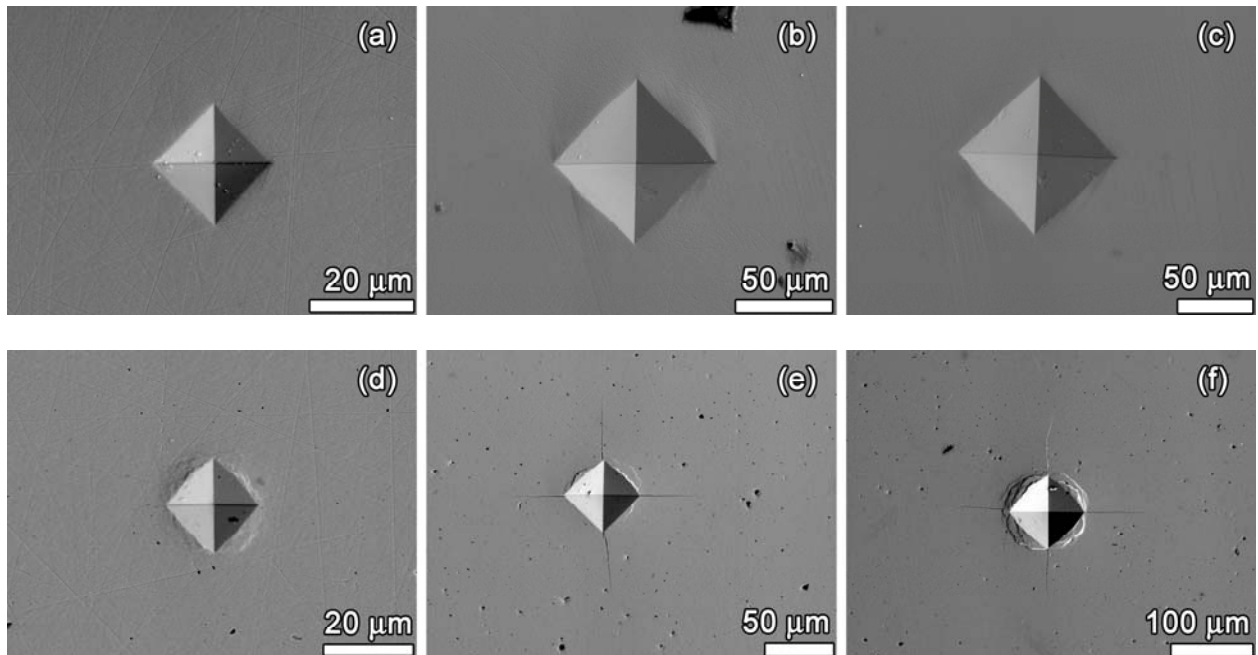


Figure 4.6 SEM micrographs of Vickers indentations at a) 0.25 N, b) 2.0 N, and c) 4.9 N for MSU-In #7A, and d) 0.25 N for MSUHP-54 #C, e) 2 N for MSUHP-53 #3, and f) 4.9 N for MSUHP-54 #C.

complete radial crack pattern in most cases, while at the 9.81 N load, considerable spalling occurred along the indent impression edges. Thus, only the 1.96 N, 2.94 N and 4.90 N load levels produced usable  $K_C$  data (Table 4.2a). The observed crack threshold behavior is consistent with the literature since for sharp indenters, including Vickers, Berkovich and cube-corner indenters, brittle materials typically display a crack initiation threshold [43, 44, 45, 46] such that below the threshold load, radial cracks do not occur.

The fact that Vickers indentation cracks were observed for the hot pressed specimens and not observed for the cast specimens may be related to the very large (roughly 1 mm) grain size of the cast specimens compared to the 1.2 to 1.4 mean grains sizes of the hot pressed specimens. In a paper that focused on crack initiation beneath sharp indenters, Lawn and Evans [47] state that “It is nevertheless apparent that the appropriate refinement of microstructure (e.g. refinement of grain size in polycrystals, reduction of pile-up length in monocrystals, elimination of microinhomogeneities in glasses) could be an important factor in the design and manufacture of ultra-high strength ceramics for contact situations. In the context of the indentation fracture, the micro-mechanics of nucleation processes is a relatively unexplored area of study”.

While the mean value a mean  $K_C$  value of  $0.35 \pm 0.04 \text{ MPa}\cdot\text{m}^{1/2}$  is relatively low, Table 4.2b shows that roughly similar  $K_C$  values have been reported in the literature for other thermoelectric materials and other chalcogenides (PbTe-PbS 8% is a chalcogenide based compound). For example, for the three chalcogenide glass systems listed in Table 4.2b, the measured  $K_C$  values range from 0.09 to  $0.8 \text{ MPa}\cdot\text{m}^{1/2}$ . Zhao et al. [49] found that for the thermoelectric  $\text{Bi}_2\text{Te}_3$ , addition of SiC nanoparticles ( $\text{SiC}_{\text{np}}$ ) in x vol%, where x = 0, 0.1, 0.5, or 1.0, resulted in an increase in  $K_C$  with the nanoparticle addition. The authors are now in the

initial stages of work involving additions of SiC<sub>np</sub> to PbTe-PbS, in anticipation that the SiC<sub>np</sub> or other nanoparticle additions may also increase the K<sub>C</sub> of PbTe-PbS.

It must be noted that Quinn and Bradt [54] have recently criticized the reliability of the Vickers indentation for determining K<sub>C</sub> via in part due to (i) the complicated crack system that arises from Vickers indentation (namely the four orthogonal radial cracks associated with Vickers indentation rather than the single crack that is preferred for fracture toughness measurements) and (ii) the lack of a sufficiently rigorous analytical treatment of the radial crack system. However, the Vickers indentation technique continues to be used in K<sub>C</sub> determinations of brittle materials [24, 25] and Leonardi and Furgiuele recently provided an analytical approach to the evaluation K<sub>C</sub> via indentation which agrees with the functional form of the fracture toughness relationship used in this study (equation (4.2)) [24].

No data is available in the literature for the elastic moduli (Young's modulus, shear modulus or Poisson's ratio) for materials in the PbTe-PbS system. However, the elastic moduli for the two Pb<sub>0.95</sub>Sn<sub>0.05</sub>Te – PbS 8% hot pressed specimens gave room temperature moduli values (E, G and  $\nu$ ) that were only a few percent lower than the values obtained by Ren et al. [15] for undoped PbTe and PbI<sub>2</sub>-doped PbTe (Table 4.3). In addition, the moduli for this study's hot pressed Pb<sub>0.95</sub>Sn<sub>0.05</sub>Te – PbS 8% specimens were also comparable to the aggregate elastic modulus values calculated from single crystal PbTe measurements by Houston et al. [55] and by Einspruch and Manning [56]. The aggregate or polycrystalline moduli (Table 4.3) for the data from both Houston et al. [55] and Einspruch and Manning [56] were calculated from the mean of the Hashin and Strikman bounds [57] determined from the measurements on single crystal PbTe

Table 4.3 Room temperature Young's modulus, E, shear modulus, G, and Poisson's ratio,  $\nu$ , measured by Resonant Ultrasound Spectroscopy (RUS) for the PbTe-PbS ( $\text{Pb}_{0.95}\text{Sn}_{0.05}\text{Te}-8\%$  PbS) polycrystalline (PC) specimens included in this study compared to doped and un-doped polycrystalline (PC) and single-crystal (SC) room-temperature modulus data from the literature.

Specimen Label	Fabrication Technique	Crystallinity	Density ( $\text{g/cm}^3$ )	Porosity	E (GPa)	G (GPa)	$\nu$	Reference
NW-In -A	Cast	PC	8.08	0.01	$47.9 \pm 0.1$	$19.15 \pm 0.01$	$0.250 \pm 0.001$	This study
NW-In -C	Cast	PC	8.00	0.02	$47.6 \pm 0.2$	$19.15 \pm 0.01$	$0.244 \pm 0.003$	This study
MSU-In #7	Cast	PC	7.85	0.04	$47.6 \pm 0.2$	$19.17 \pm 0.03$	$0.242 \pm 0.003$	This study
MSUHP-53 #A	Hot pressed	PC	7.75	0.05	$52.1 \pm 0.1$	$20.94 \pm 0.004$	$0.243 \pm 0.002$	This study
MSUHP-54 #1	Hot pressed	PC	7.91	0.03	$54.0 \pm 0.1$	$21.83 \pm 0.01$	$0.236 \pm 0.002$	This study
Un-doped PbTe	Cast	PC	7.96	NS	$57.5 \pm 0.3$	$22.32 \pm 0.04$	$0.293 \pm 0.003$	[6]
PbI <sub>2</sub> -doped PbTe	Cast	PC	7.88	NS	$57.5 \pm 0.2$	$22.81 \pm 0.02$	$0.260 \pm 0.003$	[6]
Un-doped PbTe	Czochralski Technique	SC	8.24	*	58.05	22.95	0.264	[48]
Un-doped PbTe	Teal-Little Process	SC	8.16	*	56.95	22.48	0.268	[49]

NS Not stated.

\* Single crystal specimen, presumably near theoretical density

specimens. However, comparing the cast and the hot pressed specimens, the average Young's moduli and shear moduli for the as-cast  $\text{Pb}_{0.95}\text{Sn}_{0.05}\text{Te} - \text{PbS}$  8% specimens were about 10 percent lower than the averages calculated for the powder processed/hot pressed specimens (Table 4.3).

In contrast to the grain size dependence of hardness given by equation (4.3), in the absence of microcracking the elastic moduli (Young's modulus, shear modulus and Poisson's ratio) are independent of grain size for polycrystalline specimens with grain sizes larger than about 100 nm. However, the Young's modulus of nanograined metals [58, 59] is a function of grain size. For metals such as iron, copper, titanium and palladium, the elastic moduli for specimens with a mean grain size of about 100 nm is essentially unchanged from that for specimens with micron-sized grains, but a rapid decrease in Young's modulus is observed smaller than approximately 20 to 30 nm, with a modulus drop of 10 to 15 percent in grain sizes about 10 nm compared to the modulus values for polycrystalline specimens with grain sizes larger than 100 nm [58, 59].

For nanocrystalline ceramics  $\text{MgO}$  [60] and  $\text{ZrO}_2 - 3 \text{ wt}\% \text{ Y}_2\text{O}_3$  [35], the elastic moduli are also a function of grain size. Yeheske et al. [60] found that for fully dense, transparent  $\text{MgO}$  with an average grain size of 41 nm that the Young's and shear moduli were approximately 13% lower the moduli for polycrystalline  $\text{MgO}$  with grain sizes at the submicrometer size range and larger. In a study of dense nanocrystalline  $\text{ZrO}_2 - 3 \text{ wt}\% \text{ Y}_2\text{O}_3$  with mean grains sizes ranging from 23 nm to 130 nm, Chaim et al. found the measured Young's modulus decreased monotonically with decreasing grain size. Thus while the elastic moduli of both metals and ceramics can be grain size dependent for grain sizes smaller than about 100 nm, the elastic moduli (Young's and shear moduli) are expected to be independent of grain size for the hot pressed and cast  $\text{PbTe-PbS}$

specimens included in this study, since the mean grain sizes are roughly one micron and 1 mm for the hot pressed and cast specimens, respectively. However, if future studies generate polycrystalline PbTe-PbS specimens with mean grain sizes smaller than roughly 50 nm to 100 nm, then a grain-size dependent decrease in elastic moduli may be observed.

Even for grain sizes in the micron range and larger, the elastic moduli may display a grain size dependence if thermal expansion anisotropy (TEA) is present in the material. Since PbTe-PbS has cubic symmetry, the material is isotropic with respect to thermal expansion [61] and thus no thermal-expansion-anisotropy-induced microcracking will be present [62] to explain the observed differences in the elastic moduli between the as cast and the hot pressed specimens. Nevertheless, if microcracks are present through some mechanism other than TEA (such as polishing, grinding, thermal shock, or crystallographic phase change), then the Young's and shear modulus of materials do decrease as the volumetric number density and size of microcracks increase [10]. Since the fracture strength of the brittle, large grained materials decreases with increasing grain size [63], the as-cast specimens are likely more susceptible to microcrack damage during the cutting and polishing processes involved in specimen preparation, which may in turn lead to the lower moduli for the cast compared to the hot pressed specimens (Table 4.3).

This study focuses on the room temperature mechanical properties of thermoelectric materials with the composition PbTe-PbS 8%. For thermoelectric materials, the dimensionless figure of merit,  $ZT$ , given by

$$ZT = \frac{S^2 \sigma T}{\kappa} \quad (4.4)$$

is very important, since  $ZT$  is used to measure the efficiency of the thermoelectric, where  $S$  is the Seebeck coefficient,  $s$  is the electrical conductivity,  $k$  is the total (lattice plus electronic) thermal conductivity and  $T$  is temperature in Kelvin. In the past decade,

improvements in ZT have been accomplished largely by decreasing the lattice thermal conductivity of thermoelectric materials [64, 65]. For the same PbTe-PbS 8% composition as is included in this study, Girard et al. calculated the thermal conductivity from thermal diffusivity and specific heat measurements performed on a laser flash system [66]. The room temperature value of thermal conductivity,  $k$ , determined by Girard et al. was about 1.6 W/mK at room temperature, but  $k$  decreased to about  $\sim 1$  W/mK to  $\sim 0.4$  W/mK for temperature between 400 – 500 K [66].

#### 4.4. Summary and Conclusions

Powder processing of  $\text{Pb}_{0.95}\text{Sn}_{0.05}\text{Te} - \text{PbS}$  8% ingots gave dense (relative densities of 0.94 and 0.97) hot pressed billets with grain sizes in the micron range. The mean hardness of the hot pressed specimens was  $1.18 \pm 0.09$  GPa, which is comparable to that of hot pressed LAST ( $\text{Ag}_a\text{Pb}_b\text{Sb}_c\text{Te}_d$ ). However the hot pressed PbTe-PbS specimens have a hardness,  $H$ , that is about 70 percent higher than the as-cast specimens included in this study (Figure 4.5), although there are no compositional differences between the cast and hot pressed  $\text{Pb}_{0.95}\text{Sn}_{0.05}\text{Te} - \text{PbS}$  8% specimens included in this study. The higher hardness observed in this study for the powder processed and hot pressed specimens (compared to the as-cast specimens) is likely a grain size effect, where the hardness increases with decreasing grain size (equation (4.3)) for materials with grain sizes in the micron range and larger. No indentation size effect (ISE) or reverse indentation size effect (RISE) is observed for the range of indentations loads included in this study (Figure 4.5).

This study is the first to report Young's modulus, shear modulus and Poisson's ratio values

for any composition in the PbTe-PbS system. For the hot pressed  $\text{Pb}_{0.95}\text{Sn}_{0.05}\text{Te} - \text{PbS}$  8% specimens, the measured elastic moduli were comparable to those measured in earlier studies for LAST, PbTe and  $\text{PbI}_2$ -doped PbTe [15, 55, 56] (Table 4.3). However, the Young's and shear modulus of the hot pressed PbTe-PbS specimens were about 10 percent higher than the moduli measured for the cast specimens, although for the elastic moduli the difference in grain sizes between the cast and hot pressed specimens likely does not account for the observed differences in the elastic moduli (Table 4.3). Nevertheless, the differences in moduli may stem of low strength values (and hence greater susceptibility to microcracking) in the cast specimens due to their large grain sizes. Future studies are needed to address this point.

#### Acknowledgements

The authors acknowledge the financial assistance of the Office of Naval Research Grant N00014-08-1-0613. The authors also acknowledge the Defense University Research Instrumentation Program (DURIP) Grant No. N00014-09-1-0785, Office of Naval Research, which provided funding for the purchase of the Resonant Ultrasound Spectroscopy apparatus and the laser scattering apparatus utilized in this research. In addition, funding for the hot press facility through U. S. Department of Energy Grant DE-FC26-04NT42281 is acknowledged.

## REFERENCES

#### 4.5 References

- [1] J. Androulakis, C-H Lin, H-J Kong, C. Uher, C-I Wu, T. Hogan, B. A. Cook, T. Caillat, K.M. Paraskevopoulos, and M.G. Kanatzidis, Spinodal decomposition and nucleation and growth as a means to bulk nanostructured thermoelectrics: Enhanced performance in  $Pb_{1-x}Sn_xTe-PbS$ , *J. Am. Chem. Soc.* 129 (2007) 9780-9788.
- [2] E. Quarez, K. F. Hsu, R. Pcionek, N Frangis, E. K. Polychroniadis, M. G. Kanatzidis, Nanostructuring, compositional fluctuations, and atomic ordering in the thermoelectric materials  $AgPbmSbTe_{2+m}$ . The myth of solid solutions, *J. Am. Chem. Soc.* 127 (2005) 9177 - 9190.
- [3] T. P. Hogan, A. Downey, J. Short, J. D'Angelo, C-I Wu, E. Quarez, J. Androulakis, F. P. Poudeu, J. Sootsman, D-Y Chung, M. G. Kanatzidis, S. D. Mahanti, E. Timm, H Schock, F. Ren, J. Johnson, E. D. Case, Nanostructured thermoelectric materials and high-efficiency power-generation modules, *J. Elect. Mater.* 36 (2007) 704-710.
- [4] J. Androulakis, K. F. Hsu, R. Pcionek, H. Kong, C. Uher, J. D'Angelo, A. Downey, T. Hogan M. G. Kanatzidis, Nanostructuring and high thermoelectric efficiency in p-type  $Ag(Pb_{1-y}Sny)_mSbTe_{2+m}$ , *Adv. Mater.* 18 (2006) 1170 – 1173.
- [5] D.M. Rowe (Ed.), *CRC Handbook of Thermoelectrics*, CRC Press, Boca Raton, Florida 1995.
- [6] F. Ren, E. D. Case, E. J. Timm, H. J. Schock, Hardness as a function of composition for n-type LAST thermoelectric material, *J. Alloys Compd.* 455 (2008) 340-345.
- [7] N. E. Dowling, *Mechanical Behavior of Materials*, Second Ed., Prentice Hall, Upper Saddle River, New Jersey, 1999.
- [8] S. S. Manson, *Thermal Stress and Low Cycle Fatigue*, McGraw-Hill, New York, 1966.
- [9] J. N. Reddy, *An Introduction to the Finite Element Method*, Third Ed., McGraw-Hill Higher Education, New York, 2006.
- [10] E. D. Case, in: M. H. Alibadi (Ed), *Thermo-Mechanical Fatigue and Fracture*, WIT Press, Southampton, UK, 2002, pp. 137 – 208.
- [11] E.D. Case, Y. Kim, The effect of surface-limited microcracks on the effective Young's modulus of ceramics 2. Application of analysis to particular microcrack geometries, *J. Mater. Sci.*, 28 (1993) 1885-1900.
- [12] E. D. Case, C. Glinka, Characterization of microcracks in  $YCrO_3$  using small-angle neutron-scattering and elasticity measurements, *J. Mater. Sci.* 19 (1984) 2962-2968.
- [13] F. Ren, E. D. Case, E. J. Timm, M. D. Jacobs, H. J. Schock, Weibull analysis of the biaxial

- fracture strength of a cast p-type LAST-T thermoelectric material, *Philos. Mag. Lett.* 86 (2006) 673 – 682.
- [14] F. Ren, E. D. Case, E. J. Timm, H. J. Schock, Young's modulus as a function of composition for an n-type lead-antimony-silver-telluride (LAST) thermoelectric material, *Philos. Mag.* 87 (2007) 4907 - 4934.
- [15] F. Ren, E. D. Case, J. R. Sootsman, M. G. Kanatzidis, H. Kong, C. Uher E. Lara-Curzio, R. M. Trejo, C. Uher, The high-temperature elastic moduli of polycrystalline PbTe measured by resonant ultrasound spectroscopy, *Acta Mater.* 56 (2008) 5954 – 5963.
- [16] F. Ren, E. D. Case, J. E. Ni, E. J. Timm, E. Lara-Curzio, R. M. Trejo, C.-H. Lin, M. G. Kanatzidis, Temperature-dependent elastic moduli of lead telluride-based thermoelectric materials, *Philos. Mag.* 89 (2009) 143- 167.
- [17] F. Ren, E. D. Case, E. J. Timm, E. Lara-Curzio, R. M. Trejo, Anomalous temperature-dependent Young's modulus of a cast LAST (Pb-Sb-Ag-Te) thermoelectric material, *Acta Mater.* 58 (2010) 31-38.
- [18] J. E. Ni, F. Ren, E. D. Case, E. J. Timm, Porosity dependence of elastic moduli in LAST (Lead-antimony-silver-tellurium) thermoelectric materials, *Mater. Chem. Phys.* 118 (2009) 459-466.
- [19] F. Ren, B. D. Hall, J. E. Ni, E. D. Case, E. J. Timm, H. J. Schock, C-I. Wu, J. J. D'Angelo, T. P. Hogan, R. M. Trejo, E. Lara-Curzio, in: T.P. Hogan, J. Yang, R. Funahashi (Eds) *Thermoelectric Power Generation, Materials Research Society Proceedings, Vol. 1044.* Materials Research Society, Warrendale, PA, 2008, pp 121 – 126.
- [20] C. Suryanarayana, Mechanical alloying and milling, *Prog. Mater. Sci* 46 (2001) 13.
- [21] M. N. Rahaman, *Ceramic Processing and Sintering, Second Ed.*, Marcel Dekker, New York, 2003, p. 57.
- [22] B. D. Hall, E. D. Case, F. Ren, J. Johnson and E. J. Timm, Agglomeration during wet milling of LAST (lead-antimony-silver-tellurium) powders, *Mater. Chem. Phys.* 113 (2009) 497 – 502.
- [23] V.V. Robozarov, V.A. Zykov and T.A. Gavrikova, Chemical etching of lead chalcogenides, *Inorg. Mater.* 36 (2000) 127 – 131.
- [24] A. Leonardi and F. Furgiuele, Analytical Approaches to Stress Intensity Factor Evaluation for Indentation Cracks, *J. Amer. Ceram. Soc.* 92 (2009) 1093 - 1097.
- [25] J. Jang and G. M. Pharr, Influence of indenter angle on cracking in Si and Ge during nanoindentation, *Acta Mater.* 56 (2008) 4458 – 4469.

- [26] G. R. Anstis, P. Chantikul, B. R. Lawn, D. B. Marshall, A critical-evaluation of indentation techniques for measuring fracture-toughness. 1. Direct crack measurements, *J. Amer. Ceram. Soc.* 64 (1981) 533 -538.
- [27] A. Migliori, J. L. Sarrao, *Resonant Ultrasound Spectroscopy: Applications to Physics, Materials Measurements, and Nondestructive Evaluation*, Academic Press, New York, 1997.
- [28] Saturn Digisizer 5200 Operators Manual v1.12, Micromertics Instrument Corporation, Norcross, GA, 2007, pp. 1-9.
- [29] R. L. Fullman, Measurement of particle sizes in opaque bodies, *Trans AIME* 197 (1953) 447 – 452.
- [30] E. D. Case, J. R. Smyth, V. Monthei, Grain size determinations, *J. Am. Ceram. Soc.* 64 (1981) C24-C25.
- [31] R. W. Rice, *Mechanical Properties of Ceramics and Composites*, Marcel Dekker Inc., New York, 2000.
- [32] H. Conrad, J. Narayan, On the grain size softening in nanocrystalline materials, *Scr. Mater.* 42 (2000) 1025-1030.
- [33] D. Ehre, R. Chaim, Abnormal hall-petch behavior in nanocrystalline MgO ceramic, *J. Mater. Sci.* 43 (2008) 6139-6143.
- [34] F.L. Kennard, R.C. Bradt, V.S. Stubican, Mechanical-properties of directionally solidified MgO-MgAl<sub>2</sub>O<sub>4</sub> eutectic, *J. Am. Ceram. Soc.* 59 (1976) 160-163.
- [35] R. Chaim, M. Hefetz, Effect of grain size on elastic modulus and hardness of nanocrystalline ZrO(2)-3 wt% Y(2)O(3) ceramic, *J. Mater. Sci.* 39 (2004) 3057 – 3061.
- [36] M. S. Darrow, W. B. White, R. Roy, Micro-indentation hardness variation as a function of composition for polycrystalline solutions in systems PbS/PbTe, PbS/PbTe and PbS/PbSe, *J. Mater. Sci.*, 4 (1969) 313-319.
- [37] M.S. Ablova, Sov. Effect of donor and acceptor additions on mechanical properties of PbTe, PbSe, and PbS, *Phys. Solid State*, 12 (1971) 2910.
- [38] M. L. Weaver, M. E. Stevenson , R. C. Bradt, Knoop microhardness anisotropy and the indentation size effect on the (100) of single crystal NiAl, *Mater. Sci. Eng. A345* (2003) 113 -117.
- [39] A. Ghosh, H. Li, Y.H. Han, R.C. Bradt, The frictional component of the indentation size effect in low load microhardness testing, *J. Mater. Res.* 8 (1993) 1028 -1032.

- [40] W.D. Nix, H. Gao, Indentation size effects in crystalline materials: A law for strain gradient plasticity, *J. Mech. Phys. Solids* 46 (1998) 411-425.
- [41] K Sangwal, A. Klos, Study of microindentation hardness of different planes of gadolinium calcium oxyborate single crystals, *Cryst. Res. Technol.* 40 (2005) 429 – 438.
- [42] K . Sangwal, On the reverse indentation size effect and microhardness measurement of solids, *Mater. Chem. Phys.* 63 (2000) 145 – 152.
- [43] D. S. Harding, W. C. Oliver, and G. M. Pharr, Materials Research Society Symposium Proceedings, *Thin Films: Stresses and Mechanical Properties*. S. P. Baker, P. Borgesen, P. H. Townsend, C. A. Ross, and C. A. Volkert (Eds.) Vol. 356, Materials Research Society, Warrendale, PA, 1995, pp. 663–69.
- [44] G. M. Pharr, Measurement of mechanical properties by ultra-low load indentation, *Mater. Sci. Eng.*, A253 (1998) 151–159.
- [45] K. Kese and D. J. Rowcliffe, Nanoindentation method for measuring residual stress in brittle materials, *J. Am. Ceram. Soc.* 86 (2003) 811– 816
- [46] D. J. Morris, S. B. Myers, R. F. Cook, Indentation crack initiation in ion-exchanged aluminosilicate glass, *J. Mater. Sci.* 39 (2004) 2399 – 2410.
- [47] B. R. Lawn and A. G. Evans, Model for crack initiation in elastic-plastic indentation fields, *J. Mater. Sci.* 12 (1977) 2195-2199.
- [48] K. Ueno, A Yamamoto, T. Inoue, S. Sodeoka, and H. Obara, Optimization of hot-press conditions of  $Zn_4Sb_3$  for high thermoelectric performance: III. Effect of starting particle size on thermoelectric and mechanical properties, *J. Alloys Compds.* 392 (2005) 295-299.
- [49] L. D. Zhao, B. Zhang, J. Li, M. Zhou. W. Liu, and J. Liu, Thermoelectric and mechanical properties of nano-SiC-dispersed  $Bi_2Te_3$  fabricated by mechanical alloying and spark plasma sintering, *J. Alloys Compds.* 455 (2008) 259-264.
- [50] A. K. Varshneya and D. J. Mauro, Microhardness, indentation toughness, elasticity, plasticity, and brittleness of Ge-Sb-Se chalcogenide glasses, *J Non-Cryst Solids* 353 (2007) 1291–1297.
- [51] S. Zhu, H. Ma, L. Calvez, X. Zhang, J. Lucas, J. Adam, H. Shang, and T. Rouxel, Optical and mechanical properties of far infrared transmitting glass-ceramics, *J Non-Cryst Solids* 353 (2007) 1298–1301.
- [52] J. Guin, T. Rouxel, and J. Sangleboeuf, Hardness, toughness, and scratchability of germanium-selenium chalcogenide glasses, *J. Am. Ceram. Soc.* 85 (2002) 1545–1552.
- [53] A. G. Evans and H. Johnson, Fracture mechanical study of ZnSe for laser window

- applications, *J. Am. Ceram. Soc.* 58 (1975) 244–249.
- [54] G. D. Quinn and R. C. Bradt, On the Vickers indentation fracture toughness test, *J. Amer. Ceram. Soc.* 90 (2007) 673-680.
- [55] B. Houston, R. E. Strakna, H. S. Belson, Elastic constant thermal expansion and Debye temperature of lead telluride, *J. Appl. Phys.* 39 (1968) 3913.
- [56] NG Einspruch, RJ Manning, Elastic constants of compound semiconductors ZnS, PbTe, GaSb, *J. Acoust. Soc. Am.* 35 (1963) 215.
- [57] G. Simmons, H. Wang, *Single Crystal Elastic Constants and Calculated Aggregate Properties*, MIT Press, Cambridge, MA, 1971.
- [58] J. Zhou, Z. Li, R. Zhu, Y. Li, Z. Zhang, A mixtures-based model for the grain size dependent mechanical behavior of nanocrystalline materials, *J. Mater. Process. Technol.*, 197 (2008) 325-336.
- [59] H. S. Cao, J. J. Hunsinger, O. Elkdin, Determination of elastic modulus of nanocrystalline iron and titanium by means of acoustic microscopy, *Scr. Mater.* 46 (2002) 55 – 60.
- [60] O. Yehekel, R. Chaim, Z. Shen, M. Nygren, Elastic moduli of grain boundaries in nanocrystalline MgO ceramics, *J. Mater. Res.* 20 (2005) 719 – 725.
- [61] J. F. Nye, *Physical Properties of Crystals: Their Representation By Tensors And Matrices*, Clarendon Press, Oxford, 1957.
- [62] E. D. Case, J. R. Smyth, O. Hunter, Grain size dependence of microcrack initiation in brittle materials, *J. Mater. Sci.* 15 (1980) 149-153.
- [63] M. W. Barsoum, *Fundamentals of Ceramics*, McGraw Hill, New York, 1997.
- [64] K. F. Hsu, S. Loo, F. Guo, W. Chen, J. S. Dyck, C. Uher, T Hogan, E. K. Polychroniadis, M. G. Kanatzidis, Cubic  $\text{AgPb}_m\text{SbTe}_{2+m}$ : Bulk thermoelectric materials with high figure of merit, *Science* 303 (2004) 818-821.
- [65] B Poudel, Q Hao, Y. Ma, Y. C. Lan, A. Minnich, B Yu, X Yan, D. Z. Wang, A. Muto, D Vashaee, X. Y. Chen, J. M. Liu, M. S. Dresselhaus, G Chen, Z. Ren, High-thermoelectric performance of nanostructured bismuth antimony telluride bulk alloys, *Science* 320 (2008) 634-638.
- [66] S. N. Girard, J. He, C. Li, S. Moses, G. Wang, C. Uher, V. P. Dravid, and M. G. Kanatzidis, In Situ Nanostructure Generation and Evolution within a Bulk Thermoelectric Material to Reduce Lattice Thermal Conductivity, *Nano Letters* 10 (2010) 2825-2831

The citation for this paper is: Jennifer E. Ni, Eldon D. Case, Ryan Stewart, Chun-I Wu, Timothy P. Hogan, Mercuri G. Kanatzidis, Bloating in  $(\text{Pb}_{0.95}\text{Sn}_{0.05}\text{Te})_{0.92}(\text{PbS})_{0.08}$ -0.055%  $\text{PbI}_2$  Thermoelectric Specimens as a Result of Processing Conditions, *J Electron Mater*, in press, DOI: 10.1007/s11664-011-1853-0.

5.0 Bloating in  $(\text{Pb}_{0.95}\text{Sn}_{0.05}\text{Te})_{0.92}(\text{PbS})_{0.08}$ -0.055%  $\text{PbI}_2$  thermoelectric specimens as a result of processing conditions

Jennifer E. Ni<sup>1</sup>, Eldon D. Case<sup>1</sup>, Ryan Stewart<sup>1</sup>, Chun-I Wu<sup>1</sup>, Timothy P. Hogan<sup>1</sup>, Mercuri G. Kanatzidis<sup>2</sup>

<sup>1</sup>Michigan State University, East Lansing, MI USA

<sup>2</sup>Northwestern University, Evanston, IL USA

Lead chalcogenides such as  $(\text{Pb}_{0.95}\text{Sn}_{0.05}\text{Te})_{0.92}(\text{PbS})_{0.08}$ -0.055%  $\text{PbI}_2$  have received attention due to their encouraging thermoelectric properties. For the hot pressing (HP) and pulsed electric current sintering (PECS) techniques used in this study, decomposition reactions can generate porosity (bloating). Porosity in turn can degrade electrical, thermal, and mechanical properties. In this study, microstructural observations (scanning electron microscopy) and room temperature elasticity measurements (resonant ultrasound spectroscopy) were used to characterize bloating generated during post-densification anneals. Although every HP specimen bloated during post-densification annealing, no bloating was observed for the PECS specimens processed from dry milled only powders. The lack of bloating for the annealed PECS specimens may be related to the electrical discharge intrinsic in the PECS process which reportedly cleans the powder particle surfaces during densification.

**KEYWORDS:** thermoelectrics, porosity, Young's modulus, resonant ultrasound spectroscopy

Please direct correspondence to: Eldon D. Case, Chemical Engineering and Materials Science Department, Room 2527 Engineering Building, Michigan State University, East Lansing, Michigan, 48824-1226, USA, e-mail [casee@egr.msu.edu](mailto:casee@egr.msu.edu), FAX (517)-432-1105.

## 5.1 Introduction

Powder processing of thermoelectric materials can yield specimens with much smaller grain sizes than cast specimens [1]. A reduction in grain size can in turn greatly enhance fracture strength of brittle materials [1, 2]. During powder processing, porosity,  $P$ , can result from (1) incomplete sintering [2] or (2) from gas evolution within the specimens during processing. The internal gas evolution in specimens during processing can occur via either liquid phase [3, 4] or solid phase decomposition reactions [5-9].

Solid phase decomposition reactions [5-9] may occur when the specimen is densified using high externally applied pressures. High temperature anneals in the absence of an externally applied pressure can result in increases in  $P$  with increasing temperature due to local deformation caused by pressure generated by gases evolved by decomposition reactions. Thus in this study, the volume fraction porosity  $P$  is given by  $P = P_R + P_B$ , where  $P_R$  is the porosity contribution due to residual pores and  $P_B$  is the porosity generated by bloating.

The porosity dependence of thermal, electrical and mechanical properties on porosity,  $P$ , can be written as

$$A(P) = A_D \exp(-b_{PA}P) \quad (5.1)$$

where  $A$  can be thermal conductivity [10], electrical conductivity [10], dielectric constant [11], or elastic modulus [10, 12].  $A_D$  is the value of the material property,  $A$ , for at  $P = 0$ . Also,  $b_{PA}$  is a material dependent constant [10, 12] and  $P = P_R + P_B$ . This study focuses on microstructural observations of bloating generated porosity and  $P$  versus Young's modulus,  $E$ , measurements, especially where  $P$  is generated by bloating for  $\text{Ag}_{0.86}\text{Pb}_{19}\text{Sb}_{1.0}\text{Te}_{20}$  (LAST) and  $(\text{Pb}_{0.95}\text{Sn}_{0.05}\text{Te})_{0.92}(\text{PbS})_{0.08} - 0.055\% \text{PbI}_2$  (PbTe-PbS) [13] specimens.

For both hot pressing (HP) and pulsed electric current sintering (PECS), the powder charge is placed between two movable plungers within a cylindrical die. Also, for both HP and PECS, the powder charge is heated while pressure is simultaneously applied via the plungers. However, HP and PECS are distinct powder processing techniques in that for HP the powders and die are heated by an external furnace while for PECS the powders are heated by high-current electrical pulses that pass through both the die assembly (plungers plus die) and the enclosed powder charge. Regardless of the powder processing technique, our HP specimens bloated after annealing while the specimens that are PECS processed from dry milled only powders did not bloat upon annealing (Results and Discussion). During densification, gas phase generation from decomposition reactions can be inhibited by the elevated pressures due to hot pressing (HP) and pulsed electric current sintering (PECS). However, during post-densification thermal annealing (in the absence of an externally applied confining pressure) decomposition reactions can generate porosity (bloating) which in turn can degrade electrical, thermal, and mechanical properties [10 – 12, 14]. Changes in thermal and electrical conductivity are extremely important since the efficiency of a thermoelectric device is a function of the dimensionless figure of merit,  $ZT$ , which is written as

$$ZT = \frac{\sigma S^2}{\kappa} \quad (5.2)$$

where  $\sigma$  is the electrical conductivity,  $S$  is the Seebeck coefficient,  $\kappa$  is the thermal conductivity, and  $T$  is the temperature.

Since  $\kappa$  decreases with increasing porosity [10, 14], low thermal conductivity is required for a high  $ZT$  for thermoelectric materials (equation (2)). However, the electrical conductivity,  $\sigma$ , also decreases with increasing porosity [10]. Thus, one must consider the overall effect of

porosity on ZT to determine whether increasing porosity enhances or degrades the thermoelectric properties of a material.

Calculations of the effect of nanopores on the thermal conductivity of Ge [15] and Si [16] indicate dramatic decreases in  $\kappa$  with nanoporosity. For nanoporous Ge with pore diameters = 1.0 nm and pore spacings = 0.7 nm, the calculated  $\kappa$  was 180 times smaller than the bulk value [15]. Similar decreases in  $\kappa$  were calculated for Si [16] but as was the case for Ge [15] the decreases in  $\kappa$  become large only for extremely high values of volume fraction porosity, P (P ~ 0.64 to 0.89) [16]. However, ZT may decrease with increasing nanoporosity, as noted by Lee, Dresselhaus and co-workers [14] who state that “Porous nanograined materials have enhanced Seebeck coefficient due to energy filtering effect and low thermal conductivity, which are favorable for thermoelectric applications. However, the benefit is not large enough to overcome the deficit in the electrical conductivity, so that a high sample density is necessary for nanograined SiGe” [14]. Thus bloating generated porosity may degrade both ZT and mechanical properties.

## 5.2 Experimental Procedure

The specimens were densified with HP or PECS with  $\text{Ag}_{0.86}\text{Pb}_{19}\text{Sb}_{1.0}\text{Te}_{20}$  and  $(\text{Pb}_{0.95}\text{Sn}_{0.05}\text{Te})_{0.92}(\text{PbS})_{0.08}$ - 0.055%  $\text{PbI}_2$  powders that were (i) crushed, ground, sieved, and re-ground (CGSR), (ii) dry milled (DM), (iii) wet milled (WM) with hexane, or (iv) dry and then wet milled with hexane (D/WM) (Table 5.1). A 53 micron sieve (Retsch, Newtown, PA) was used for each powder processing technique in this study (Table 5.1). The hot pressed and PECS specimens were pressed using the temperature-pressure-time profiles in Table 5.1 with a 22 mm diameter graphite die. In this study, two separate sets of specimens were used to (i) directly

Table 5.1 The powder processing conditions and sintering parameters for the hot pressed (HP) and pulsed electric current sintering (PECS) densified specimens processed using powders that were crushed, ground, sieved, and re-ground (CGSR) powder was either (1) set aside for densification, (2) dry milled (DM), (3) dry milled and then wet milled (D/WM), or (4) wet milled (WM). For the post-densification anneals, the heating and cooling rates were 5 K/min and 2 K/min for specimens prepared for SEM observation and RUS elasticity measurements, respectively.

Specimen (composition)	Powder Processing	Sintering Max		Post-densification annealing parameters	
		Temperature/ Pressure/ Time	Pressure/ Time	Temperature	Time
Bloating observed via SEM					
HP-DM-01 <sup>a</sup>	DM	673 K/74.4 MPa/90 min		723 K	4 hours <sup>b</sup>
HP-CGSR-01 <sup>a</sup>	CGSR	673 K/74.4 MPa/90 min		973 K	6 hours <sup>b</sup>
HP-D/WM-01	D/WM <sup>c</sup>	673 K/74.4 MPa/90 min		693 K	2 hours <sup>b</sup>
PECS-WM-01	WM <sup>d</sup>	823 K/60 MPa/20 min		823 K	2 hours <sup>e</sup>
PECS-DM-01	DM	823 K /60 MPa/20 min		663 K, 823 K, 936 K	2 hours <sup>e</sup>
Bloating measured via RUS elasticity measurements					
HP-D/WM-02a	D/WM <sup>c</sup>	723 K/74.4 MPa/120 min		603 K, 633 K, 663 K, 693 K	1 min <sup>e</sup>
HP-D/WM-02b	D/WM <sup>c</sup>	723 K/74.4 MPa/120 min		543 K, 573 K, 603 K, 633 K, 663 K, 693 K	1 min <sup>e</sup>
HP-D/WM-02c	D/WM <sup>c</sup>	723 K/74.4 MPa/120 min		603 K, 633 K, 663 K, 693 K	1 min <sup>e</sup>
HP-D/WM-01a	D/WM <sup>c</sup>	723 K/74.4 MPa/120 min		603 K, 633 K, 663 K, 693 K	1 min <sup>e</sup>
HP-D/WM-01b	D/WM <sup>c</sup>	723 K/74.4 MPa/120 min		663 K, 693 K	1 min <sup>e</sup>
HP-WM-01a	WM <sup>d</sup>	723 K/74.4 MPa/120 min		663 K, 693 K	1 min <sup>e</sup>
HP- WM-01b	WM <sup>d</sup>	723 K/74.4 MPa/120 min		603 K, 633 K, 663 K, 693 K	1 min <sup>e</sup>
PECS-D/WM-01	D/WM <sup>c</sup>	823 K /60 MPa/20 min		603 K, 633 K, 663 K, 693 K	1 min <sup>e</sup>
PECS-DM-02	DM	623 K /60 MPa/20 min		773 K	1 min <sup>e</sup>

<sup>a</sup> Specimen composition is  $\text{Ag}_{0.86}\text{Pb}_{19}\text{Sb}_{1.0}\text{Te}_{20}$ , all other specimens in the table are  $(\text{Pb}_{0.95}\text{Sn}_{0.05}\text{Te})_{0.92}(\text{PbS})_{0.08} - 0.055\% \text{PbI}_2$

<sup>b</sup> Annealed in flowing Ar atmosphere

<sup>c</sup> Wet milled with hexane as the milling fluid

<sup>d</sup> Wet milled with ethanol as the milling fluid

<sup>e</sup> Annealed in flowing Ar (96%) – H<sub>2</sub>(4%) atmosphere

examine the microstructure of fracture surfaces using scanning electron microscopy (SEM) and (ii) non-destructively measure the porosity dependent Young's modulus using resonant ultrasound spectroscopy (RUS) analysis (Table 5.1). Four SEM specimens were annealed at temperatures ranging from 693 K to 973 K (Table 5.1) and one SEM specimen was successively annealed at 663 K, 823 K, and 936 K (Table 5.1). The nine RUS specimens were successively annealed for temperatures ranging from 543 K to 773 K (Table 5.1). Details of the RUS experimental procedure are given elsewhere [12].

### 5.3 Results and Discussion

Using planetary milled powders, the mean grain sizes of the as-densified  $(\text{Pb}_{0.95}\text{Sn}_{0.05}\text{Te})_{0.92}(\text{PbS})_{0.08}-0.055\% \text{PbI}_2$  specimens were 1 micron to 10 microns for both HP and PECS processing [12, 17]. The mean grain size for the HP as-densified specimen was 20 microns starting from CGSR powders. Both the HP and PECS produced specimens that ranged in density from about 0.92 to 0.97 with spherical or quasi-spherical pores at grain boundaries and triple points, with submicron to 3 microns diameter pore sizes (Figures 5.1-5.3).

However, upon annealing bloating occurred (Figures 5.1 and 5.2) for the as-densified HP specimens processed from powders that were (i) CGSR (Figure 5.1), (ii) DM (Figure 5.1), and (iii) D/WM (Figure 5.2). The as-densified PECS specimens processed from WM powders bloated (Figure 5.2). Bloating in both the HP and PECS specimens generated spherical or quasi-spherical pores along grain boundaries with pore diameters ranging from 1 micron to 20 microns (Figures 5.1 and 5.2). Also, the PECS PbTe-PbS WM and HP LAST CGSR specimens had lenticular pores from 10 microns in length and 1 micron wide to about 30 microns in length and 5 microns wide (Figures 5.1 and 5.2).

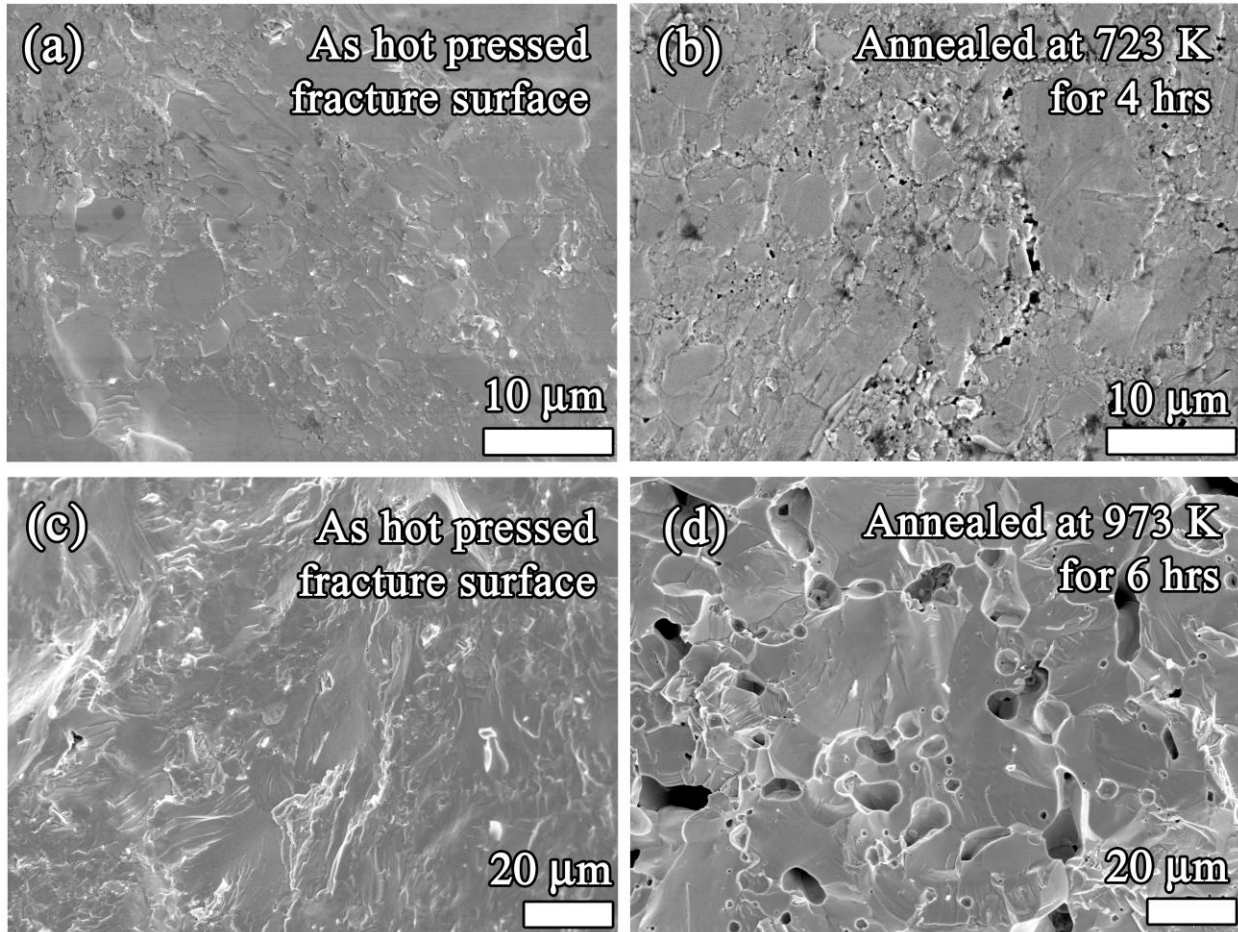


Fig. 5.1 The as-densified fracture surfaces of (a) HP-DM-01 and (c) HP-CGSR-01 do not show bloating. Annealing (b) HP-DM-01 at 723 K for 4 hours and (d) HP-CGSR-01 at 973 K for 6 hours resulted in bloating as evidenced by the increased porosity of the internal fracture surfaces. All annealing was performed in flowing Ar.

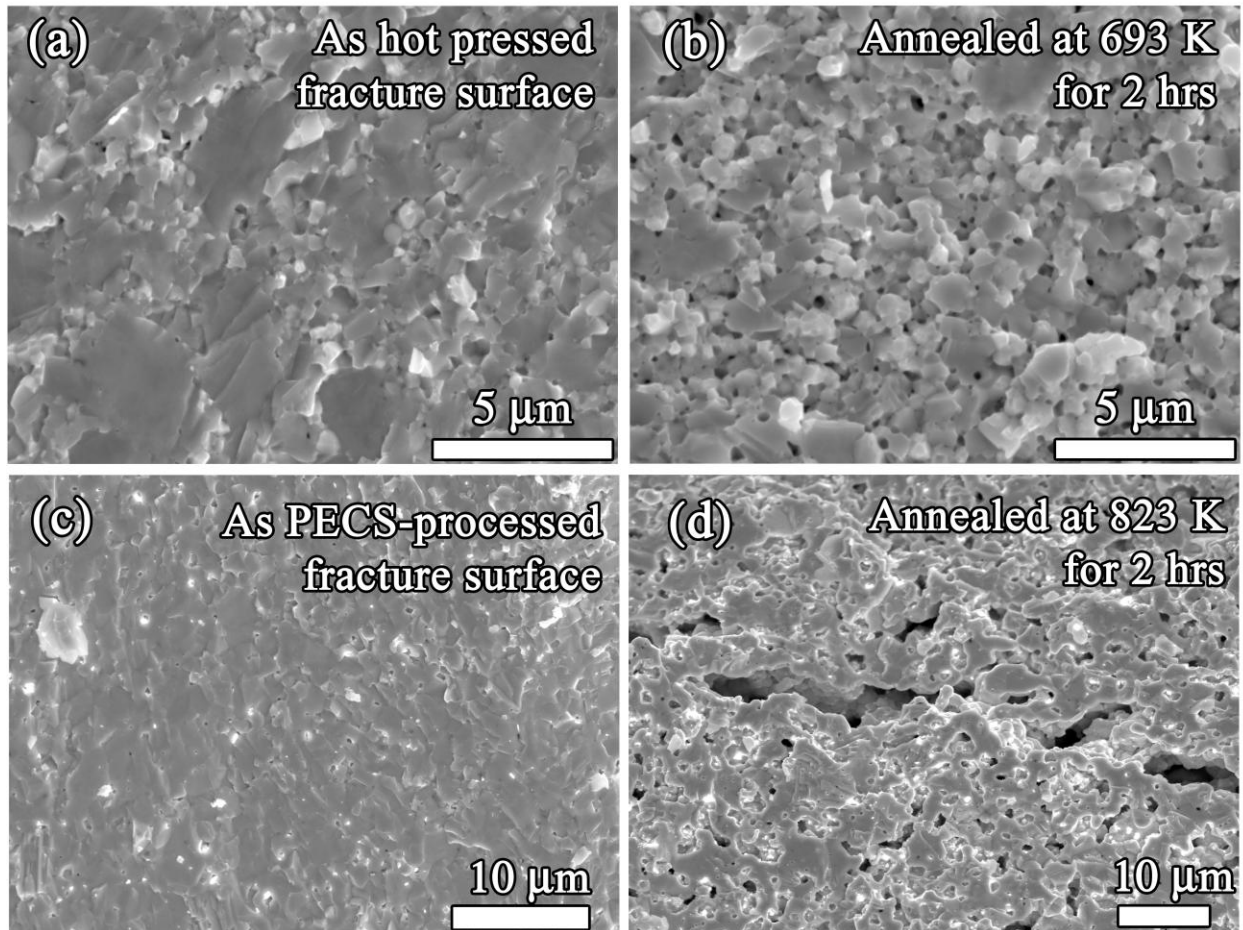


Fig. 5.2 The as-densified fracture surfaces of (a) HP-D/WM-01 and (c) PECS-WM-01 do not show bloating. Annealing (b) HP-D/WM-01 at 693 K for 2 hours and (d) PECS-WM-01 at 823 K for 2 hours resulted in bloating as evidenced by the increased porosity of the internal fracture surfaces. All annealing was performed in flowing Ar or Ar (96%)-H<sub>2</sub> (4%).

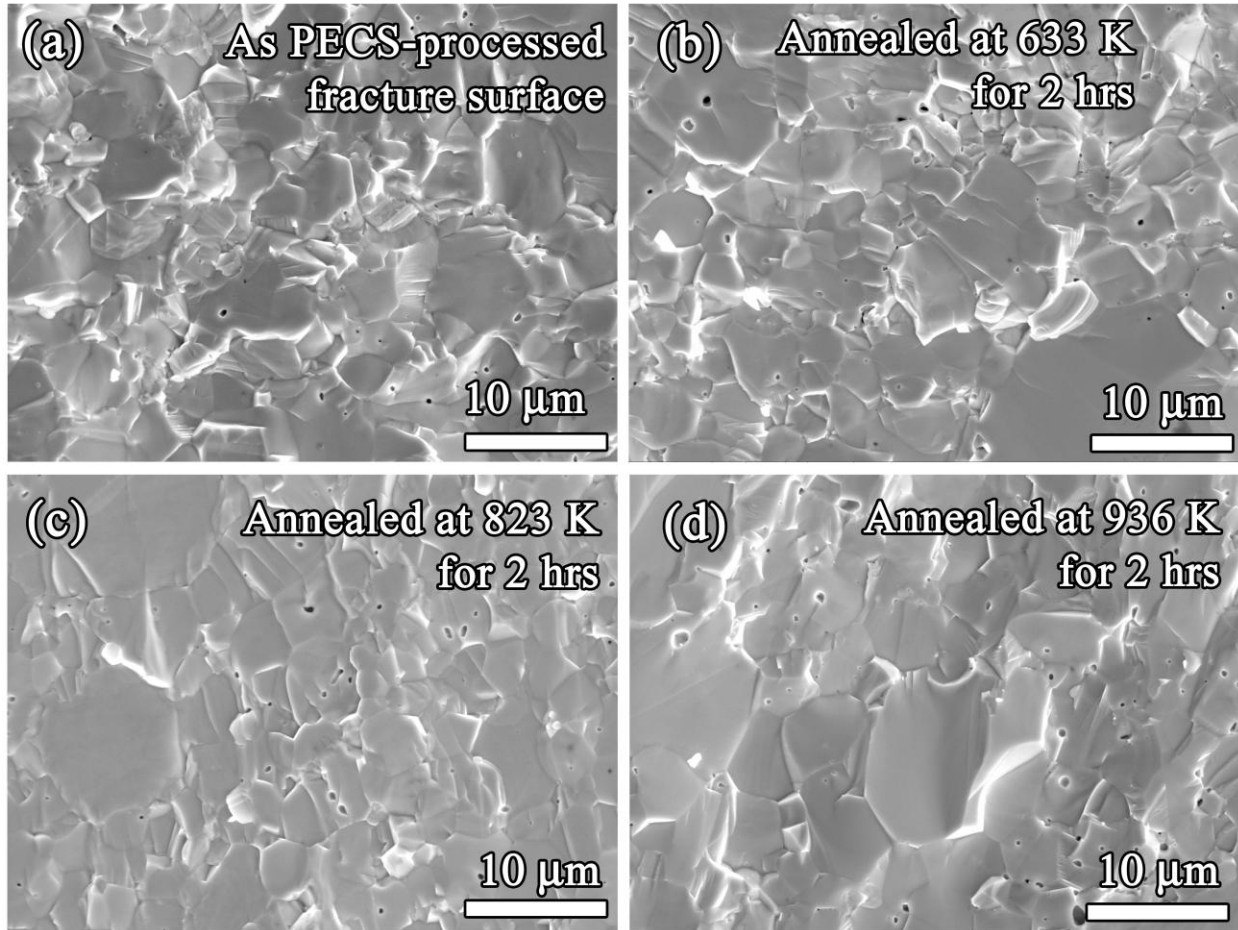


Fig. 5.3 In contrast to the annealing behavior depicted in Figures 5.1 and 5.2, the (a) as-densified PECS-DM-02 did not bloat after annealing at (b) 663 K for 2 hours, (c) 823 K for 2 hours, and (d) 936 K for 2 hours. All annealing was performed in flowing Ar (96%)-H<sub>2</sub> (4%).

After annealing from two to six hours at temperatures from 693 K to 973 K (Table 5.1), the areal number density of pores increased by 10 to 30 fold compared to the pore areal density on the fracture surfaces of the as-densified specimens of HP specimens from powder processed by CGSR (Figure 5.1), DM (Figure 5.1), and D/WM (Figure 5.2) and PECS from powder processed by WM (Figure 5.2). The series of anneals from 543 K to 693 K on hot pressed specimen HP-D/WM-02b (Table 5.1) induced surface blistering that ranged from 0.5 mm to 1 mm in diameter and internal porosity that consisted of six lenticular pores per  $12,000 \mu\text{m}^2$  that were about 20 microns long and 5 microns wide. In contrast, the PECS densified specimens fabricated using DM powders did not bloat (Figure 5.3) or blister when annealed for 2 hours at 663 K, 823 K, and 936 K (Table 5.1).

For the nine as-densified RUS specimens, the mass and volume were measured before and after each post-densification anneal to monitor the change in density. Before post-densification annealing,  $P = P_R$  where  $P_R$  ranged from 0.03 to 0.08. Following post-densification anneals  $P_B$  increased as temperature increased. For example, after the 603 K post-densification anneal,  $P$  ranged from 0.04 to 0.11 and after the 693 K anneal,  $P$  ranged from 0.05 to 0.22 (Figure 5.4). For the RUS analysis, the exception was the PECS-DM-02 specimen which did not bloat after a series anneals, including a 773 K post-densification anneal (Figure 5.4, Table 5.1). The decrease in the Young's modulus,  $E$ , with increasing porosity is consistent with equation (1) (Figure 5.4), where the least-squares fit of  $E$  versus  $P$  (equation (1)) yielded an  $r^2 = 0.990$ ,  $b_{PE} = 1.33 \pm 0.02$  and  $E_D = 56.17 \pm 0.13$  GPa for the 9 as-densified and 32 post-densification annealed elastic moduli measurements.

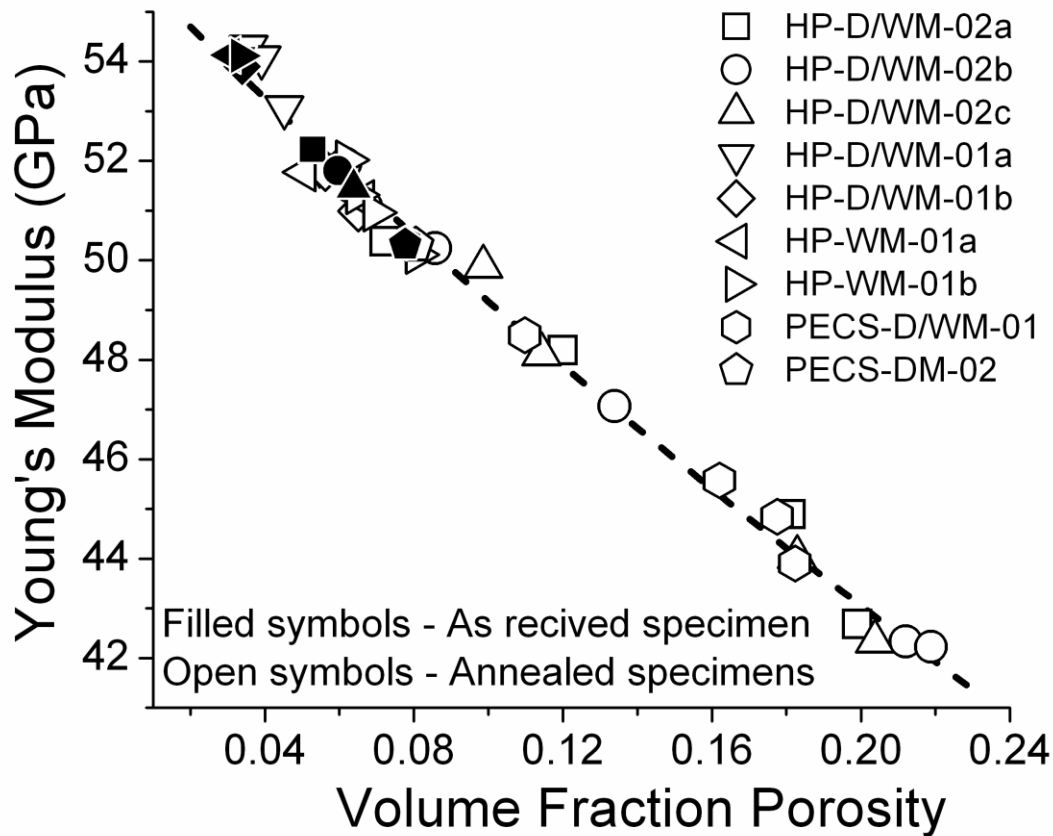


Fig. 5.4 The bloating (Figures 5.1 and 5.2) or lack of bloating (Figure 5.3) observed in the SEM study is also evident in the RUS measurements of Young's modulus,  $E$ , versus volume fraction porosity,  $P$ . For the nine as-densified HP and PECS specimens along with the 32 annealing measurements on the same nine specimens (Table 5.1), as  $P$  increased,  $E$  decreased. The filled symbols and open symbols represent the  $E$  values for the as-densified and annealed specimens, respectively. Equation (5.1), widely used to describe the  $E$  versus  $P$  behavior for brittle materials [10, 11], also fits the  $E$  versus  $P$  behavior well ( $r^2 = 0.990$ ) for the 41 RUS measurements included in this study. The dashed line represents the least-squares fit to equation (5.1).

In order to compare the value of the Young's modulus,  $E_D$ , found from equation (1) to the literature, we can use values of the aggregate Young's modulus calculated from single crystal PbTe data where  $E$  was 58.08 GPa [18] or 56.95 GPa [19]. Thus the  $E_D$  value of  $56.17 \pm 0.13$  GPa that was calculated from the least-squares fit of equation (1) to this study's modulus-porosity data for  $(\text{Pb}_{0.95}\text{Sn}_{0.05}\text{Te})_{0.92}(\text{PbS})_{0.08}$ -0.055%  $\text{PbI}_2$  specimens is within approximately two percent of the mean of the two literature values for PbTe [18,19] listed above.

Groza et al. found that the electrical discharge that is intrinsic to the PECS process cleaned the oxide surface layers from the AlN particles during sintering [20]. In this study, the PECS densification process may have removed contaminating surface layers from the powder processed  $(\text{Pb}_{0.95}\text{Sn}_{0.05}\text{Te})_{0.92}(\text{PbS})_{0.08}$ -0.055%  $\text{PbI}_2$  particles. This surface cleaning may have in turn removed the source of a solid phase decomposition reaction, thus allowing the densified PECS specimens to be annealed up to 936 K without bloating (Table 5.1, Figure 5.3). Although the dry milled PECS specimens did not bloat (Figure 5.3), in contrast the wet milled PECS specimens did bloat during post-densification anneals (Figure 5.2d). Perhaps the hexane or ethanol used during the wet milling (Table 5.1 footnotes) left a carbonaceous residue which was not entirely removed by the PECS process. Such a residue could decompose during post-densification annealing, causing bloating (Figure 5.2d).

#### 5.4 Summary and Conclusions

As-densified specimens fabricated by both PECS and HP for each of the four powder processing modes (CGSR, DM, WM, and D/WM) gave dense specimens with spherical porosity confined to grain boundaries. Post-densification anneals resulted in bloating ( $P$  increased) for all

HP specimens. For the PECS fabrication, bloating occurred for the specimens processed with WM and D/WM powders. Only the PECS DM specimens did not bloat upon annealing, perhaps due to the intrinsic cleaning of the powder particle surfaces during sintering [20].

#### Acknowledgements

This research was supported by the Office of Naval Research, Grant N00014-08-1-0613 and the Department of Energy, “Revolutionary Materials for Solid State Energy Conversion Center,” an Energy Frontiers Research Center funded by the U.S. Department of Energy, Office of Basic Energy Sciences under award number DE-SC0001054. Ed Timm of the Mechanical Engineering Department, Michigan State University assisted the authors with hot pressing and cutting the specimens.

## REFERENCES

## 5.5 References

- [1] F. Ren and E. D. Case, E. J. Timm, M. D. Jacobs and H. J. Schock, Weibull analysis of the biaxial fracture strength of a cast p-type LAST-T thermoelectric material, *Philos. Mag. Lett.*, 86 673 – 682 (2006)
- [2] M.W. Barsoum, *Fundamentals of Ceramics*, ed. by B. Cantor and M.J. Goringe (IOP Publishing, London, 2003)
- [3] N.M.P. Low, Formation of cellular-structure glass with carbonate compounds and natural mica powders, *J. Mater. Sci.* 16 800-808 (1981)
- [4] P. Colombo, Conventional and novel processing methods for cellular ceramics, *Phil. Trans. R. Soc. A*, 364 109-124 (2006)
- [5] D. Holz, S. Wu, S. Scheppokat, N. Claussen, Effect of processing parameters on phase and microstructure evolution in RBAO ceramics, *J. Am. Ceram. Soc.*, 77, 2509-17 (1994)
- [6] M. H. O'Brien, O. Hunter, Jr., E. D. Case, Mechanical effects of thermal cycling on United State and Australian Synroc-B, *J. Mater. Sci. Lett.*, 4, 367-369 (1985)
- [7] H. Wen, Y. Zhao, Z. Zhang, O. Ertorer, S. Dong, E. J. Lavernia, The influence of oxygen and nitrogen contamination on the densification behavior of cryomilled copper powders during spark plasma sintering, *J. Mater. Sci.*, 46, 3006–3012 (2011)
- [8] V.N. Antsiferov, V.B. Kul'met'eva, S.E. Porozova, B.L. Krasnyi, V. P. Tarasovskii, A.B. Krasnyi, *Russ. Application of mechanochemical activation in production of zircon ceramics*, *J. Non-Ferrous Metals* 51, 82–187 (2010)
- [9] L. Stoch, Explosive thermal dehydration of solids, *J. Thermal Analy.*, 37, 1415-1429 (1991)
- [10] R.W. Rice, *Porosity of Ceramics* (Marcel Dekker, New York, 1998)
- [11] T.P. Hoepfner, E.D. Case, The influence of the microstructure on the hardness of sintered hydroxyapatite, *Ceram. Int.*, 29 (2003) 699–706
- [12] J.E. Ni, F. Ren, E.D. Case, E.J. Timm, Porosity dependence of elastic moduli in LAST (Lead-antimony-silver-tellurium) thermoelectric materials, *Mater. Chem. Phys*, 118, 459–466 (2009)
- [13] J. Androulakis, C-H Lin, H-J Kong, C. Uher, C-I Wu, T. Hogan, B.A. Cook, T. Caillat, K.M. Paraskevopoulos, M.G. Kanatzidis, Spinodal decomposition and nucleation and growth as a means to bulk nanostructured thermoelectrics: Enhanced performance in  $Pb_{1-x}Sn_xTe-PbS$ , *J. Am. Chem. Soc.* 129, 9780-9788 (2007)

- [14] H. Lee, D. Vashaee, Z. Wang, M.S. Dresselhaus, Z.F. Ren, G. Chen Effects of nanoscale porosity on thermoelectric properties of SiGe, *J. Appl. Phys.* 107, 094308, (2010)
- [15] Lee J.H., Grossman, J.C, Thermoelectric properties of nanoporous Ge, *Appl. Phys. Lett.* 95, 013106 (2009)
- [16] Lee J.H., Grossman, J.C, J. Reed, G. Galli, Lattice thermal conductivity of nanoporous Si: Molecular dynamics study, *Appl. Phys. Lett.* 91, 223110 (2007)
- [17] J.E. Ni, E.D. Case, K.N. Khabir, R.C. Stewart, C.I. Wu, T.P. Hogan, E.J. Timm, S.N. Girard, M.G. Kanatzidis, Room temperature Young's modulus, shear modulus, Poisson's ratio and hardness of PbTe-PbS thermoelectric materials, *Mat. Sci. Eng. B*, 170, 58–66 (2010)
- [18] B. Houston, R.E. Strakna, H.S. Belson, Elastic constants thermal expansion and Debye temperature of lead telluride, *J. Appl. Phys.*, 39, 3913 - 3917 (1968)
- [19] N.G. Einspruch, R.J. Manning, Elastic constants of compound semiconductors ZnS, PbTe, GaSb, *J. Acoust. Soc. Am.*, 35, 215 - 216 (1963)
- [20] J.R. Groza, S.H. Risbud, K. Yamazaki, Plasma activated sintering of additive-free AlN powders to near-theoretical density in 5 minutes, *J. Mater. Res.*, 7, 2643 - 2645 (1992)

## 6.0 Fracture mode, microstructure, and temperature-dependent elastic moduli for thermoelectric composites of PbTe-PbS with SiC nanoparticle additions

Jennifer E. Ni<sup>1</sup>, Eldon D. Case<sup>1</sup>, Robert D. Schmidt<sup>1</sup>, Chun-I Wu<sup>2</sup>, Timothy Hogan<sup>2</sup>, Rosa Trejo<sup>3</sup>, Edgar Lara-Curzio<sup>3</sup>, Steven N. Girard<sup>4</sup>, Mercuri G. Kanatzidis<sup>4</sup>

<sup>1</sup>Chemical Engineering and Materials Science and <sup>2</sup>Electrical and Computer Engineering, Michigan State University, East Lansing, MI, 48824

<sup>3</sup>High Temperature Materials Laboratory, Oak Ridge National Laboratory, Oak Ridge TN 37380

<sup>4</sup>Department of Chemistry, Northwestern University, Evanston, IL, 60208

### Abstract

Twenty-six  $(\text{Pb}_{0.95}\text{Sn}_{0.05}\text{Te})_{0.92}(\text{PbS})_{0.08}$ -0.055%  $\text{PbI}_2$ -SiC nanoparticle ( $\text{SiC}_{\text{np}}$ ) composite thermoelectric specimens were hot pressed or pulsed electric current sintered (PECS) from powders that were dry milled, wet milled, or a combination of dry and wet milled. The Young's modulus,  $E$ , and Poisson's ratio,  $\nu$ , were measured by resonant ultrasound spectroscopy (RUS) as a function of temperature,  $T$ , from room temperature to 663 K. Also, porosity-induced bloating was monitored (1) indirectly through  $E$  versus  $T$  measurements (2) directly via observation of fracture surfaces (scanning electron microscopy) or (3) by measurements of volume change. For hot pressed specimens, an observed hysteresis in  $E$  versus  $T$  for  $T > 603$  K was attributed to bloating. For two hour post-densification anneals up to 936 K, seven out of seven specimens densified by PECS from dry milled powders showed no observable bloating, but post densification annealing increased the porosity of three hot pressed and three PECS specimens, likely via bloating.  $\text{SiC}_{\text{np}}$  additions (1 to 3.5 vol %) changed the fracture mode from intergranular to transgranular, and inhibited grain growth.  $\text{SiC}_{\text{np}}$  additions limited bloating in the wet milled PECS specimens yet led to limited bloating in the dry milled specimens at high temperatures.

Keywords: Elastic properties; Porosity; Thermoelectric; Nanocomposites

### 6.1.0 Introduction

Thermoelectric (TE) materials undergo numerous thermal cycles during waste heat recovery applications. However, it has been reported recently that thermoelectric materials, including CoSb<sub>3</sub>-based n-type skutterudite, FeSb<sub>3</sub>-based p-type skutterudite [Schmidt 2012, Schmidt DOI 2012] and PbTe-PbS [Ni DOI 2012 ] can undergo bloating at elevated temperatures, where bloating refers to a process observed in a variety of solids in which there is a temperature-dependent generation of pores within a dense specimen that is caused by internal gas evolution [Oppenheimer 2010] and/or solid or liquid decomposition reactions [Low 1981, Colombo 2006, O'Brien 1985, Wen 2011] during heating. Such an instability of microstructure in a thermoelectric could lead to porosity-dependent decreases in thermal and electrical conductivity [Jung 2011, Lee 2010, Alvarez 2010] which in turn could affect the figure of merit, ZT, where

$$ZT = \frac{S^2 \sigma_e T}{k} \quad (6.1)$$

where S is the Seebeck coefficient,  $\sigma_e$  is the electrical conductivity, T is the temperature and k is the thermal conductivity. In addition to  $\sigma_e$  and k, other porosity-dependent thermal and electrical properties include thermal diffusivity [Park 2009], the dielectric constant [Geis 2002, Hoepfner 2002, Yang 2010] and dielectric breakdown voltage [Geis 2002, Kishimoto 1991]. In addition, porosity-dependent mechanical properties include fracture strength [Park 2009, Hu 2010], internal friction [Wang 2000], fracture surface energy [Vandeperre 2004, Case 1981], hardness [Hoepfner 2003], Young's modulus [Ni 2009, Ren 2009 HA] and shear modulus [Ni 2009, Ren 2009 HA]. Since porosity affects a broad spectrum of physical properties, pores

generated by bloating have the potential to significantly affect the performance and mechanical integrity of thermoelectrics.

$(\text{Pb}_{0.95}\text{Sn}_{0.05}\text{Te})_{0.92}(\text{PbS})_{0.08}$ -0.055%  $\text{PbI}_2$  has a maximum ZT of 1.5 at 642 K

[Androulakis 2007] making it a candidate for waste-heat recovery applications. For TE materials used in harvesting waste energy, the temperature-dependent Young's modulus,  $E(T)$ , Poisson's ratio,  $\nu(T)$ , and thermal expansion,  $\alpha(T)$ , are required for both analytic and finite element analysis of stress,  $\sigma$ , induced by thermal gradients or thermal transients, such that

$$\sigma(T) = \frac{E(T)\alpha(T)\Delta T}{(1-\nu(T))} \quad (6.2)$$

where  $\Delta T$  is the temperature gradient or the temperature change experienced during a thermal transient.

In this study, the temperature-dependent Young's modulus,  $E(T)$ , shear modulus,  $G(T)$ , and Poisson's ratio,  $\nu(T)$ , of the  $(\text{Pb}_{0.95}\text{Sn}_{0.05}\text{Te})_{0.92}(\text{PbS})_{0.08}$ -0.055%  $\text{PbI}_2$  -SiC nanoparticle ( $\text{SiC}_{\text{np}}$ ) composites were measured using resonant ultrasound spectroscopy (RUS), from room temperature to a maximum of 663 K. In addition to the  $E(T)$  and  $\nu(T)$  measurements, bloating was monitored for twenty-six PbTe-PbS-SiC nanocomposite specimens (1) indirectly by analyzing the hysteresis in  $E(T)$  when it is present (Section 6.4.3.2), (2) directly by measuring the volume change after post-densification annealing using micrometers (Section 6.4.2.3), or (3) directly by observing the fracture surfaces (scanning electron microscopy, SEM) (Section 6.4.2.4).

Also in this study, a combination of dry milling and pulsed electric current sintering (PECS) successfully limited bloating in PbTe-PbS after post-densification annealing for two hours at

temperatures up to 936 K. A maximum annealing temperature,  $T_{\text{ann max}}$ , of 936 K was selected since  $T_{\text{ann max}}$  exceeds the likely maximum use temperature for PbTe-PbS (8%) [Androulakis 2007] by roughly 200 K to 300 K. Also, the addition of SiC nanoparticles changed the fracture mode and inhibited grain growth.

## 6.2.0 Background: Nanostructures in thermoelectric materials

Thermoelectric nanocomposites are typically formed (i) by precipitation or spinodal decomposition from the bulk [Johnsen 2011, Kanatzidis 2010] or (ii) by the addition of a powder nanoparticle phase during powder processing [Li 2006, Liu 2011, Li 2011, Xiong 2009]. The nanostructures reduce the lattice thermal conductivity by phonon scattering, which in turn increases the figure of merit, ZT (Eq. (6.1)) [Johnsen 2011, Kanatzidis 2010]. For example, ZT improved by 10 % to 36 % for thermoelectrics with nanoparticle additions of 0.1 vol % [Liu 2011] and 0.24% SiC [Li 2006], 0.1 vol %  $\text{Al}_2\text{O}_3$  [Li 2011], and 0.4 vol%  $\text{TiO}_2$  [Xiong 2009].

In general, nanoparticles also affect mechanical properties such as fracture toughness in nanocomposite WC– $\text{ZrO}_2$ –Co [Mukhopadhyay 2010], carbides [Karakasidis 2011, Voevodin 2000], borides [Karakasidis 2011, Voevodin 2000] and oxides [Karakasidis 2011, Voevodin 2000]. Nanoparticle inclusions from 1.0 vol% [Karakasidis 2011] to 10.0 vol% [Mukhopadhyay 2010] either increase or decrease the fracture toughness,  $K_{\text{C}}$ , of brittle materials has been attributed to a transition of the fracture mode from intergranular to transgranular [Yamada 2010].

For thermoelectric materials in particular,  $\text{SiC}_{\text{np}}$  nanoparticle additions of 0.24 vol% to  $\text{Bi}_2\text{Te}_3$  increased ZT (Eq. (6.1)) by 18% [Li 2006]. Also, additions of 0.1 vol%  $\text{SiC}_{\text{np}}$  to

$\text{Bi}_{0.5}\text{Sb}_{1.5}\text{Te}_3$  increased the ZT, fracture toughness and hardness, each by roughly 10% [Liu 2011]. Zhao et al. [Zhao 2008] added from 0.1 vol% to 1.2 vol%  $\text{SiC}_{\text{np}}$  to PECS-processed  $\text{Bi}_2\text{Te}_3$ , resulting in maximum increases of 30% in E, a 28% in hardness, and an 18 % in fracture toughness, although ZT decreased for the  $\text{SiC}_{\text{np}}$  loadings that gave the optimal mechanical properties. However, despite the numerous studies focused on the effect of nanostructures on the transport properties of thermoelectrics, the work by Liu [Liu 2011] and Zhao [Zhao 2008] are the only studies currently in the literature that deal with the effects of nanoparticle additions on mechanical properties of thermoelectrics.

### 6.3.0 Experimental Procedure

Cast  $(\text{Pb}_{0.95}\text{Sn}_{0.05}\text{Te})_{0.92}(\text{PbS})_{0.08-0.055\%}$   $\text{PbI}_2$  (PbTe-PbS) ingots were fabricated from  $\text{PbI}_2$ , Pb, Te, SnTe and PbS powders, each of which were at least 99.99% pure [Ni 2010]. The cast ingots were crushed and ground using a mechanical mortar and pestle until all the powders passed through a 53-micron sieve [Ni 2010, Pilchak 2007]. The powder size was then further reduced using a planetary mill (PM100, Retsch, Newtown, PA) by (i) dry milling, (ii) wet milling with ethanol or (iii) dry and wet milling with hexane (Table 6.1). All powder processing took place inside a glove box under an argon atmosphere.

Composite thermoelectric specimens were fabricated using 1.0 to 3.5 volume percent nanoparticles of 95% pure beta SiC (Nanostructured & Amorphous Materials, Inc., Houston, TX), with a vendor-specified average particle size of 50 nm to 60 nm. The milled PbTe-PbS powders and  $\text{SiC}_{\text{np}}$  powders were first homogeneously mixed by planetary milling for three hours

Table 6.1 The processing conditions for twenty-six  $(\text{Pb}_{0.95}\text{Sn}_{0.05}\text{Te})_{0.92}(\text{PbS})_{0.08}$ -0.055%  $\text{PbI}_2$  specimen included in this study. Using resonant ultrasound spectroscopy, the temperature-dependent elastic moduli  $(E(T))$  were measured for twelve specimens and the room-temperature elastic moduli as a function of porosity  $(E(P))$  were measured for four specimens. The microstructure (M) was examined using scanning electron microscopy for 15 specimens.

Specimen Label	SiC <sub>np</sub> Vol%	Powder Processing Technique	Sintering Max Temperature/ Pressure/ Time	Measurement technique
PECS-05	0.0	D/WM (H)	823 K /60 MPa/20 min	E(P)
PECS-32	0.0	DM	623 K /60 MPa/5 min	E(P)
PECS-33	0.0	DM	573 K /60 MPa/5 min	E(P)
PECS-35	0.0	DM	493 K /60 MPa/5 min	E(P)
HP-53 #A	0.0	D/WM (H)	723 K/74.4 MPa/120 min	$E(T)^b$ , M
HP-53 #B	0.0	D/WM (H)	723 K/74.4 MPa/120 min	$E(T)^b$
HP-53 #C	0.0	D/WM (H)	723 K/74.4 MPa/120 min	$E(T)^b$
HP-54 #1	0.0	D/WM (H)	723 K/74.4 MPa/120 min	$E(T)^b$ , M
HP-54 #2	0.0	D/WM (H)	723 K/74.4 MPa/120 min	$E(T)^b$ ,
HP-55 #1	0.0	WM (E)	723 K/74.4 MPa/120 min	$E(T)^b$ , M
HP-55 #2	0.0	WM (E)	723 K/74.4 MPa/120 min	$E(T)^b$
PECS-01	0.0	D/WM (H)	823 K /60 MPa/20 min	$E(T)^b$
PECS-06S <sup>a</sup>	0.0	DM	823 K /60 MPa/22 min	$E(T)^b$
PECS-02	0.0	WM (E)	823 K /60 MPa/20 min	M
PECS-10	0.0	D/WM (H)	673 K /60 MPa/20 min	M
PECS-11	0.0	DM	823 K /60 MPa/20 min	M
PECS-15	0.0	DM	673 K /60 MPa/20 min	M
PECS-20	0.0	DM	723 K /60 MPa/20 min	M
PECS-23	0.0	DM	723 K /60 MPa/20 min	M
PECS-25	0.0	DM	823 K /60 MPa/20 min	M
PECS-27	0.0	DM	823 K /60 MPa/20 min	M
PECS -06	1.0	D/WM (H)	823 K /60 MPa/20 min	$E(T)^b$ , M
PECS-18	2.0	DM	673 K /60 MPa/20 min	$E(T)^b$ , M
PECS-16	2.5	DM	673 K /60 MPa/20 min	M
PECS-17	3.0	DM	673 K /60 MPa/20 min	M
PECS-07 <sup>a</sup>	3.5	D/WM (H)	823 K /60 MPa/20 min	$E(T)^b$

<sup>a</sup> Disc shaped specimen. All other specimens in the study were parallelepipeds.

<sup>b</sup> Room-temperature elastic moduli for these specimens was reported in a previous paper, this study reports on the temperature-dependent elastic moduli

at 150 rpm then densified (Table 6.1) using either hot pressing, HP, (HP200, Thermal Technology LLC, Santa Rosa, CA) or pulsed electric current sintering, PECS, (SPS 10-4, Thermal Technology LLC, Santa Rosa, CA). Further details of the specimen fabrication processes are available elsewhere [Ni 2010, Ren 2009 LAST, Ni DOI 2012].

The specimen mass and dimensions were measured using a micrometer and an electronic balance to calculate the mass density. The micrometer and electronic balance were calibrated using blocks and test gauges, respectively [Ni DOI 2012].

Using a non-destructive method, resonant ultrasound spectroscopy (RUS) [Ren 2009 LAST, Ren 2008, Migilori 1997], the Young's modulus,  $E$ , shear modulus,  $G$ , and Poisson's ratio,  $\nu$ , were determined at room temperature and high temperature. The elastic moduli were calculated using commercially available software packages (RUSpec and CylModel, Quasar International, Inc., Albuquerque, NM) from the dimensions, mass density and resonant frequencies of the specimen. Further details of the RUS procedure are available elsewhere [Ren 2009 LAST, Ren 2008].

The RUS mechanical resonance spectra were taken at 30 K temperature intervals from room temperature to maximum temperatures of 543 K, 603 K, or 663 K. The heating and cooling rates were 5 K/minute for each thermal cycle. Both the as-densified specimens and the post-densified specimens were annealed in flowing argon for two hours at temperatures from 693 K to 936 K. The temperature-dependent changes in specimen dimension were accounted for using the coefficient of thermal expansion of  $21.5 \times 10^{-6} \text{ K}^{-1}$  obtained from dilatometric and x-ray diffraction measurements for PbTe-PbS specimens with chemical compositions that were nominally identical to the specimens in this study [Ni to be submitted].

SEM micrographs of the internal fractured surfaces were used to (1) monitor the changes

in porosity due to bloating and (2) measure average grain size (Table 6.1). The surface areal fraction of pores was approximated from the number of pores and the mean pore area determined from SEM micrographs. The average grain size was determined using the linear intercept method [Fullman 1953, Ni 2010].

In order to determine the effect of  $\text{SiC}_{\text{np}}$  on the grain growth of the PbTe-PbS matrix due to post-densification annealing (Section 6.4.2.3), we first determined a statistically sufficient number of micrographs per specimen,  $N$ , to reduce the uncertainty in grain size measurement to the point that grain growth trends (if any) were apparent. In order to calculate the sample size,  $N$ , a grain size,  $GS$ , distribution must be determined. For both metallic and ceramic polycrystalline materials a lognormal grain size distribution is often reported [Zhu 2005, Berbenni 2007, Betz 2000]. Assuming a lognormal distribution for the PbTe-PbS matrix in our PbTe-PbS- $\text{SiC}_{\text{np}}$  composites we determined  $N$  using a lognormal 95% confidence interval for the mean  $GS$  [Limpert 2001]

$$\left( \overline{GS}^* / s^{*2}, \overline{GS}^* \left( s^{*2} \right) \right) = (LL, UL) \quad (6.3a)$$

where

$$\overline{GS}^* = \exp \left( \frac{1}{N} \sum_{i=1}^N \log(GS_i) \right) = \left( \prod_{i=1}^N GS_i \right)^{\frac{1}{N}} \quad (6.3b)$$

and

$$s^* = \exp \left( \left[ \frac{1}{N-1} \sum_{i=1}^N \left[ \log \left( \frac{GS_i}{\overline{GS}^*} \right) \right]^2 \right]^{\frac{1}{2}} \right). \quad (6.3c)$$

Table 6.2a A comparison of the as-densified specimens mean grain sizes,  $G_{SDNS}$ , for different powder processing (dry milling (DM), wet milling (WM), and dry and wet milling (D/WM)) and sintering techniques (hot pressed (HP) and PECS-processed). The difference in powder processing is the likely cause of the factor of two difference between the four wet milled hot pressed and PECS processed specimens and six dry milled PECS-processed specimens. The PECS specimens were sintered at the stated temperature for 20 minutes. For the as-densified dry milled PECS-processed specimens, the mode-mixity was calculated as the areal fraction of the transgranular grains appearing on a specimen's fracture surface. In general, as the mode mixity increased to 1.0, transgranular fracture dominates and the fracture toughness increases.

<b>Specimen Label</b>	<b>SiC<sub>np</sub> additions</b>	<b>Powder Processing Technique</b>	<b>Sintering temperature</b>	<b><math>G_{SDNS}</math> (microns)</b>	<b>Mode-mixity</b>	<b>Reference</b>
HP-53	0.0 vol%	D/WM (H)	723 K	$1.6 \pm 0.1$	0.11	This study
HP-54	0.0 vol%	D/WM (H)	723 K	$1.6 \pm 0.1$	0.10	This study
HP-55	0.0 vol%	WM (E)	723 K	$1.7 \pm 0.2$	0.12	This study
PECS-01	0.0 vol%	D/WM (H)	823 K	$2.1 \pm 0.2$	0.15	This study
PECS-15	0.0 vol%	DM	673 K	$4.9 \pm 0.4$	0.18	This study
PECS-20	0.0 vol%	DM	723 K	$4.8 \pm 0.2$	0.14	This study
PECS-27	0.0 vol%	DM	823 K	$4.9 \pm 0.3$	0.13	This study
PECS-18	2.0 vol%	DM	673 K	$4.7 \pm 0.2$	0.91	This study
PECS-16	2.5 vol%	DM	673 K	$4.7 \pm 0.3$	0.95	This study
PECS-17	3.0 vol%	DM	673 K	$4.5 \pm 0.2$	0.96	This study

Table 6.2b Mean grain sizes of the as-densified and the annealed specimens are designated by  $GS_{DNS}$  and  $GS_{ANN}$ , respectively. For dry milled PECS-processed specimens with 0.0 vol%  $SiC_{np}$ , the  $GS_{ANN}$  increased in three specimens after post-densification anneals up to 936 K. However, the inclusion of  $SiC_{np}$  limited grain growth in three specimens during post-densification anneals up to 873 K.

Specimen Label	$SiC_{np}$ additions	Sintering temperature <sup>a</sup>	Annealing temperature	$GS_{DNS}$ (microns)	$GS_{ANN}$ (microns)	$GS_{ANN}/GS_{DNS}$
PECS-15	0.0 vol%	673	723 K	$4.9 \pm 0.4$	$5.9 \pm 0.2$	1.2
PECS-20	0.0 vol%	723	723 K	$4.8 \pm 0.2$	$5.9 \pm 0.4$	1.2
PECS-27	0.0 vol%	823	723 K	$4.9 \pm 0.3$	$5.9 \pm 0.2$	1.2
PECS-15	0.0 vol%	673	873 K	$4.9 \pm 0.4$	$6.4 \pm 0.1$	1.3
PECS-20	0.0 vol%	723	873 K	$4.8 \pm 0.2$	$6.4 \pm 0.1$	1.3
PECS-27	0.0 vol%	823	873 K	$4.9 \pm 0.3$	$6.6 \pm 0.1$	1.3
PECS-15	0.0 vol%	673	936 K	$4.9 \pm 0.4$	$6.9 \pm 0.1$	1.4
PECS-20	0.0 vol%	723	936 K	$4.8 \pm 0.2$	$7.0 \pm 0.2$	1.5
PECS-27	0.0 vol%	823	936 K	$4.9 \pm 0.3$	$6.9 \pm 0.1$	1.4
PECS-18	2.0 vol%	673	723 K	$4.7 \pm 0.2$	$4.7 \pm 0.2$	1.0
PECS-16	2.5 vol%	673	723 K	$4.7 \pm 0.3$	$4.6 \pm 0.2$	1.0
PECS-17	3.0 vol%	673	723 K	$4.5 \pm 0.2$	$4.7 \pm 0.2$	1.0
PECS-18	2.0 vol%	673	873 K	$4.7 \pm 0.2$	$5.4 \pm 0.2$	1.1
PECS-16	2.5 vol%	673	873 K	$4.7 \pm 0.3$	$5.2 \pm 0.1$	1.1
PECS-17	3.0 vol%	673	873 K	$4.5 \pm 0.2$	$5.3 \pm 0.1$	1.2

<sup>a</sup>All specimens in this table were sintered at a maximum pressure of 60 MPa for 20 minutes

We proposed that a conservative estimate of the GS range of the PbTe-PbS matrix was 1 micron to 15 microns, the lower limit, LL, and upper limit, UL, respectively (Eq. (6.3a)). Ten ‘pilot studies’ conducted using randomly generated grain sizes (MatLab) between the LL and UL (Eqs. 6.3a – 6.3c) [CSTAT] determined that the statistically sufficient number of micrographs per specimen, N, was five. Thus, for every GS measurement reported in this study (Table 6.2a and 6.2b), five micrographs per specimen were analyzed at the same magnification (3000x).

#### 6.4.0 Results and Discussion

The key results presented in this study are: (1) the feasibility of tailoring the processing procedure to inhibit post-densification bloating and (2) characterizing mechanical properties, including elasticity measurements. Elasticity data is needed for designers to calculate stresses and strains in thermoelectric elements (Eq. (6.2)), which arise, for example, due to thermal transients incurred in waste heat recovery applications. Also, observed changes in the fracture mode and grain growth behavior are linked to both processing and mechanical behavior.

#### 6.4. Results and discussion

##### 6.4.1.1 Room temperature elasticity measurements of as-densified specimens

Room temperature RUS measurements of Young’s modulus, E, shear modulus, G, and Poisson’s ratio,  $\nu$ , were performed for three hot-pressed and six PECS-processed specimens (Figs. 6.1a and 6.1b). Fig. 6.1 includes data from two types of porosity (i) residual porosity  $P_R$ , from incomplete sintering of the as-densified specimens and (ii) porosity  $P_B$ , generated by bloating during post-densification annealing, where the total porosity  $P = P_R + P_B$ . The

Table 6.3 The least-squares fitting parameters  $E_{P=0}$  and  $b_{PE}$  (Eq. (6.4a)) and  $G_{P=0}$  and  $b_{PG}$  (Eq. (6.4b)) to the Young's modulus and shear modulus to the four as-densified and four post-densified specimens in Figure 6.1.

Fit to Eq. (6.3a)			Fit to Eq. (6.3b)		
$E_{P=0}$	$b_{PE}$	$r^2$	$G_{P=0}$	$b_{PG}$	$r^2$
$56.0 \pm 0.4$	$1.31 \pm 0.06$	0.990	$22.6 \pm 0.2$	$1.31 \pm 0.07$	0.984

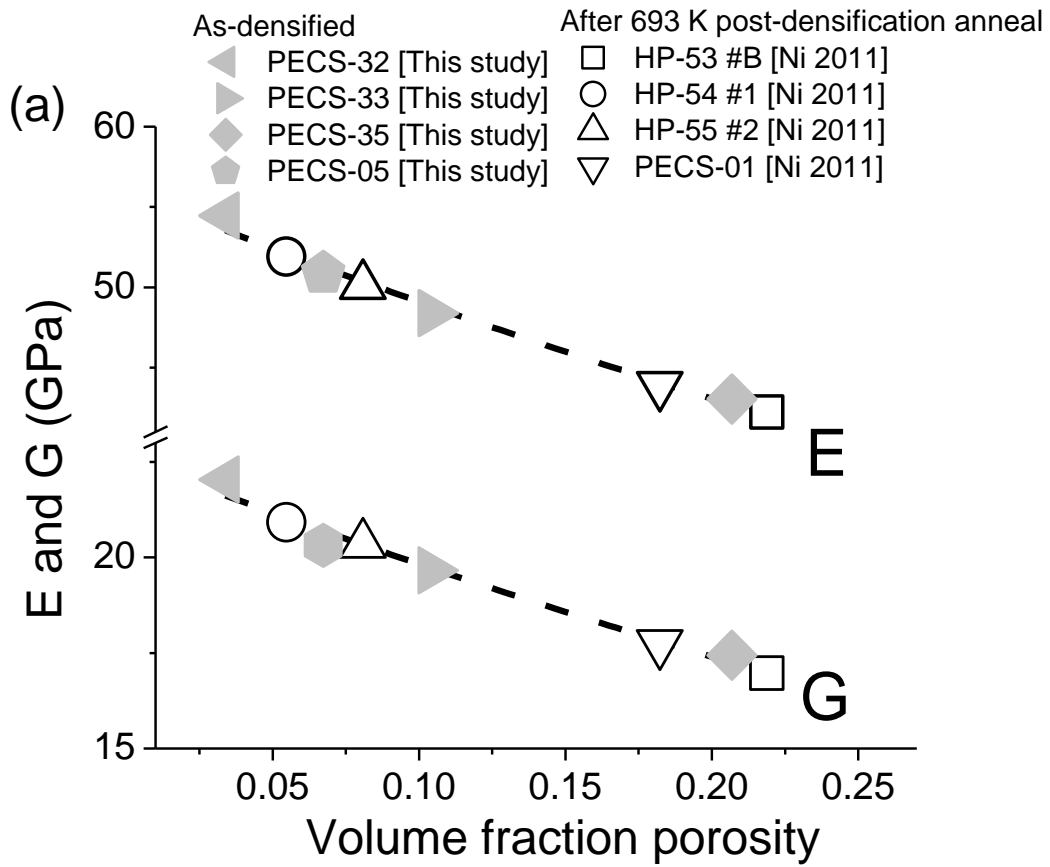


Fig 6.1

Fig. 6.1 (cont'd)

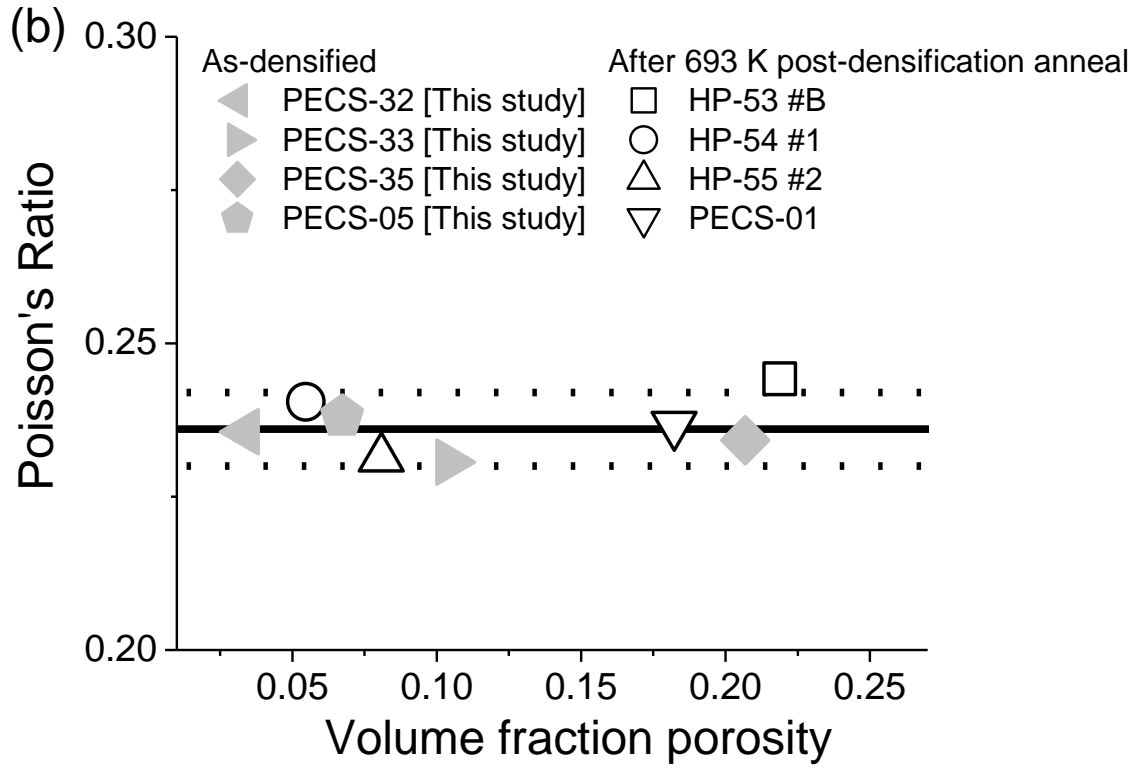


Fig. 6.1 (cont'd) The porosity dependence of the (a) Young's modulus,  $E$ , shear modulus,  $G$ , and (b) Poisson's ratio for four as-densified PECS-processed specimens (filled symbols) and four thermally annealed hot pressed and PECS-processed specimens with 0.0 vol%  $\text{SiC}_{\text{np}}$ . Each individual specimen is represented by the same symbol in figure (a) and (b). The least-squares fit to Eq. (6.4a) to these 8 specimens is represented by the dashed line. The solid line and dotted lines represent the average and standard deviation in Poisson's ratio, respectively.

porosity-dependent E and G behaviors for  $P = P_R + P_B$  are consistent with the empirical E and G versus porosity relationships (Table 6.3) [Rice 1998],

$$E(P) = E_{P=0} \exp(-b_P E P) \quad (6.4a)$$

$$G(P) = G_{P=0} \exp(-b_P G P) \quad (6.4b)$$

where  $P_B = 0$  for specimens that have not bloated. Four as-densified specimens, sintered via PECS from 493 K to 823 K had residual porosities,  $P_R$ , of  $0.03 < P_R < 0.21$  (Fig. 6.1). An additional four specimens were annealed to 693 K [Ni DOI 2012].

In contrast to E and G, Poisson's ratio,  $\nu$ , was relatively insensitive to porosity (Fig. 6.1b), with a mean and standard deviation value  $0.236 \pm 0.006$  over the entire range of P included in this study (Fig. 6.1b). These results are consistent with a review by Boccaccini in which Poisson's ratio is independent of P for a number of brittle materials with  $\nu$  near 0.25 [Boccaccini 1994].

#### 6.4.1.2 Microstructure of as-densified fracture surfaces

The as-densified HP and PECS-processed PbTe-PbS specimens fracture surfaces included residual spherical or quasi-spherical pores from submicron to 3 microns in diameter located at grain boundaries and triple points (Figs. 6.2 and 6.3).

The mean grain size of the hot pressed and the PECS processed specimens fabricated from milled and dry/wet milled powders was  $1.6 \pm 0.2$  microns (Table 6.2a), which is about 2.5 times smaller than the mean grain size of  $4.5 \pm 0.2$  to  $4.9 \pm 0.4$  microns for the specimens densified via PECS from powders that were dry milled only (Table 6.2a). This difference between the mean grain sizes of the DM and WM specimens is likely due the smaller grindability limit for wet

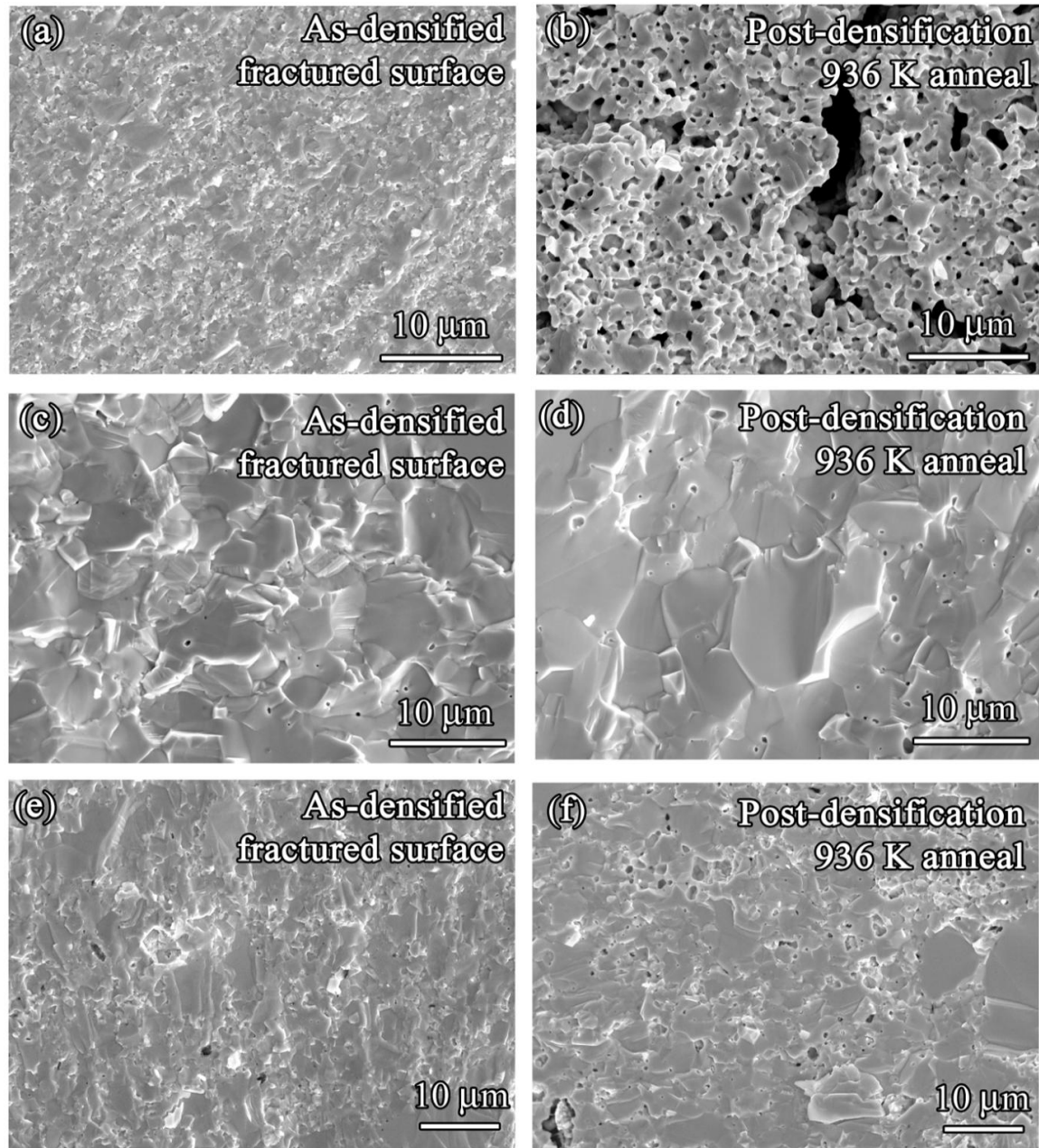


Fig. 6.2 The as-densified and post-densification fracture surfaces of (a, b) D/WM PECS-10, (c, d) DM PECS-20 and (e, f) DM PECS -18 (with 2.0 vol% SiC<sub>np</sub>). Few pores are evident in the SEM micrographs of the as-densified fracture surfaces. Annealing at 936 K for 2 hours resulted in bloating for (b) D/WM PECS-10 and (f) DM PECS -18 (with 2.0 vol% SiC<sub>np</sub>) specimens as evidenced by the increased porosity of the internal fracture surface while, in contrast, the (d) DM PECS-20 specimen did not bloat after annealing under identical conditions.

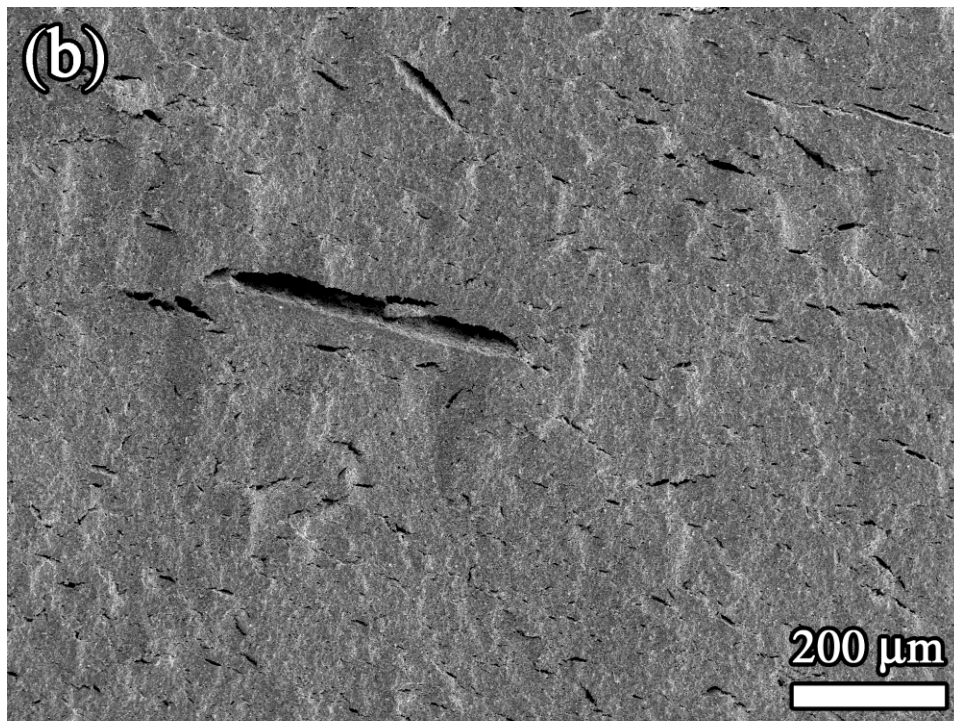
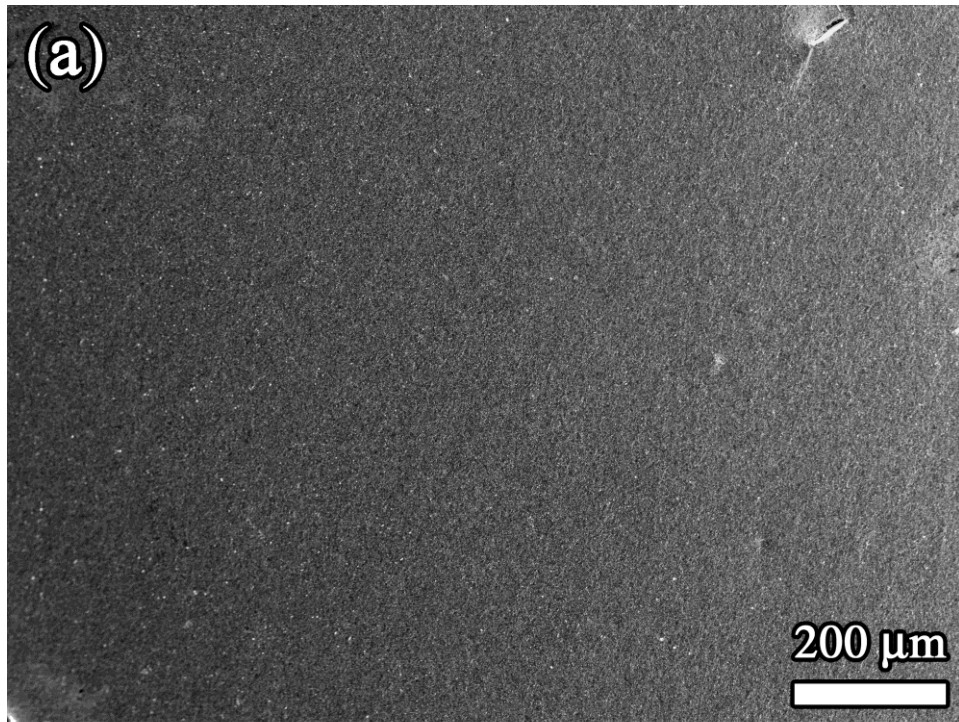


Fig. 6.3 The (a) as-densified and (b) post-densification fracture surfaces of PECS-10. After post-densification annealing to 936 K for 2 hours, long lenticular pores were observable on the fresh fracture surface of D/WM PECS-10.

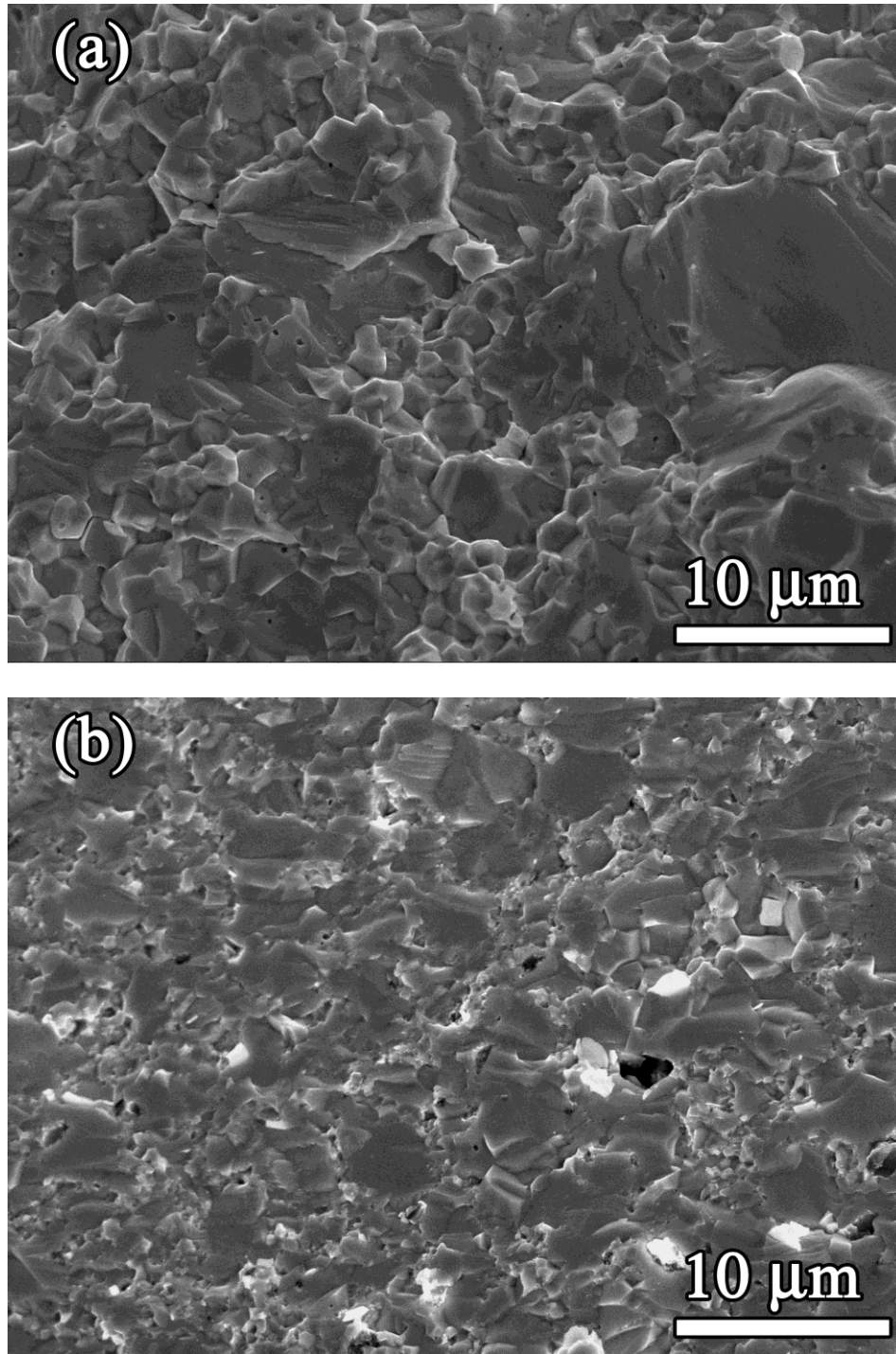


Fig. 6.4 The (a) fracture surfaces of the specimen without added SiC<sub>np</sub>, PECS-15, exhibits a much higher fraction of intergranular fracture than (b) the specimen with 2.5 vol% SiC<sub>np</sub>, PECS-16 (Table 6.2a). Both specimens were PECS-processed at 673 K for 20 minutes using a pressure of 60 MPa.

milled powders compared to dry milled powders [Hall 2109].

The literature shows that fine-grained brittle materials can be densified using short PECS processing times, however during PECS processing grain growth may not be a strong function of the sintering temperature [Xu 2012, Yoshida 2011, Teber 2012, Kim 2007]. For example, Teber sintered TiC specimens via PECS for five minutes at T between 1623 K and 1923 K with a resulting mean grain size range from only 0.43 microns to 0.76 microns [Teber 2012]. Consistent with the Teber et al. results, in this study the mean grain sizes for the six as-densified DM PECS composite specimens (with 0.0, 2.0, 2.5, and 3.0 vol% SiC<sub>np</sub>) were essentially independent of the sintering temperature (Table 6.2a) when sintered at T from 673 K to 823 K. Also, the mean grain size was independent of the volume fraction of SiC<sub>np</sub>.

The fracture mode observed for the PbTe-PbS-SiC<sub>np</sub> was a function of the SiC<sub>np</sub> loading. For specimens with 0 vol% SiC<sub>np</sub> the fracture mode was predominantly intergranular (Fig. 6.4a) while for specimens that included SiC<sub>np</sub> additions, the fracture mode was mostly transgranular (Table 6.2b and Fig. 6.2b). The effect of SiC<sub>np</sub> additions on the fracture mode will be discussed in the following section.

#### 6.4.1.3 Mechanical property implications of SiC<sub>np</sub> additions

In this study, the fracture mode shifted from intergranular to transgranular as a function of the volume fraction loading of SiC<sub>np</sub> (Table 6.2a and Fig. 6.4). Adding nanoparticles to brittle materials has been observed to result in similar dramatic shifts in the fracture mode that are associated with changes in fracture toughness,  $K_{IC}$ , where  $K_{IC}$  may either increase [Kawabata

1977, Mukhopadhyay 2010, Karakasidis 2011] or decrease [Karakasidis 2011, Jang 2010, Yamada 2010].

Vickers indentation was used to attempt to directly determine whether or not the observed change in fracture mode was accompanied by a change in  $K_C$  for the PbTe-PbS-SiC<sub>np</sub> specimens included in this study. However, Vickers indentation loads of 2.94 N and 4.90 N failed to produce radial cracks, a 9.81 N load generated radial cracks 150 microns long that radiated from the sides rather than the corners of the indentation impression and a 19.6 N load fractured the specimen. Thus, although the SiC<sub>np</sub> addition to PbTe-PbS did result in a shift in fracture mode (Table 6.2a and Fig. 6.4), the lack of a well-developed radial crack system made it impossible to use the Vickers indentation technique to determine  $K_C$ .

#### 6.4.2 Room temperature microstructure and elastic moduli analysis following post-densification annealing

In this study, three independent methods were used to study bloating in the PbTe-PbS specimens: (1) direct measurements via micrometer of specimen volume before and after post-densification annealing (Section 6.4.2.1), (2) direct measurements of porosity on fracture surfaces as observed on SEM micrographs of internal fracture surfaces of annealed specimens (4.2.4), and (3) indirect measurements via elasticity measurements at room temperature as a function of annealing temperature (Section 6.4.2.3.) and temperature-dependent elasticity measurements taken during thermal cycling (Section 6.4.3).

##### 6.4.2.1 Volume change after post-densification annealing

Although the mass of each of the densified specimens in this study did not change following

RUS measurements to temperatures up to 663 K, a volume change greater than 0.7% did occur for the four hot pressed PbTe-PbS specimens annealed at temperatures higher than 603 K (Table 6.4). None of the PECS-processed specimens had a volume change greater than 0.4% (Table 6.4). The volume of specimen PECS-06S decreased by 1.8% which was likely due to further densification since the post-densification annealing temperature of 663 K was higher than the densification temperature of 623 K.

Although while specimen volume changes during annealing could be in principle produced by either microcracking or bloating, a volume change measurable with a micrometer is likely caused by bloating during post-densification annealing rather than microcracking, since the strains induced by microcrack crack opening displacements (CODs) are quite small. As discussed by Wilson [Wilson 1993] and Liu [Liu 1991, Liu 1992], microcrack-induced strains in Mg-PSZ and 3Y-TZP ranged from  $10 \times 10^{-6}$  to  $80 \times 10^{-6}$  [Wilson 1993, Liu 1991, Liu 1992]. For a comparable range of strain, the PbTe-PbS specimens included in this study would experience dimension changes of roughly 0.02 microns to 1.6 microns. In addition, for polycrystalline YCrO<sub>3</sub> with a mean microcrack COD of 25 nm (determined by small angle neutron scattering [Case 1984]) and given the volumetric crack number density in YCrO<sub>3</sub> the corresponding dimensional change would be roughly 0.2 microns. Thus in these examples, the dimensional changes induced by microcracking damage are too small to be resolved using a micrometer. However, the volume changes observed by the external micrometer measurements are consistent with the internal porosity changes observed via SEM for the specimens in this study.

Table 6.4 The relative volume change twelve specimens for each HT-RUS heating/cooling cycle.

<b>Specimen Label<sup>a</sup></b>	<b>SiCnp Additions</b>	<b>Powder Processing</b>	<b>Sintering Max Temp/Pressure</b>	<b>HT-RUS Temperature Range (K)</b>	<b>Relative Volume change</b>	<b>Bloated?</b>
HP-53 #A	0.0 vol%	D/WM (H)	723 K / 74.4 MPa	293 - 603	0.018	Yes
HP -55 #1	0.0 vol%	WM (E)	723 K /74.4 MPa	293 - 663	0.016	Yes
HP-53 #C-TC2	0.0 vol%	D/WM (H)	723 K /74.4 MPa	293 - 603	0.007	Yes
HP -54 #2	0.0 vol%	D/WM (H)	723 K /74.4 MPa	293 - 663	0.007	Yes
HP -55 #2	0.0 vol%	WM (E)	723 K /74.4 MPa	293 - 603	0.005	No
PECS-06S-TC1	0.0 vol%	DM	823 K /60 MPa	293 - 603	0.004	No
HP-53 #B	0.0 vol%	D/WM (H)	723 K /74.4 MPa	293 - 543	0.003	No
HP -54 #1	0.0 vol%	D/WM (H)	723 K /74.4 MPa	293 - 603	0.001	No
PECS-07-TC2	3.5 vol%	D/WM (H)	823 K /60 MPa	293 - 663	0.001	No
PECS-06	1.0 vol%	D/WM (H)	823 K /60 MPa	293 - 603	0.000	No
PECS-07-TC1	3.5 vol%	D/WM (H)	823 K /60 MPa	293 - 603	0.000	No
HP-53 #C-TC1	0.0 vol%	D/WM (H)	723 K /74.4 MPa	293 - 543	-0.003	No
PECS-18	2.0 vol%	DM	673 K /60 MPa	293 - 663	-0.004	No
PECS-06S-TC2	0.0 vol%	DM	823 K /60 MPa	293 - 663	-0.018	No
PECS-01	0.0 vol%	D/WM (H)	823 K /60 MPa	293 - 603	NA <sup>b</sup>	No

<sup>a</sup> For specimens with more than one thermal cycle TC- 1 denotes the first thermal cycle and TC- 2 denotes the second thermal cycle.

<sup>b</sup> Volume not measured after HT-RUS

#### 6.4.2.2 Bloating-induced porosity generated by post-densification annealing

Following the two hour post-densification anneals in flowing argon for temperatures up to 936 K, fresh internal fracture surfaces of fifteen hot pressed and PECS processed PbTe-PbS-SiC<sub>np</sub> nanocomposite specimens were examined by SEM (Table 6.1, Fig. 6.2). The seven as-densified PECS processed dry milled (DM) only PbTe-PbS specimens did not bloat after a two hour anneal up to 936 K (Table 6.1, Figs. 6.2c and 6.2d).

However, one wet milled (WM) PECS-processed and three dry/wet milled (D/WM) PECS-processed specimens did bloat, generating (i) spherical and quasi-spherical pores 1 to 5 microns in diameter (Fig. 6.2b) and (ii) lenticular pores from 10 microns in length and 1 micron wide (Fig. 6.2b) to about 400 microns in length and 50 microns wide (Fig. 6.3). Bloating in the WM and D/WM PECS-processed specimens (Figs. 6.2b and 6.3b) and a lack of bloating in DM PECS-processed specimens (Fig. 6.2d) indicates that the wet milling process may leave a residue on the powder particle surface which decomposes during annealing, causing bloating.

#### 6.4.2.3 Effect of SiC<sub>np</sub> additions on bloating and grain growth

In this study, specimens that were annealed following densification were examined to determine the effect of nanoparticle additions on both (i) bloating (porosity) and (ii) grain growth. The relative change in volume fraction porosity,  $\Delta P$ , the associated change in Young's modulus,  $\Delta E$ , were calculated using

$$\Delta P = \left| \frac{P_{As-D} - P_{Ann}}{P_{As-D}} \right| \text{ and } \Delta E = \left| \frac{E_{As-D} - E_{Ann}}{E_{As-D}} \right| \quad (6.5)$$

where  $P_{As-D}$  and  $E_{As-D}$  are the P and E for the as-densified specimens, respectively, and  $P_{Ann}$

and  $E_{Ann}$  are the P and E for the specimens after a post-densification annealed, respectively, where E was obtained by room temperature RUS measurements. Three dry/wet milled PECS specimens (PECS-01, -06, and -07), each of which were densified at 823 K with 60 MPa for 20 minutes (Table 6.1), were subsequently annealed at 693 K (1 minute hold time) with heating and cooling rates of 2 K/min (Table 6.5). PECS-01 had 0.0 vol%  $SiC_{np}$ , PECS-06 had 1.0 vol%  $SiC_{np}$ , and PECS-07 had 3.5 vol%  $SiC_{np}$  (Table 6.5).  $SiC_{np}$  additions to the dry/wet milled PECS specimens reduced but did not eliminate bloating, since after annealing, PECS-01 (Table 6.5),  $\Delta P$  was 1.25 (Eq. (6.5)) and  $\Delta E$  was 0.12 (Eq. (6.5)), where E was measured by RUS and P was measured using micrometers.

However for both PECS-06 and -07 (Table 6.5)  $\Delta P$  was roughly 0.25 (Eq. (6.5)) and  $\Delta E$  was about 0.02 (Eq. (6.5)). Thus, both  $\Delta P$  and  $\Delta E$  were considerably lower for the wet milled/PECS processed nanocomposite specimens than the specimen without  $SiC_{np}$  additions, so the  $SiC_{np}$  limit the bloating observed in wet milled/PECS processed specimens. Nevertheless, the  $\Delta P$  and  $\Delta E$  values were very similar for each of the  $SiC_{np}$  loadings, which indicate that the extent of bloating may be relatively insensitive to the volume fraction of  $SiC_{np}$  added over the  $SiC_{np}$  range of 1.0 to 3.5 vol% used in this study. The decrease in bloating that resulted from  $SiC_{np}$  addition may be related to localized creep processes, since during bloating the local deformation that occurs at elevated temperature due to the high local gas pressure is likely a creep mechanism. However, it has been shown recently that Ce-based inclusions in  $CoSb_3$ -based skutterudites [Schmidt 2012] can limit grain boundary sliding and the associated anelastic drop-

Table 6.5 In this study, the inclusion of SiC<sub>np</sub> inhibited porosity (bloating) for PECS-processed PbTe-PbS specimens. After a post-densification anneal at 693 K for two hours, for the PbTe-PbS specimen without SiC<sub>np</sub>, PECS-01, the volume fraction porosity, P, however, for two specimens with SiC<sub>np</sub>, P increased only by 20%. E is the Young's modulus measured at room temperature using resonant ultrasound spectroscopy.

Specimen Label <sup>a</sup>	SiC <sub>np</sub> vol%	As-densified specimen		After 693 K post-densification anneal		Reference
		P	E (GPa)	P	E (GPa)	
PECS-01 <sup>b</sup>	0.0	0.08	50.3 ± 0.1	0.18	43.9 ± 0.1	[Ni 2011]
PECS -06 <sup>b</sup>	1.0	0.04	53.3 ± 0.1	0.05	52.3 ± 0.1	This study
PECS-07-TC2 <sup>c</sup>	3.5	0.05	56.2 ± 0.1	0.06	54.3 ± 0.1	This study

<sup>a</sup> PECS denotes pulsed electric current sintering

<sup>b</sup> Parallelepiped-shaped specimen

<sup>c</sup> Disc-shaped specimen

off in Young's modulus at elevated temperatures, thus the  $\text{SiC}_{\text{np}}$  in the PbTe-PbS specimens in this study may act similarly to inhibit creep locally and thus limit bloating.

Three PbTe-PbS specimens were each PECS processed for 20 minutes at 673 K with a pressure of 60 MPa (Table 6.1) from dry milled only powders with  $\text{SiC}_{\text{np}}$  loadings of 2.0, 2.5, and 3.0 volume percent and were subsequently annealed in flowing argon gas at 936 K for two hours. SEM observations of the annealed specimens showed that in contrast to the DM PECS specimens without  $\text{SiC}_{\text{np}}$  (Section 6.4.2.2) the addition of  $\text{SiC}_{\text{np}}$  apparently caused limited bloating for the three PbTe-PbS specimens with  $\text{SiC}_{\text{np}}$  additions (Fig. 6.2f). The bloating induced quasi-spherical pores 1 to 3 microns in diameter, located along the grain boundaries (Fig. 6.2f). As gauged by the surface area porosity fraction measured from SEM micrographs, the bloating in the dry milled only PbTe-PbS specimens with  $\text{SiC}_{\text{np}}$  additions was a factor of 10 less (Fig. 6.2f) than the bloating in the WM and D/WM PbTe-PbS specimens without  $\text{SiC}_{\text{np}}$  additions (Fig. 6.2e, Section 6.4.2.2). The limited bloating in the DM PECS-processed specimens with  $\text{SiC}_{\text{np}}$  additions is likely related to  $\text{SiC}_{\text{np}}$  purity, as will be discussed in Section 6.4.2.4.

In summary, the action of the  $\text{SiC}_{\text{np}}$  additions to PbTe-PbS is somewhat complex. When added to wet milled/PECS processed specimens, the  $\text{SiC}_{\text{np}}$  greatly suppresses, but does not eliminate bloating. This suppression in bloating may be related to the inhibition of localized creep (bloating) processes by  $\text{SiC}_{\text{np}}$ , in an analogous manner to the effect of Ce-based inclusions in skutterudites [Schmidt 2012]. For  $\text{SiC}_{\text{np}}$  additions to dry milled PECS-processed specimens,

a minor increase in bloating was observed which is likely related to the SiC<sub>np</sub> purity (Section 6.4.2.4).

In addition to inhibiting bloating, SiC<sub>np</sub> also inhibited grain growth in this study (Table 6.2b), which agrees with studies of grain growth inhibition by nanoparticle addition to non-thermoelectric materials [Brochin 2000, Zhang 2011]. However, for the DM PECS-processed specimens without SiC<sub>np</sub> addition, post-densification anneals in flowing argon from 723 K to 936 K for 2 hours produced grain growth of up to 40 percent (Table 6.2b). In contrast, post-densification anneals up to 873 K, SiC<sub>np</sub> additions of 2.0, 2.5, and 3.0 vol% inhibited grain growth (Table 6.2b).

In this study, a thermal annealing/grain growth study was not performed for the hot pressed specimens and WM PECS-processed specimens since the bloating that occurs during annealing precludes performing a grain growth study (Section 6.4.2.2). Also, although grain growth studies were done in DM only PECS specimens with 2.0%, 2.5% and 3.0% volume fraction SiC<sub>np</sub> loadings (Table 6.2b), the grain growth was not accessed after a 973 K anneal, again due to bloating in the specimens.

#### 6.4.2.4 Cleaning of powder surfaces by PECS

The lack of bloating in the PECS specimens processed using dry milled powders may be related to the reported cleaning of surface contamination during PECS processing [Groza 1992, Rishbud 1994, Anderson 1999]. For example, transmission electron microscopy of grain boundaries in PECS densified aluminum nitride [Groza 1992, Rishbud 1994], W and NiAl [Anderson 1999] demonstrated that the grain boundary oxide layers present in conventionally

densified specimens were absent in the PECS processed materials, indicating surface impurities had been removed from the powder surfaces during PECS processing. For the PbTe-PbS specimens included in this study, surface contaminate cleaning may explain the difference between the hot pressing results (in which the specimens did bloat) and the PECS-processed dry milled only powders, where the specimens did not bloat.

However, for the PECS processed PbTe-PbS specimens from DM powders, the addition of SiC<sub>np</sub> did lead to limited bloating, thus the PECS process likely did not entirely clean contaminates from the SiC<sub>np</sub> that apparently lead to bloating. Thus, for SiC<sub>np</sub> (i) contaminants may well be much more tenacious on the SiC<sub>np</sub> surfaces than on the PbTe-PbS particle surfaces, making surface cleaning much more difficult and/or (ii) the SiC<sub>np</sub> contaminants may be volumetrically distributed rather than being limited to surfaces, making the removal of surface contaminant layers ineffective for SiC<sub>np</sub>.

In addition, there was limited bloating for the PbTe-PbS wet milled powders that were PECS processed. Thus, once again the PECS process may not have entirely cleaned contaminants from the powder surfaces of the wet milled powders, including perhaps carboneous residues of the hexane milling fluid.

#### 6.4.3 High Temperature elasticity measurements

In general for temperatures above the Debye temperature and in the absence of phase transformations [Schmidt 2012], bloating or microcracking, the Young's and shear moduli decrease linearly with increasing temperature for most brittle materials (shown schematically in Fig. 6.5a) are described well by Eqs. (6.6a) and (6.6b), respectively, such that

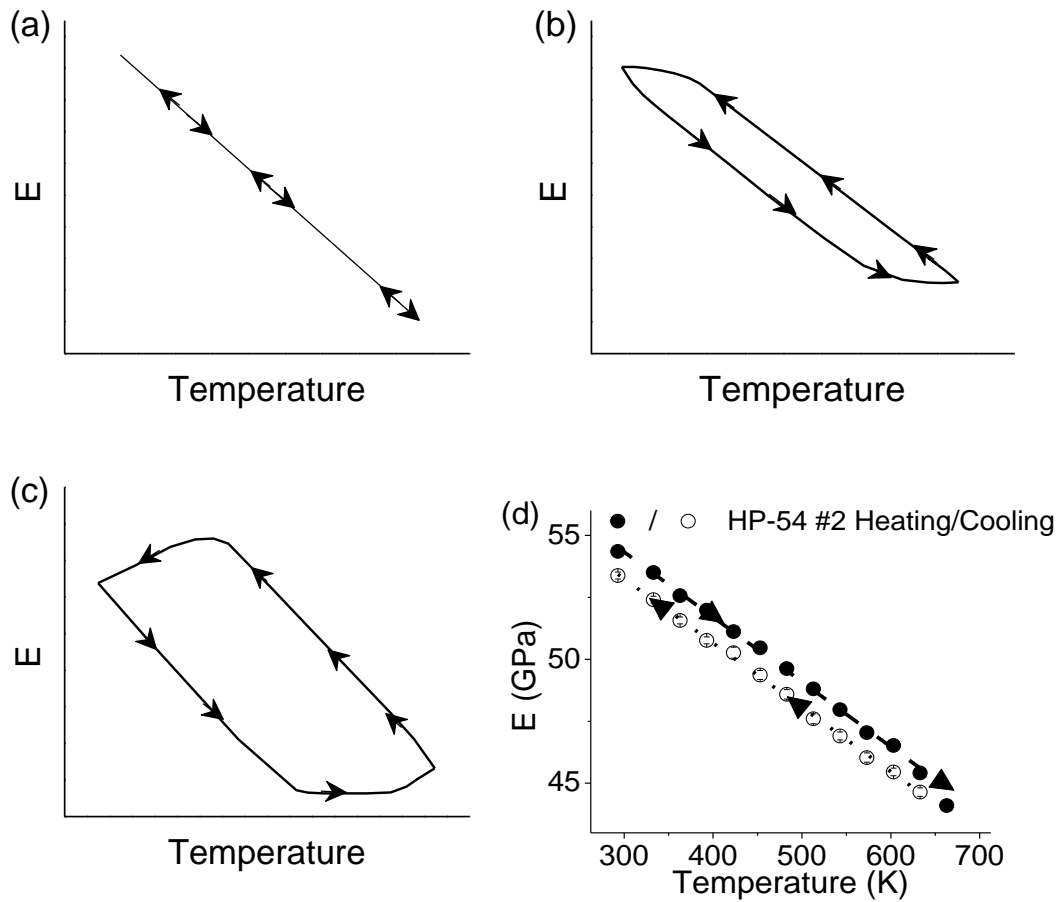


Fig. 6.5 Schematics of hysteresis between heating and cooling in Young's modulus due to (a – c) microcracking and (d) due to bloating. In this study, the specimen HP-54#2 bloated when thermally cycled to 663 K (d). The dashed and dashed-dot lines represent the least-squares fit to Eq. (6.6a) to heating and cooling, respectively.

$$E = E_{RT} - b_{TE}(T - T_{RT}) \quad (6.6a)$$

$$G = G_{RT} - b_{TG}(T - T_{RT}) \quad (6.6b)$$

where in Eqs. (6.6a) and (6.6b)  $E_{RT}$  and  $G_{RT}$  is the Young's and shear modulus at room temperature,  $b_{TE}$  and  $b_{TG}$  describes the Young's and shear modulus-temperature behavior,  $T$  is temperature, and  $T_{RT}$  is the room temperature [Wachtman 2009]. However, either microcracking (Figs. 5b and 5c) or bloating (Fig. 6.5d) can lead to a hysteresis between the heating and cooling of the elastic moduli measured during a temperature cycle.

For the seven hot pressed and five PECS processed PbTe-PbS specimens with  $SiC_{np}$  loadings of 0, 1.0, 2.0 and 3.5 vol% (Table 6.6), the slopes of the Young's modulus as a function of temperature,  $b_{TE}$  (Eq. (6.6a)), were independent of temperature and ranged from  $200 \pm 5.2 \times 10^{-4}$  GPa/K to  $265 \pm 7.4 \times 10^{-4}$  GPa/K (Table 6.6). Each specimen was thermally cycled at least once, with three specimens (Table 6.6) thermally cycled twice, for a total of 15 thermal cycles on the 12 elasticity specimens.

The slopes of the shear modulus as a function of temperature,  $b_{TG}$  (Eq. (6.6b)), were independent of temperature and ranged from  $80 \pm 1.6 \times 10^{-4}$  GPa/K to  $110 \pm 2.2 \times 10^{-4}$  GPa/K (slope values not included in Table 6.6). Also, the values of  $b_{TE}$  (Eq. (6.6a)) and  $b_{TG}$  (Eq. (6.6b)) did not change systematically as the  $SiC_{np}$  loading increased from 0.0 vol% to 3.5 vol% (Table 6.6). The values of  $b_{TE}$  obtained in this study are comparable to the values reported in

Table 6.6 The least-squares fitting parameters,  $E_{RT}$  and  $b_{TE}$ , equation (6.6a) for the seven hot pressed and five PECS-processed PbTe-PbS thermoelectrics included in this study. P is the volume fraction porosity before thermal cycling, N is the number of E versus temperature data points in the least-squares fit and  $r^2$  is the coefficient of determination for the least-squares fit to equation (6.6a). For specimens where there was no observable hysteresis, a single entry is given. Specimens HP-53 #A, HP -53 #C-TC2, HP -54 #2, and HP -55 #1 have an observable hysteresis in E versus T, thus there are two entries, one for heating and one for cooling.

Specimen Label <sup>a</sup>	SiC <sub>np</sub> vol%	P	$E_{RT}$ (GPa)	$b_{TE} \times 10^4$ (GPa K <sup>-1</sup> )	$r^2$	N	Temperature range (K)
HP-53 #A Heating <sup>b</sup>	0.0	0.05	52.8 ± 0.1	260 ± 3.5	0.999	9	333-573
HP-53 #A Cooling <sup>b</sup>			51.9 ± 0.1	260 ± 4.9	0.998	9	333-573
HP -53 #C-TC2 Heating <sup>b</sup>	0.0	0.06	51.9 ± 0.1	220 ± 4.1	0.998	9	333-573
HP -53 #C -TC2 Cooling <sup>b</sup>			50.6 ± 0.1	200 ± 5.2	0.996	8	363-573
HP -54 #2 Heating <sup>c</sup>	0.0	0.03	54.5 ± 0.7	262 ± 3.0	0.998	13	293-663
HP -54 #2 Cooling <sup>c</sup>			53.4 ± 0.06	259 ± 3.0	0.999	13	293-663
HP -55 #1 Heating <sup>c</sup>	0.0	0.03	55.4 ± 0.12	240 ± 5.6	0.994	13	293-663
HP -55 #1 Cooling <sup>c</sup>			54.0 ± 0.07	220 ± 3.3	0.998	13	293-663
HP -53 #C-TC1	0.0	0.07	51.0 ± 0.05	230 ± 3.6	0.996	17	293-543
HP -53 #B	0.0	0.06	53.0 ± 0.03	260 ± 2.2	0.999	17	293-543
HP -54 #1	0.0	0.03	54.5 ± 0.06	230 ± 3.3	0.997	20	293-603
HP -55 #2	0.0	0.03	54.0 ± 0.14	265 ± 7.4	0.993	41	293-603
PECS-01	0.0	0.08	50.4 ± 0.03	204 ± 1.7	0.999	21	293-603
PECS-06S-TC1	0.0	0.08	50.2 ± 0.05	230 ± 2.6	0.998	21	293-603
PECS-06S-TC2	0.0	0.08	50.3 ± 0.07	238 ± 3.2	0.996	25	293-663
PECS -06	1.0	0.05	53.5 ± 0.06	225 ± 3.3	0.996	21	293-603
PECS-18	2.0	0.06	56.4 ± 0.05	244 ± 2.5	0.998	25	293-663
PECS -07-TC1	3.5	0.07	56.1 ± 0.05	270 ± 2.2	0.998	25	293-663
PECS -07-TC2	3.5	0.07	56.2 ± 0.02	273 ± 1.3	0.999	21	293-603

<sup>a</sup>In the specimen labels, HP denotes hot pressing and PECS denotes pulsed electric current sintering

<sup>b</sup>Hysteresis upon thermal cycling up to 603 K,

<sup>c</sup>Hysteresis upon thermal cycling up to 663 K

Table 6.7 In the open literature for doped PbTe-based thermoelectrics,  $E_{RT}$  and  $b_{TE}$ , the least-squares fitting parameters from equation (6.6a), are similar to the least-squares fitting parameters in this study (Table 6.2).  $P$  is volume fraction porosity,  $N$  is the number of data points in the least-squares fit and  $r^2$  is the coefficient of determination.

Specimen Composition	Fabrication Technique	$P$	$E_{RT}$ (GPa)	$b_{TE} \times 10^4$ (GPa K <sup>-1</sup> )	$r^2$	$N$	Temperature range (K)	Reference
PbTe	Cast	0.05 <sup>a</sup>	57.6 ± 0.07	260 ± 2.7	0.998	20	298 – 773	[Ren 2008]
PbI <sub>2</sub> -doped PbTe	Cast	NA <sup>b</sup>	57.9 ± 0.13	360 ± 6.2	0.996	16	298 - 673	[Ren 2008]
PbTe	CT <sup>d</sup>	SC <sup>c</sup>	58.5 ± 0.06	330 ± 4.4	0.999	6	50 - 303	[Houston 1968]
Pb <sub>0.95</sub> Sn <sub>0.05</sub> Te <sub>0.92</sub> S <sub>0.08</sub>	Cast	0.01	51.7 ± 0.04	170 ± 1.7	0.998	21	273 - 773	[Ren 2009]
Ag <sub>0.43</sub> Pb <sub>18</sub> Sb <sub>1.2</sub> Te <sub>20</sub>	Cast	0.02	51.0 ± 0.01	200 ± 3.8	0.993	20	273 - 773	[Ren 2009]
Ag <sub>0.43</sub> Pb <sub>18</sub> Sb <sub>1.2</sub> Te <sub>20</sub>	HP	0.02	53.3 ± 0.18	250 ± 1.2	0.981	10	273 - 523	[Ren 2009]
Ag <sub>0.43</sub> Pb <sub>18</sub> Sb <sub>1.2</sub> Te <sub>20</sub>	HP	0.06	46.4 ± 0.10	250 ± 5.7	0.990	21	273 - 603	[Ren 2009]

<sup>a</sup>The volume fraction porosity was calculated assuming the single crystal density was at theoretical density

<sup>b</sup> $P$  values not specified by the authors [Ren 2008]

<sup>c</sup>Single crystal assumed to be theoretical density

<sup>d</sup>CT is the Czochralski Technique

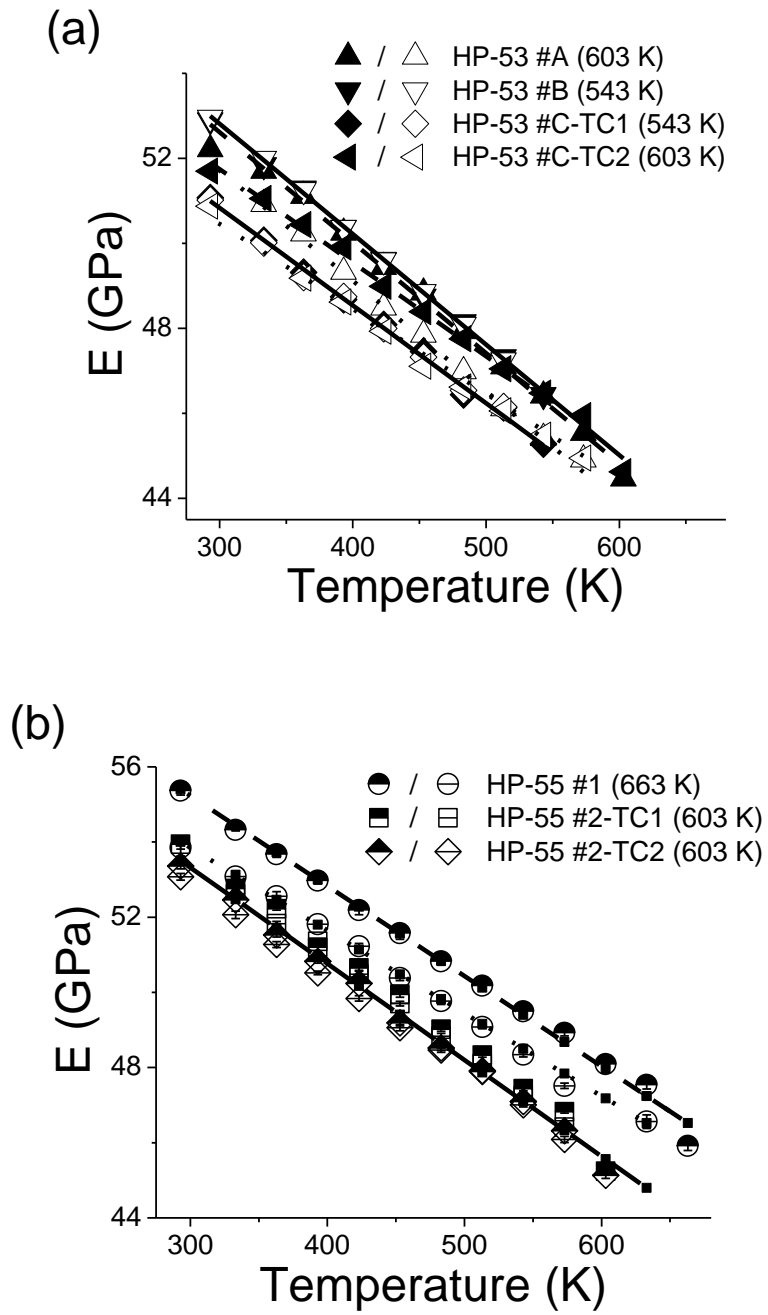


Fig. 6.6

Fig. 6.6 (cont'd)

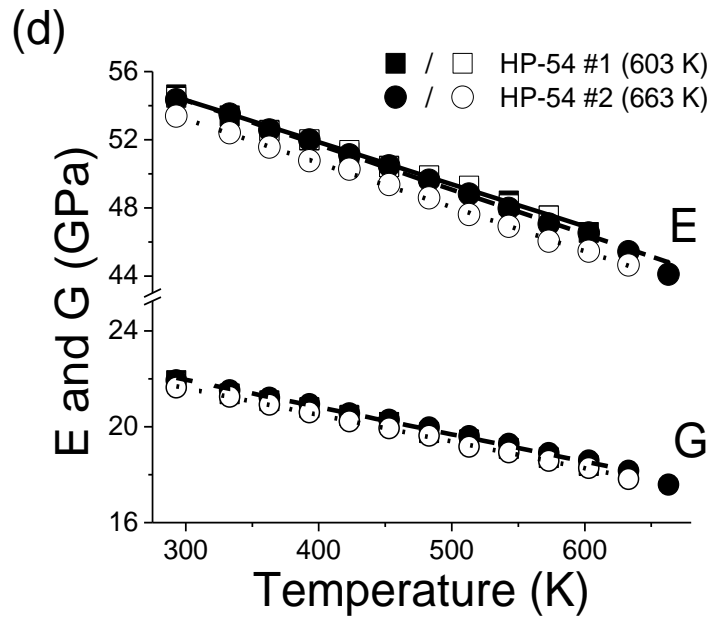
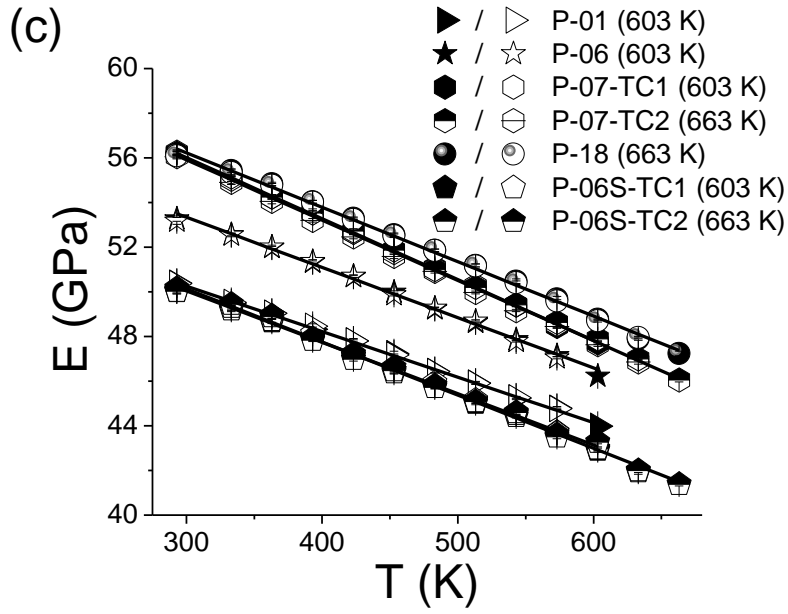


Fig. 6.6 (cont'd)

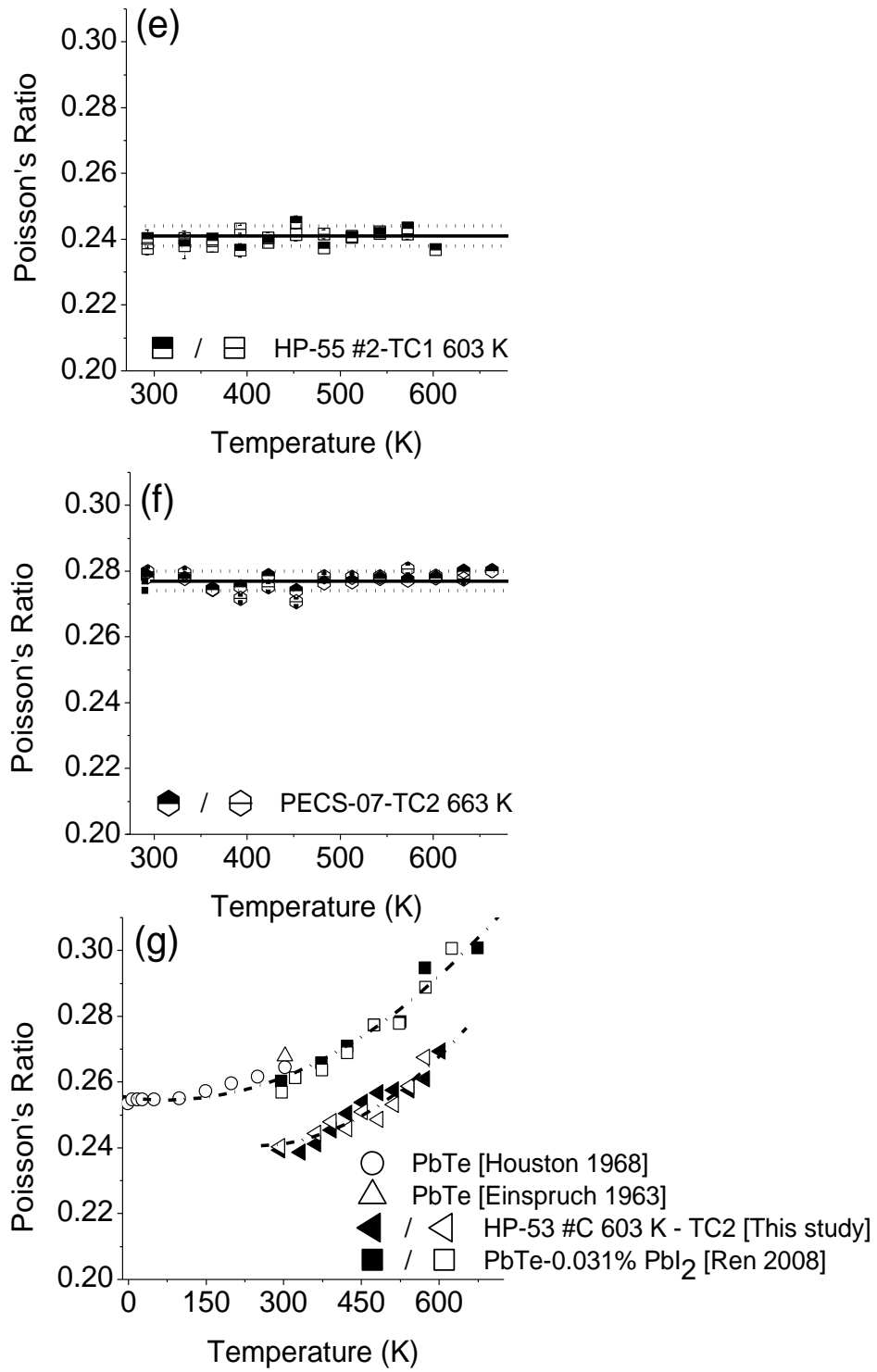


Fig. 6.6 (cont'd ) Temperature dependence of the (a - d) Young's modulus,  $E$ , (d) shear modulus,  $G$ , and (e-f) Poisson's ratio,  $\nu$ , for hot pressed (HP) and PECS-processed PbTe-PbS specimens upon heating (filled symbols) and cooling (open symbols). For  $E$  and  $G$ , the symbol size is greater than the error bars. In parentheses, next to the specimen label, is the maximum temperature for each thermal cycle. The least-squares fit to Eq. (6.6a) to the Young's modulus during heating, cooling, and heating/cooling is represented by the dashed, dotted, and solid lines, respectively. A least-squares fit to Eq. (6.7) to the temperature-dependent Poisson's ratio is represented by the dashed-dot line. The hysteresis in  $E$  versus  $T$  for specimens HP-53 #A, HP-53 #C-TC2, HP -54 #2, and HP -55 #1 is not apparent in the figures because of the number of temperature-dependent Young's moduli data points.

the literature for other PbTe-based thermoelectrics [Ren 2008, Ren 2009 LAST, Houston 1968] (Table 6.7).

#### 6.4.3.1 Temperature behavior of Poisson's ratio as a function of SiC<sub>np</sub> addition

For the twelve PbTe-PbS specimens with and without SiC<sub>np</sub> additions the Poisson's ratio ranged between 0.23 and 0.28 and either stayed constant (Figs. 6.6e and 6.6f) or increased (Fig. 6.6g) between room temperature and maximum temperatures of 543 K, 603 K and 663 K.

Similar behavior was observed by Ren et al. for cast and hot pressed Ag<sub>0.43</sub>Pb<sub>18</sub>Sb<sub>1.2</sub>Te<sub>20</sub> and Pb<sub>0.95</sub>Sn<sub>0.05</sub>Te<sub>0.92</sub>S<sub>0.08</sub> specimens, where the Poisson's ratio either remained constant or increased with increasing temperatures for maximum temperatures of 573 K, 623 K and 773 K [Ren 2009 LAST].

In an elasticity study of PbTe, Ren et al. presented an empirical relationship the temperature dependent Poisson's ratio,  $\nu(T)$ , (Eq. (6.7)) for a combined data set that included (i) 0 to 300 K data from Houston [Houston 1968], 300 K data Einspruch [Einspruch 1963] and 300 K to 670 K for PbTe-0.031% PbI<sub>2</sub> from [Ren 2008] such that

$$\nu(T) = \nu_{RT} + a_1(T - T_{RT}) + a_2(T - T_{RT})^2 \quad (6.7)$$

where  $\nu_{RT}$  is the room temperature Poisson's ratio,  $T$  is temperature,  $T_{RT}$  is room temperature and  $a_1$  and  $a_2$  are material-dependent constants [Ren 2008] with an  $r^2$  of 0.959 (Fig. 6.6g) for temperatures from 0 K to 670 K. Similarly, in this study, the temperature dependence of Poisson's ratio (Fig. 6.6g) was described well by Eq. (6.7).

#### 6.4.3.2 Hysteresis in elastic moduli measurements for hot pressed specimens

In general, microcracking leads to a drop in the elastic modulus [Case 1981Al<sub>2</sub>O<sub>3</sub>, Case 1983, Case 1981Gd<sub>2</sub>O<sub>3</sub>] but upon heating, microcracks may heal via mass transport mechanisms such as (1) mass diffusion, (2) growth of reaction products or (3) flow of viscous fluid. For example, microcrack healing by mass diffusion has been reported in alumina [Case 1981Al<sub>2</sub>O<sub>3</sub>, Wilson 1997, Bykov 2010, Rödel 1990], Ti-, Ca-, and Mg-doped alumina [Powers 1993, Powers 1992], SiC [Narushima 2001], MgTi<sub>2</sub>O<sub>5</sub> [Case 1983], Gd<sub>2</sub>O<sub>3</sub> [Case 1981Gd<sub>2</sub>O<sub>3</sub>], where such healing can occur under vacuum conditions for temperatures greater than 0.6 of the melting point [Case 1983]. Also microcrack healing can occur via by viscous glassy-phase filling in ZrO<sub>2</sub> cast refractories [Sibil 2009] and synthetic clay (Laponite) [Renard 2009] and by crack surface oxidation in Ti<sub>3</sub>AlC<sub>2</sub> [Song 2008] and zirconia-based thermal barrier coatings [Rico 2009].

For E versus T and G versus T plots, hysteresis between heating and cooling (Figure 6.5b and 6.5c) has been observed for microcracked and thermally cycled Al<sub>2</sub>O<sub>3</sub>, [Case 1981 Al<sub>2</sub>O<sub>3</sub>, Case 1983, Yousef 2005], Gd<sub>2</sub>O<sub>3</sub> [Case 1983], Eu<sub>2</sub>O<sub>3</sub> [Dole 1977] and HfO<sub>2</sub> [Dole 1977], MgTi<sub>2</sub>O<sub>5</sub> [Bush 1959, Bush 1958] and cast refractories [Chotard 2008, Patapy 2009] was caused by microcrack healing during heating and then the reformation of microcracks during cooling (Figs. 6.5b and 6.5c) [Case 1981 Al<sub>2</sub>O<sub>3</sub>, Case 1983, Bush 1959, Chotard 2008]. The area of the hysteresis loop (Figs. 6.5b and 6.5c) increases with increasing grain size [Case 1981 Al<sub>2</sub>O<sub>3</sub>, Case 1983].

For the four hot pressed PbTe-PbS specimens thermally cycled at T > 603 K, a hysteresis in the temperature dependent elastic moduli was observed between the heating and cooling

measurements. In contrast to the hot pressed specimens, none of the five PECS PbTe-PbS specimens had a hysteresis in the E versus T when thermally cycled up to 663 K.

#### 6.4.3.3 Observations in the literature of elasticity changes due to bloating during post-densification annealing of other materials

In the literature, bloating during post-densification annealing was observed in Synroc B (with major phases of  $\text{BaAl}_2\text{TiO}_{16}$ ,  $\text{CaTiO}_3$ , and  $\text{CaZrTiO}_7$ ) [O'Brien 1985] and Ti-6V-4Al alloys [Oppenheimer 2010]. For Synroc B, thermal annealing up to a maximum temperature of 1473 K induced bloating was observed indirectly through a decrease in E of up to roughly 25% and directly by optical microscopy [O'Brien 1985].

Also, in order to tailor the porosity and enhance bone in-growth in the biomedical alloy Ti-6V-4Al, Oppenheimer et al. intentionally induced bloating in densified specimens [Oppenheimer 2010, Oppenheimer 2009]. Ti-6V-4Al powders in sealed metal canisters backfilled with argon [Oppenheimer 2010, Oppenheimer 2009] were hot pressed yielding specimens with P values  $\ll$  1 percent. Then, post-densification anneals to 1303 K of 18 Ti-6V-4Al specimens yielded P values from 0.09 to 0.52 [Oppenheimer 2010] via bloating of previously dense specimens. In this study we found that a least-squares fit Oppenheimer's E versus P data [Oppenheimer 2010] for bloated Ti-6V-4Al specimens to the empirical exponential relationship Eq. (6.4a) described the Ti-6V-4Al bloating results well, with an  $r^2$  of 0.934 (Fig. 6.7). This indicates that the decrease in E with P in Oppenheimer's intentionally bloated Ti-6V-4Al specimens followed a similar functional form (Eq. (6.4a)) as was observed for the bloated PbTe-PbS specimens in this study. Thus, the present authors believe that the controlled bloating Ti-6V-4Al specimens [Oppenheimer 2010] is directly analogous to the bloating observed in this study for PbTe-PbS.

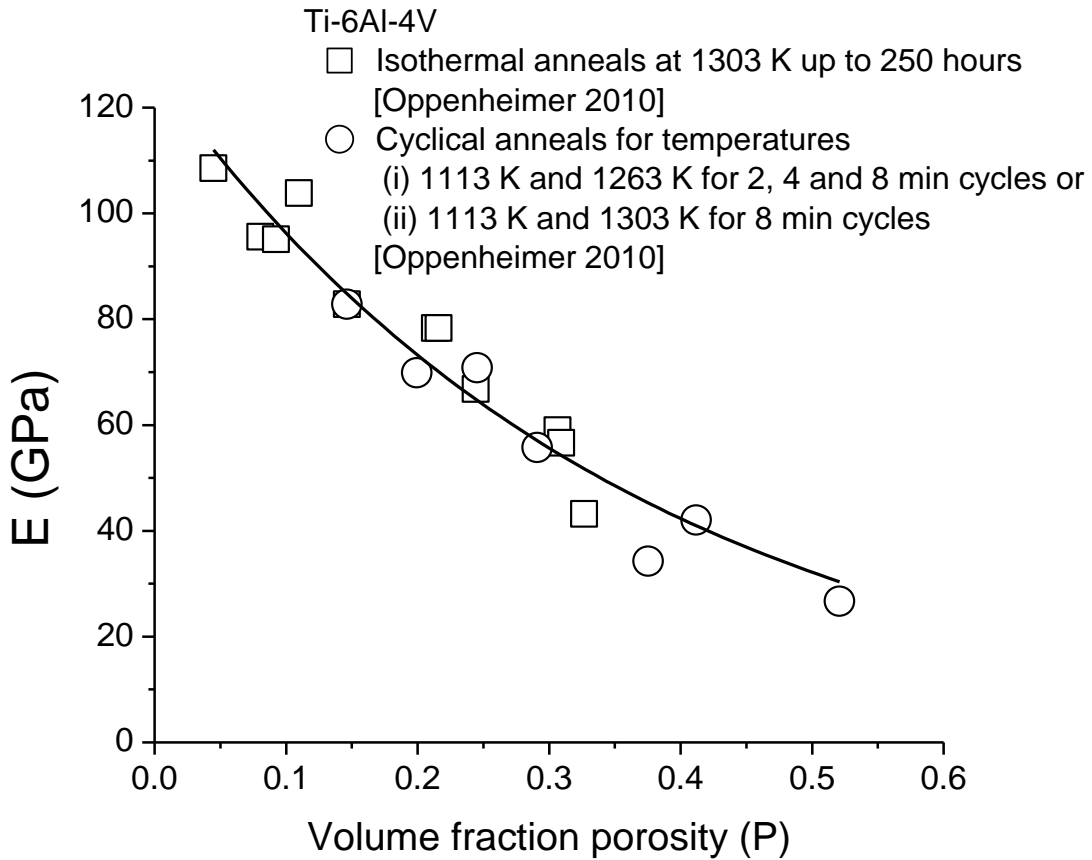


Fig. 6.7 The Young's modulus as a function of volume fraction porosity,  $P$ , for Ti-6Al-4V specimens after post-densification anneals up to 1303 K [Oppenheimer 2010]. This behavior is consistent with the empirical exponential decrease common to brittle materials (Eq. (6.4a)). The solid line represents a least-squares fit to Eq. (6.4a) of the Oppenheimer et al. Young's modulus versus  $P$  data [Oppenheimer 2010].

### 6.5.0 Summary and Conclusions

In this study, a total of 26 PbTe-PbS specimens were fabricated by either hot pressing or PECS-processing powders that were dry milled only, wet milled only, or dry/wet milled (Table 6.1). This study includes results on both processing and mechanical properties.

In terms of processing, this study expands on the previous preliminary results that for polycrystalline PbTe-PbS, a combination of PECS-processing and dry milling inhibits bloating during post-densification anneals up to 936 K. We propose that the absence of bloating for the DM PECS processed specimens may be related to the reported “cleaning” of powder surfaces by the PECS process itself [Groza 1992, Rishbud 1994, Anderson 1999]. Using dry milling together with PECS processing to eliminate bloating will have the extremely beneficial effect of stabilizing the high temperature microstructure of these materials.

Also, RUS measurements of the Young’s and shear moduli and Poisson’s ratio were performed for 12 specimens over temperatures ranging from RT up to as high as 663 K (Table 6.6). For each of 15 heating and cooling cycles, E and G decreased linearly with increasing temperature (Eqs. (6.6a) and (6.6b)) where  $b_{TE}$  (Eq. (6.6a)) ranged from 0.020 GPa/K to 0.027 GPa/K (Table 6.6),  $b_{TG}$  (Eq. (6.6b)) ranged from 0.008 GPa/K and 0.011 GPa/K. The elasticity measurements provide information needed by designers to predict the stress and strain of thermoelectric components that are incorporated in thermoelectric generators.

Annealing of as-densified specimens can generate porosity and porosity in turn affects the thermal, electrical and mechanical properties of materials, thus the processing aspects of this study are intertwined with the mechanical property aspects.

SEM examination of the 15 PbTe-PbS specimens that underwent post-densification thermal anneals up to 936 K in a flowing Ar-H<sub>2</sub> atmosphere revealed a temperature-dependent bloating

that was present in hot pressed specimen and each PECS specimen processed with wet milled powders. However, for seven out of seven of dry milled, PECS-processed specimens, no bloating was observed by SEM even for two-hour anneals at 936 K, which is roughly 200 K higher than the proposed use temperature for these materials. Thus PECS processing in conjunction with dry milled only PbTe-PbS powders stabilizes the high temperature microstructure of these materials.

SiC<sub>np</sub> addition did limit bloating in wet milled/PECS processed materials, likely due to an enhanced resistance to grain boundary sliding/creep processes brought about by the SiC<sub>np</sub> inclusions, in an analogous manner to the grain boundary sliding resistance afforded by Ce-based inclusions in a n-type skutterudite [Schmidt 2012].

Also, SiC<sub>np</sub> additions of 2.0, 2.5 and 3.0 vol% did (i) modestly inhibit grain growth during high temperature anneals (Table 6.2b) as well as (ii) alter the fracture mode of the specimens (Fig. 6.4, Table 6.2a). Grain growth inhibition is favorable for enhancing fracture strength. In addition, the dramatic change in fracture mode from intergranular to transgranular (Table 6.2a, Fig. 6.4) likely signals an increase in fracture toughness with SiC<sub>np</sub> additions (Section 6.3.1.2).

Future work will include examining the effect of SiC<sub>np</sub> purity on bloating to determine if SiC<sub>np</sub> purities higher than 95% may reduce the bloating in specimens densified by PECS from dry milled only powders.

#### Acknowledgments

The authors acknowledge the financial support of Office of Naval Research Grant N00014-08-1-

0613. In addition some supplemental support (assistance of Robert Schmidt) was received from the Department of Energy, “Revolutionary Materials for Solid State Energy Conversion Center,” an Energy Frontiers Research Center funded by the U.S. Department of Energy, Office of Basic Energy Sciences under award number DE-SC0001054. Research through the Oak Ridge National Laboratory's High Temperature Materials Laboratory User Program was sponsored by the U. S. Department of Energy, Office of Energy Efficiency and Renewable Energy, Vehicle Technologies Program. Edward Timm and Karl Dersch, Michigan State University, assisted the authors with hot pressing, PECS and specimen cutting. The Center for Statistical Training and Consulting at Michigan State University provided advice on the error analysis in this study.

## REFERENCES

## 6.6.0 References

- [Aitchinson 1957] Aitchinson J, Brown JAC. The Lognormal Distribution Massachusetts: Cambridge University Press; 1957.
- [Alvarez 2010] Alvarez FX, Jou D, Sellitto A. Pore-size dependence of the thermal conductivity of porous silicon: A phonon hydrodynamic approach, *Appl Phys Lett* 2010; 97: 033103.
- [Anderson 1999] Anderson KR, Groza JR, Fendorf, Echer CJ, Surface oxide debonding in field assisted powder sintering, *Mater. Sci. Eng.* 1999 A270: 278–282.
- [Androulakis 2007] Androulakis J, Lin C, Kong H, Uher C, Wu C, Hogan T, Cook BA, Caillat T, Paraskevopoulos KM, Kanatzidis MG. Spinodal decomposition and nucleation and growth as a means to bulk nanostructured thermoelectrics: Enhanced performance in  $Pb_{1-x}Sn_xTe-PbS$ , *J Am Chem Soc* 2007; 129: 9780–9788.
- [Berbenni 2007] Berbenni S, Favier V, Berveiller M. Micro-macro modelling of the effects of the grain size distribution on the plastic flow stress of heterogeneous materials, *Comput Mater Sci* 2007; 39: 96–105.
- [Betz 2000] Betz U, Sturm A, Löffler JF, Wagner W, Wiedenmann A, Hahn H. Microstructural development during final-stage sintering of nanostructured zirconia based ceramics, *Mater Sci Eng* 2000; A281: 68–74.
- [Boccaccini 1994] Boccaccini AR. Effective elastic moduli of porous ceramic materials, *J Am Ceram Soc* 1994; 77: 2779.
- [Brochin 2000] Brochin F, Lenoir B, Devaux X, Martin-Lopez R, Scherrer H. Preparation and transport properties of polycrystalline Bi and Bi-SiO<sub>2</sub> nanocomposites, *J Appl Phys* 2000; 88: 3269-3275.
- [Bush 1958] Bush EA, Hummel FA. High-temperature mechanical properties of ceramic materials-magnesium dititanate, *J Am Ceram Soc* 1958; 41: 189–195.
- [Bush 1959] Bush EA, Hummel FA. High-temperature mechanical properties of ceramic materials – beta-eucryptite, *J Am Ceram Soc* 1959; 42:388–391.
- [Bykov 2010] Bykov YV, Egorov SV, Ereemeev AG, Kholoptsev VV, Plotnikov IV, Rybakov KI, Semenov VE, Sorokin AA. Effects of microwave heating in nanostructured ceramic materials, *Powder Metall Met Ceram* 2010; 49; 31-41
- [Case 1981 Gd<sub>2</sub>O<sub>3</sub>] ED Case, JR Smyth, Hunter O. Microcracking behavior of monoclinic Gd<sub>2</sub>O<sub>3</sub>, *J Nucl Mater* 1981; 102:135-142.

- [Case 1981] Case ED, Smyth JR. Room-temperature fracture energy of monoclinic  $Gd_2O_3$ , *J Mater Sci* 1981; 16: 3215-3217.
- [Case 1981Al<sub>2</sub>O<sub>3</sub>] Case ED, Smyth JR, Hunter Jr. O. Microcracking in large-grain  $Al_2O_3$ , *Mater Sci Eng* 1981; 51:175–179.
- [Case 1983] Case ED, Smyth JR, Hunter Jr. O. Microcrack healing during the temperature cycling of single phase ceramics, in: Bradt RC, Evans AG, Hasselman DPH, Lange FF. (Eds.). *Fracture Mechanics of Ceramics*, Vol 5. New York: Plenum; 1983, pp 507 – 530.
- [Case 1984] Case ED, Glinka CJ. Characterization of microcracks in  $YCrO_3$  using small-angle neutron-scattering and elasticity measurements, *J Mater Sci* 1984; 19: 2962-2968.
- [Chotard 2008] Chotard T, Soro J, Lemercier H, Huger M, Gault C. High temperature characterisation of cordierite-mullite refractory by ultrasonic means, *J Eur Ceram Soc* 2008;28: 2129–2135.
- [Colombo 2006] Colombo P. Conventional and novel processing methods for cellular ceramics, *Phil Trans R Soc A* 2006; 364:109-124.
- [CSTAT] Personal communication with Center for Statistical Training and Consulting, Michigan State University, October 2011 February 2012.
- [Dole 1977] Dole SL, Hunter O, Calderwood FW, Bray DJ. Elastic properties of monoclinic hafnium oxide at room temperature, *J Am Ceram Soc* 1978; 61: 486-490.
- [Fullman 1953] Fullman RL. Measurement of particle sizes in opaque bodies, *Trans. AIME* 1953; 197: 447–452.
- [Groza 1992] Groza JR, Risbud SH, Yamazaki K. Plasma activated sintering of additive-free  $AlN$  powders to near theoretical density in 5 minutes, *J Mater Res* 1992; 7: 2643-2645.
- [Hall 2009] Hall BD, Case ED, Ren F, Johnson J, Timm EJ. Agglomeration during wet milling of LAST (lead-antimony-silver-tellurium) powders, *Mater Chem Phys* 2009; 113: 497-502.
- [Hoepfner 2002] Hoepfner TP, Case ED. The porosity dependence of the dielectric constant for sintered hydroxyapatite, *J Biomed Mater Res* 2002; 60: 643 - 650.
- [Hoepfner 2003] Hoepfner TP, Case ED. The porosity dependence of the dielectric constant for sintered hydroxyapatite, *Ceram Int* 2003; 29: 699 - 706.
- [Houston 1968] Houston B, Strakna RE, Belson HS. Elastic constants, thermal expansion, and Debye temperature of lead telluride, *J Appl Phys* 1968; 39: 3913.

- [Hu 2010] Hu LF, Wang CA. Effect of sintering temperature on compressive strength of porous yttria-stabilized zirconia ceramics, *Ceram Int* 2010; 36: 1697 - 1710.
- [Jang 2010] Jang B-K, Kim S-Y, Han I-S, Seo D-W, Hong K-S, Woo S-K, Sakka Y. Influence of uni and bi-modal SiC composition on mechanical properties and microstructure of reaction-bonded SiC ceramics, *J Ceram Soc Jpn* 2010;118: 1028-1031.
- [Johnsen 2011] Johnsen S, He JQ, Androulakis J, Dravid VP, Todorov I, Chung DY, Kanatzidis MG. High Performance Thermoelectrics from Earth-Abundant Materials: Enhanced Figure of Merit in PbS by Second Phase Nanostructures, *J Am Chem Soc* 2011; 133: 3460-3470.
- [Jung 2011] Jung SY, Seo WS, Lim YS, Shin S, Cho HH, Park HH. Thermoelectric Properties of Nb-Doped Ordered Mesoporous TiO<sub>2</sub>, *J Electron Mater* 2011; 40: 652-656.
- [Kanatzidis 2010] Kanatzidis MG. Nanostructured Thermoelectrics: The New Paradigm?, *Chem Mat* 2010; 22: 648-659.
- [Karakasidis 2011] Karakasidis TE, Charitidis CA. Influence of nano-inclusions' grain boundaries on crack propagation modes in materials, *Mater Sci Eng B* 2011; 176:490–493.
- [Kawabata 1977] Kawabata T, Izumi, O. Relationship between fracture toughness and transgranular fracture in an Al-6.0% 2n-2.5% Mg alloy, *Acta Metall Mater* 1977; 25: 505-512.
- [Kim 2007] Kim B-N, Hiraga K, Morita K, Yoshida H. Spark plasma sintering of transparent alumina, *Scripta Materialia* 2007; 57: 607–610.
- [Kishimoto 1991] Kishimoto A, Koumoto K, Yanagida H, Nameki M. Microstructure dependence of mechanical and dielectric strengths, *Eng Fract Mech* 1991; 40: 927 - 930.
- [Lee 2010] Lee H, Vashaee D, Wang Z, Dresselhaus MS, Ren ZF, Chen G. Effects of nanoscale porosity on thermoelectric properties of SiGe, *J Appl Phys* 2010; 107: 094308.
- [Li 2006] Li J-F, Liu J. Effect of nano-SiC dispersion on thermoelectric properties of Bi<sub>2</sub>Te<sub>3</sub> polycrystals, *Phys Stat Sol* 2006; 203: 3768–3773.
- [Li 2011] Li F, Huang X, Sun Z, Ding J, Jiang J, Jiang W, Chen L. Enhanced thermoelectric properties of n-type Bi<sub>2</sub>Te<sub>3</sub>-based nanocomposite fabricated by spark plasma sintering, *J Alloy Compd* 2011;509: 4769–4773.
- [Liu 1991] Liu S-Y, Chen I-W. Fatigue of yttria-stabilized zirconia, *J Am Ceram Soc* 1991; 74: 1197-1205
- [Liu 1992] Liu S-Y, Chen I-W. Fatigue deformation mechanism of zirconia ceramics, *J Am*

- Ceram Soc 1992; 75: 1191-1204.
- [Liu 2011] Liu D-W, Li J-F, Chen C, Zhang B-P. Effects of SiC Nanodispersion on the Thermoelectric Properties of p-Type and n-Type Bi(2)Te(3)-Based Alloys, *J Electron Mater* 2011; 40: 992-998.
- [Low 1981] Low NMP. Formation of cellular-structure glass with carbonate compounds and natural mica powders, *J Mater Sci* 1981; 16: 800-808.
- [Migliori 1997] Migliori A, Sarrao JL. *Resonant Ultrasound Spectroscopy: Applications to Physics, Materials Measurements, and Nondestructive Evaluation*, New York: Academic Press; 1997.
- [Mukhopadhyay 2010] Mukhopadhyay A, Chakravarty D, Basu B. Spark Plasma-Sintered WC-ZrO(2)-Co Nanocomposites with High Fracture Toughness and Strength, *J Am Ceram Soc* 2010; 93: 1754–1763.
- [Narushima 2001] Narushima T, Glaeser AM. High-temperature morphological evolution of lithographically introduced cavities in silicon carbide, *J Am Ceram Soc* 2001; 84: 921–28.
- [Ni 2009] Ni, JE, Ren F, Case ED, Timm EJ. Porosity dependence of elastic moduli in LAST (Lead-antimony-silver-tellurium) thermoelectric materials, *Mater Chem Phy* 2009; 118: 459 - 466.
- [Ni 2010] Ni JE, Case ED, Khabir KN, Stewart RC, Wu C, Hogan TP, Timm EJ, Girard SN, Kanatzidis MG. Room temperature Young's modulus, shear modulus, Poisson's ratio and hardness of PbTe-PbS thermoelectric materials, *Mater Sci Eng B* 2010; 170: 58–66.
- [Ni DOI 2012] Ni JE, Case ED, Stewart RC, Wu C, Hogan TP, Kanatzidis MG. Bloating in  $(\text{Pb}_{0.95}\text{Sn}_{0.05}\text{Te})_{0.92}(\text{PbS})_{0.08}-0.055\% \text{PbI}_2$  Thermoelectric Specimens as a Result of Processing Conditions, *J Electron Mater*, in press, DOI: 10.1007/s11664-011-1853-0.
- [Ni to be submitted] Ni JE, Case ED, Schmidt RD, Wu C-I, Hogan TP, Trejo RM, Kirkham MJ, Lara-Curzio E, Kanatzidis MG, The effect of processing on microstrain during thermal expansion measurements for  $(\text{Pb}_{0.95}\text{Sn}_{0.05}\text{Te})_{0.92}(\text{PbS})_{0.08}-0.055\% \text{PbI}_2$  thermoelectric material, *Philos. Mag.* in press.
- [O'Brien 1985] O'Brien MH, Hunter Jr. O, Case ED, Mechanical effects of thermal cycling on United States and Australian Synroc-B, *J Mater Sci Lett* 1985; 4: 367-369.
- [Oppenheimer 2009] Oppenheimer S, Dunand DC. Porous NiTi by creep expansion of argon-filled pores, *Mater Sci Eng A* 2009; 523: 70–76
- [Oppenheimer 2010] Oppenheimer S, Dunand DC. Solid-state foaming of Ti-6Al-4V by creep or superplastic expansion of argon-filled pores, *Acta Mater* 2010; 58: 4387–4397.

- [Park 2009] Park YH, Hinoki T, Kohyama A. Development of multi-functional NITE-porous SiC for ceramic insulators, *J Nuclear Mater* 2009; 386–388: 1014 - 1017.
- [Patapy 2009] Patapy C, Gault C, Huger M, Chotard T. Acoustic characterization and microstructure of high zirconia electrofused refractories, *J Eur Ceram Soc* 2009; 29: 3355–3362.
- [Pilchak 2007] Pilchak AL, Ren F, Case ED, Timm EJ, Wu C-I, Hogan TP, Schock HJ. Characterization of dry milled powders of LAST (lead-antimony-silver-tellurium) thermoelectric material, *Philos Mag* 2007; 87: 4567 – 4591.
- [Powers 1992] Powers JD, Glaeser AM. High-temperature healing of crack-like flaws in Mg-ion-implanted and Ca-ion-implanted sapphire, *J Am Ceram Soc* 1992; 75: 2547–2558.
- [Powers 1993] Powers JD, Glaeser AM. High-temperature healing of crack-like flaws in titanium ion-implanted sapphire, *J Am Ceram Soc* 1993; 76: 2225–2234.
- [Ren 2008] Ren F, Case ED, Sootsman JR, Kanatzidis MG, Kong H, Uher C, Lara-Curzio E, Trejo RM. The high-temperature elastic moduli of polycrystalline PbTe measured by resonant ultrasound spectroscopy, *Acta Mater* 2008; 56: 5954–5963.
- [Ren 2009 HA] Ren F, Case ED, Morrison A, Tafesse M, Baumann MJ. Resonant ultrasound spectroscopy measurement of Young's modulus, shear modulus and Poisson's ratio as a function of porosity for alumina and hydroxyapatite, *Philos Mag* 2009; 89: 1163 - 1182.
- [Ren 2009 LAST] Ren F, Case ED, Ni JE, Timm EJ, Lara-Curzio E, Trejo RM, Lin C-H, Kanatzidis MG. Temperature-dependent elastic moduli of lead telluride-based thermoelectric materials, *Philos Mag* 2009; 89: 143 -167.
- [Renard 2009] Renard F, Dysthe DK, Feder JG, Meakin P, Morris SJS, Jamtveit B. Pattern formation during healing of fluid-filled cracks: an analog experiment, *Geofluids* 2009; 9: 365–372.
- [Rice 1998] Rice RW. *Porosity of Ceramics*, New York: Marcel Dekker; 1998.
- [Rico 2009] Rico A, Gómez-García J, Múnez CJ, Poza P, Utrilla V. Mechanical properties of thermal barrier coatings after isothermal oxidation. Depth sensing indentation analysis, *Surf Coat Technol* 2009; 203: 2307–2314.
- [Rishbud 1994] Rishbud SH, Groza JR, Kim MJ, Philos. Clean grain-boundaries in alumina nitride ceramics densified without additives by a plasma-activated sintering process, *Mag. B*, 1994 69: 525–533.
- [Rödel 1990] Rödel J, Glaeser AM. High-temperature healing of lithographically introduced cracks in sapphire, *J Am Ceram Soc* 1990; 73: 592–601.

- [Schmidt 2012] Schmidt RD, Case ED, Ni JE, Sakamoto JS, Trejo RM, Lara-Curzio E, Temperature-dependent Young's modulus, shear modulus and Poisson's ratio of p-type  $\text{Ce}_{0.9}\text{Fe}_{3.5}\text{Co}_{0.5}\text{Sb}_{12}$  and n-type  $\text{Co}_{0.95}\text{Pd}_{0.05}\text{Te}_{0.05}\text{Sb}_3$  skutterudite thermoelectric materials," *Philosophical Magazine, Philos. Mag.*, 2012; 92: 727-759
- [Schmidt DOI 2012] Schmidt RD, Case ED, Ni JE, Sakamoto JS, Trejo RM, Lara-Curzio E, Payzant EA, Kirkham MJ, Peascoe-Meisner RA, The temperature dependence of thermal expansion for p-type  $\text{Ce}_{0.9}\text{Fe}_{3.5}\text{Co}_{0.5}\text{Sb}_{12}$  and n-type  $\text{Co}_{0.95}\text{Pd}_{0.05}\text{Te}_{0.05}\text{Sb}_3$  skutterudite thermoelectric materials, *Philos. Mag.* DOI: 10.1080/14786435.2011.644815
- [Sibil 2009] Sibil A, Erauw JP, Cambier F, R'Mili M, Godin N, Fantozzi G. Study of damage of high zirconia fused-cast refractories by measurement of Young's modulus, *Mater Sci Eng A-Struct Mater Prop Microstruct. Process* 2009; 521–22: 221–223.
- [Simmons 1971] Simmons G and Wang H, *Single Crystal Elastic Constants and Calculated Aggregate Properties: A Handbook*, second ed. Cambridge: The MIT Press; 1971.
- [Song 2008] Song GM, Pei YT, Sloof WG, Li SB, De Hosson JThM, van der Zwaag S. Oxidation-induced crack healing in  $\text{Ti}_3\text{AlC}_2$  ceramics, *Scr Mater* 2008; 58: 13–16.
- [Teber 2012] Teber A, Schoenstein F, Têtard F, Abdellaoui M, Jouini N. Effect of SPS process sintering on the microstructure and mechanical properties of nanocrystalline TiC for tools application, *Int. Journal of Refractory Metals and Hard Materials* 2012;30: 64–70.
- [Vandeperre 2004] Vandeperre LJ, Wang J, Clegg WJ. Effects of porosity on the measured fracture energy of brittle materials, *Philos Mag* 2004; 84: 3689-3704.
- [Voevodin 2000] Voevodin AA, Zabinski JS. Supertough wear-resistant coatings with 'chameleon' surface adaptation, *Thin Solid Films* 2000; 370: 223-231.
- [Wachtman 2009] Wachtman JB, Cannon WR, Matthewson MJ. *Mechanical Properties of Ceramics*, second ed. New York: Wiley Interscience; 2009.
- [Wang 2000] Wang C, Zhu ZG, Hou XH, Li HJ. Damping characteristics of CVI-densified carbon-carbon composites, *Carbon* 2000; 38: 1821 – 1824.
- [Wen 2011] Wen H, Zhao Y, Zhang Z, Ertorer O, Dong S, Lavernia EJ. The influence of oxygen and nitrogen contamination on the densification behavior of cryomilled copper powders during spark plasma sintering, *J Mater Sci* 2011; 46: 3006–3012.
- [Wilson 1993] Wilson, BA, Case, ED. Comparison of mechanical fatigue with thermal fatigue in ceramics, *Scr Metall Materialia* 1993; 28: 1571-1576.
- [Wilson 1997] Wilson BA, Lee K-Y, Case ED. Diffusive crack-healing behavior in polycrystalline alumina: A comparison between microwave annealing and conventional

- annealing, *Mater Res Bull* 1997; 32: 1607-1616.
- [Wu 2006] Wu J, Norvell WA, Welch RM. Kriging on highly skewed data for DTPA-extractable soil Zn with auxiliary information for pH and organic carbon, *Geoderma* 2006; 134: 187–199.
- [Xiong 2009] Xiong Z, Chen X, Zhao X, Bai S, Huang X, Chen L. Effects of nano-TiO<sub>2</sub> dispersion on the thermoelectric properties of filled-skutterudite Ba<sub>0.22</sub>Co<sub>4</sub>Sb<sub>12</sub>, *Solid State Sci* 2009;11: 1612-1616
- [Xu 2012] Xu C, Cai Y, Flodström K, Li Z, Esmailzadeh S, Zhang G-J. Int. Spark plasma sintering of B<sub>4</sub>C ceramics: The effects of milling medium and TiB<sub>2</sub> addition, *J Refract Met H* 2012; 30: 139–144
- [Yamada 2010] Yamada M, Sekine K, Kumazawa T, Tanabe Y. Relationship between the cone crack and fracture mode in ceramics under high-velocity-projectile impact, *J Ceram Soc Jpn* 2010;118: 903-908.
- [Yang 2010] Yang A, Wang CA, Guo R, Huang Y, Nan CW. Effects of sintering behavior on microstructure and piezoelectric properties of porous PZT ceramics, *Ceram Int* 2010; 36: 549 - 554.
- [Yoshida 2011] Yoshida H, Morita K, Kim B-N, Hiraga K, Yamanaka K, Soga K, Yamamoto T., Low-Temperature Spark Plasma Sintering of Yttria Ceramics with Ultrafine Grain Size, *J Am Ceram Soc* 2011; 94: 3301–3307.
- [Yousef 2005] Galal Yousef S, Rödel J, Fuller Jr. ER, Zimmermann A, El-Dasher BS. Microcrack evolution in alumina ceramics: Experiment and simulation, *J Am Ceram Soc* 2005; 88: 2809–2816.
- [Zhang 2011] Zhang ZH, Topping T, Li Y, Vogt R, Zhou YZ, Haines C, Paras J, Kapoor D, Schoenung JM, Lavernia EJ. Mechanical behavior of ultrafine-grained Al composites reinforced with B<sub>4</sub>C nanoparticles, *Scr Mater* 2011; 65: 652-655.
- [Zhao 2008] Zhao L-D, Zhang B-P, Li J-F, Zhou M, Liu W-S, Liu, Thermoelectric and mechanical properties of nano-SiC-dispersed Bi<sub>2</sub>Te<sub>3</sub> fabricated by mechanical alloying and spark plasma sintering, *J. Journal of Alloys and Compounds* 455 (2008) 259–264
- [Zhu 2005] Zhu B, Asaro RJ, Krysl P, Bailey R. Transition of deformation mechanisms and its connection to grain size distribution in nanocrystalline metals, *Acta Mater* 2005; 53: 4825–4838

7.0 The effect of processing on strain during thermal expansion measurements for  
(Pb<sub>0.95</sub>Sn<sub>0.05</sub>Te)<sub>0.92</sub>(PbS)<sub>0.08</sub>-0.055% PbI<sub>2</sub> thermoelectric material

Jennifer E. Ni<sup>1</sup>, Eldon D. Case<sup>1</sup>, Robert D. Schmidt<sup>1</sup>, Chun-I Wu<sup>2</sup>, Timothy Hogan<sup>2</sup>, Rosa Trejo<sup>3</sup>, Melanie Kirkham<sup>3</sup>, Edgar Lara-Curzio<sup>3</sup>, Mercuri G. Kanatzidis<sup>4</sup>

<sup>1</sup>Chemical Engineering and Materials Science and <sup>2</sup>Electrical and Computer Engineering, Michigan State University, East Lansing, MI, 48824

<sup>3</sup>High Temperature Materials Laboratory, Oak Ridge National Laboratory, Oak Ridge TN 37380

<sup>4</sup>Department of Chemistry, Northwestern University, Evanston, IL, 60208

Abstract

The coefficient of thermal expansion (CTE) is a key design parameter for thermoelectric (TE) materials, especially in energy harvesting applications since stresses generated by such factors as CTE mismatch, thermal gradients and thermal transients scale with the CTE of the TE material. For the thermoelectric material PbTe-PbS (8%), over the temperature ranges of 293 K to 543 K and 293 K to 773 K an average coefficient of thermal expansion,  $\alpha_{\text{avg}}$  of  $21.5 \times 10^{-6} \text{ K}^{-1}$  was measured using (1) dilatometry and (2) high-temperature x-ray diffraction (HT-XRD) for powder, bulk specimens cut from cast ingot, hot pressed billets or pulsed electric current sintering (PECS) processed billets. The CTE values measured via dilatometry and HT-XRD are similar to other Pb-based chalcogenides found in the literature.

Keywords: Thermoelectrics; Coefficient of thermal expansion; Bloating

### 7.1.0 Introduction

For the thermoelectric (TE) material  $(\text{Pb}_{0.95}\text{Sn}_{0.05}\text{Te})_{0.92}(\text{PbS})_{0.08}$ -0.055%  $\text{PbI}_2$  included in this study the  $ZT$  has been reported to be about 1.5 at 642 K [Androulakis 2007], where the dimensionless figure of merit,  $ZT$ , is a measure of the performance of thermoelectric materials

$$ZT = \frac{S^2 \sigma T}{\kappa} \quad (7.1)$$

where  $S$  is the Seebeck coefficient,  $\sigma$  is the electrical conductivity,  $\kappa$  is the thermal conductivity, and  $T$  is temperature.

Given the dependence of  $ZT$  on thermal and electrical conductivity these transport properties are routinely included in studies of TE materials. However the practical application of thermoelectric materials requires that the thermoelectric materials have sufficient mechanical integrity for in-use conditions. Waste heat recovery will subject TE materials to rapid heating and cooling so thermomechanical properties, so designers require detailed information on the temperature-dependent coefficient of thermal expansion (CTE) and elasticity, since for a given temperature change,  $\Delta T$ , the induced temperature-dependent mechanical stresses,  $\sigma(T)$ , is approximated by

$$\sigma(T) = \frac{E(T)\alpha(T)\Delta T}{(1 - \nu(T))} \quad (7.2)$$

where the temperature-dependent coefficient of thermal expansion, the Young's modulus, and Poisson's ratio,  $\alpha(T)$ ,  $E(T)$ , and  $\nu(T)$ , respectively.

In general there is limited thermomechanical data for thermoelectric materials although for  $\text{PbTe-PbS}$  the current authors have reported on the room temperature hardness and elastic moduli [Ni 2010] and the temperature-dependent elastic moduli [Ni in preparation]. This study

determines  $\alpha(T)$  for  $(\text{Pb}_{0.95}\text{Sn}_{0.05}\text{Te})_{0.92}(\text{PbS})_{0.08}$ -0.055%  $\text{PbI}_2$  completes the data set needed to evaluate Eq. (7.2). Along with the room temperature [Ni 2010] and high temperature elastic moduli [Ni in preparation] this study comprise a portion of the authors' and co-workers' efforts to characterize the temperature-dependent elasticity of LAST [Ren 2009 E LAST], PbTe [Ren 2008 E PbTe], and the skutterudites  $\text{Co}_{0.95}\text{Pd}_{0.05}\text{Te}_{0.05}\text{Sb}_3$  and  $\text{Ce}_{0.9}\text{Fe}_{3.5}\text{Co}_{0.5}\text{Sb}_{12}$  skutterudites [Schmidt 2012]. In addition to reporting E,  $\alpha(T)$  was determined for LAST (lead-antimony-silver-tellurium) [Ren 2009 CTE] and  $\text{Co}_{0.95}\text{Pd}_{0.05}\text{Te}_{0.05}\text{Sb}_3$  and  $\text{Ce}_{0.9}\text{Fe}_{3.5}\text{Co}_{0.5}\text{Sb}_{12}$  skutterudites [Schmidt 2012]. For LAST compositions, this group has also evaluated the composition dependence of hardness [Ren 2008 Hcomp] and elastic modulus [Ren 2007 Ecomp] as well as the porosity-dependence of room temperature moduli for LAST [Ni 2009] and PbTe-PbS [Ni in press].

In both metals [Oppenheimer 2010] and ceramics [O'Brien 1985, Kingery 1976], bloating, which is swelling, blistering or an increase porosity in the bulk material, sometimes occurs in specimens densified using elevated temperature and pressure, such as the hot pressing and PECS processes used in this study, when a densified specimen is thermally annealed without a confining pressure [Ni in press, Schmidt 2011]. Bloating can result from a decomposition reaction in which a gaseous species evolves internally during thermal annealing in the absence of an external confining pressure [Kingery 1976]. In this study, bloating refers to an increase in porosity due a post-densification annealing.

Specifically for thermoelectrics, both the thermal conductivity and electrical conductivity will decrease with increasing porosity [Rice 1998]. A decrease in thermal conductivity and electrical conductivity can affect ZT (Eq. (7.1)). In addition to thermal conductivity and

electrical conductivity mechanical properties, such as Young's modulus [Ni 2009], hardness and fracture strength, decrease with increasing porosity [Rice 1998].

In this study, the coefficient of thermal expansion,  $\alpha(T)$ , was measured for powder specimens and bulk cast, hot pressed, and pulsed electric current sintered (PECS) specimens. The  $\alpha(T)$  was measured using (1) dilatometry and (2) high temperature x-ray diffraction from room temperature up to a maximum temperature of 663 K. Dilatometry measurements also indirectly monitored possible bloating in bulk specimens. Possible bloating due to post-densification annealing was also monitored using scanning electron microscopy (SEM).

## 7.2.0 Experimental procedure

### 7.2.1 Specimen preparation

The PbTe-PbS ingots were cast in a rocking furnace using constituent powders that were at least 99.99% pure. The cast ingots were either (i) cut into parallelepipeds or (ii) milled into powders for subsequent densification via hot pressing (HP200, Thermal Technology LLC, Santa Rosa, CA) or pulsed electric current sintering (SPS 10-4, Thermal Technology LLC, Santa Rosa, CA). The powder was dry milled (DM) [Pilchak 2007], wet milled (WM) or dry/wet milled (WM) [Hall 2009] in a planetary mill (PM100, Retsch, Newtown, PA) (Table 7.1). Powder characterization was performed using a laser scattering apparatus (Saturn Digisizer, Micromeritics, Norcross, GA) a scanning electron microscope (SEM). After densification, the grain sizes were measured on micrographs of fracture surfaces using a linear intercept method and a stereo projection factor of 1.5 [Fullman 1953].

Table 7.1a The processing conditions for specimens included in this study that were measured using dilatometry (TMA), high-temperature x-ray diffraction (HT-XRD) and scanning electron microscopy (SEM) All PbTe-PbS powder and bulk specimens have the same composition,  $(\text{Pb}_{0.95}\text{Sn}_{0.05}\text{Te})_{0.92}(\text{PbS})_{0.08-0.055\%} \text{PbI}_2$

Specimen Label	SiC nanoparticle additions	Powder Processing Technique	Densification method	Sintering Max Temp/Pressure/Time	MT <sup>a</sup>
CIW040S	0.0 vol%	None	Cast	Cast	TMA
HP-53	0.0 vol%	WM (H) <sup>b</sup>	Hot pressed	723 K /74.4 MPa/120 min	SEM, TMA
HP -54	0.0 vol%	WM (H) <sup>b</sup>	Hot pressed	723 K /74.4 MPa/120 min	SEM, TMA
HP -55	0.0 vol%	WM (E) <sup>c</sup>	Hot pressed	723 K /74.4 MPa/120 min	SEM, TMA
PECS-02	0.0 vol%	WM (E) <sup>c</sup>	PECS <sup>e</sup>	823 K /60 MPa/20 min	SEM
PECS-10S	0.0 vol%	DM <sup>d</sup>	PECS <sup>e</sup>	673 K /60 MPa/20 min	SEM
PECS-11	0.0 vol%	DM <sup>d</sup>	PECS <sup>e</sup>	823 K /60 MPa/20 min	SEM
PECS-15	0.0 vol%	DM <sup>d</sup>	PECS <sup>e</sup>	673 K /60 MPa/20 min	SEM, TMA
PECS-20	0.0 vol%	DM <sup>d</sup>	PECS <sup>e</sup>	723 K /60 MPa/20 min	SEM
PECS-23	0.0 vol%	DM <sup>d</sup>	PECS <sup>e</sup>	723 K /60 MPa/20 min	SEM
PECS-25	0.0 vol%	DM <sup>d</sup>	PECS <sup>e</sup>	823 K /60 MPa/20 min	SEM
PECS-27	0.0 vol%	DM <sup>d</sup>	PECS <sup>e</sup>	823 K /60 MPa/20 min	SEM
PbTe-PbS-9	0.0 vol%	WM (H) <sup>b</sup>		Powder specimen	HT-XRD
CIW036S	0.0 vol%	WM (H) <sup>b</sup>		Powder specimen	HT-XRD
CIW040S	0.0 vol%	WM (H) <sup>b</sup>		Powder specimen	HT-XRD
CIW063S	0.0 vol%	WM (H) <sup>b</sup>		Powder specimen	HT-XRD
CIW064S	0.0 vol%	DM <sup>d</sup>		Powder specimen	HT-XRD
CIW041S	0.0 vol%	WM (H) <sup>b</sup>		Powder specimen	HT-XRD

<sup>a</sup> Measurement technique

<sup>b</sup> Dry and wet milled with hexane

<sup>c</sup> Wet milled only with ethanol

<sup>d</sup> Dry milled only

<sup>e</sup> Pulsed electric current sintering

Table 7.1b The powder processing, measurement technique, ramp rate and temperature ranges for the CTE measurements included in this study. For each dilatometer test, the atmosphere was flowing 96 % Ar-4% H<sub>2</sub>, whereas for the HT-XRD measurements the atmosphere was 96 % N<sub>2</sub>-4% H<sub>2</sub>.

Specimen Label	Powder Processing Technique	Measurement Technique	Dimensions (mm) <sup>d</sup>	Ramp rate	Temperature range
CIW040S	None	dilatometer	10.3    x 7.6 x 5.1	1.5 K/min	293 K - 663 K
CIW040S	None	dilatometer	10.3    x 7.6 x 5.1	1.5 K/min	293 K - 773 K
HP-53 #C	Wet milled (hexane)	dilatometer	6.3    x 5.0 x 5.0	2 K/min	293 K - 543 K <sup>a</sup> 293 K - 603 K
HP-54 #2	Wet milled (hexane)	dilatometer	10.0    x 5.0 x 7.0	2 K/min	293 K - 603 K <sup>b</sup> 293 K - 663 K
HP-54 #3	Wet milled (hexane)	dilatometer	10.0    x 6.9 x 4.9	1.5 K/min	293 K - 603 K
HP-55 #2	Wet milled (ethanol)	dilatometer	9.9    x 6.8 x 6.0	2 K/min	293 K - 603 K <sup>b</sup> 293 K - 663 K
HP-55 #3	Wet milled (ethanol)	dilatometer	9.9    x 6.9 x 6.0	1.5 K/min	293 K - 663 K
HP-55 #9	Wet milled (ethanol)	dilatometer	6.05    <sup>c</sup>	2 K/min	293 K - 603 K <sup>b</sup> 293 K - 663 K
PECS -17	Dry milled only	dilatometer	4.1    x 5.4 x 4.6	1.5 K/min	293 K - 663 K
PECS-15	Dry milled only	dilatometer	8.9    x 5.0 x 3.9	1.5 K/min	293 K - 663 K
PECS -15	Dry milled only	dilatometer	8.9    x 5.0 x 3.9	2 K/min	293 K - 603 K <sup>b</sup> 293 K - 663 K
PbTe-PbS 9	Wet milled (hexane)	HT-XRD	Powder specimen	3 K/min	293 K - 603 K
CIW036S	Wet milled (hexane)	HT-XRD	Powder specimen	3 K/min	293 K - 663 K
CIW040S	Wet milled (hexane)	HT-XRD	Powder specimen	3 K/min	293 K - 663 K
CIW063S	Wet milled (hexane)	HT-XRD	Powder specimen	3 K/min	293 K - 663 K
CIW064	Dry milled only	HT-XRD	Powder specimen	3 K/min	293 K - 693 K
CIW041S	Wet milled (hexane)	HT-XRD	Powder specimen	3 K/min	293 K - 693 K

<sup>a</sup> half cycles 1-6: 293 K - 543 K, half cycles 9-12: 293 K - 603 K

<sup>b</sup> half cycles 1-6: 293 K - 603 K, half cycles 9-12: 293 K - 663 K

<sup>c</sup> Only one set of parallel surfaces

<sup>d</sup> The dimension that was parallel to the probe is identified by ||

### 7.2.2 Microstructural analysis via scanning electron microscopy

The size, shape and volume density of the pores were examined using micrographs from scanning electron microscopy. Bloating was monitored on fresh fracture surfaces of as-densified and post-densification PbTe-PbS specimens using scanning electron microscopy. The as-densified specimens were annealed at maximum temperatures between 693 K to 936 K for 2 hours in a flowing Ar (96%) – H<sub>2</sub> (4%) atmosphere..

### 7.2.3 Thermal expansion experimental procedure

Two independent experimental techniques were used for thermal expansion measurements on the PbTe-PbS specimens included in this study: (i) a dilatometer (Thermomechanical Analyzer, TMA, Q400, TA Instruments, New Castle, DE) for the bulk specimens and (ii) x-ray diffraction for powder specimens.

#### 7.2.3.1 Dilatometry measurements

For the temperature-dependent thermal expansion measurements of the bulk parallelepiped-shaped specimens via dilatometry, a 0.25 N force was applied to the silica dilatometer rod prior to commencing the thermal expansion measurements. The force was held constant throughout testing. To reduce oxidation during testing in the unsealed TMA chamber, the chamber was flushed with a flowing atmosphere of 50 mL/min of 96% - argon/4% hydrogen gas for one hour prior to heating the chamber. The gas flow was continued during the entire time that the chamber was heated or cooled. For the dilatometry measurements, for each specimen, the thermal expansion measurements were performed on six to twelve half thermal cycles, where a heating and a cooling half cycle comprises a full thermal cycle. The specimens were either (i) continuously cycled for three or four full thermal cycles from room temperature to 603 K, 663 K,

693 K, or 773 K (Table 7.1b) or (ii) continuously cycled for three full thermal cycles from room temperature up to 543 K or 603 K and then subsequently cycled an additional three full thermal cycles from room temperature to either 603 K or 663 K (Table 7.1b).

### 7.2.3.2 High-temperature x-ray diffraction measurements

The lattice parameter for the both powder specimens was determined using high-temperature x-ray diffraction (XRD, X'Pert Pro MPD X-Ray Diffraction System, PANalytical, Natick, MA) and the CTE was computed from the temperature-dependent changes in lattice parameter. The XRD measurements were calibrated by running NIST standard reference material LaB<sub>6</sub> powder, SRM 660a, from 19° to 140°2 $\theta$ , with a step size of 0.01700°2 $\theta$  and a scan rate of 45.72 seconds per step. For each of the five dry milled only and one dry/wet milled powder specimens in this study, an XRD run was performed from 15° to 140° 2 $\theta$ , with step size of 0.001°, using a Cu K- $\alpha$  source and a fixed divergence slit size of 0.25. Using heating and cooling rates of 5 K/minute and a nitrogen atmosphere the maximum temperatures ranged from 543 K to 663 K (Table 7.1b). A XRD scan was collected at 30 K intervals with a 5 minute dwell time for each of the scans. At each 30 K interval, the lattice parameters were computed using a Reitveld analysis program (X'Pert analysis, PANalytical, Natick, MA).

## 7.3.0 Results and discussion

### 7.3.1 Possible bloating monitored via SEM

For the as-densified fracture surfaces, each of the hot pressed and PECS-processed specimens had spherical and quasi-spherical pores that ranged from submicron to three microns in diameter (Figure 7.1). The mean grain size for the specimens densified from wet milled

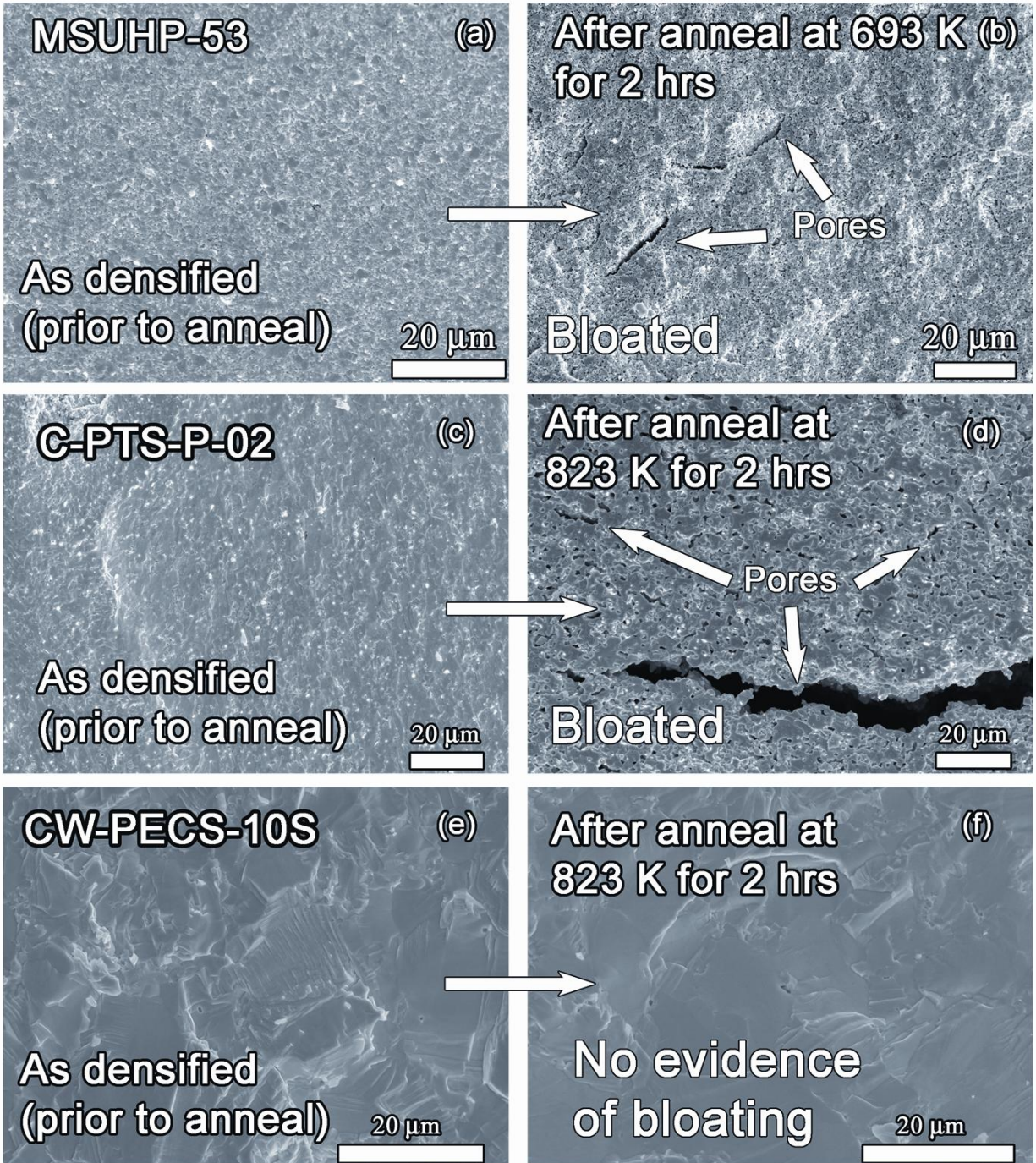


Figure 7.1: The micrographs for the as-densified fractured surfaces for PbTe-PbS (a) hot pressed, HP-53 and PECS-process specimens (c) PECS-02, and (e) PECS-10S do not show bloating. The annealed internal fractured surfaces for (b) HP-53 and (d) PECS-02 surfaces did show evidence of bloating, whereas PECS-10S, processed from dry milled powders, did not show evidence of bloating. Table 7.1a gives the processing conditions for micrographs (a) – (f). All post-densification annealing was performed in flowing 96% Ar + 4% H<sub>2</sub> gas.

powders (Table 7.1) was roughly 1.6 microns. The specimens densified from dry milled only powders mean grain size was approximately 5 microns.

After annealing up to 936 K, each of the six thermally annealed PbTe-PbS specimens processed from dry milled only powders showed no observable bloating (Table 7.1, Figure 7.1). In contrast, the hot pressed (Figure 7.1b) and PECS-processed (Figure 7.1d) specimens annealed over 693 K showed observable bloating. After the post-densification annealing the quasi-spherical pores ranged in size between three and ten microns (Figure 7.1b and 7.1d). In addition, there were long lenticular pores that were 15 microns wide and over 100 microns long (Figure 7.1d). Thus, in this study, bloating is suppressed for PECS processed powders that were dry milled only (no wet milling) at least under the conditions of a 2 hour anneal at 823 K in an flowing 96% argon/4% hydrogen environment (Table 7.1).

However, bloating may occur in the dry milled only PECS specimens at higher annealing temperature and/or annealing longer times. Further post-densification annealing studies will be conducted to investigate the possible bloating in the  $(\text{Pb}_{0.95}\text{Sn}_{0.05}\text{Te})_{0.92}(\text{PbS})_{0.08}$ -0.055%  $\text{PbI}_2$  specimens for annealing times up to 24 hours and annealing temperatures up to 900 K.

For both the PbTe-PbS included in this study and included in previous studies, the bloating is likely linked with a volatile phase that generates a gaseous phase (and hence bloating) upon annealing the specimens outside the confining pressure of PECS or a hot press.

### 7.3.2 Thermal Expansion Results

#### 7.3.2.1 CTE measurements via dilatometer (TMA)

The average linear CTE,  $\alpha_{\text{CTE}}$ , was calculated between 325 K and 595 K for each half cycle for the 11 specimens using

Table 7.2. The mean CTE, calculated from the TMA thermal expansion data for four hot pressed (HP- specimens), one PECS pressed (PECS- specimens) and two cast ingot (CIW) ( $\text{Pb}_{0.95}\text{Sn}_{0.05}\text{Te}_{0.92}(\text{PbS})_{0.08}$ -0.055%  $\text{PbI}_2$  specimens. The specimens were thermally cycled three or four times from room temperature to a maximum temperature, which is indicated in the table. The temperature range over which the data was analyzed was 325 K – 595 K.

<b>Specimen Label</b>	<b>Fabrication technique</b>	<b>Maximum temperature</b>	<b>Mean CTE (<math>\times 10^6 \text{ K}^{-1}</math>)</b>
CIW040S	Cast	603 K	$21.5 \pm 0.1$
CIW040S	Cast	773 K	$21.5 \pm 0.1$
HP-53 #C	Hot pressed	543K, 603 K <sup>a</sup>	$21.7 \pm 0.3$
HP-54 #2	Hot pressed	603K, 663 K <sup>a</sup>	$21.9 \pm 0.1$
HP-54 #3	Hot pressed	603 K	$21.3 \pm 0.3$
HP-55 #1	Hot pressed	603K, 663 K <sup>a</sup>	$21.1 \pm 0.1$
HP-55 #2	Hot pressed	603K, 663 K <sup>a</sup>	$21.6 \pm 0.1$
HP-55 #3	Hot pressed	693 K	$21.4 \pm 0.1$
PECS -15	PECS	663 K	$21.4 \pm 0.1$
PECS -15	PECS	603K, 663 K <sup>a</sup>	$21.7 \pm 0.1$

<sup>a</sup>This specimen was thermally cycled for six half cycles to the first temperature, and then subsequently cycled an additional six half cycles to the second temperature

$$\alpha_{\text{avg}} = \frac{1}{L_{T_{\text{min}}}} \frac{L_{T_{\text{max}}} - L_{T_{\text{min}}}}{T_2 - T_1} \quad (7.3a)$$

where  $L_{T_{\text{min}}}$  and  $L_{T_{\text{max}}}$  are the length of the specimen at 325 K and 595 K, respectively and  $T_{\text{min}}$  and  $T_{\text{max}}$  are temperatures 325 K and 595 K, respectively (Table 7.2).

For each half thermal cycle of the (i) six hot pressed specimens, (ii) one PECS processed specimen and (iii) two cast PbTe-PbS specimens, the average CTE values were between  $21.3 \times 10^{-6} \text{ K}^{-1}$  to  $21.5 \times 10^{-6} \text{ K}^{-1}$  (Table 7.2).

Thus, despite the fact that the specimens were processed via three different techniques, namely cast, hot pressed and PECS processed, the average CTE values were very similar (Table 7.2). The consistency among the average CTE values for each half cycle might be expected since the CTE is relatively insensitive to microstructural parameters such as porosity and grain size [Rice 2000, Charvat 1957, Panigrahi 2005, Turi 1995].

For the 10 specimens, the mean  $\alpha_{\text{avg}}$  was approximately  $21.5 \times 10^{-6} \text{ K}^{-1}$  (Table 7.2). The mean  $\alpha_{\text{avg}}$  was calculated without the first heating cycle, HT1, as settling of the dilatometer probe on the specimen during the first heating cycle can result in a hysteresis between the first heating cycle and the cooling cycle [Ren 2009 CTE] (Figure 7.2).

An unrecovered dimensional change was observed between the half cycles for the hot pressed specimens thermally cycled at  $T > 603 \text{ K}$  (Figure 7.2). This will be discussed further in Section 7.3.3.

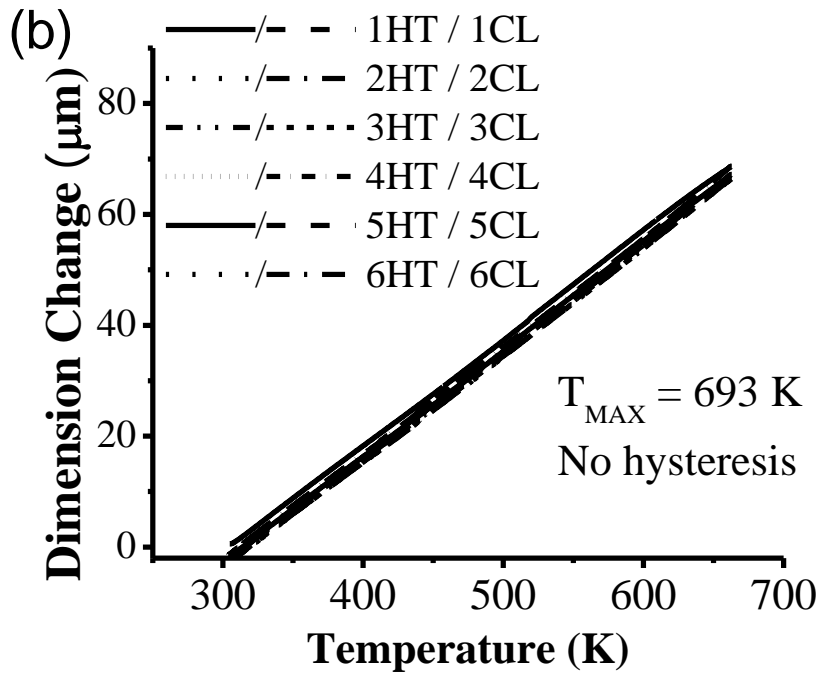
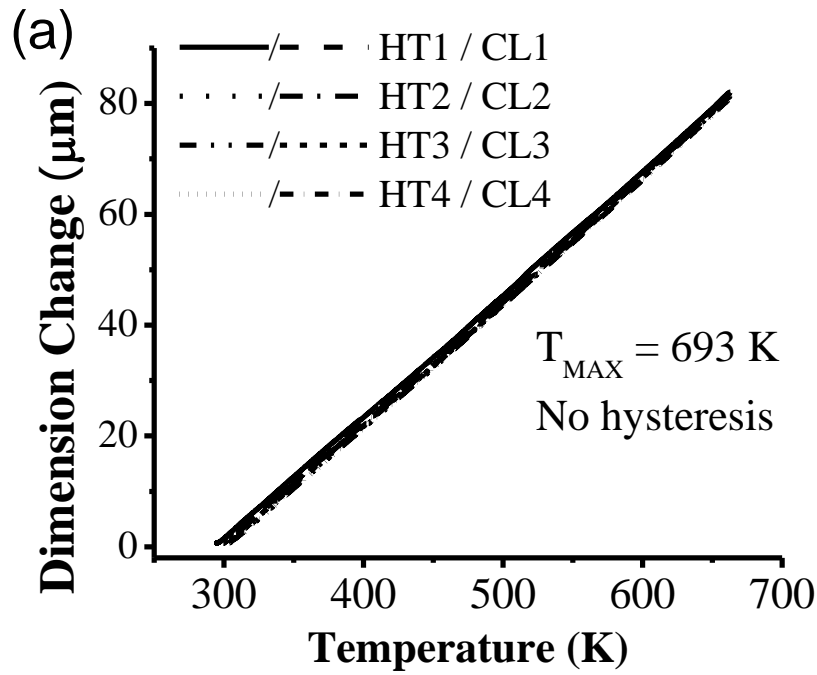


Figure 7.2

Figure 7.2 (cont'd)

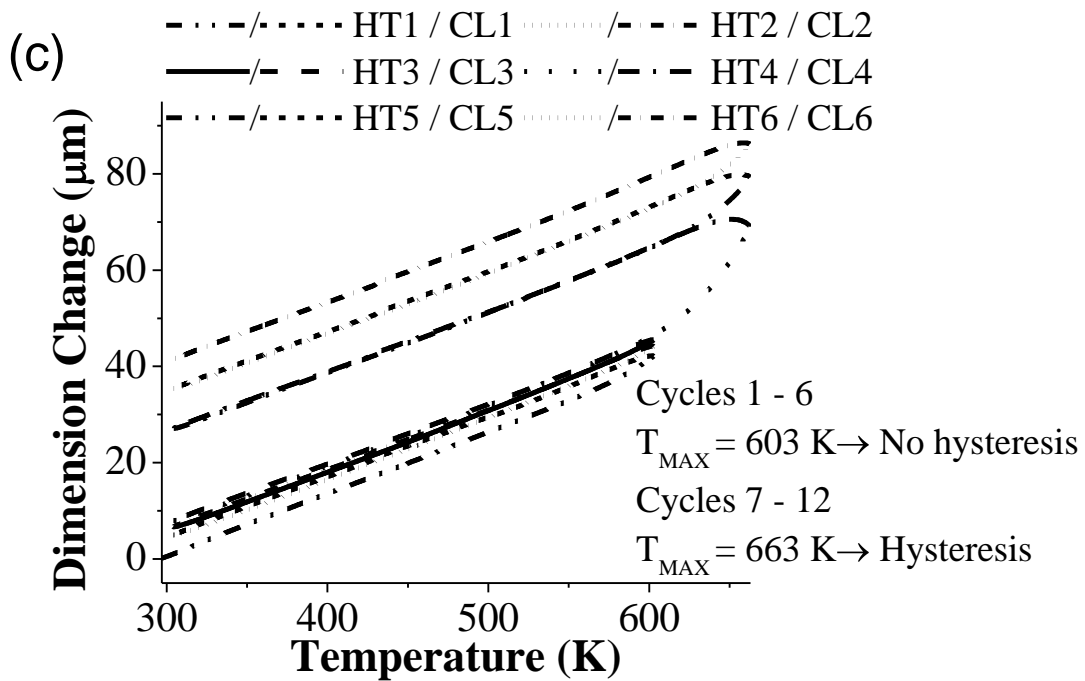


Figure 7.2 (cont'd) The dimensional change as a function of temperature for (a) a cast ingot (CIW040S) from room temperature to 693 K, (b) a PECS-processed specimen (PECS-15) from room temperature to 663 and (c) a hot pressed specimen (HP-55) from room temperature to 603 K and 663 K. For MSUHP-55 #1, hot pressed from wet milled powders, the hysteresis between heating and cooling increased when the maximum temperature increased from 603 K to 663 K. Although a hysteresis between the heating and cooling curves was observed for the hot pressed specimen, no hysteresis between the heating and cooling curves was observed for the cast ingot and the PECS-processed specimen.

Table 7.3 For six powder PbTe-PbS specimens thermally cycled over the given temperature range, the average coefficient of thermal expansion,  $\alpha(T)$ , measured using HT-XRD. Equation (7.3b) described well the temperature dependence of the lattice parameter. The least-squares fit of the data to equation (7.3b) yielded a coefficient of determination,  $r^2$ , greater than 0.992 in each case.

<b>Powder Name</b>	<b>Powder Processing Method</b>	<b>Fabrication Technique</b>	<b>Temperature range (K)</b>	<b>Average <math>\alpha(T)</math> (<math>10^{-6} \text{ K}^{-1}</math>)</b>	<b><math>r^2</math></b>
CIW041S	Wet milled (hexane)	Powder	300 – 693 K	$20.9 \pm 0.1$	0.999
CIW064S	Dry milled only	Powder	300 – 693 K	$20.9 \pm 0.1$	0.999
PbTe-PbS-9	Wet milled (hexane)	Powder	300 – 603 K	$21.7 \pm 0.2$	0.998
CIW036S	Wet milled (hexane)	Powder	300 – 663 K	$21.7 \pm 0.3$	0.992
CIW040S	Wet milled (hexane)	Powder	300 – 663 K	$21.1 \pm 0.3$	0.994
CIW063S	Wet milled (hexane)	Powder	300 – 663 K	$21.4 \pm 0.3$	0.993

### 7.3.2.2. CTE measurements via x-ray diffraction

For six different powder specimens annealed up to 693 K using high temperature x-ray diffraction (HT-XRD), the mean coefficient of thermal expansion,  $\alpha_{\text{mean}}$ , was  $21.4 \pm 0.3 \times 10^{-6} \text{ K}^{-1}$  (Table 7.3). The temperature-dependent coefficient of thermal expansion,  $\alpha(T)$ , was calculated using

$$a_0(T) = \alpha(T)(T - T_{\text{RT}}) + a_{0\text{-RT}} \quad (7.3b)$$

where  $a_0(T)$  was the temperature-dependent lattice parameter,  $T$  was temperature in Kelvin,  $T_{\text{RT}}$  was the room temperature, and  $a_{0\text{-RT}}$  is the lattice parameter at room temperature. During heating of HT-XRD measurements, for each of the five powder specimens, a peak appeared at approximately 440 K, identified as PbSnS, that was present during cooling. The PbSnS peak d-spacing was  $2.97852 \text{ \AA}$  and hkl was [002]. Upon the emergence of the PbS peak, the lattice parameter increased (Figure 7.3). The average CTE,  $\alpha(T)$ , was therefore calculated from the temperature dependent lattice parameter during cooling for each of the six powder specimens (Figure 7.3).

### 7.3.2.3 Comparison of the CTE results to the literature

For the specimens PbTe-PbS included in this study, the mean CTE over the temperature range from room temperature to 603 K was about  $21.5 \times 10^{-6} \text{ K}^{-1}$  for the cast, hot pressed and PECS processed specimens (Table 7.2 and Figure 7.1), which is comparable to the CTE values determined for other PbTe-based thermoelectric materials [Ren 2009, Houston 1968]. For example, the average CTE values ranged from 20 to  $24 \times 10^{-6} \text{ K}^{-1}$  (Table 7.4) measured by

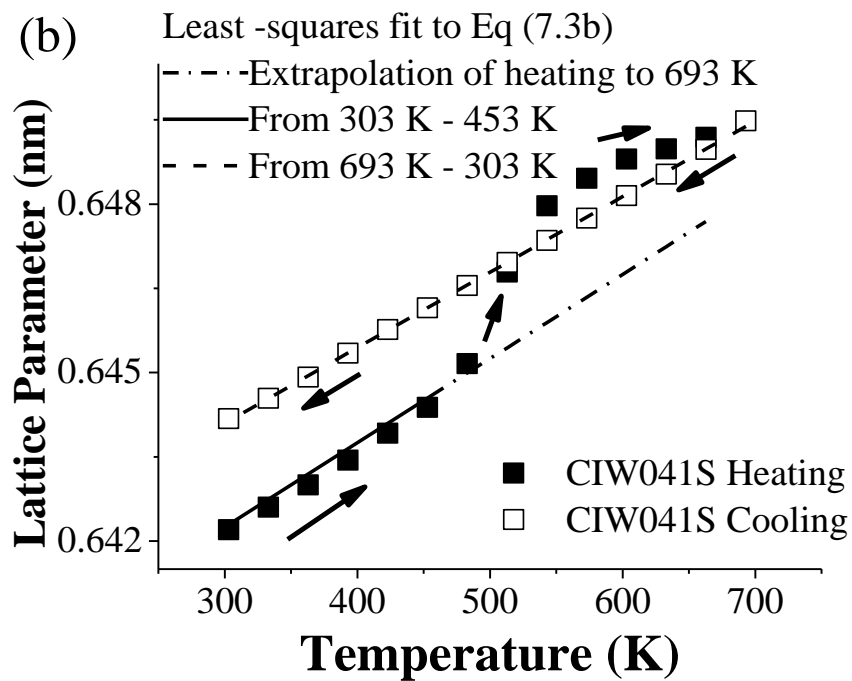
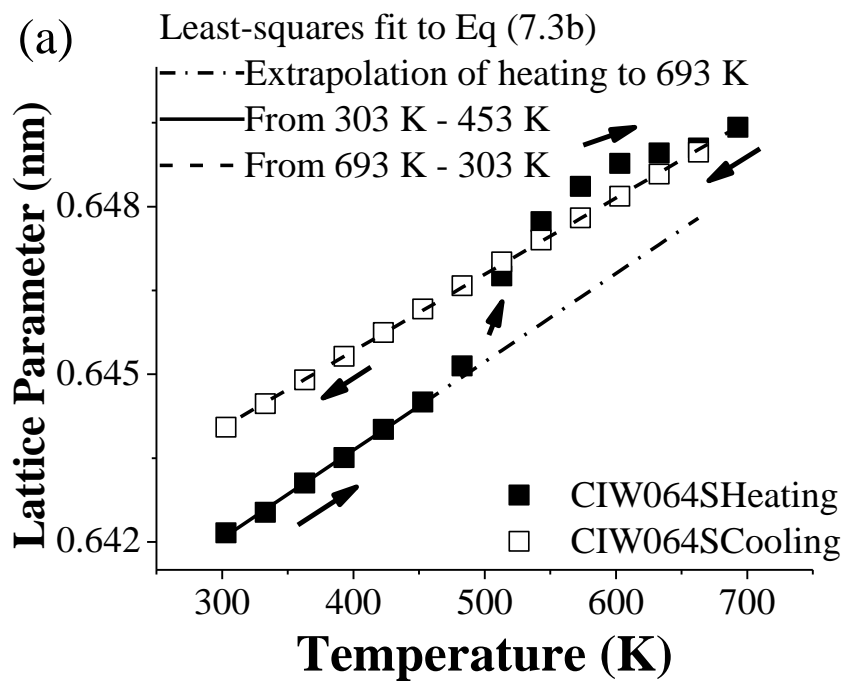


Figure 7.3

Figure 7.3 (cont'd)

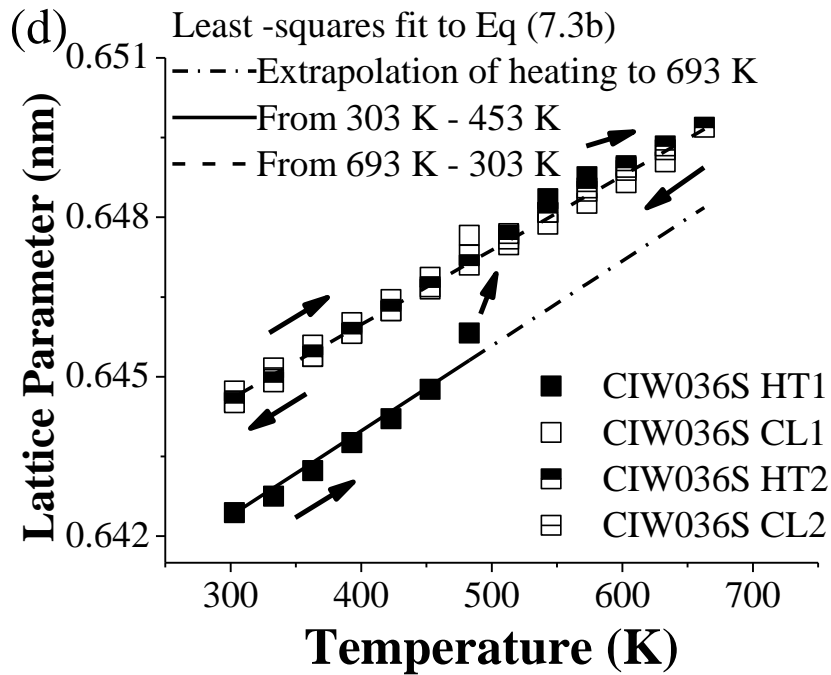
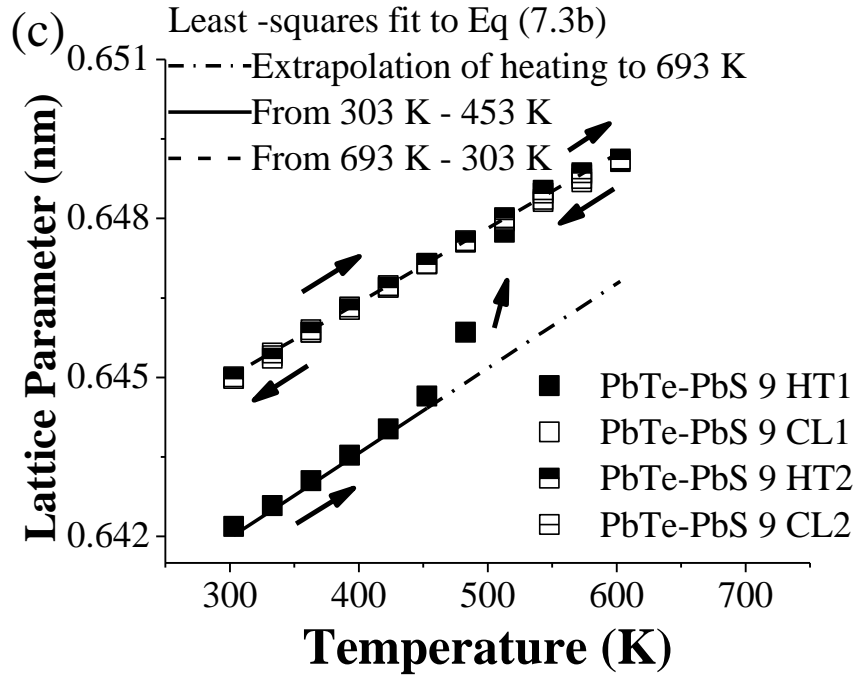


Figure 7.3 (cont'd)

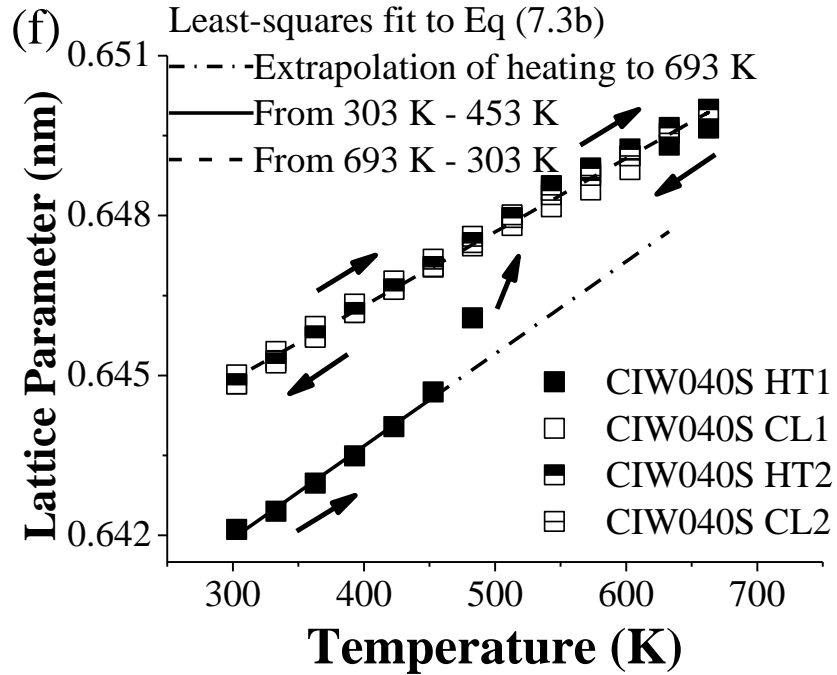
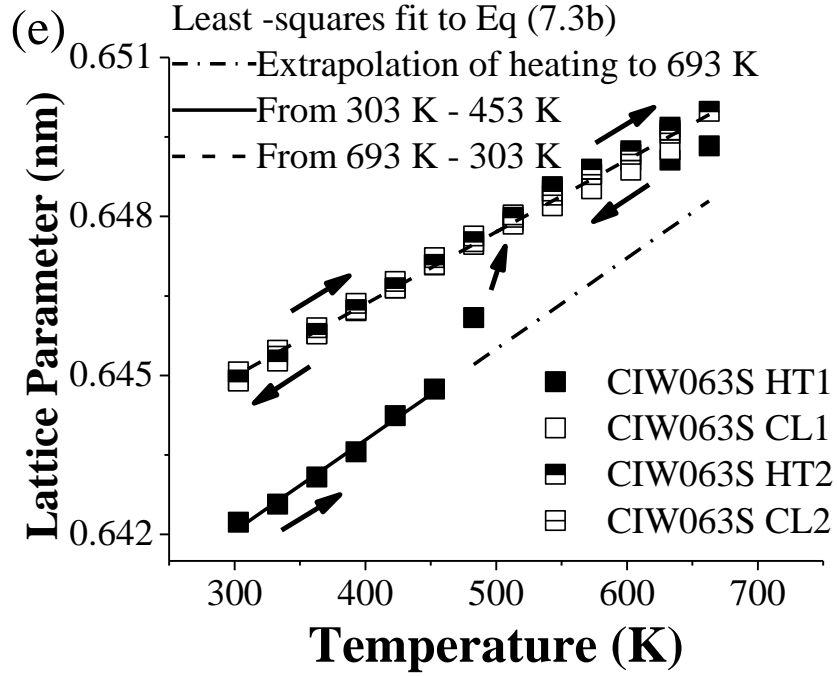


Figure 7.3 (cont'd) The apparent shift in lattice parameter at about 450 K to 500 K is likely correlated with the appearance of a PbSnS peak in HT-XRD that begins to appear at roughly 440 K. For powder specimens that were (a) dry milled only and (b) – (f) wet and dry milled (Table 7.1a) the shift in lattice parameter occurred only during the first thermal cycle. The solid lines represent the least-squares fit of equation (7.3b) between 303 K and 453 K for the first thermal cycle. The dashed-dot line is an extrapolation of the temperature-dependent lattice parameter during heating to 693 K. The dashed lines represent the least-square fit of the temperature-dependent lattice parameter heating and cooling data to equation (7.3b). The arrows indicate the cycling direction.

Table 7.4 The average CTE for thermoelectrics in the literature. The fabrication technique, density, temperature range, and measurement method for each composition.

Specimen Composition	Fabrication Technique	Density (g/cm <sup>3</sup> )	Temperature range (K)	Measurement Method	Average CTE (10 <sup>-6</sup> K <sup>-1</sup> )	Reference
Ag <sub>0.86</sub> Pb <sub>19</sub> Sb 1.0Te <sub>20</sub> (N155)	Cast	8.16	RT - 673	Dilatometer	22.1 ± 0.3	[Ren 2009 CTE]
Ag <sub>0.86</sub> Pb <sub>19</sub> Sb 1.0Te <sub>20</sub> (HP20)	Hot pressed	8.06	RT - 673	Dilatometer	22.2 ± 0.4	[Ren 2009 CTE]
Ag <sub>0.43</sub> Pb <sub>18</sub> Sb 1.2Te <sub>20</sub> (HP6)	Hot pressed	7.58	RT - 673	Dilatometer	20.6 ± 0.5	[Ren 2009 CTE]
Ag <sub>0.43</sub> Pb <sub>18</sub> Sb 1.2Te <sub>20</sub> (N43)	Cast	7.81	RT - 673	Dilatometer	21.0 ± 0.2	[Ren 2009 CTE]
Ag <sub>0.43</sub> Pb <sub>18</sub> Sb 1.2Te <sub>20</sub> (HP6)	Hot pressed	7.58	RT - 623	HT-XRD	20.8 ± 0.5	[Ren 2009 CTE]
Ag <sub>0.86</sub> Pb <sub>19</sub> Sb 1.0Te <sub>20</sub> (N155)	Planetary Milled	Powder	RT - 623	HT-XRD	24.2 ± 0.3	[Ren 2009 CTE]
PbTe	Czochralski Technique	8.24	RT	Capacitive cell	20.4 ± 0.4	[Houston 1968]
PbTe	Czochralski Technique	8.24	RT	Capacitive cell	19.7	[Houston 1968]
Ba <sub>8</sub> Ga <sub>16</sub> Ge <sub>30</sub>	Czochralski Technique	NS <sup>a</sup>	300 - 973	Dilatometer	14.2	[Okamoto 2008]
Sr <sub>8</sub> Ga <sub>16</sub> Ge <sub>30</sub>	Czochralski Technique	NS <sup>a</sup>	300 - 973	Dilatometer	14.1	[Okamoto 2008]
Co <sub>0.95</sub> Pd <sub>0.05</sub> T e <sub>0.05</sub> Sb <sub>3</sub> + 0.1 atomic% Ce	Hot pressed	7.58	323 - 698	Dilatometer	11.6 ± 0.3	[Schmidt 2012 DOI]
Co <sub>0.95</sub> Pd <sub>0.05</sub> T e <sub>0.05</sub> Sb <sub>3</sub>	Planetary Milled	Powder	303 - 773	HT-XRD	10.7 ± 0.2	[Schmidt 2012 DOI]
	Hot pressed	7.27	323 - 723	Dilatometer	10.1 ± 0.2	
Ce <sub>0.9</sub> Fe <sub>3.5</sub> Co <sub>0.5</sub> Sb <sub>12</sub>	Planetary Milled	Powder	303 - 773	HT-XRD	10.3 ± 0.1	[Schmidt 2012 DOI]
	Hot pressed	7.56	323 - 573	Dilatometer	13.0 ± 0.1	
CoSb <sub>3</sub>	Hot pressed	NS <sup>a</sup>	120 - 220	Dilatometer	9.1	[Rogl 2010]

<sup>a</sup>Not given by the author

TMA and HT-XRD for cast and hot pressed LAST thermoelectric materials (lead-antimony-silver-tellurium, with compositions  $\text{Ag}_{0.86}\text{Pb}_{19}\text{Sb}_{1.0}\text{Te}_{20}$  and  $\text{Ag}_{0.43}\text{Pb}_{18}\text{Sb}_{1.2}\text{Te}_{20}$  [Ren 2009]). For undoped PbTe single crystals grown by the Czochralski technique, Houston et al. [Houston 1968] used capacitive cell measurements to measure an average room temperature CTE value of about  $20.4 \times 10^{-6} \text{ K}^{-1}$  (Table 7.4). The CTE of PbTe-based materials is greater than many thermoelectric materials. For example the CTE for clathrates,  $\text{Ba}_8\text{Ga}_{16}\text{Ge}_{30}$  and  $\text{Sr}_8\text{Ga}_{16}\text{Ge}_{30}$ , is  $14.2 \times 10^{-6} \text{ K}^{-1}$  [Okamoto 2008] (Table 7.4) and for skutterudites, the CTE is roughly  $10 \times 10^{-6} \text{ K}^{-1}$  [Rogl 2010, Schmidt 2012 DOI] (Table 7.4).

### 7.3.3 Hysteresis in thermal expansion measured by dilatometry

#### 7.3.3.1 Hysteresis in thermal expansion caused by bloating

In the literature, a hysteresis has been observed in dilatometric  $\Delta L/L_0$  measurements between heating and cooling for alumina-magnesia refractory castables [Auvray 2007, Auvray 2008], SiC refractory castables [Bahloul 2010],  $\text{Al}_{1.8}\text{Mg}_{0.1}\text{Ti}_{1.1}\text{O}_5$  [Giordano 2002], alumina-aluminum titanate composite [Hasselman 1993], alumina-based cement castables [Kakroudi 2009, Nonnet 1999], magnesium dititanate [Bush 1958], beta-eucryptite ( $\text{Li}_2\text{O}-\text{Al}_2\text{O}_3-2\text{SiO}_2$ ) [Bush 1959], cordierite-mullite refractory [Chotard 2008], itacolumite (natural occurring quartz) [Doncieux 2008],  $\text{MgTi}_2\text{O}_5$  [Kyszyk 1973],  $\text{Y}_4\text{Al}_2\text{O}_9$  [Yamane 1995] and thermoelectric skutterudites [Schmidt in press]. The hysteresis in thermal expansion between heating and cooling has been attributed to microcracking due to thermal expansion anisotropy and thermal

expansion mismatch [Auvray 2007, Auvray 2008, Giordano 2002 Bahloul 2010, Kakroudi 2009, Nonnet 1999, Bush 1958, Bush 1959]. Other secondary mechanisms cited were dehydration [Auvray 2007, Auvray 2008] and sintering [Bahloul 2010].

For the hysteresis caused by microcracking, the temperature dependent thermal expansion curve during heating is greater than then thermal expansion curve during cooling [Auvray 2007, Auvray 2008, Bahloul 2010, Bahloul 2010, Hasselman 1993, Kakroudi 2009, Nonnet 1999, Bush 1958, Bush 1959, Bejjauoui 2010, Chotard 2008, Doncieux 2008, Kyszyk 1973, Yamane 1995]. During heating, microcracks in the specimen heal due to diffusion [Case 1983, Hasselman 1993], then during cooling microcracks are reinitiated and reformed, causing the hysteresis between heating and cooling [Case 1983, Hasselman 1993] . However, for the PbTe-PbS specimens in this study and skutterudites in the literature [Schmidt in press], the thermal expansion curve during cooling was greater than the thermal expansion curve during heating, indicating a different hysteresis mechanism, such as bloating. In addition to the hysteresis in thermal expansion, there was also an observable increase in volume fraction porosity (bloating) after post-densification annealing observed in SEM (Section 7.3.1, Figure 7.1).

In this study, possible bloating was measured indirectly using dilatometry by thermal cycling up to 543 K, 603 K, 693 K or 773 K. To quantify the hysteresis, the strain,  $\varepsilon$ , was calculated using

$$\varepsilon = (L_T - L_{iRT})/L_{iRT} \quad (7.4)$$

where  $L_T - L_{iRT}$  is the change in specimen length as a function of temperature and  $L_{iRT}$  is the specimen's length at the beginning of the test. The  $\varepsilon$  was calculated at 10 degree intervals from

room temperature to 543 K, 603 K, 693 K or 773 K for each cycle,  $c_i$ , where “i” represents the  $i$ th half cycle.

The thermal expansion of a polycrystalline alumina specimen, measured between room temperature and 1273 K, with a maximum strain of 0.008, was used as a standard. The cast and PECS-processed PbTe-PbS specimens, which did not have an observable hysteresis in temperature when thermally cycled between room temperature to 773 K and 663 K (Figure 7.2a and 7.2b), respectively, had a maximum strain of 0.008, similar to the strain of the polycrystalline alumina standard.

The five hot pressed PbTe-PbS specimens, thermally cycled between room temperature and  $T < 603$  K (Figure 7.2c and Table 7.2b), had an average maximum strain between 0.006 and 0.008 and no observable hysteresis. In contrast, the four hot pressed specimens thermally cycled between room temperature and  $663 \text{ K} < T < 693 \text{ K}$  average maximum strain was roughly 0.014 and had an observable hysteresis in thermal expansion between heating and cooling when (Figure 7.2).

At room temperature, the average strain (Equation (7.3b)) for cycles  $< c_2$  was  $0.0005 \pm 0.0001$  for the specimens without an observable hysteresis, the alumina standard and the cast (Figure 7.2a) and PECS-processed PbTe-PbS specimens (Figure 7.2b). For the four hot pressed specimens with an observable hysteresis, the average strain (Equation (7.3b)) at room temperature for cycles  $< c_2$  was  $0.004 \pm 0.0001$ , a factor of 40 higher than the microstrain for the specimens with no observable hysteresis. The increase in microstrain for specimens thermally cycled between room temperature and  $T > 603$  K indicates that the bloating-causing decomposition reaction likely occurs at temperatures greater than 603 K.

### 7.3.3.2 Comparison to bloating monitored by elastic moduli measurements

In a previous study of hot pressed PbTe-PbS specimens of the same composition and processing conditions, Ni et al. observed a hysteresis in Young's and shear modulus during thermal cycling up to 663 K [Ni in preparation]. However, the dilatometry in this study is more sensitive to changes in porosity than the temperature-dependent elastic moduli measurements. The change in porosity,  $\Delta P$ , due to the change in Young's modulus,  $E$ , can be extrapolated using the empirical porosity-modulus relationship

$$E(P) = E_0 \exp(-b_{PE}P) \rightarrow \Delta P = b_{PE} [E(P)] \Delta E \quad (7.5)$$

where the  $E_0$ , the Young's modulus of a theoretically dense specimen and  $b_{PE}$ , the change in modulus with porosity,  $P$ , were 1.5 and 56 GPa, respectively. The elastic moduli measurements were sensitive to changes in volume fraction porosity greater than 0.01.

For thermal expansion measurements, dilatometry measures the change in dimension as a function of temperature. There was not a change in mass during thermally cycling, so the fractional change in volume measured using dilatometry resulted in a change in porosity. The change in porosity,  $\Delta P$ , is a function of the change in volume,  $\Delta V$ , due to annealing

$$\Delta P = \frac{m}{\rho_{th} V^2} \Delta V \quad (7.6)$$

where  $m$  is the mass,  $\rho_{th}$  is the theoretical density of the material, and  $V$  is volume. For the specimens in this study,  $\Delta P$  was calculated using equation (7.6) and the measured mass and dimensions before thermal expansion measurements. The change in volume was calculated using the strain at room temperature and the dimensions of the specimens measured using

micrometers before thermal cycling. The dilatometric measurements were more sensitive than elastic moduli measurements and distinguished changes in volume fraction porosity greater than 0.005.

#### 7.4.0 Summary and Conclusions

For PbTe-PbS specimens, the CTE, measured for five powder specimens using HT-HRD and ten bulk specimens using dilatometry, were in agreement, with a mean CTE of  $21.4 \pm 0.3 \times 10^{-6} \text{ K}^{-1}$ . An unrecoverable strain for the hot pressed and wet milled bulk specimens was observed at temperatures greater than 603 K. This hysteresis between thermal cycles is likely a result of bloating. However, there was no hysteresis in the PECS dry milled PECS specimen when annealed up to 663 K or any observable bloating for the micrographs of the fracture surfaces. The bloating in the four hot pressed specimens measured indirectly using dilatometry was confirmed by comparing the porosity of fracture surfaces of as-densified and post-densified surfaces. There was no bloating observed for DM PECS-processed specimens, where as there was bloating at temperatures as low as 693 K for hot pressed specimens.

#### Acknowledgements

The authors acknowledge the financial support of Office of Naval Research Grant N00014-08-1-0613. Equipment purchases were funded by the Defense University Research Instrumentation Program (DURIP) Grant No. N00014-07-1-0735 (Resonant Ultrasound Spectroscopy apparatus and the laser scattering apparatus) and N00014-09-1-0785 (pulsed electric current sintering apparatus) Office of Naval Research. Research through the Oak Ridge National Laboratory's High Temperature Materials Laboratory User Program was sponsored by the U. S. Department of Energy, Office of Energy Efficiency and Renewable Energy, Vehicle Technologies Program. The

authors also acknowledge Ed Timm, Mechanical Engineering Department, Michigan State University and Karl Dersch, Computer and Electrical Engineering Department, for their assistance with hot pressing and cutting selected hot pressed specimens and Pulsed Electric Current Sintering apparatus. All microscopy was performed at the Center for Advanced Microscopy at Michigan State University.

## REFERENCES

## 7.5.0 References

- [Androulakis 2007] Androulakis, J., Lin, C. H., Kong, H. J., Uher, C., Wu, C. I., T, H. Cook, B. A., T, C., Paraskevopoulos, M., Kanatzidis, M. G. *J. Am. Chem. Soc.* 2007, 129, 9780.
- [Auvray 2007] Jean-Michel Auvray, Christian Gault, Marc Huger, Evolution of elastic properties and microstructural changes versus temperature in bonding phases of alumina and alumina–magnesia refractory castables, *Journal of the European Ceramic Society* 27 (2007) 3489–3496
- [Auvray 2008] Jean-Michel Auvray, Christian Gault, Marc Huger, Microstructural changes and evolutions of elastic properties versus temperature of alumina and alumina–magnesia refractory castables *Journal of the European Ceramic Society* 28 (2008) 1953–1960.
- [Bahloul 2010] O. Bahloul, T. Chotard, M. Huger, C. Gault Young’s modulus evolution at high temperature of SiC refractory Castables, *J Mater Sci* (2010) 45:3652–3660
- [Bejjaoui 2010] R. Bejjaoui, A. Benhammou, L. Nibou, B. Tanouti, J.P. Bonnet, A. Yaacoubi, A. Ammar, Synthesis and characterization of cordierite ceramic from Moroccan stevensite and andalusite, *Applied Clay Science* 49 (2010) 336–340
- [Bush 1958] E. A. Bush and F. A. Hummel, “High-Temperature Mechanical Properties of Ceramic Materials: I, Magnesium Ditungstate,” *Journal of the American Ceramic Society*, Volume 41, Issue 6, pages 189–195, June 1958
- [Bush 1959] E. A. Bush and F. A. Hummel, “High-Temperature Mechanical Properties of Ceramic Materials: II, Beta-Eucryptite,” *Journal of the American Ceramic Society*, Volume 42, Issue 8, pages 388–391, August 1959.
- [Charvat 1957] F.R. Charvat, W. D. Kingery, Thermal Conductivity: XIII, Effect of Microstructure on Conductivity of Single-Phase Ceramics, *Journal of the American Ceramic Society*, 40 (1957) 306–315.
- [Chotard 2008] T. Chotard, J. Soro, H. Lemercier, M. Huger, C. Gault, High temperature characterisation of cordierite–mulliterefractory by ultrasonic means, *Journal of the European Ceramic Society* 28 2129–2135 (2008)
- [Doncieux 2008] A. Doncieux , D. Stagnol, M. Huger, T. Chotard, C. Gault, T. Ota, S. Hashimoto, Thermo-elastic behaviour of a natural quartzite: itacolumite, *J Mater Sci* (2008) 43:4167–4174
- [Francome 1958] M. H. Francome, *British Journal of Applied Physics*, 9 (1958) 415.
- [Fullman 1953] R. L. Fullman, Measurement of particle sizes in opaque bodies, *Trans AIME* 197 (1953) 447 – 452.

- [Giordano 2002] L. Giordano, M. Viviania, C. Bottino, M.T. Buscaglia, V. Buscaglia, P. Nannib, Microstructure and thermal expansion of  $\text{Al}_2\text{TiO}_5\text{-MgTi}_2\text{O}_5$  solid solutions obtained by reaction sintering, *Journal of the European Ceramic Society* 22 (2002) 1811–1822
- [Hall 2009] Hall BD, Case ED, Ren F, Johnson J, Timm EJ. Agglomeration during wet milling of LAST (lead-antimony-silver-tellurium) powders, *Mater Chem Phys* 2009; 113: 497- 502.
- [Hasselman 1993] D. P. H. Hasselman, K.Y. Donaldson, E.M. Anderson, T.A. Johnson, Effect of Thermal History on the Thermal Diffusivity and Thermal Expansion of an Alumina–Aluminum Titanate Composite, *J. Am. Ceram. Soc.* 76 (1993) 2180-2184.
- [Houston 1968] B. Houston, R. E. Strakna, H. S. Belson, *J. Appl. Phys.* 39 (1968) 3913.
- [Hsu 2004] KF Hsu, S Loo, F Guo, W Chen, JS Dyck, C Uher, T Hogan, EK Polychroniadis, MG Kanatzidis, *Science*, 303 (2004) 818.
- [Joshi 2008] Giri Joshi, Hohyun Lee, Yucheng Lan, Xiaowei Wang, Gaohua Zhu, Dezhi Wang, Ryan W. Gould, Diana C. Cuff, Ming Y. Tang, Mildred S. Dresselhaus, Gang Chen, and Zhifeng Ren, Enhanced thermoelectric figure-of-merit in nanostructured p-type silicon germanium bulk alloys, *Nano Lett.* 8, 4670-4674, (2008).
- [Kakroudi 2009] M. Ghassemi Kakroudi, E. Yeugo-Fogaing, M. Huger, C. Gault, T. Chotard, Influence of the thermal history on the mechanical properties of two alumina based castables, *Journal of the European Ceramic Society* 29 (2009) 3197–3204.
- [Kanatzidis 2010] M. G. Kanatzidis, Nanostructured Thermoelectrics: The New Paradigm?, *Chem. Mater.* 2010, 22, 648–659.
- [Kuszyk 1973] J. A. Kuszyk and R. C. Bradt, “Influence of Grain Size on Effects of Thermal Expansion Anisotropy in  $\text{MgTi}_2\text{O}_5$ ,” *Journal of the American Ceramic Society*, Volume 56, Issue 8, pages 420–423, August 1973
- [Lin 2009] Lin, H., Bozin, E. S., Billinge, S. J. L., Androulakis, J., Malliakas, C. D., Lin, C. H., Kanatzidis, M. G. *Phys. Rev. B* 2009, 80, (4).
- [Ni 2009] J.E. Ni, F. Ren, E.D. Case, E.J. Timm, Porosity dependence of elastic moduli in LAST (Lead–antimony–silver–tellurium) thermoelectric materials, *Materials Chemistry and Physics* 118 (2009) 459–466.
- [Ni 2010] J.E. Ni, E.D. Case, K.N. Khabira, R.C. Stewart, C-I Wu, Timothy P. Hogan, E.J. Timm, S.N. Girard, M.G. Kanatzidis, Room temperature Young’s modulus, shear modulus, Poisson’s ratio hardness of  $\text{PbTe-PbS}$  thermoelectric materials *Materials Science and Engineering B* 170 (2010) 58–66.
- [Ni in preparation] J.E. Ni, E.D. Case, R.D. Schmidt, C-I Wu, T. Hogan, R.M. Trejo, E. Lara-

Curzio, S N. Girard, M.G. Kanatzidis, Fracture mode, microstructure, and temperature-dependent elastic moduli for thermoelectric composites of PbTe-PbS with SiC nanoparticle additions, to be submitted

[Ni in press] J.E. Ni, E.D. Case, R. Stewart, C-I Wu, T.P. Hogan, M.G. Kanatzidis, Bloating in  $(\text{Pb}_{0.95}\text{Sn}_{0.05}\text{Te})_{0.92}(\text{PbS})_{0.08}$ -0.055% $\text{PbI}_2$  Thermoelectric Specimens as a Result of Processing Conditions Journal of Electronic Materials, DOI: 10.1007/s11664-011-1853-0, in press

[Nonnet 1999] Emmanuel Nonnet, Nicolas Lequeux and Philippe Boch, Elastic Properties of High Alumina Cement Castables from Room Temperature to 1600<sup>o</sup>C, Journal of the European Ceramic Society 19 (1999) 1575-1583.

[O'Brien 1985] O'Brien MH, Hunter Jr. O, Case ED, Mechanical effects of thermal cycling on United States and Australian Synroc-B, J Mater Sci Lett 1985; 4: 367-369.

[Okamoto 2008] Okamoto, N. L., Nakano, T., Tanaka, K., Inui, H., Mechanical and thermal properties of single crystals of the type-I clathrate compounds  $\text{Ba}_8\text{Ga}_{16}\text{Ge}_{30}$  and  $\text{Sr}_8\text{Ga}_{16}\text{Ge}_{30}$ , J. Appl. Phys. (2008) 104: AR 013529.

[Oppenheimer 2009] Oppenheimer S, Dunand DC. Porous NiTi by creep expansion of argon-filled pores, Mater Sci Eng A 2009; 523: 70–76

[Oppenheimer 2010] Oppenheimer S, Dunand DC. Solid-state foaming of Ti-6Al-4V by creep or superplastic expansion of argon-filled pores, Acta Mater 2010; 58: 4387–4397

[Panigrahi 2005] B.B. Panigrahi, V.V. Dabhade, M.M. Godkhindi, Thermal expansion behaviour of nanocrystalline titanium powder compacts, Materials Letters 59 (2005) 2539–254.

[Pilchak 2007] A. L. Pilchak, F. Ren, E. D. Case, E.J. Timm, H.J. Schock, C-I Wu, T.P. Hogan, Characterization of dry milled powders of LAST (lead-antimony-silver-tellurium) thermoelectric material, Phil. Mag. 87 (2007) 4567-4591.

[Poudel 2008] B. Poudel, Q. Hao, Y. Ma, Y. Lan, A. Minnich, B. Yu, X. Yan, D. Wang, A. Muto, D. Vashaee, X. Chen, J.Liu, M.S. Dresselhaus, G. Chen, Z. Ren, Antimony telluride bulk alloys high-thermoelectric performance of nanostructured bismuth, Science 320, 634-638 (2008).

[Ren 2007 Ecomp] F.Ren, E.D.Case, E.J.Timm, H.J. Schock, Young's modulus as a function of composition for an n-type lead-antimony-silver-telluride (LAST) thermoelectric material, Philosophical Magazine, 87 (2007)4907-4934.

[Ren 2008 E PbTe] F. Ren, E.D. Case, J.R. Sootsman, M.G. Kanatzidis, H. Kong, C. Uher, E. Lara-Curzio, R.M. Trejo, The high-temperature elastic moduli of polycrystalline PbTe measured by resonant ultrasound spectroscopy Acta Materialia 56 (2008) 5954–5963.

- [Ren 2008 Hcomp] F. Ren, E.D. Case, E.J. Timm, H.J. Schock, Hardness as a function of composition for n-type LAST thermoelectric material, *Journal of Alloys and Compounds* 455 (2008) 340–345
- [Ren 2009 CTE] F. Ren, B.D. Hall, E.D. Case, E.J. Timm, R.M. Trejo, R.A. Meisner, E. Lara-Curzio, Temperature-dependent thermal expansion of cast and hot-pressed LAST (Pb-Sb-Ag-Te) thermoelectric materials, *Philosophical Magazine*, 89: (2009) 1439 -1455.
- [Ren 2009 E LAST] F. Ren, E.D. Case, J.E. Ni, E.J. Timm, E. Lara-Curzio, R.M. Trejo, C.-H Lin, M.G. Kanatzidis, (Temperature-dependent elastic moduli of lead telluride-based thermoelectric materials, *Philosophical Magazine*, 89 (2009) 143-167.
- [Rice 1998] Rice RW. *Porosity of Ceramics*, New York: Marcel Dekker; 1998.
- [Rice 2000] R. W. Rice, *Mechanical Properties of Ceramics and Composites*, Marcel Dekker Inc., New York, 2000.
- [Rogl 2010] G. Rogl, L. Zhang, P. Rogl, A. Grytsiv, M. Falmbigl, D. Rajs, M. Kreigisch, H. Müller, E. Bauer, J. Koppensteiner, W. Schranz, M. Zehetbauer, Z. Henkie and M.B. Maple, *J. Appl. Phys.* 107 (2010) 043507.
- [Schmidt 2012] R.D. Schmidt, E.D. Case, J.E. Ni, J.S. Sakamoto, R.M. Trejo, E. Lara-Curzio Temperature-dependent Young's modulus, shear modulus and Poisson's ratio of p-type  $\text{Ce}_{0.9}\text{Fe}_{3.5}\text{Co}_{0.5}\text{Sb}_{12}$  and n-type  $\text{Co}_{0.95}\text{Pd}_{0.05}\text{Te}_{0.05}\text{Sb}_3$  skutterudite thermoelectric materials, *Philosophical Magazine*, 92 (2012) 727-759.
- [Schmidt in press CTE] R.D. Schmidt, E.D. Case, J.E. Ni, J.S. Sakamoto, R.M. Trejo, E. Lara-Curzio, E. A. Payzant, M.J. Kirkham, R.A. Peascoe-Meisner, The temperature dependence of thermal expansion for p-type  $\text{Ce}_{0.9}\text{Fe}_{3.5}\text{Co}_{0.5}\text{Sb}_{12}$  and n-type  $\text{Co}_{0.95}\text{Pd}_{0.05}\text{Te}_{0.05}\text{Sb}_3$  skutterudite thermoelectric materials, *Philosophical Magazine*, DOI:10.1080/14786435.2011.644815 in press
- [Turi 1995] T. Turi, U. Erb, *Mater. Sci. Eng. A*, Thermal expansion and heat capacity of porosity-free nanocrystalline materials, 204 (1995) 34-38.
- [Yamane 1995] Hisanori Yamane, Kazuhiro Ogawara, Mamoru Omori, Toshio Hirai, Thermal expansion and a thermal phase transition of  $\text{Y}_4\text{Al}_2\text{O}_3$  ceramics, *Journal of the American Ceramic Society*, 78 : 5, 1230-1232, 1995

## 8.0 Summary and Conclusions

### 8.1.0 Porosity dependence of the elastic moduli for LAST

Similar to other brittle materials [Rice 2000], the hot pressed LAST specimens in this study Young's and shear moduli decrease with porosity can be best described by the linear empirical equations

$$E(P) = E_d(1 - b_{PE}P) \quad \text{and} \quad G(P) = G_d(1 - b_{PG}P). \quad (8.1)$$

over the range of porosity,  $0.01 \leq P \leq 0.14$  (Figure 3.3). For specimens with porosity higher than in this study the exponential form might be a better fit [Rice 1998]. There was scatter in the Poisson's ratio, especially between about  $0.03 \leq P \leq 0.04$ , however, with increasing  $P$ , Poisson's ratio value tended to decrease.

Knowledge of the porosity dependence of the elastic moduli is critical to numerical or analytical stress-strain calculations for both the cast and hot pressed materials. When microcracking is present, understanding the decrement in moduli due to porosity can help us separate the effects of microcracking and porosity for a given porous, microcracked specimen.

### 8.2.0 Room temperature mechanical properties for PbTe-PbS

This is the first study to measure the hardness, fracture toughness and elastic moduli for  $(\text{Pb}_{0.95}\text{Sn}_{0.05}\text{Te})_{0.92}(\text{PbS})_{0.08}$ -0.055%  $\text{PbI}_2$  specimens. As mentioned in the previous section (Section 8.1.0), the elastic moduli are needed for stress-strain analysis. The hardness and fracture toughness are associated with a material's machinability as well as its resistance to wear.

### 8.2.1 Hardness measured via Vickers indentation

The mean hardness of the six dense ( $P = 0.03$ ) hot pressed PbTe-PbS 8% specimens was  $1.18 \pm 0.09$  GPa which is comparable to that of hot pressed LAST ( $\text{Ag}_a\text{Pb}_b\text{Sb}_c\text{Te}_d$ ) (Table 6.1). The mean hardness was  $0.70 \pm 0.06$  for four as-cast specimens, which is 70 % lower than the mean hardness of the hot pressed specimens of same composition (Table 6.1). The higher hardness observed in this study for hot pressed specimens (compared to the as-cast specimens) is likely a grain size effect. Therefore, specimens that are fabricated using powder processing techniques and densified using hot pressing or PECS will likely have better machinability and resistance to wear than those specimens that are cut from cast ingots.

### 8.2.2 Fracture toughness measured via Vickers indentation

Measured using Vickers indentation, the average fracture toughness of the six hot pressed PbTe-PbS specimens with no  $\text{SiC}_{\text{np}}$  was approximately  $0.35 \pm 0.04 \text{ MPa}\cdot\text{m}^{1/2}$  (Table 6.2). The mean fracture toughness is comparable to other thermoelectric materials [Lawn 1977, Uneo 2005, Zhao 2008, Evans 1975] and other chalcogenides [Varshneya 2007, Zhu 2007, Guin 2002].

### 8.2.3 Elastic moduli measured via resonant ultrasound spectroscopy

For PbTe-PbS specimens, the 13 as-densified and 32 post-densification annealed elastic moduli measurements with volume fraction porosities ranging from 0.03 to 0.32 the decrease in  $E$  with increasing  $P$  was consistent with

$$E(P) = E_D \exp(-b_P P) \quad (8.2)$$

where  $E_D$  is the  $E$  when  $P = 0$  and  $b_{PE}$  is a material dependent constant over the porosity range,  $0.03 \leq P \leq 0.21$ . For PbTe-PbS the least-squares fit to the exponential relationship (Eq. 8.2) had an  $r^2 = 0.990$ ,  $b_{PE} = 1.33$  and  $E_D = 56.17$  GPa. The  $E_D$  is consistent with the literature where for single crystal PbTe, the aggregate Young's modulus, 58.08 GPa [Houston 1968] and 56.95 GPa [Einspruch 1963]. As was discussed in Section 8.1.0, knowledge of the  $E$  versus  $P$  relationship are used for stress-strain calculations and decoupling  $E$  decreases due to porosity or microcracking damage.

For the nine as-densified HP and PECS specimens, along with the 32 annealing measurements on the same nine specimens, each of the hot pressed specimens modulus decreased with a corresponding increase in  $P$  after post-densification anneals between 603 K and 693 K (Figures 5.4 and 6.1). The decrease in  $E$  due to post-densification annealing is consistent with an increase in porosity (likely due to bloating). The PECS specimens processed from wet milled powders (Table 5.1) also bloated during post-densification annealing up to 693 K (Figure 5.1) The further implications of bloating during post-densification annealing will be discussed in the following section (Section 8.3.0).

### 8.3.0 Bloating monitored via SEM for PbTe-PbS specimens

Seven PECS-processed dry milled only specimens had no observable bloating for post-densification annealing  $< 936$  K (Figure 5.3). After post-densification annealing  $T < 723$  K hot pressed LAST specimens had observable bloating for post-densification annealing for dry milled only and CGSR specimens (Figure 5.1). In addition, hot pressed and PECS-processed PbTe-PbS specimens had observable bloating for post-densification annealing  $T < 693$  K for dry/wet milled specimens and wet milled only specimens (Figure 5.2).

No observable bloating for the combination of dry milling only and densification via PECS for  $\text{Pb}_{0.95}\text{Sn}_{0.05}\text{Te} - \text{PbS } 8\% + 0.055 \text{ mol\% PbI}_2$  in observation via SEM up to 936 K and when monitored via elasticity measurements up to 773 K. The lack of bloating is perhaps due to the inherent cleaning of surface contamination of the powder particle surfaces during sintering [Groza 1992]. The D/WM process may have produced organic-based residues on the powder particle surface that were not present in the DM powders.

Microstructural instability, such as bloating, during in-use temperatures will cause a decrease in both electrical and thermal conductivity, which in turn can affect ZT (Eq. (1.1)). In addition, the increase in bloating-dependent porosity will decrease both elastic moduli and fracture strength. As the PbTe-PbS TE in-use high temperature will range between 723 K and 823 K, this fabrication technique inhibits (for specimens without  $\text{SiC}_{\text{np}}$ ) or limits (for specimens with  $\text{SiC}_{\text{np}}$ ) bloating during in use conditions, providing a more stable microstructure.

#### 8.4.0 Temperature-dependent elastic moduli and CTE for PbTe-PbS

##### 8.4.1 Temperature dependent elastic moduli measured via RUS

For the 15  $(\text{Pb}_{0.95}\text{Sn}_{0.05}\text{Te})_{0.92}(\text{PbS})_{0.08}-0.055\% \text{ PbI}_2$  heating cooling cycles (11 specimens) included in this study the elastic moduli decreased with increasing temperature, T, according to

$$E = E_{\text{RT}} - b_{\text{TE}}(T - T_{\text{RT}}) \text{ and } G = G_{\text{RT}} - b_{\text{TG}}(T - T_{\text{RT}}) \quad (8.3)$$

where  $b_{\text{TE}}$  and  $b_{\text{TG}}$  describes the Young's and shear modulus-temperature behavior, and the room-temperature,  $T_{\text{RT}}$ , Young's modulus,  $E_{\text{RT}}$ , and shear modulus,  $G_{\text{RT}}$ , values were  $53.0 \pm$

2.2 GPa (Table 6.6) and  $21.2 \pm 0.8$  GPa, respectively. For the PbTe-PbS-SiC<sub>np</sub> composite specimens  $b_{TE}$  and  $b_{TG}$  ranged from 0.020 GPa/K to 0.027 GPa/K and 0.008 GPa/K to 0.011 GPa/K (Table 6.6), respectively. The values for  $b_{TE}$  and  $b_{TG}$  are similar to the slopes for PbTe and PbTe-doped specimens in the literature where  $b_{TE}$  (Eq. 8.3) ranged from 0.017 GPa/K to 0.036 GPa/K [Ren 2009] and  $b_{TG}$  (Eq. 8.3) ranged from 0.008 GPa/K to 0.016 GPa/K [Ren 2009]. The temperature-dependent elastic moduli

#### 8.4.2 Temperature dependent coefficient of thermal expansion measured via dilatometry and high-temperature x-ray diffraction

For temperature ranges of 293 K to 543 K and 293 K to 693 K, the average coefficient of thermal expansion was (i)  $21.5 \pm 0.2 \times 10^{-6} \text{ K}^{-1}$  measured using dilatometry and (ii)  $21.3 \pm 0.4 \times 10^{-6} \text{ K}^{-1}$  measured using high-temperature x-ray diffraction (HT-XRD). These values of CTE agree with similar PbTe-based chalcogenides in the literature with an average CTE of roughly  $20.5 \times 10^{-6} \text{ K}^{-1}$  [Houston 1968, Ren 2009]. The coefficient of thermal expansion was used to calculate the change in dimensions during high-temperature RUS measurements.

#### 8.4.3 Bloating monitored using HT-RUS and dilatometry

Hot pressed specimens showed a hysteresis in elastic moduli (Figure 6.5) and thermal expansion (Figure 7.1) between heating and cooling when thermally cycled over 603 K. In contrast, the PECS-processed specimens showed no hysteresis in both the elastic moduli (Figure

6.1) and thermal expansion (Figure 7.1) measurements between heating and cooling up to 693 K.

However, the bloating monitored using temperature-dependent elastic moduli measurements could only distinguish changes in volume fraction porosity that were greater than 0.01. In comparison, the dilatometry measurements of the thermal expansion were sensitive to changes in  $P$  as low as 0.006. Therefore, though RUS is a non-destructive method to monitor changes in elastic moduli with temperature, unsurprisingly, dilatometry has a higher sensitivity to changes in porosity.

#### 8.5.0 Room temperature elastic moduli for LLZO

This work (Appendix A) presents the first room temperature Young's modulus, shear modulus, bulk modulus, Poisson's ratio, and hardness values for  $\text{Li}_7\text{La}_3\text{Zr}_2\text{O}_{12}$  garnet fabricated using hot pressing. The mean Vickers hardness was  $6.3 \pm 0.3$  GPa and  $5.2 \pm 0.4$  for the  $P = 0.03$  and  $0.06$  hot pressed LLZO specimens, respectively. The Young's modulus was  $149.8 \pm 0.4$  GPa for  $P = 0.03$  and  $132.6 \pm 0.2$  GPa for  $P = 0.06$ .

As this is the first work in the literature for the mechanical properties of the  $\text{Li}_7\text{La}_3\text{Zr}_2\text{O}_{12}$  composition, the values of hardness and elastic moduli were compared to the  $H$ ,  $E$ , and  $G$  of other garnet materials in the literature. The mechanical properties were consistent with the trend (equation (A.2)) of a power law decrease in  $E$  (Fig. A.2a),  $G$  (Fig. A.2b), and  $H$  (Fig. A.2c). The elastic moduli measured in this study are used to help model stress-strain calculations that a solid-state battery undergoes during in use conditions.

## 8.6.0 Future Work

### 8.6.1 Higher purity SiC<sub>np</sub>

Currently limited bloating is observed in dry milled PECS-processed specimens with SiC<sub>np</sub>. The vendor specified purity of the SiC<sub>np</sub> is 95% metals basis. The limited bloating could be a result of contaminants on the SiC<sub>np</sub> powder particle surfaces that are resistant to the PECS “cleaning” process. A bloating study of higher purity SiC<sub>np</sub> powders (for example vendor specified 99% purity, Alpha Aesar) in PbTe-PbS is needed to investigate this further.

### 8.6.2 SiC<sub>np</sub> fracture toughness

The fracture mode changed from transgranular to intergranular for PbTe-PbS specimens with and without SiC<sub>np</sub>, respectively. The change of fracture mode may indicate a possible change in fracture toughness [ Kawabata 1977, Mukhopadhyay 2010, Karakasidis 2011]. Unfortunately, Vickers indentations failed to produce a complete radial crack system to measure fracture toughness. Future work would involve using a cube corner Berkovich indentation tip to indent the specimens to calculate fracture toughness. The lower crack pop-in thresholds of a cube corner Berkovich indentation tip could potentially cause a complete radial crack system to measure fracture toughness.

### 8.6.3 Fracture strength and Weibull analysis of PbTe-PbS specimens with and without SiC<sub>np</sub>

During in use conditions, the TE materials are subjected to mechanical loads and vibrations, as well as thermal stresses. Therefore, an understanding of the fracture strength for the specimens both with and without SiC<sub>np</sub> are needed for modeling. In addition, as the TE legs are electrically in series, the entire module will fail if one leg fractures. Therefore, a Weibull analysis, which is based on extremal value statistics, is needed to evaluate the fracture strength of brittle materials. Weibull analysis is a "weakest link" model in which failure in brittle materials occurs at the largest flaw.

The fracture strength is measured using either a four point bending or biaxial fracture, with parallelepipeds or cylindrical disks, respectively. To date, we have been unable to fabricate the 20 specimens needed for a complete Weibull analysis.

## REFERENCES

## 8.7.0 References

- [Bateman 1966] T.B. Bateman, Elastic moduli of single crystal europium iron garnet and yttrium iron garnet, *J. Appl. Phys.* 37 (1966) 2194-219
- [Clark 1961] A.E. Clark and R.E. Stranka, Elastic constants of single-crystal YIG, *J. Appl. Phys.* 32 (1961) 1172-1173.
- [Evans 1975] A. G. Evans and H. Johnson, *J. Am. Ceram. Soc.* 58 (1975) 244–249.
- [Graham 1970] L.J. Graham and R. Change, Elastic moduli of single-crystal gadolinium gallium garnet, *J. Appl. Phys.* 41 (1970) 2247-2248.
- [Guin 2002] J.Guin, T. Rouxel, and J. Sangleboeuf, *J. Am. Ceram. Soc.* 85 (2002) 1545–1552.
- [Karakasidis 2011] Karakasidis TE, Charitidis CA. Influence of nano-inclusions' grain boundaries on crack propagation modes in materials, *Mater Sci Eng B* 2011; 176:490–493.
- [Kawabata 1977] Kawabata T, Izumi, O. Relationship between fracture toughness and transgranular fracture in an Al-6.0% Zn-2.5% Mg alloy, *Acta Metall Mater* 1977; 25: 505-512.
- [Lawn 1977] B. R. Lawn and A. G. Evans, *J. Mater. Sci.* 12 (1977) 2195-2199.
- [Mezeix 2006] L. Mezeix and D.J. Green, Comparison of the Mechanical Properties of Single Crystal and Polycrystalline Yttrium Aluminum Garnet, *Int. J. Appl. Ceram. Technol.* 3 (2006) 166–176
- [Mukhopadhyay 2010] Mukhopadhyay A, Chakravarty D, Basu B. Spark Plasma-Sintered WC-ZrO(2)-Co Nanocomposites with High Fracture Toughness and Strength, *J Am Ceram Soc* 2010; 93: 1754–1763.
- [Ren 2009] Ren, F., Case, E. D., Ni, J. E., Timm, E. J., Lara-Curzio, E., Trejo, R. M., Lin, C. -H. and Kanatzidis, M.G. Temperature-dependent elastic moduli of lead telluride-based thermoelectric materials, *Philosophical Magazine*, 89 (2009) 143 —167.
- [Rice 2000] R. W. Rice, *Mechanical Properties of Ceramics and Composites*, Marcel Dekker Inc., New York, 2000.
- [Saunders 1992] G. A. Saunders, S. C. Parker, and N. Benbattouche, H. I. Alberts, Elastic and nonlinear acoustic properties of the terbium iron garnet  $Tb_3Fe_5O_{12}$ , in relation to those of other garnets, *Phys. Rev. B* 46 (1992) 8756 – 8767
- [Schmidt 2012] Schmidt RD, Case ED, Ni JE, Sakamoto JS, Trejo RM, Lara-Curzio E, Temperature-dependent Young's modulus, shear modulus and Poisson's ratio of p-type

Ce<sub>0.9</sub>Fe<sub>3.5</sub>Co<sub>0.5</sub>Sb<sub>12</sub> and n-type Co<sub>0.95</sub>Pd<sub>0.05</sub>Te<sub>0.05</sub>Sb<sub>3</sub> skutterudite thermoelectric materials,” Philosophical Magazine, Philos. Mag., 2012; 92: 727-759

[Simmons 1971] G. Simmons, H. Wang, Single crystal elastic constants and calculated aggregate properties: A handbook, Cambridge, MA, The MIT Press, 1971.

[Uneo 2005] K. Uneo, A Yamamoto, T. Inoue, S. Sodeoka, and H. Obara, J. Alloys Compds. 392 (2005) 295-299.

[Varshneya 2007] A. K. Varshneya and D. J. Mauro, J Non-Cryst Solids 353 (2007) 1291–1297.

[Winkler 1955]H.G.F. Winkler, Struktur und Eigenschaften der Kristalle, Springer Vaerlag, Berlin, Germany, 1955.

[Zhao 2008] L. D. Zhao., B. Zhang, J. Li, M. Zhou. W. Liu, and J. Liu, J. Alloys Compds. 455 (2008) 259-264.

[Zhu 2007] S. Zhu, H. Ma, L. Calvez, X. Zhang, J. Lucas, J. Adam, H. Shang, and T. Rouxel, J Non-Cryst Solids 353 (2007) 1298–1301.

## APPENDICES

## APPENDIX A

This chapter was submitted to Journal of Alloys and Compounds

Appendix A: Room temperature elastic moduli and Vickers hardness of hot pressed LLZO cubic garnet

Jennifer E. Ni<sup>1</sup>, Eldon D. Case<sup>1</sup>, Jeffrey S Sakamoto<sup>1</sup>, Ezhiyl Rangasamy<sup>1</sup>,  
Jeffrey B Wolfenstine<sup>2</sup>

<sup>1</sup>Chemical Engineering and Materials Science Department, Michigan State University,  
East Lansing, MI 48824 USA

<sup>2</sup>Army Research Laboratory, RDRL-SED-C, 2800 Powder Mill Road, Adelphi, MD 20783, USA

ABSTRACT

Cubic garnet  $\text{Li}_{6.24}\text{La}_3\text{Zr}_2\text{Al}_{0.24}\text{O}_{11.98}$  (LLZO) is a candidate material for use as an electrolyte in Li-Air and Li-S batteries. The use of LLZO in practical devices will require LLZO to have good mechanical integrity in terms of scratch resistance (hardness) and an adequate stiffness (elastic modulus). In this paper the powders were fabricated using powder processing. All specimens were then densified via hot pressing. The room temperature elastic moduli (Young's modulus, shear modulus, bulk modulus, and Poisson's ratio) and hardness were measured using resonant ultrasound spectroscopy (RUS), and Vickers indentation, respectively. For volume fraction porosity,  $P$ , the Young's modulus was  $149.8 \pm 0.4$  GPa ( $P = 0.03$ ) and  $132.6 \pm 0.2$  GPa ( $P = 0.06$ ). The mean Vickers hardness was  $6.3 \pm 0.3$  GPa for  $P = 0.03$  and  $5.2 \pm 0.4$  for  $P = 0.06$ .

Keywords: energy storage materials, elasticity, ultrasonics, mechanical properties.

### A.1.0 Introduction

Recently, there has been interest in the development of Li-Air and Li-S batteries for high energy applications [1]. One Li-Air configuration involves the use of a lithium anode in a non-aqueous electrolyte which is separated from an aqueous electrolyte containing the air cathode by a solid state Li-ion conducting membrane [2-4]. For the case of Li-S a possible configuration involves a solid Li-ion conducting membrane separating molten lithium from molten sulfur.

To be used as a membrane in these situations the material must have high relative density, high total Li-ion conductivity and good chemical stability. In addition, the material should also exhibit good mechanical properties. The elastic moduli are needed for stress-strain calculations and hardness is a measure of the resistance to scratching and point contact damage. For example, both Young's modulus and Poisson's ratio are often used to construct stiffness matrices for stress-strain calculations via finite element analyses [5]. One material that has recently become of interest as a possible membrane material for Li-Air and Li-S batteries based on the garnet structure is a cubic  $\text{Li}_7\text{La}_3\text{Zr}_2\text{O}_{12}$  (LLZO). There have been studies on the ionic conductivity and chemical stability of cubic  $\text{Li}_7\text{La}_3\text{Zr}_2\text{O}_{12}$  prepared by powder processed and chemical methods (i.e., Pechini) [6-10].

No mechanical properties are available in the literature for cubic LLZO garnet materials. This study is the first to report the Young's modulus, shear modulus, bulk modulus and hardness of dense, hot pressed cubic  $\text{Li}_{6.24}\text{La}_3\text{Zr}_2\text{Al}_{0.24}\text{O}_{11.98}$ .

### A.2.0 Experimental Procedure

#### A.2.1 Specimen Preparation

Lithium carbonate (Puratronic 99.998%, Alfa Aesar), lanthanum (III) hydroxide (99.95%, Alfa Aesar), zirconium oxide (99.9%, Inframat Advanced Materials LLC) and gamma aluminum oxide (99.9 %, 50 nm, Mager Scientific Inc) precursors were used to synthesize single-phase cubic  $\text{Li}_{6.24}\text{La}_3\text{Zr}_2\text{Al}_{0.24}\text{O}_{11.98}$  (LLZO) [11]. The precursors were mixed in an agate milling vial using a Retsch PM-100 planetary mill. After mixing, the powders were loaded into a stainless steel die and cold pressed into pellets at 100 MPa. The pellets were placed in boron nitride coated  $\text{Al}_2\text{O}_3$  combustion boats (Coors Combustion boat from Sigma Aldrich) fired in air at  $1000^\circ\text{C}$  for 4 hours and reground in an agate milling vial using a Retsch PM-100 planetary mill. The boron nitride (BN) coating prevented the reaction between the  $\text{Al}_2\text{O}_3$  crucible and the LLZO pellets. The reground LLZO powders were hot-pressed at  $1000^\circ\text{C}$  under 40 MPa pressure for 1 hour under flowing argon. The resulting pellet was removed from the hot press and heated in air at  $1000^\circ\text{C}$  for 4 hours to burn off residual graphite from the hot pressing die. The LLZO specimens were mounted in Crystalbond wax (Buehler, Lake Bluff, IL) and cut into rectangular parallelepipeds using a diamond saw.

The bulk densities of the rectangular parallelepiped hot-pressed specimens were determined from the mass and dimensions (Table A.1) measured using a micrometer (Mitutoyo, 293-832, Aurora, IL) and an electronic balance (Ohaus Adventurer, AR2140, Pinebrook, NJ). The electronic balance and the micrometer were calibrated using commercial test weights (1 g, 2 g, 5 g and 10 g, Tromner ASTM class 7) and gauge blocks (ranging in dimension from 1 mm to 20 mm, Mitutoyo Grade 0), respectively.

Table A.1. The specimen geometry, dimensions, density, volume fraction porosity, P and measurement techniques for the LLZO rectangular parallelepiped, RP, and crescent-shaped, CR, specimens included in this study. The specimens were powder processed from ingot and densified by hot pressing. The elastic moduli were measured using resonant ultrasound spectroscopy (RUS) and the hardness was measured via Vickers indentations.

Specimen Label	Specimen geometry	Dimensions	Density (g/cm <sup>3</sup> )	P	Measurement technique
LLZO-01a	RP	7.9 mm x 6.3 mm x 2.8 mm	4.97	0.03	RUS
LLZO-01b	CR	9.0 mm x 4.5 mm <sup>a</sup>	NA <sup>b</sup>	NA <sup>b</sup>	Vickers indentations
LLZO-02a	RP	8.0 mm x 7.1 mm x 2.5 mm	4.78	0.06	RUS
LLZO-02b	CR	7.3 mm x 2.7 mm <sup>a</sup>	NA <sup>b</sup>	NA <sup>b</sup>	Vickers indentations
LLZO-02c	CR	8.2 mm x 3.0 mm <sup>a</sup>	NA <sup>b</sup>	NA <sup>b</sup>	Vickers indentations

<sup>a</sup> Dimensions refer to length and maximum width of the crescent shaped specimens

<sup>b</sup> Not available

The relative density values and hence, the porosity was determined by dividing the bulk density by the  $\rho_{\text{theo}}$  of cubic Al-containing LLZO ( $\sim 5.107 \text{ g/cm}^3$  [9]). Four crescent-shaped specimens were cut from the edges of the disc-shaped hot pressed billets. The resulting parallelepiped specimens were used for elasticity measurements and the crescent-shaped specimens were used for hardness testing (Table A.1). Each of the hardness and elasticity specimens were polished using successively smaller diamond paste with grit sizes down to one micron (Diamond polishing compounds, Leco, St. Joseph, MI).

#### A.2.2 X-ray diffraction and scanning electron microscopy

The microstructure of the hot-pressed specimens was examined on uncoated fracture surfaces using scanning electron microscopy (SEM) with an accelerating voltage of 1 and 3 kV. Phase purity was evaluated from x-ray diffraction data obtained with a Rigaku Ultima III diffractometer using Cu  $K_{\alpha}$  radiation. The lattice constant was determined by obtaining the diffraction data in parallel beam geometry and fitting the data using Rietveld refinement [12] with RIQAS software (Materials Data Inc.).

#### A.2.3 Vickers indentation measurements

The Vickers hardness,  $H$ , was measured using a Shimadzu hardness tester (Shimadzu HMV-2000, Kyoto, Japan). Before indentation, the indenter was calibrated using a commercially available standard hardness block (761-048, Yamamoto Scientific Tools Lab, Co., Ltd., Japan). The average hardness of the LLZO specimens was determined using ten indentations per load on the polished surface at loads of 2.9 N and 4.9 N with a 5 second loading time. To avoid the interference between stress fields of closely spaced indentations or perturbations caused by

specimen edge effects, separation distances of at least 500  $\mu\text{m}$  were maintained between adjacent indentation sites. No indentations were placed closer than roughly 1000  $\mu\text{m}$  from the nearest free edge of the specimen. The H values were calculated using

$$H = \frac{1.8544F}{(2a)^2} \quad (\text{A.1})$$

where F is the applied force and 2a is the diagonal of the diamond indentation impression [13].

#### A.2.4 Resonant ultrasound spectroscopy (RUS) measurements

The elastic moduli were determined using resonant ultrasound spectroscopy (RUS), which is a non-destructive dynamic method. Two piezoelectric transducers induce mechanical vibrations in the specimen and an additional piezoelectric transducer detects the vibrations. Using commercially available software (Quasar, Magnuflux, Albuquerque, NM), the elastic moduli were calculated from the resonant vibrational frequencies, the dimensions and mass of the specimen. Additional details on the RUS experimental procedure are found elsewhere [14].

### A.3.0 Results and Discussion

#### A.3.1 Microstructure and lattice parameter of LLZO specimens

In this study, the LLZO microstructure was observed on a (i) fracture surface of LLZO-01 (Fig. A.1a) and (ii) at five sites approximately three mm apart along a diametral fracture for LLZO-02 (Figs. A.1b- A.1e). Measured using the linear intercept method with a stereographic projection factor of 1.5 [15], the fracture surfaces of hot pressed LLZO-01 and 02 had equiaxed grains with average grain sizes of 4.5 and 5.0 microns, respectively (Fig. A.1a, A.1c- A.1e). The pores were spherical or quasi-spherical with diameters ranging from submicron to roughly

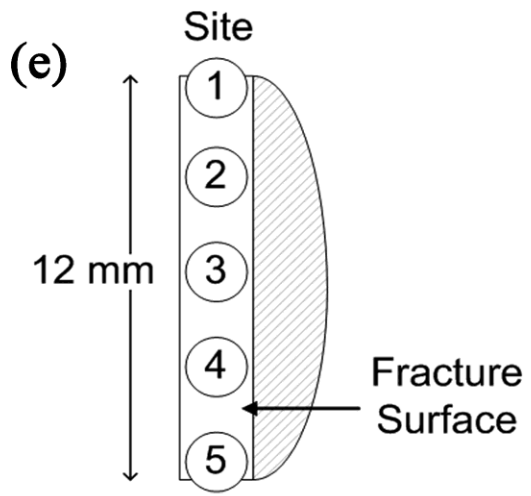
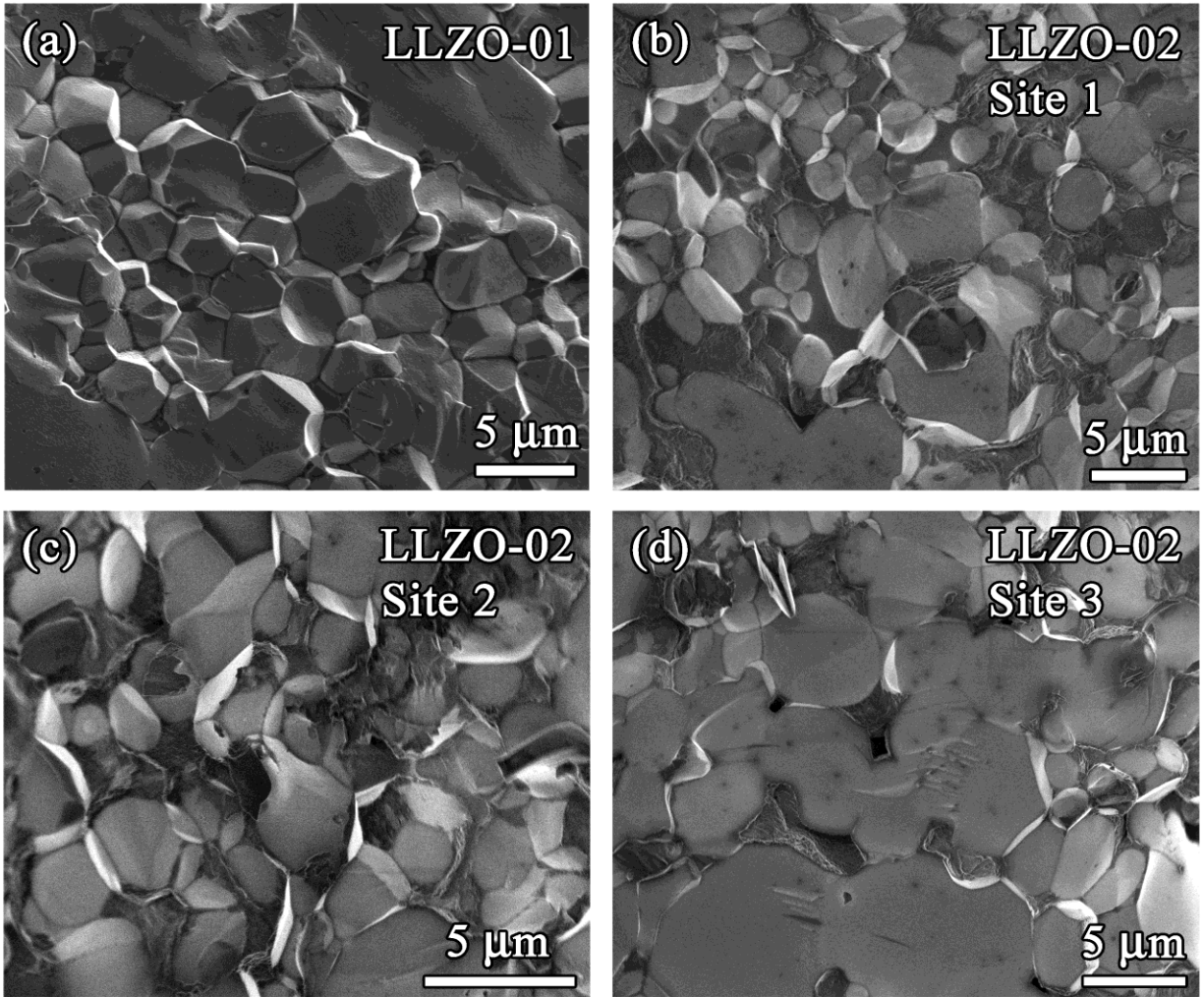


Figure A.1

Figure A.1 (cont'd). The fracture surfaces for the hot pressed specimens (a) LLZO-01 and (c – d) LLZO-02. The fracture surface of LLZO-02 was examined at (e) five different sites along the diametral fracture. Each site was roughly 3 mm apart and sites 1 and 5 were approximately 0.5 mm from the specimen edge. For each micrograph the grain size was measured using the linear intercept method and a stereographic projection factor of 1.5 [15].

three microns. Thus the microstructure appeared to be homogenous for the two hot pressed LLZO specimens included in this study (Fig. A.1).

X-ray diffraction confirmed that after hot-pressing the pellet was single-phase cubic LLZO. After burning off the graphite residue, the pellet appeared bright white. Applying Rietveld analysis to the x-ray-diffraction data yielded a lattice parameter value,  $a_0$ , of 12.9773 Å for the single-phase cubic  $\text{Li}_{6.24}\text{La}_3\text{Zr}_2\text{Al}_{0.24}\text{O}_{11.98}$  included in this study.

### A.3.2 Elastic moduli measured via RUS

With RUS, the mechanical vibrational spectra of two hot pressed LLZO specimens were measured (Tables A.1 and A.2) over the frequency interval from 150 kHz to 1000 kHz. The elastic moduli were calculated using commercially available software. Table A.2 compares the data for elastic moduli for LLZO from this study to polycrystalline yttrium iron garnets from the literature [16, 17].

In this study, for the specimen with  $P = 0.03$ , the Young's modulus,  $E$ , shear modulus,  $G$ , bulk modulus,  $B$  and Poisson's ratio,  $\nu$ , were  $149.8 \pm 0.4$  GPa,  $59.6 \pm 0.1$  GPa,  $102.8 \pm 0.3$  GPa and 0.257, respectively (Table A.2). For  $P = 0.06$ ,  $E = 132.6 \pm 0.2$  GPa,  $G = 52.1 \pm 0.04$  GPa,  $B = 97.7 \pm 0.2$  GPa and  $\nu = 0.274$  (Table A.2). The elastic moduli decreased with increasing porosity in agreement with the general trend for bulk polycrystalline specimens [14, 16, 18 - 20].

### A.3.3 Hardness measured via Vickers indentation testing

For indentation loads of 2.9 N and 4.9 N, the average Vickers hardness (equation (A.1)) of 10 indentations per load was  $6.4 \pm 0.4$  GPa and  $6.2 \pm 0.3$  for  $P = 0.03$  and  $5.2 \pm 0.4$  GPa and  $5.3 \pm 0.4$  GPa for  $P = 0.06$ . The hardness decreases with increasing porosity which is in agreement

Table A.2. The density, volume fraction porosity, P, Young's modulus, E, bulk modulus, B, shear modulus, G, and Poisson's ratio,  $\nu$ , for the hot pressed rectangular parallelepiped specimens included in this study as well as for polycrystalline garnet specimens from the literature.

Specimen Label	Density (g/cm <sup>3</sup> )	P	Measurement Technique	E (GPa)	B (GPa)	G (GPa)	$\nu$	Reference
LLZO-01a	4.97	0.03	RUS	149.8 ± 0.4	102.8 ± 0.3	59.6 ± 0.1	0.257 ± 0.002	This study
LLZO-02a	4.78	0.06	RUS	132.6 ± 0.2	97.7 ± 0.2	52.1 ± 0.04	0.274 ± 0.001	This study
Y <sub>3</sub> Fe <sub>5</sub> O <sub>12</sub> (YIG)	5.01	0.004	sonic resonance technique	196.3	NA <sup>a</sup>	76.5	0.277	[16]
Y <sub>3</sub> Fe <sub>5</sub> O <sub>12</sub> (YIG)	4.572	0.115	Pulse-echo	157.7	117.4	61.8	0.276	[17]
Y <sub>2.9</sub> Fe <sub>5.1</sub> O <sub>12</sub>	4.825	0.064	Pulse-echo	144.9	96.3	58.0	0.249	[17]
Y <sub>2.7</sub> Fe <sub>5.3</sub> O <sub>12</sub>	4.901	0.043	Pulse-echo	98.4	71.3	38.8	0.270	[17]
Y <sub>2.5</sub> Fe <sub>5.5</sub> O <sub>12</sub>	4.833	0.047	Pulse-echo	78.3	64.3	30.2	0.296	[17]

<sup>a</sup> Not available

with the general trend for bulk polycrystalline specimens that H decreases with increasing volume fraction porosity, P [18, 20, 21].

#### A.3.4 Comparison of LLZO elastic moduli and hardness with literature data for other garnets

Since this is the first study of the elastic moduli and hardness for LLZO, it is important to compare values obtained in this study with the moduli and hardness of other garnets in the literature. For a given crystal structure the mechanical properties as a function of lattice parameter,  $a_0$ , can be represented by the empirical relationship

$$A = b_A a_0^{-m_A} \quad (\text{A.2})$$

where mechanical property A is Young's modulus, E, bulk modulus, B, shear modulus, G, or hardness, H. Also  $b_A$  is a material-dependent constant and  $m_A$  is the exponent for the particular mechanical property [22-24]. For example, we use  $m_G$  to denote the exponent for the shear modulus, G, in equation (A.2).

The exponents  $m_B$ ,  $m_G$ , and  $m_H$  (equation (A.2)) depend on the crystal structure [22, 23, 25 - 28] (Table A.3). The  $r^2$  values for the literature data (Table A.3) ranged from 0.983 to 0.999 for the moduli and hardness except for an  $r^2$  of 0.886 for the FCC metals [25], thus equation (A.2) describes relatively well the decrease in B, G, and H with increasing  $a_0$ . Although a direct relationship between Young's modulus and lattice parameter has not been illustrated in the open literature, a number of papers imply that in addition to the shear modulus the Young's modulus is proportional to the interatomic distance [29 - 32]. The E and G values for garnets [33-38], including data for LLZO, are plotted in Fig. A.2a and Fig. A.2b, respectively, as function of  $a_0$ .

Table A.3. The exponents  $m_B$ ,  $m_G$ , and  $m_H$  obtained by a least-squares fit to equation (A.2) for bulk modulus, B, shear modulus, G, and hardness, H data, respectively from the literature for various cubic crystalline structures. The coefficient of determination,  $r^2$ , along with the number of particular compositions of a given crystal structure included in the least-squares fit, N, are listed within the parentheses given below each of the numerical values of the fitted exponents.

Crystal Structure	$m_B^a$ ( $r^2$ , N)	$m_G^b$ ( $r^2$ , N)	$m_H$ ( $r^2$ , N)	Reference
Alkaline halide (rock salt)	NA <sup>e</sup>	$3.2 \pm 0.2$ (0.983, 7)	$3.0^d$ (0.996 <sup>d</sup> , 11)	[22, 23, 24, 25]
Alkaline earth oxides (rock salt)	$3.3 \pm 0.1$ (0.998, 8)	NA <sup>e</sup>	$3.0^d$ (0.998 <sup>d</sup> , 4)	[22, 23]
Alkaline earth sulfides (rock salt)	NA <sup>e</sup>	NA <sup>e</sup>	$3.0^d$ (0.990, 4)	[28]
Face-center-cubic metals	NA <sup>e</sup>	$6.4 \pm 1.3^c$ (0.886, 7)	NA <sup>e</sup>	[25]
Zincblende semiconductors	NA <sup>e</sup>	$4.7 \pm 0.1$ (0.999, 9)	NA <sup>e</sup>	[25]

<sup>a</sup> Gilman reported  $m_B = 4$  for alkaline earth oxides [22]. Gilman did not report the  $r^2$  values [22].

<sup>b</sup> Gilman reported  $m_G = 4$  and 5 for alkaline halides and zincblende semiconductors, respectively [22, 25]. Gilman did not report the  $r^2$  values [22, 25].

<sup>c</sup> Exponent  $m_G$  value excluding thorium. If thorium is included in the analysis, then  $r^2 = 0.758$  and  $m_G = 5.2$ . Gilman reported  $m_G = 6.35$  when the plot included Th [25].

<sup>d</sup> Reported by Gilman [23]. All other exponents and  $r^2$  values in this table were calculated by the present authors.

<sup>e</sup> Not available

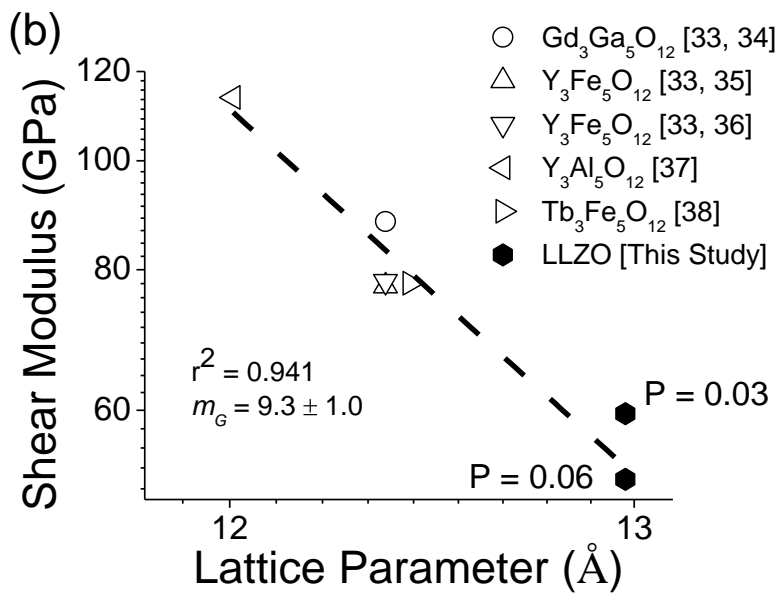
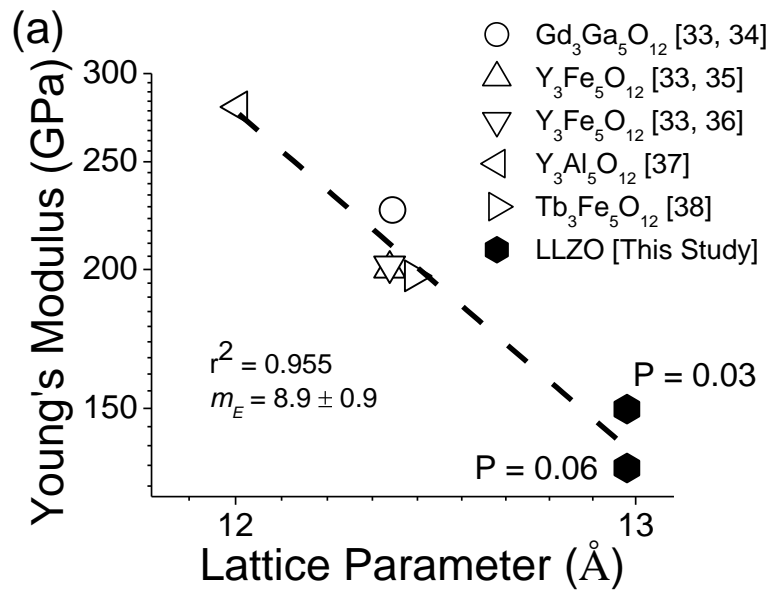


Figure A.2

Figure A.2 (cont'd)

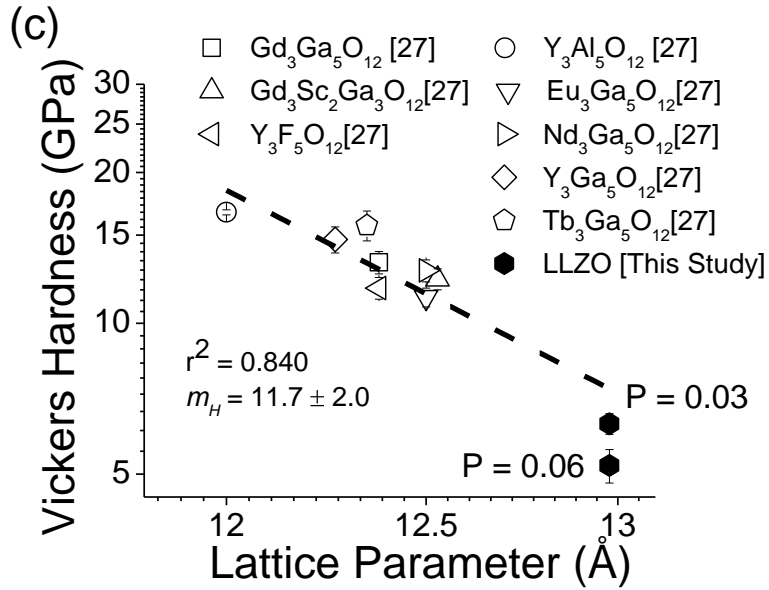


Figure A.2 (cont'd). The (a) Young's modulus, (b) shear modulus, and (c) hardness as a function of lattice parameter for the aggregate average values for single crystal garnet data in the literature (open symbols) and the LLZO garnet specimens in this study (filled symbol). In (a), (b), and (c) the dashed line represents the least-squares fit of equation (A.2) to the data in this study and single crystal garnet in the literature [27, 33 - 38]. The scatter in hardness, H, is likely due to the different mechanisms that can affect H (Section 3.3).

From both Fig. A.2a and A.2b it is observed that the LLZO data is in excellent agreement with single crystal literature data for other garnets. The fit of equation (A.2) to the E and G data for all garnets shown including LLZO, yielded  $r^2$  values of 0.936 and 0.914, respectively (Fig. A.2a and A.2b).

In general H decreases with increasing  $a_0$  via a power law relationship (equation (A.2), Table A.3). In particular for the cubic garnet structure, the H versus  $a_0$  relationship also follows equation (A.2) (Fig. A.2c), as does the cubic garnet LLZO in this study. The hardness data for LLZO (this study) agrees relatively well with the single crystal literature data (Fig. A.2c) [27]. However, the  $r^2$  value of 0.840 indicates greater scatter in the H versus  $a_0$  data fit to equation (A.2) (Fig. A.2c) compared to the scatter observed in E (Fig. A.2a) and G (Fig. A.2b). For both single crystal and polycrystalline garnets, the observed scatter in H (Fig. A.2c) may reflect the H dependence on the load, loading rate, the dislocation density, or residual stresses [39]. In general, for polycrystalline materials, H is also a function of grain size [40] and porosity [20].

The Poisson's ratio,  $\nu$ , (which unlike E, B, and G is relatively insensitive to P [41]) ranged from 0.226 to 0.295 for 21 single crystal and polycrystalline cubic garnets in the literature [16, 17, 33 - 38, 42, 43]. For LLZO in this study, the Poisson's ratio is bracketed by the  $\nu$  values for cubic garnets in the literature (Table A.2).

#### A.4.0 Summary and Conclusions

This work presents the first room temperature Young's modulus, shear modulus, bulk modulus, Poisson's ratio, and hardness values for  $\text{Li}_7\text{La}_3\text{Zr}_2\text{O}_{12}$  garnet fabricated using hot pressing. Dense ( $P = 0.03$  to  $0.06$ ) billets with mean grain sizes of roughly 5 microns were

produced by hot pressing. For loads 2.9 and 4.9 N, the mean Vickers hardness,  $H$ , was  $6.3 \pm 0.3$  GPa and  $5.2 \pm 0.4$  for the  $P = 0.03$  and  $0.06$  hot pressed LLZO specimens, respectively. The Young's modulus was  $149.8 \pm 0.4$  GPa for  $P = 0.03$  (Table A.2) and  $132.6 \pm 0.2$  GPa for  $P = 0.06$ .

The values of  $E$ ,  $B$ ,  $G$ , and  $H$  for  $\text{Li}_7\text{La}_3\text{Zr}_2\text{O}_{12}$  found in this study are consistent with the trend (equation (A.2)) of a power law decrease in mechanical properties with increasing lattice parameter observed for other garnet materials in the literature for  $E$  (Fig. A.2a) [33 - 38],  $B$  [33 - 38],  $G$  (Fig. A.2b) [33 - 38], and  $H$  (Fig. A. 2c) [27].

#### Acknowledgements

We would like to acknowledge the financial support of the U.S. Army Research Office (ARO) and Army Research Laboratory (ARL) under grant W911NF-10-2-0089-P00001.

## REFERENCES

#### A.5.0 References

- [1] J. B. Goodenough, Y. Kim, Challenges for rechargeable batteries, *J. Power Sources* 196 (2011) 6688 - 6694.
- [2] I. Kowalczyk, J. Read, M. Salomon, Li-air batteries: A classic example of limitations owing to solubilities, *Pure Appl. Chem.* 79:5 (2007) 851 - 860.
- [3] S. J. Visco, B. D. Katz, Y. S. Nimon, L. C. De Jonghe, Protected active metal electrode and battery cell structures with non-aqueous interlayer architecture, *US Pat.* 7,282,295 B2 (2007).
- [4] J. Wolfenstine, J. L. Allen, J. Sumner, J. Sakamoto, Electrical and mechanical properties of hot-pressed versus sintered  $\text{LiTi}_2(\text{PO}_4)_3$ , *Solid State Ionics* 180 (2009) 961 - 967.
- [5] J. N. Reddy, *An Introduction to the Finite Element Method*, Third Ed., McGraw-Hill Higher Education, New York, 2006.
- [6] Y. Shimonishi, A. Toda, T. Zhang, A. Hirano, N. Imanishi, O. Yamamoto, Y. Takeda, Synthesis of garnet-type  $\text{Li}_{7-x}\text{La}_3\text{Zr}_2\text{O}_{12-1/2x}$  and its stability in aqueous solutions, *Solid State Ion.* 183 (2011) 48 -53.
- [7] M. Kotobuki, H. Munakata, K. Kanamura, Y. Sato, T. Yoshida, Compatibility of  $\text{Li}_7\text{La}_3\text{Zr}_2\text{O}_{12}$  Solid Electrolyte to All-Solid-State Battery Using Li Metal Anode, *J. Electrochem. Soc.* 157 (2010) A1076 – A1079.
- [8] I. Kokal, M. Somer, P.H.L. Notten, H.T. Hintzen, Sol-gel synthesis and lithium ion conductivity of  $\text{Li}_7\text{La}_3\text{Zr}_2\text{O}_{12}$  with garnet-related type structure, *Solid State Ion.* 185 (2011) 42 - 46.
- [9] C. A. Geiger, E. Alekseev, B. Lazic, M. Fisch, T. Armbruster, R. Langner, M. Fechtelkord, N. Kim, T. Pettke, W. Weppner, Crystal Chemistry and Stability of  $\text{Li}_7\text{La}_3\text{Zr}_2\text{O}_{12}$  Garnet: A Fast Lithium-Ion Conductor, *Inorganic Chem.* 50 (2011) 1089 -1097.
- [10] R. Murugan, V. Thangadurai, W. Weppner, Fast lithium ion conduction in garnet-type  $\text{Li}_7\text{La}_3\text{Zr}_2\text{O}_{12}$ , *Angew. Chem. Int. Ed.* 46 (2007) 7778 - 7781.
- [11] E. Rangasamy, J. Wolfenstine, J.S. Sakamoto, The role of Al and Li concentration on the formation of cubic garnet solid electrolyte of nominal composition  $\text{Li}_7\text{La}_3\text{Zr}_2\text{O}_{12}$ , Submitted to *Solid State Ion.* 2011.
- [12] H. M. Rietveld, A Profile Refinement Method for Nuclear and Magnetic Structures, *J. Appl. Crystallogr.* 2 (1969) 65 - 71.

- [13] J. B. Wachtman, W.R. Cannon, M.J. Matthewson, Mechanical properties of ceramics, 2nd edition, New Jersey, John Wiley and Sons, Inc, 2009.
- [14] F. Ren, E. D. Case, A. Morrison, M. Tafesse, M. J. Baumann, Resonant ultrasound spectroscopy measurement of Young's modulus, shear modulus and Poisson's ratio as a function of porosity for alumina and hydroxyapatite, *Philos. Mag.* 89 (2009) 1163 – 1182.
- [15] R. L. Fullman, Measurement of particle sizes in opaque bodies, *Trans AIME*, 197 (1953) 447 – 452.
- [16] H. M. Chou, E. D. Case, Characterization of some mechanical properties of polycrystalline yttrium iron garnet (YIG) by non-destructive methods, *J. Mater. Sci. Lett.* 7 (1988) 1217-1220
- [17] P.U. Sharma and K.B. Modi, Effect of Fe<sup>3+</sup> substitution on elastic properties of yttrium iron garnet *Phys. Scr.* 81 (2010) 015601
- [18] A. Dey, A. K. Mukhopadhyay, Fracture toughness of microplasma-sprayed hydroxyapatite coating by nanoindentation, *Int. J. Appl. Ceram. Technol.* 8 (2011) 572–590.
- [19] J. E. Ni, F. Ren, E. D. Case, E. J. Timm, Porosity dependence of elastic moduli in LAST (Lead-antimony-silver-tellurium) thermoelectric materials, *Mater. Chem. Phys.* 118 (2009) 459-466.
- [20] R. W. Rice, Porosity of Ceramics, Marcel Dekker, Inc., New York, 1998.
- [21] T. P. Hoepfner, E. D. Case, The influence of the microstructure on the hardness of sintered hydroxyapatite, *Ceram. Int.* 29 (2003) 699-706.
- [22] J.J. Gilman, Micromechanics of flow in solids, New York, McGraw Hill, 1969.
- [23] J.J. Gilman, Chemistry and physics of mechanical hardness, New Jersey, John Wiley and Sons, Inc, 2009.
- [24] W.A. Wooster, Physical Properties and atomic arrangements in crystals, *Rep. Prog. Phys.* 16 (1953) 62 – 82.
- [25] J.J. Gilman, Strength of ceramic crystals, Mechanical behavior of crystalline solids, Proceedings of American Ceramic Society Symposium, Nat'l. Bur. Std. Monograph 59, (1963) 79-102
- [26] A.R. Ruffa, Theory of the electronic polarizabilities of ions in crystals: Applications to the alkali halide crystals, *Phys. Rev.* 130 (1963) 1412-1423.

- [27] D. B. Sirdeshmukh, K. G. Subhadra, K. K. Rag, T. T. Rao, Hardness of crystals with NaCl structure and the significance of the Gilman-Chin parameter, *Cryst. Res. Technol.* 30 (1995) 861 - 866.
- [28] H.G.F. Winkler, *Struktur und Eigenschaften der Kristalle*, Springer Vaerlag, Berlin, Germany, 1955.
- [29] M. Liu, B. Shi, J. Guo, X. Cai, H. Song, Lattice constant dependence of elastic modulus for ultrafine grained mild steel, *Scr. Mater.* 49 (2003) 167–171.
- [30] A.K. Vijh, A correlation between dielectric breakdown and mechanical strengths of alkali halides, *J. Mater. Sci.* 10 (1975) 1087-1088.
- [31] D. Ravinder, K. Vijaya Kumar, B.S. Boyanov, Elastic behaviour of Cu–Zn ferrites, *Mater. Lett.* 38 (1999) 22–27
- [32] A. Makishima, J.D. Mackenzie, Direct calculation of Young's modulus of glass, *J. Non-Cryst. Solids* 12 (1973) 35-45.
- [33] G. Simmons, H. Wang, *Single crystal elastic constants and calculated aggregate properties: A handbook*, Cambridge, MA, The MIT Press, 1971.
- [34] L.J. Graham and R. Change, Elastic moduli of single-crystal gadolinium gallium garnet, *J. Appl. Phys.* 41 (1970) 2247-2248.
- [35] T.B. Bateman, Elastic moduli of single crystal europium iron garnet and yttrium iron garnet, *J. Appl. Phys.* 37 (1966) 2194-219
- [36] A.E. Clark and R.E. Stranka, Elastic constants of single-crystal YIG, *J. Appl. Phys.* 32 (1961) 1172-1173.
- [37] L. Mezeix and D.J. Green, Comparison of the Mechanical Properties of Single Crystal and Polycrystalline Yttrium Aluminum Garnet, *Int. J. Appl. Ceram. Technol.* 3 (2006) 166–176
- [38] G. A. Saunders, S. C. Parker, and N. Benbattouche, H. I. Alberts, Elastic and nonlinear acoustic properties of the terbium iron garnet  $Tb_3Fe_5O_{12}$ , in relation to those of other garnets, *Phys. Rev. B* 46 (1992) 8756 – 8767
- [39] J.J. Gilman, Hardness-A strength microprobe, in: J.H. Westbrook, H. Conrad (Eds.), *The science of hardness testing and it's research applications*, American Society for Metals, United States of America, 1973, pp. 51-74.
- [40] R.W. Rice, *Mechanical Properties of Ceramics and Composites*, Marcel Dekker Inc., New York, 2000.

- [41] A.R. Boccaccini, Comment on Effective Elastic Moduli of Porous Ceramic Materials, *J. Am. Ceram. Soc.* 77 (1994) 2779- 2781.
- [42] R.K. Verma, Elasticity of some high-density crystals, *J. Geophys. Research*, 65 (1960) 757-766.
- [43] N. Soga, Elastic constants of garnet under pressure and temperature, *J. Geophys. Res.* 72 (1967) 4227-4234.

## APPENDIX B

## Appendix B: Milling parameters and processing conditions for PbTe-PbS PECS specimens

The following table and figures report the different powder processing and temperature-pressure-time profiles used to fabricate the PbTe-PbS pulsed electric current sintered (PECS) specimens to date.

Table B.1 The powder processing for each PECS-processed PbTe-PbS specimen. All milling was performed using a planetary mill in an argon-atmosphere glove box. The specimens were fabricated using powders that were (1) dry milled, (2) wet milled, or (3) dry and wet milled. The media referenced in this table were alumina spheres. The mix mill refers to the planetary milling of PbTe-PbS powders with SiC nanoparticles (SiC).

<b>Name</b>	<b>Ingot</b>	<b>Dry Mill</b>	<b>Wet Mill</b>	<b>Mix Mill</b>
C-PTS-P-01	CIW063S	Media=10mm, 114g. 3hr, 150RPM	Media= 140g of D=20mm, 60g of D=3mm. 150 RPM 6hrs 25 ml Hexane	None
C-PTS-P-02	CIW063S	None	Media= 3mm, 200g Al <sub>2</sub> O <sub>3</sub> . 9 hours, 150 RPM, 35ml ethanol	None
C-PTS-P-03	CIW063S	Media=10mm, 114g. 3hr, 150RPM	Media= 140g of D=20mm, 60g of D=3mm. 150 RPM 6hrs 25 ml Hexane	9.9g B1AH+0.1g SiC. Media= 114g of D=10mm 110RPM 3hrs (2.5 vol% SiC)
C-PTS-P-04	CIW063S	None	Media= 3mm, 200g Al <sub>2</sub> O <sub>3</sub> . 9 hours, 150 RPM, 35ml ethanol	9.9g B1A E+0.1g SiC. Media= 114g of D=10mm 110RPM 3hrs (2.5 vol% SiC)
C-PTS-P-05	CIW063S	Media=10mm, 114g. 3hr, 150RPM	Media= 140g of D=20mm, 60g of D=3mm. 150 RPM 6hrs 25 ml Hexane	None
C-PTS-P-06	CIW063S	Media=10mm, 114g. 3hr, 150RPM	Media= 140g of D=20mm, 60g of D=3mm. 150 RPM 6hrs 25 ml Hexane	9.96g B1BH+0.04g SiC. Media= 114g of D=10mm, 110RPM 3hrs (1 vol% SiC)
C-PTS-P-07	CIW063S	Media=10mm, 114g. 3hr, 150RPM	Media= 140g of D=20mm, 60g of D=3mm. 150 RPM 6hrs 25 ml Hexane	9.86g B1BH+0.14g SiC Media= 114g of D=10mm, 110RPM 3hrs (3.5 vol% SiC)

Table B.1 (cont'd)

<b>Name</b>	<b>Ingot</b>	<b>Dry Mill</b>	<b>Wet Mill</b>	<b>Mix Mill</b>
C-PTS-P-08	CIW064S	Media=10mm, 114g. 3hr, 150RPM	None	None
C-PTS-P-09	CIW063S	Media=10mm, 114g. 3hr, 150RPM	Media= 140g of D=20mm, 60g of D=3mm. 150 RPM 6hrs 25 ml Hexane	None
C-PTS-P-10	CIW063S	Media=10mm, 114g. 3hr, 150RPM	Media= 140g of D=20mm, 60g of D=3mm. 150 RPM 6hrs 25 ml Hexane	None
C-PTS-P-11	CIW064S	Media=10mm, 114g. 3hr, 150RPM	None	None
C-PTS-P-12	CIW064S	Media=10mm, 114g. 3hr, 150RPM	None	9.9g B2+0.1g SiC. Media= 114g of D=10mm 110RPM 3hrs (2.5 vol% SiC)
C-PTS-P-13	CIW064S	Media=10mm, 114g. 3hr, 150RPM	None	None
C-PTS-P-14	CIW064S	Media=10mm, 114g. 3hr, 150RPM	None	9.88g B3+0.12g SiC. Media= 114g of D=10mm 110RPM 3hrs (3 vol% SiC)
C-PTS-P-15	CIW064S	Media=10mm, 114g. 3hr, 150RPM	None	None

Table B.1 (cont'd)

<b>Name</b>	<b>Ingot</b>	<b>Dry Mill</b>	<b>Wet Mill</b>	<b>Mix Mill</b>
C-PTS-P-16	CIW066S	Media=10mm, 114g. 3hr, 150RPM	None	9.9g B3+0.1g SiC. Media= 114g of D=10mm 110RPM 3hrs (2.5 vol% SiC)
C-PTS-P-17	CIW064S	Media=10mm, 114g. 3hr, 150RPM	None	9.88g B3+0.12g SiC. Media= 114g of D=10mm 110RPM 3hrs (3 vol% SiC)
C-PTS-P-18	CIW064S	Media=10mm, 114g. 3hr, 150RPM	None	9.92g B3+0.08g SiC. Media= 114g of D=10mm 110RPM 3hrs (2 vol% SiC)
C-PTS-P-19	CIW064S	Media=10mm, 114g. 3hr, 150RPM	None	None
C-PTS-P-20	CIW066S	Media=10mm, 114g. 3hr, 150RPM	None	None
C-PTS-P-21	CIW066S	Media=10mm, 114g. 3hr, 150RPM	None	None
C-PTS-P-22	CIW064S	Media=10mm, 114g. 3hr, 150RPM	None	None
C-PTS-P-23	CIW064S	Media=10mm, 114g. 3hr, 150RPM	None	None
C-PTS-P-24	CIW66S	Media=10mm, 114g. 3hr, 150RPM	None	None

Table B.1 (cont'd)

<b>Name</b>	<b>Ingot</b>	<b>Dry Mill</b>	<b>Wet Mill</b>	<b>Mix Mill</b>
C-PTS-P-25	CIW064S	Media=10mm, 114g. 3hr, 150RPM	None	None
C-PTS-P-26	CIW066S	Media=10mm, 114g. 3hr, 150RPM	None	None
C-PTS-P-27	CIW066S	Media=10mm, 114g. 3hr, 150RPM	None	None
C-PTS-P-28	CIW066S	Media=10mm, 114g. 3hr, 150RPM	None	None
C-PTS-P-29	CIW036S	Media=10mm, 114g. 3hr, 150RPM	Media= 140g of D=20mm, 60g of D=3mm. 150 RPM 6hrs 25 ml Hexane	None
C-PTS-P-30	CIW036S	Media=10mm, 114g. 3hr, 150RPM	Media= 140g of D=20mm, 60g of D=3mm. 150 RPM 6hrs 25 ml Hexane	None
C-PTS-P-31	CIW036S	Media=10mm, 114g. 3hr, 150RPM	Media= 140g of D=20mm, 60g of D=3mm. 150 RPM 6hrs 25 ml Hexane	None
C-PTS-P-32	CIW070S	Media=10mm, 114g. 3hr, 150RPM	None	None
C-PTS-P-33	CIW070S	Media=10mm, 114g. 3hr, 150RPM	None	None
C-PTS-P-34	CIW070S	Media=10mm, 114g. 3hr, 150RPM	None	None

Table B.1 (cont'd)

<b>Name</b>	<b>Ingot</b>	<b>Dry Mill</b>	<b>Wet Mill</b>	<b>Mix Mill</b>
C-PTS-P-35	CIW070S	Media=10mm, 114g. 3hr, 150RPM	None	None
C-PTS-P-36	CIW089S	Media=10mm, 114g. 3hr, 150RPM	None	9.92g PbTe-PbS+0.08g SiC. Media= 114g of D=10mm 110RPM 3hrs (2 vol% SiC)
C-PTS-P-37	CIW089S	Media=10mm, 114g. 3hr, 150RPM	None	9.88g PbTe-PbS +0.12g SiC. Media= 114g of D=10mm 110RPM 3hrs (3 vol% SiC)

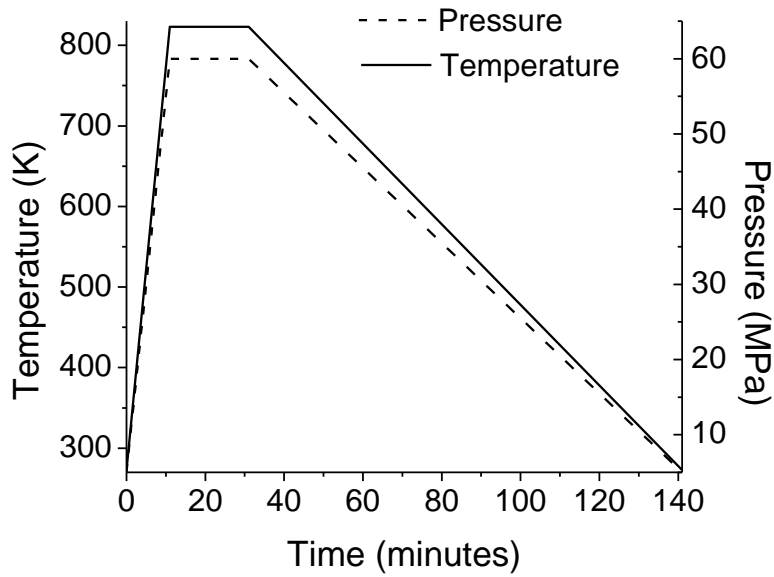


Figure B.1 The temperature-pressure-time profile for PECS-processed specimens, C-PTS-P-01, C-PTS-P-02, C-PTS-P-03, and C-PTS-P-04. The heating rate and cooling rate was 50 K/minute and 5 K/minute, respectively. The ramp rate for pressure during heating was 5 MPa/min and 0.5 MPa/min during cooling. The specimens were sintered at the maximum temperature and pressure for 20 minutes

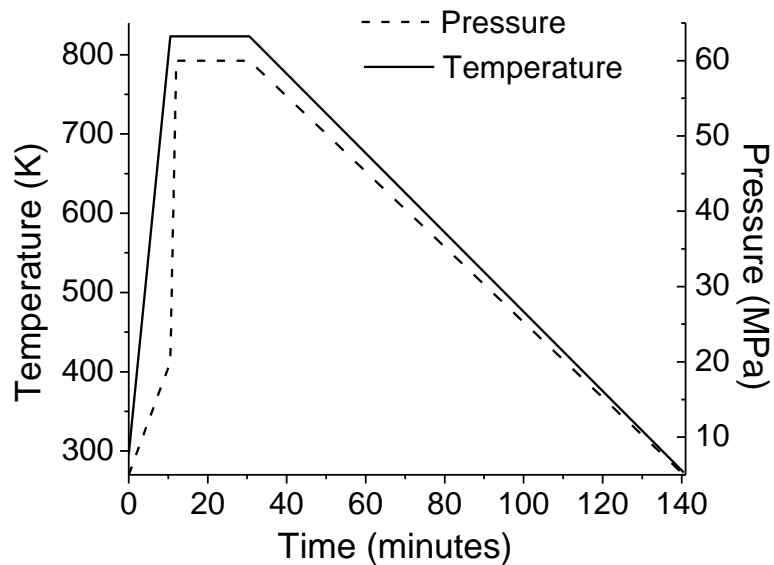


Figure B.2 The temperature-pressure-time profile for PECS-processed specimens, C-PTS-P-05, C-PTS-P-06, and C-PTS-P-07. The heating rate and cooling rate was 50 K/minute and 5 K/minute, respectively. The maximum temperature was held for 20 minutes. The pressure was held at 20 MPa during heating until the specimen reached the maximum temperature. Once the specimen reached 823 K, the pressure was increased to 60 MPa.

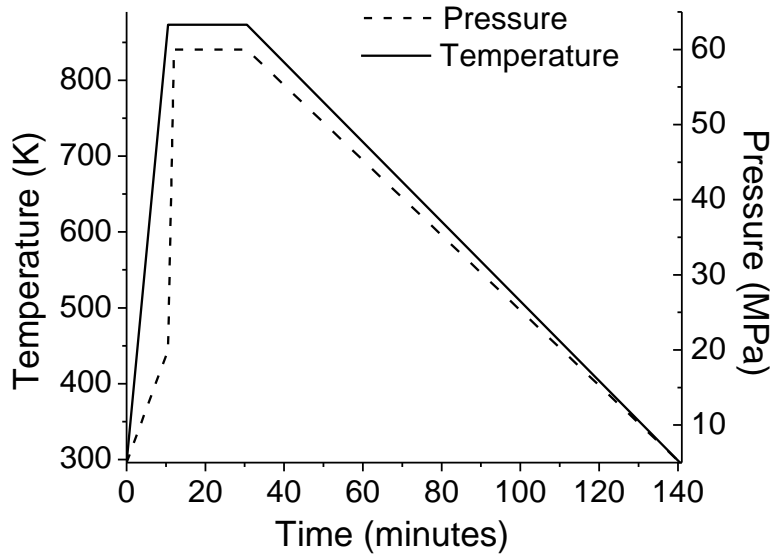


Figure B.3 The temperature-pressure-time profile for PECS-processed specimen, C-PTS-P-08. The heating rate and cooling rate was 50 K/minute and 5 K/minute, respectively. The maximum temperature was held for 20 minutes. The pressure was held at 20 MPa during heating until the specimen reached the maximum temperature, 873 K. Once the specimen reached 873 K, the pressure was increased to 60 MPa.

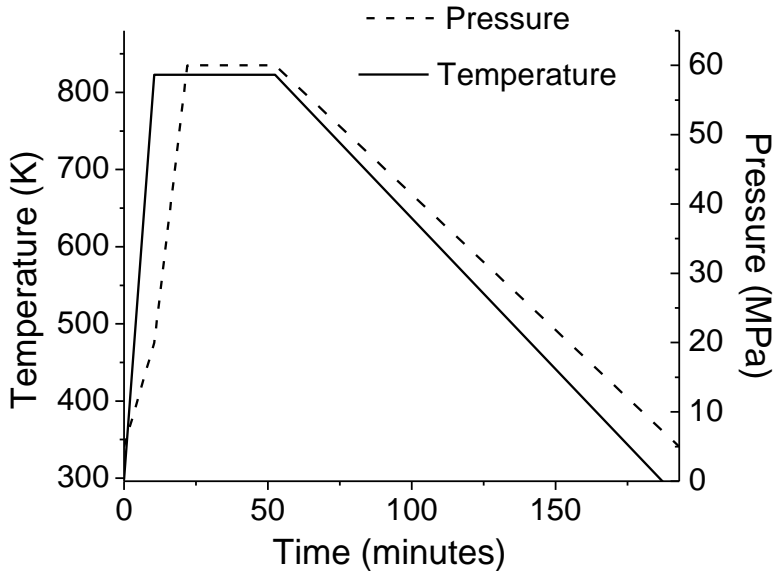


Figure B.4 The temperature-pressure-time profile for PECS-processed specimen, C-PTS-P-09. The heating rate and cooling rate was 50 K/minute and 5 K/minute, respectively. The maximum temperature was held for 30 minutes. The pressure was held at 20 MPa during heating until the specimen reached the maximum temperature, 873 K. Once the specimen reached 823 K, the pressure was increased to 60 MPa. The longer sintering time was due to a miscommunication with Karl Dresch.

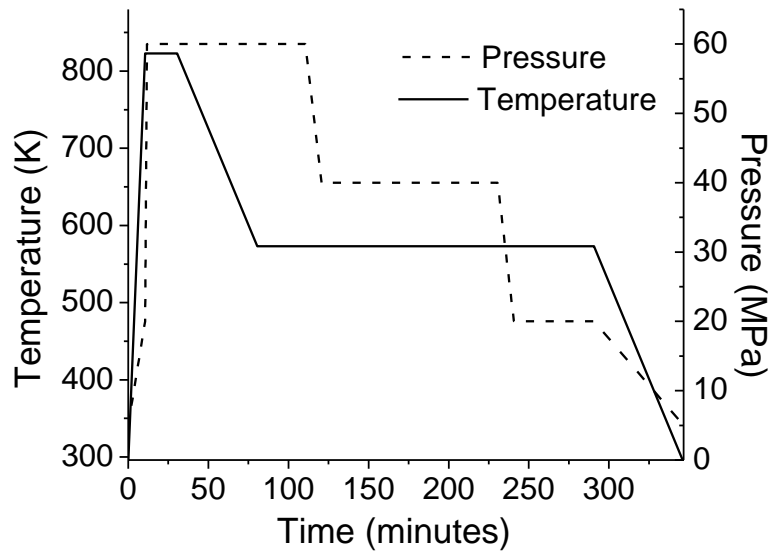


Figure B.5 The temperature-pressure-time profile for PECS-processed specimens, C-PTS-P-10, C-PTS-P-11, and C-PTS-P-12. The heating rate and cooling rate was 50 K/minute and 5 K/minute, respectively. The maximum temperature was held for 20 minutes. The pressure was held at 20 MPa during heating until the specimen reached the maximum temperature. Once the specimen reached 823 K, the pressure was increased to 60 MPa. To reduce possible residual stresses, the specimen was cooled to 573 K and thermally annealed for 120 minutes. The pressure was slowly reduced in steps during cooling.

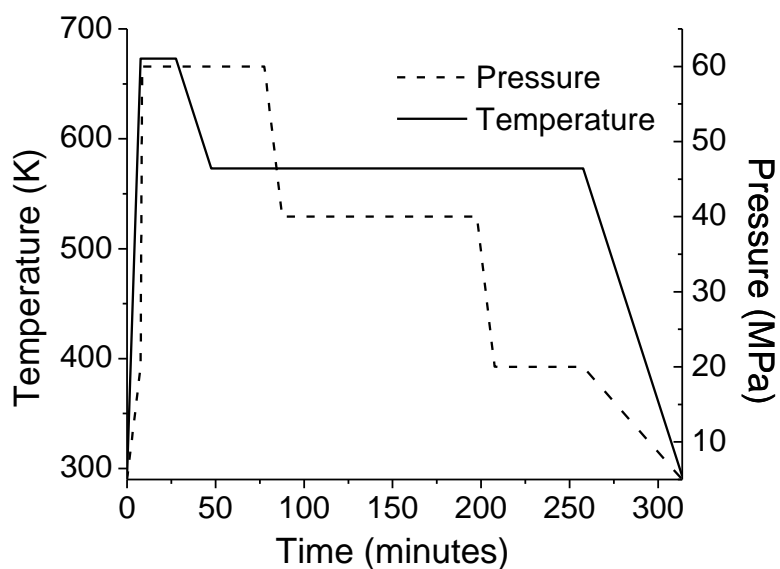


Figure B.6 The temperature-pressure-time profile for PECS-processed specimens, C-PTS-P-13, C-PTS-P-14, C-PTS-P-15, C-PTS-P-16, C-PTS-P-17, C-PTS-P-18, and C-PTS-P-19. The heating rate and cooling rate was 50 K/minute and 5 K/minute, respectively. The maximum temperature was held for 20 minutes. The pressure was held at 20 MPa during heating until the specimen reached the maximum temperature. Once the specimen reached 673 K, the pressure was increased to 60 MPa. To reduce possible residual stresses, the specimen was cooled to 573 K and thermally annealed for 120 minutes. The pressure was slowly reduced in steps during cooling.

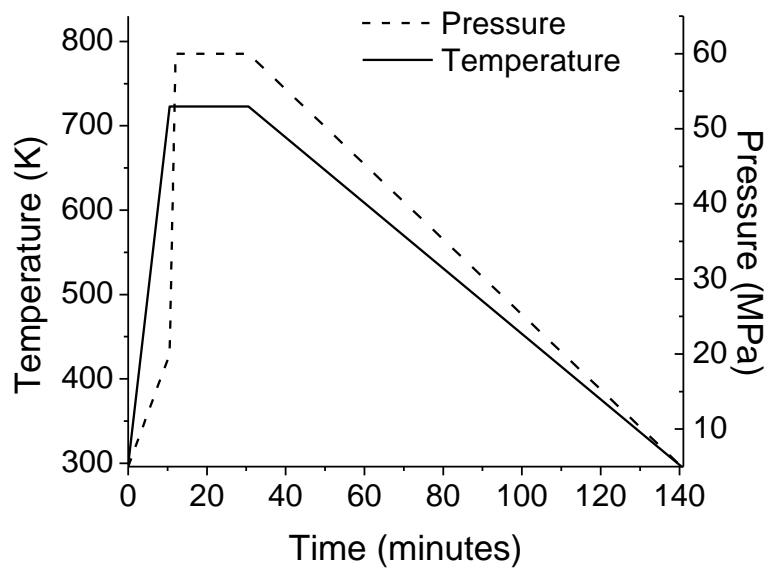


Figure B.7 The temperature-pressure-time profile for PECS-processed specimens, C-PTS-P-20, C-PTS-P-21, C-PTS-P-22, C-PTS-P-23, and C-PTS-P-24. The heating rate and cooling rate was 50 K/minute and 5 K/minute, respectively. The maximum temperature was held for 20 minutes. The pressure was held at 20 MPa during heating until the specimen reached the maximum temperature. Once the specimen reached 723 K, the pressure was increased to 60 MPa. The pressure decreased during cooling at a ramp rate of 0.64 MPa/minute.

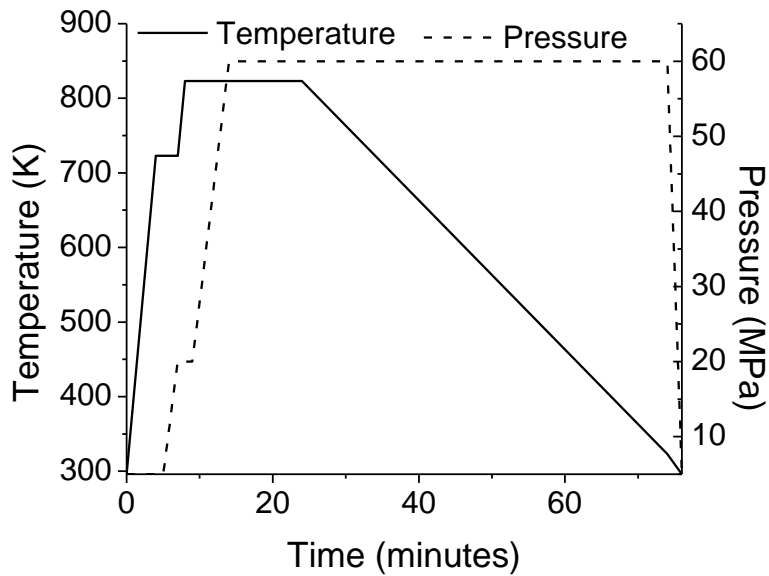


Figure B.8 The temperature-pressure-time profile for PECS-processed specimens C-PTS-P-25 and C-PTS-P-29. The maximum temperature of 723 K was held for 16 minutes. The heating rate and cooling rate was 100 K/minute and 10 K/minute, respectively The pressure was held at 60 MPa until the specimen reached room temperature.

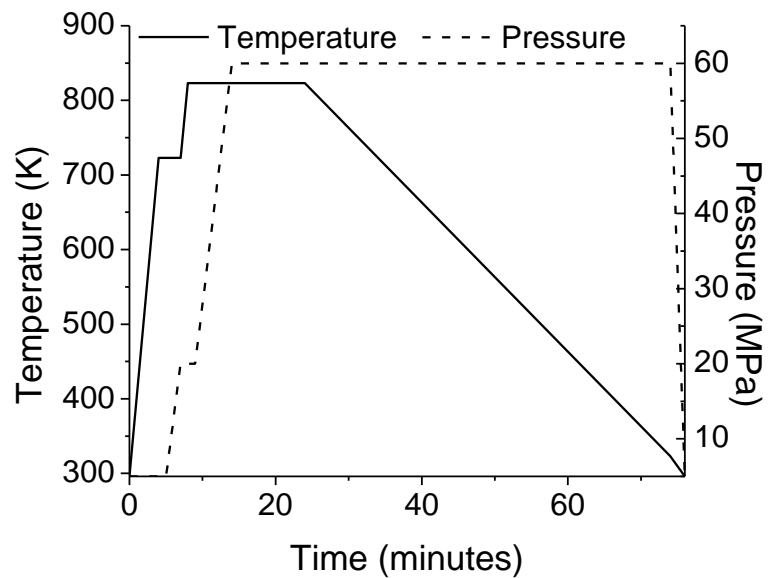


Figure B.9 The temperature-pressure-time profile for PECS-processed specimens C-PTS-P-26 and C-PTS-P-30. The maximum temperature of 723 K was held for 16 minutes. The heating rate and cooling rate was 100 K/minute and 5 K/minute, respectively The pressure was held at 60 MPa until the specimen reached room temperature.

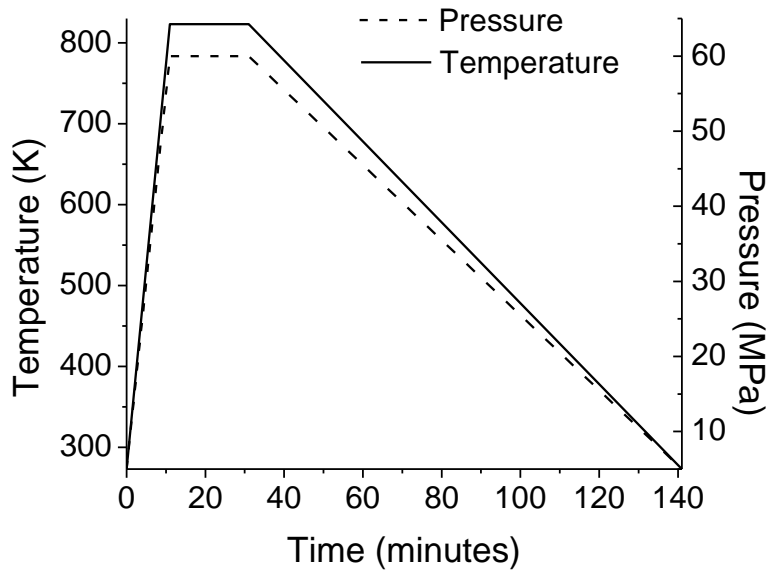


Figure B.10 The temperature-pressure-time profile for PECS-processed specimens C-PTS-P-27 and C-PTS-P-31. The heating rate and cooling rate was 50 K/minute and 5 K/minute, respectively. The ramp rate for pressure during heating was 5 MPa/min and 0.5 MPa/min during cooling. The specimens were sintered at the maximum temperature and pressure for 20 minutes.

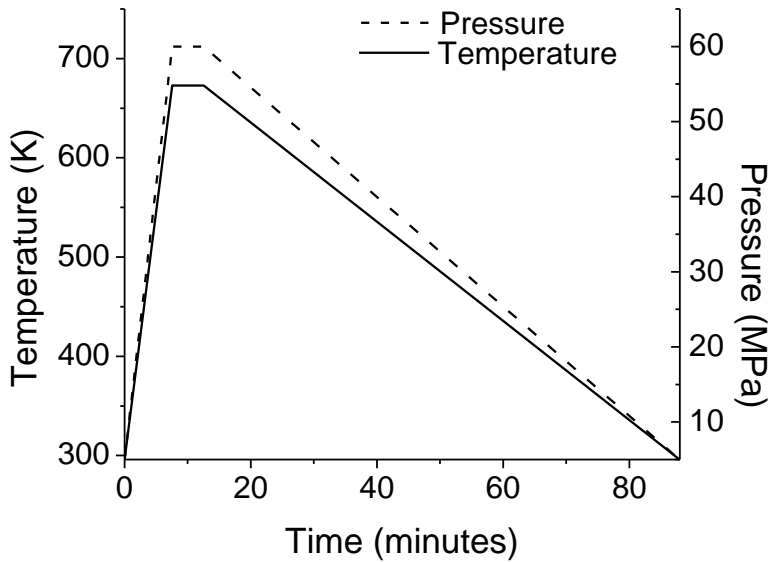


Figure B.11 The temperature-pressure-time profile for PECS-processed specimen C-PTS-P-28. The heating rate and cooling rate was 50 K/minute and 5 K/minute, respectively. The ramp rate for pressure during heating was 5 MPa/min and 0.5 MPa/min during cooling. The specimen was sintered at the maximum temperature and pressure for 5 minutes.

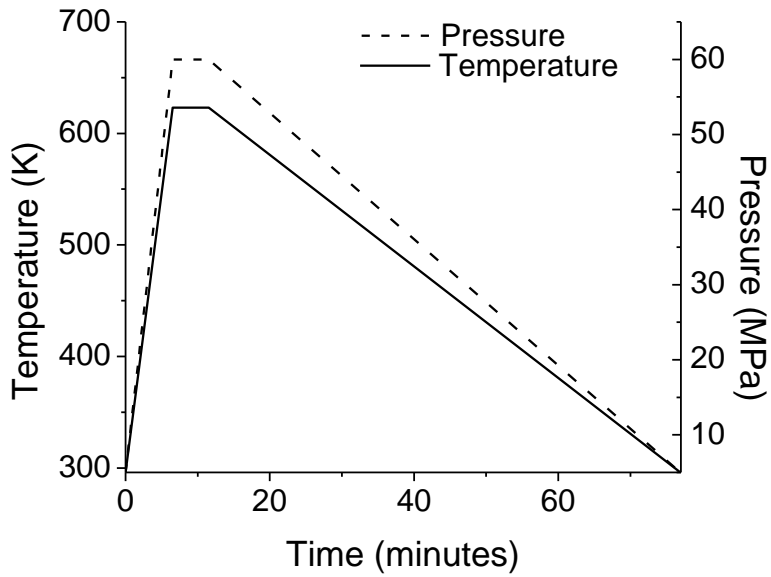


Figure B.12 The temperature-pressure-time profile for PECS-processed specimens, C-PTS-P-32, C-PTS-P-36, and C-PTS-P-37. The heating rate and cooling rate was 50 K/minute and 5 K/minute, respectively. The ramp rate for pressure during heating was 5 MPa/min and 0.5 MPa/min during cooling. The specimens were sintered at the maximum temperature and pressure for 5 minutes.

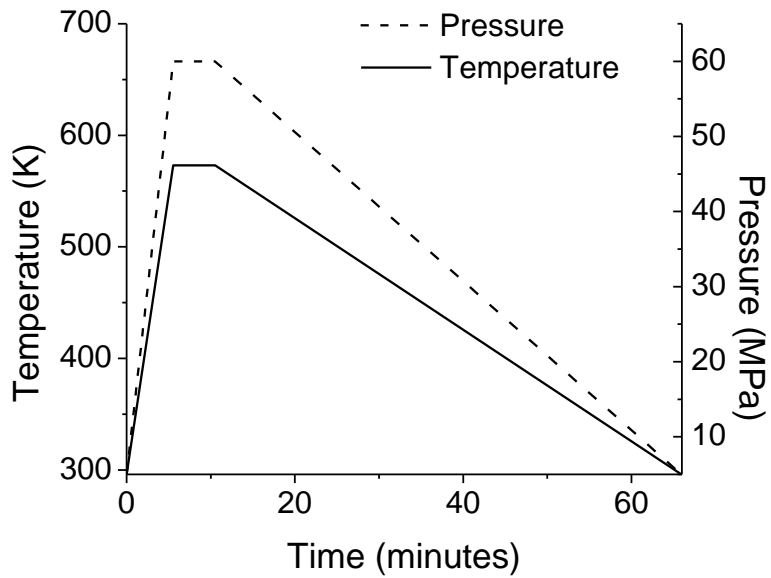


Figure B.13 The temperature-pressure-time profile for PECS-processed specimen C-PTS-P-33. The heating rate and cooling rate was 50 K/minute and 5 K/minute, respectively. The ramp rate for pressure during heating was 5 MPa/min and 0.5 MPa/min during cooling. The specimen was sintered at the maximum temperature and pressure for 5 minutes.

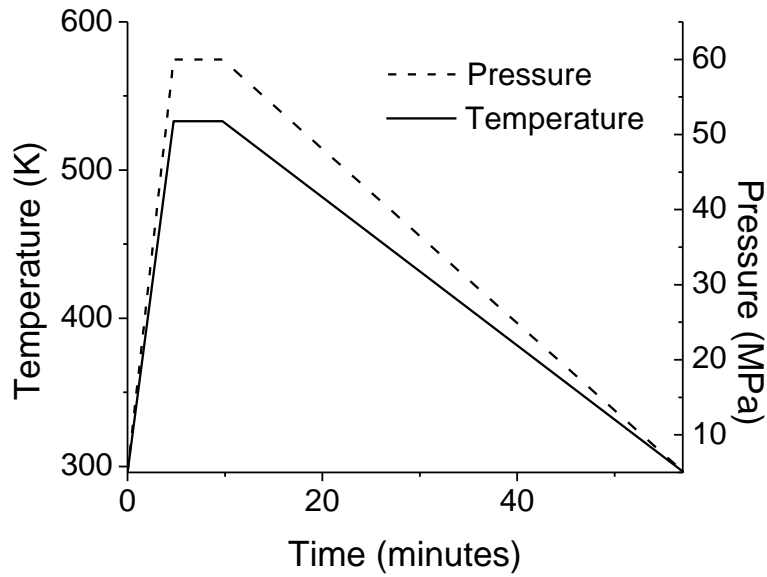


Figure B.14 The temperature-pressure-time profile for PECS-processed specimen C-PTS-P-34. The heating rate and cooling rate was 50 K/minute and 5 K/minute, respectively. The ramp rate for pressure during heating was 5 MPa/min and 0.5 MPa/min during cooling. The specimen was sintered at the maximum temperature and pressure for 5 minutes.

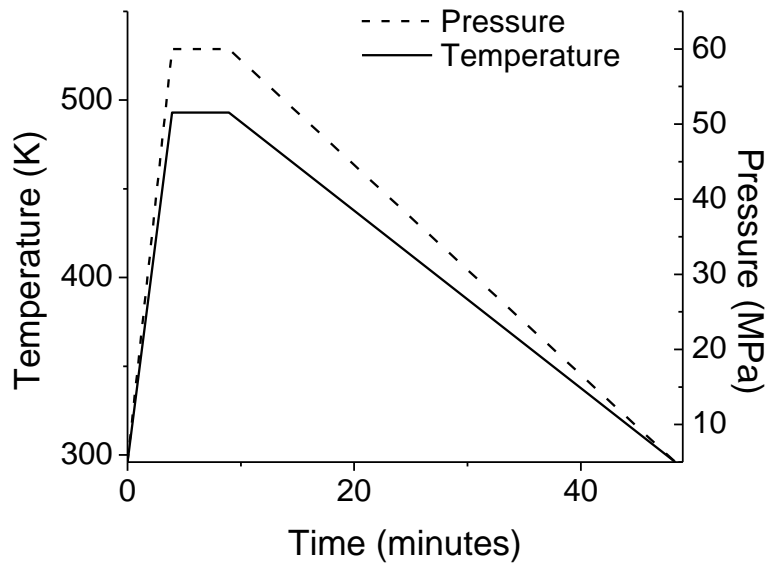


Figure B.15 The temperature-pressure-time profile for PECS-processed specimen C-PTS-P-35. The heating rate and cooling rate was 50 K/minute and 5 K/minute, respectively. The ramp rate for pressure during heating was 5 MPa/min and 0.5 MPa/min during cooling. The specimen was sintered at the maximum temperature and pressure for 5 minutes.